A thesis submitted to the University of Manchester for the degree of Doctor of Philosophy (PhD) in the Faculty of Engineering and Physical Sciences

For research on

Controls on the Matrix Permeability and Acoustic Velocities in Jurassic Haynesville Shale USA

Submitted to

The Department of Earth, Atmospheric and Environmental Science
The University of Manchester

Bashir, Yusuf Abba
Oct 2022

Table of Contents

Chapter 1 – Introduction **28**

1.1 Overview 28

1.2 Objectives 30

Chapter 2 – Background 31

2.1 Mudstones 31

2.1.2 Mudstone (Shale) mineralogy 31

2.1.3 Depositional Environment and Diagenesis 32

2.1.4 Burial and Diagenesis 33

2.2 Petrography of mudstones: pore spaces over a range of scales 34

2.3 Permeability of Mudstones 38

2.3.1 Permeability Measurement 38

2.3.2 Darcy's law 39

2.3.3 Knudsen number and flow regimes 40

2.3.4 Slip-flow and Klinkenberg correction 41

2.3.5 Permeability Modelling 42

2.4 Dependence of permeability on effective pressure 44

2.5 Elastic pore closure 46

2.6 Seismic velocities, porosity, and permeability 47

2.7 The effective pressure coefficients 48

Chapter 3-Characterization of Test Materials 51

3.1 Haynesville Shale Geological setting 51

3.2 Haynesville Core and Log 53

3.3 Mineralogy and petrography of the samples studied 57

3.3.1 Petrographic Study 57

3.3.2 X-ray diffraction (XRD) 58

3.4.1 Mineralogical and microstructural observations of the samples 63

3.5 General observations concerning mode of occurrence of key minerals. ... 70

(a) Detrital minerals 70

(b) Diagenetic Minerals 71

3.6 Relationship Between Rock Fabric and Mineralogy 72

3.7 General observations of samples pertaining to experimental methods employed 72

3.8 Conductive Porosity 73

3.9 Samples selected for permeability and velocity measurements. 74

3.10 Sample preparation for high pressure testing. 74

3.11 Organic Carbon Analysis 75

Chapter 4 – Experimental Methods for Permeability and Acoustic Velocity Measurements 86

4.1 Introduction 86

4.2 Permeability measurement 86

4.3 Apparatus and calibration 87

4.3.1 The CoreTest rig. 87

4.3.2 Pressure Transducers Calibration 90

4.3.3 The BigRig 92

4.4 Oscillating pore pressure method 92

4.5 Pulse transient (decay) method 95

4.6 Permeability measurement under steady state conditions; The constant pressure difference technique. 98

4.7 Experimental procedures 100

4.7.1 Oscillatory Pore Pressure measurements 100

4.7.2 Pulse Transient (Decay) measurements 101

4.7.3 Constant Pressure Difference test (steady-state flow) 102

4.8 Testing Darcy's law for the flow of argon gas through shale 104

4.9 Acoustic Velocity measurements. 106

4.10 Influence of elastic anisotropy 108

4.11 Bulk Moduli 108

4.13 Experimental Methods 112

4.14 Reservoir Modelling 120

Chapter 5: Experimental Results 1-Permeability and Bulk Modulus Measurement 122

5.1 Permeability Measurements 130

5.1.1 Influence of pressure cycling at constant pore pressure. 130

5.2 Influence of different constant pore pressures on permeability 132

5.3 Permeability at low pore pressures –slip flow 136

5.4 Permeability Anisotropy 141

5.5 Pore Volumometry 142

5.6 Permeability measurements using the CoreTest Rig. 144

5.7 Influence of Mineralogy and Porosity on Permeability 146

Chapter 6: Experimental Results 2-Acoustic velocity measurements. 148

6.1 Acoustic Velocity Measurements 148

6.1.1 Measurements on dry samples without pore pressure 151

6.1.2 Pore Pressure effect on Vp 153

6.1.3 Analysis of the pore pressure effect on P-velocities 155

6.2 Three different pore pressure coefficients – summary so far. 158

6.3 Influence of liquid saturation on $\boldsymbol{Vp}$ 159

Chapter 7 – Discussion 164

7.1 Influence of effective pressure on permeability of Haynesville shale 165

7.1.1 Comparison of data within the Haynesville shale dataset 165

7.1.2 Implications of the range of permeabilities observed with effective pressure variation. 166

7.1.3 Pore space storativity and pore volumometry 168

7.2 The effective pressure law and the relationship between permeability and acoustic velocity data 169

7.3 Influence of Porosity on Permeability 172

7.4 Influence of fluid replacement on acoustic wave velocity 173

7.5 Incorporating pressure sensitivity into reservoir modelling. 177

Chapter 8 – Summary and Conclusions 184

8.1 Summary of the study.....184

8.2 summary of Main Findings 185

8.3 Future Work 187

LIST OF FIGURES

*Figure 2.1 Ternary diagram for Hayneville shale from the same bore hole as the samples used in this study, taken from Dowey and Taylor (2020).*_____ ***32***

Figure 2.2 Compaction of a mixture of clays and detrital phyllosilicates around silt grains, showing development of preferred orientation of phyllosilicates platelets and residual porosity; adapted from (Philipp et al., 2017) _____ ***34***

*Figure 2.3 A: Intra organic pores shown in organic matter Spherical intra organic pores C & D Cracklike and intermittent pores at the interface of organic matter and other minerals (Ma et al., 2017)*_____ ***36***

Figure 2.4 E–F: Inter mineral pores between minerals, G: irregular-shape Intra mineral pores within pyrite framboids, H: Intra mineral pores within carbonate minerals such as calcite. BSE- backscattered electron image. SE-secondary electron image. (Ma et al., 2017) _____ ***36***

Figure 2.5 These are two transmission electron microscopy (TEM and STEM) images from the study of Ma et al. (2017) showing the nanometric-scale pores that form the connected (conductive) networks in Haynesville shale. A is a TEM image of lattice fringes in clay showing intra-mineral pores with a crack-like geometry. Scanning TEM image B shows a cluster of small clay platelets supporting 40 nm and smaller intergranular porosity _____ ***37***

Figure 2. 6 Diagram shows the relationship between Knudsen number, pore diameter and pore pressure for argon gas. For pore pressure greater than 10 MPa slip flow should only be encountered for pore throat radius less than ~30 nm. _____ ***41***

Figure 2. 7 Left - Conceptual pore model developed by Zoback & Byrelee (1975) sandstone with strong stress-supporting frame (black) and high compressibility clays (grey) lining pores (white). Right – Kwon (2001) model where clay forms a connected matrix in which flow paths reside. Given the Heller et al. (2014) observation of alpha<1, the model on the right is supported – where effective pore widths are similarly affected by changes in confining and pore pressure. _____ ***45***

*Figure 3.1 Strike-Oriented Chronostratigraphic diagram including a type well, sequence stratigraphy, ages and eustatic sea level curves. Adapted from (Hammes 2009). **52***
*Figure 3.2 Map of Study area showing Late Jurassic structural elements and the red striped area is the Haynesville Shale productive area. The structures are controlled by the opening of early Gulf of Mexico basin that controlled the Haynesville deposition in east Texas and West Louisiana. Areas in blue and red crosses are highs while the green are basins. Image from (Hammes et al. 2011) **53***
*Figure 3.3 Paleogeographic Map of Jurassic Haynesville Shale deposition (after Hammes et al. 2011) with the Hewitt Land core sample location (HB). **54***
*Figure 3.4 Core description of Hewitt land LLC 4 Well, highlighting sedimentary features, and horizontal lines on log represent mineralized veins. The facies column shows grainsize, mineral and textural observations noted during the core logging and thin section studies. The core is dominated by shell fragments, light fractures, and bioturbation. Produced by Yusuf Bashir **55***
*Figure 3.5 The slabbed core used for the analysis, ranging in depth in between 11372 -11802 ft. The image is courtesy of Weatherford laboratories. The empty slots are slabs in other school laboratories. **56***
*Figure 3.6 A shows a ternary diagram that characterizes the modal composition of the samples on the basis of (qtz + fsp + pyrite), (phyllosilicates, i.e. detrital mica + clays, and organic (maceral) particles and (total carbonate for a wide range of shales of different origins (from Rutter et al. 2017), including previously published compositional information for Haynesville shale (Hammes, 2009; Sone & Zoback, 2013). B shows the corresponding data for the samples used in the present study. With respect to carbonate content, YB03 is particularly calcite-rich (47 wt%) and YB06 is particularly rich in dolomite (38.3wt %) plus calcite (20 wt%). The remainder contain less than 18 wt% total carbonates. **63***
Figure 3.7 Thin section photomicrographs of sample YB01. This sample is rich in phyllosilicate (XRD analysis shows 29wt% phyllosilicate and 13wt% calcite. Diagenetic pyrite is also present within the samples. The sample recorded the highest total organic carbon of all samples (2.48 wt% TOC). (A) Clusters of microfossils with cavities filled with secondary calcite, in a finer matrix of fine-silt sized quartz and phyllosilicate grains (crossed polars; thin section normal to foliation). (B) Cluster of microfossils with cavities filled with secondary sparry

calcite, leaving residual occluded voids in their centres, in a finer matrix of fine-silt sized quartz and phyllosilicate grains (crossed polars, normal to foliation). (C) Microfossil (foraminiferid) with cavities filled with secondary sparry calcite, and partially with spheroids of pyrite, in a finer matrix of fine-silt sized quartz and phyllosilicate grains. (Crossed polars, thin section normal to foliation)... ***64***

Figure 3.8 Thin section photomicrographs of sample YB 02 which is rich in phyllosilicate (XRD 30%) Both imaged are of the same field (PPL and XP) and viewed normal to foliation. The sample belongs to the group that are carbonate-poor and contain similar proportions of framework silicates and phyllosilicates and is relatively well foliated. YB 02 is fine grained with similar average concentrations of sand and silt size grains. The sample He porosity is 8.16% which is relatively termed porous. Thin section view (A) shows fine silt-sized detrital grains in a phyllosilicate-rich matrix, with sinuous calcite veins. View (B) shows more clearly the fine-silt sized detrital grains in a phyllosilicate-rich matrix. ***65***

Figure 3.9 Thin section photomicrographs of YB 03 (views along foliation) showing remarkable bioturbation which has destroyed continuity of layering. The sample rock is only weakly banded but fissile with calcareous fossil fragments in matrix of finer-grained clays and detrital micas and silicates. (Fine silt-sized) A) Optical micrograph, crossed polars, view parallel to foliation showing cracks. Compared to the relatively carbonate-poor samples, the foliation is not very evident from the orientation of elongate particles, but cracks have opened during the sectioning process, and these have become filled with blue impregnation resin. These have formed parallel to bedding. There is a large proportion of calcareous fossil debris, together with secondary calcite cement, and a matrix of fine silt-sized clastic grains and a phyllosilicate matrix B) shows similar image (Optical micrograph, crossed polars), view normal to foliation..... ***66***

Figure 3.10 YB04 A) view parallel to bedding XPL Optical micrograph, cut normal to layering, showing silt and smaller-sized clastic grains in a phyllosilicate matrix. Ellipsoidal particles are strongly flattened rip-up clasts (intraclasts) that may have had a strong shape factor before they were redeposited. The rock contains a small proportion of shelly fossil debris. B) view normal to foliation, plane-polarized light, view onto plane of layering. The lithic rip-up clasts that appear as strongly flattened ellipsoids in the previous picture here display an

*equant shape, supporting the view that this rock displays a transversely isotropic fabric..... **67***
*Figure 3.11Sample YB05 A) Optical micrograph, crossed polars, view onto plane of layering, showing uniform arrangement of fine silt sized clastic grains in a phyllosilicate matrix with shelly calcite fragments. B) Larger magnification image of the central part of the previous image, showing calcareous fossil fragments in fine silt sized clastic grains within a phyllosilicate matrix..... **68***
*Figure 3.12Thin section photomicrographs of YB06, the samples are two images of similar fields but different magnifications, A) PPL, B) right one XP, both showing aview onto plane of layering, with a uniform granular texture of carbonate grains (ferroan dolomite and calcite carbonate mud) in a matrix of finer framework silicate and phyllosilicate grains. **68***
*Figure 3.13 Thin section photomicrographs of YB07 A)YB07 is microstructurally similar to YB03, but with much less carbonate. This sample is viewed along the foliation (crossed polars) and is better foliated than YB03 owing to the smaller carbonate content and greater phyllosilicate content. B) is a plane polarized light optical image viewed normal to the plane of foliation. Fossil debris and sinuous carbonate veins can be seen in an apparently isotropic clastic matrix. **69***
*Figure 3.14Thin section photomicrographs of Sample YB08 A) viewed normal to the foliation. Microstructurally and mineralogically similar to YB04, this rock also shows in this view apparently equant rip-up clasts set in an extremely fine matrix of flattened and oriented silt-sized clasts and phyllosilicate matrix. B) similarly oriented but higher magnification (Cross polars), this image displays the extremely fine granularity of the rock. **70***
*Figure 3.15 A & B Graphs showing weight loss data during oven drying expressed as changes to the densities of samples YB03, YB08, YB06, YB07 and YB01. The densities became constant after 240 hours of drying. The oven was controlled at 60° to inhibit dehydroxylation of swelling clays and thermal damage to organic matter particles. **75***
*Figure 3.16 General diagram showing the different fractions of the total organic matter of analysed rocks, the corresponding parameters and their recording (Lafargue et al. 1998). **77***
Figure 3.17 The first and second Flame Ionisation Detector (FID) stages are named S1 and S2 respectively. S1 is amount of Hydrocarbon (HC) already present in the sample and it also represents thermally vaporised free

hydrocarbon contained in the rock while S2 is the amount of hydrocarbons generated by degradation of OC during between 350°C & 650°C it represents hydrocarbon produced from the cracking of sedimentary organic matter..... ***77***
Figure 3.18 Examples of pyrograms for Haynesville YB 07 and YB 02 samples showing the S1 and S2 peaks. ***78***
Figure 3.19 FID column within the instrument, the Flame Ionisation Detector detects the hydrocarbon within the samples. ***79***
Figure 3.20 HI (hydrogen index) vs Tmax cross plot: the plot shows the kerogen type and maturity range of the samples..... ***79***
Figure 3. 21 Van Krevelen diagram of the Haynesville samples, it shows they all fall within the type IV of the kerogen types, which is the gas-prone section.. ***80***
Figure 3.22 Example of a calibration of the helium porosimeter, showing how P1/P2 varies as the volume of steel discs in the sample chamber is increased. Errors of measurement can be estimated from the parameters of the linear regression. ***82***
Figure 3.23 A) External photographic view of the Res Lab Porosimeter B) A schematic diagram showing the layout of the Porosimeter, with a representation of a porous rock cylinder inside volume V2 C) Specimen vessel (volume V2) and calibration disc set provided with the Porosimeter..... ***84***
Figure 3.24 Comparative porosities estimated from the XRD and helium imbibition methods. The XRD results are equal to or greater than the helium porosities, suggesting that in some samples there has been incomplete flooding of the pore spaces with helium..... ***85***

Figure 4.1 The CoreTest rig used for permeability measurements. ***88***
Figure 4.2 CoreTest Permeameter plumbing outline showing the valves. The pore pressure connections to the sample ends are labelled DOWN I and UP II. ***89***
Figure 4.3 A schematic diagram of the CoreTest permeameter data-logging arrangements as used for permeability measurements. ***89***
Figure 4.4 a) Plot displaying the calibrations and illustrating between the transducers' voltage outputs and pressure measured using a Bourdon tube gauge. b) The regression analysis table for the confining pressure (Cp), upstream and downstream pressures. ***90***

Figure 4.5 Plot illustrating the caliper position and the corresponding voltage output from the LVDT on the pore Volumometer..... ***91***
Figure 4.6 Images of the big rig. (a) shows a pore volumometer and its control unit, and in (b), which shows an image of the whole rig, the pore volumometer can be seen mounted in the right front side of the cylindrical safety shield around the pressure vessel. ***92***
Figure 4.7 Sinusoidally oscillating upstream pressure (blue) and the downstream response recorded (red), with decreased amplitude and phase shifted (Mckernan et al., 2014). ***93***
Figure 4.8 Solution space showing the region in which physically meaningful values of A *and* θ *can be found, delimited by the iso-* ξ *lines* $\xi = 0$ *&* $\xi = \infty$*. Storativity* (ξ) *is directly proportional to porosity. The gain and phase shift coordinates of the typical point shown also correspond to coordinates defined by the intersection of lines of constant ξ and η. .....* ***95***
Figure 4.9 a) Schematic plot of data displayed in a pulse transient experiment, here upstream pressure is red, while downstream pressure is black. b) Plot of log of the time-decaying pressure ratio, in this case for samples of gneiss of two different permeabilities; the permeability is measured from the gradient of the fitted line (ω)*(data of Rutter, pers.Comm.2020) .....* ***95***
Figure 4.10 Comparison of permeabilities measured using the oscillating pore pressure method (Bernabé et al. 2006) and the transient pulse decay method (Brace et al. 1968) Transient pulse decay measurements were processed using both equation 6 (CUI et al. 2009) (grey circles) and equation 7 (CUI et al., 2009) which takes porosity into account. Data for Whitby shale, after McKernan et al. (2017). ***98***
Figure 4.11 Graph showing the National Institute of Standards and Technology (NIST) chemistry webbook page used for the correction of viscosity for pressure. ***103***
Figure 4.12 Oscillatory pore pressure technique of permeability measurement with a constant period of 200 sec, constant confining pressure of 18.2 MPa, in order to test the validity of Darcy's law. The results plotted as log permeability against a six-fold change in pore pressure wave amplitude show that the permeability remains unchanged within experimental error (estimated to be ± 0.1 log units), hence Darcy's law is followed within experimental error. ***105***

Figure 4.13 Example of the influence of confining pressure on P and S wave velocities, zero pore pressure, dry, for Darley Dale sandstone (Rutter, pers. Comm. 2020). S velocities are lower than P velocities and typically the curves diverge to higher confining pressures. ***107***
Figure 4.14 (a) shows the variation of the gas deviation factor z for argon gas as a function of pressure in bars (data of Gosman et al. 1969), with a polynomial fit. (b) shows the derived curve of real gas/ideal gas compressibility ratio for argon gas with a polynomial fit $y=-4.470226E-12x^4 + 1.103348E-08x^3 - 8.324170E-06x^2 + 1.068256E-03x + 9.955813E-01$ *(where y is the compressibility ratio and x is pressure in bars) valid up to 1000 bars (100 MPa). Ideal gas compressibility is taken as* $1pgas$ ***111***
Figure 4.15 A schematic diagrams showing the ultrasonic velocity experimental setup...... ***112***
Figure 4.16 Dead time vs pressure in microseconds. The dead time was measured without the sample in the assembly, confining pressure was increased and time of flight of the waves was measured...... ***113***
Figure 4.17 The Green Rig apparatus used for the acoustic wave velocity measurements. The green panels are the steel plates that provide safety screening for the user. The left-hand side has the electrical system used for control functions and for monitoring the data. The vessel uses oil as a confining medium while argon gas is used as pore fluid. The pore pressure volumometer for argon is mounted behind the apparatus and is identical to the pore volumometer dedicated for use with water that can be seen to the left of the Heise pressure gauge. ***117***
Figure 4.18 Electrical control and signal handling system used for monitoring and data recording during experiments on the Green Rig. The digital multimeters read confining pressure, pore pressure and pore volumometer displacement. Other items drive the acoustic signals and provide measurement and control for the pore pressure servo-controllers...... ***118***
Figure 4.19 A sample assembly for acoustic velocity experiments, with the 25 mm diameter specimen inside the (black) heat-shrink rubber tubing, between the two transducer housings. The right hand end is the closure plug that seals the top end of the pressure vessel. ***119***

*Figure 5.1 Sensitivity of log permeability to confining pressure shown at constant pore pressure of 10 MPa, seven pressure cycles were measured (labelled). Estimated uncertainty in permeability values is ±0.1 log units. The first pressure increment shows non-recoverable permeability loss, whereas subsequent pressure cycles showing nearly non-linear elastic behaviour. **131***

*Figure 5.2 YB 03P log Permeability plotted as a function of confining pressure at 10MPa, 20 MPa(series4), 30 MPa (series5), 40 MPa (series6), 50 MPa (series7) and 60 MPa (series14) pore pressure. It shows the movement of the data points towards the right as the pore pressure is increased, in accordance with the principle of effective pressure. **131***

*Figure 5.3 Analysis of permeability data for three tight rock types tested over a range of pore pressures, all on the BigRig, to demonstrate the effective pressure principle applied to permeability (from Rutter, Mecklenburg, and Bashir, 2022). In the equations for best-fit curves, y = log(k) and x = Pc – n Pp. Pore pressures for Pennant sandstone (a tight gas sandstone) were 10, 30 and 50 MPa, with n = 0.86, for Haynesville shale were 10, 20, 30, 40, 50 and 60 MPa with n = 1.1, and for Bowland shale were 10, 25, 40 and 50 MPa with n = 1.1 but increasing in value with effective pressure. All curves are concave upwards and diverge with increasing effective pressure, so that permeability differences are most pronounced at highest effective pressures. **132***

*Figure 5.4 Data for YB 03 sample showing log permeability variation with confining and pore pressure using equation 5.2. Here total confining pressure is used for the horizontal axis and contoured for pore pressure. The pore pressure is presented in a colour bar, while the sample log_{10} permeability is presented with the coloured circles and fitted lines at constant pore pressure. **134***

*Figure 5.5 Pulse transient tests from series YB03U (table 5.1). The log of ratio of instantaneous pore pressure to the whole pore pressure step range is plotted against elapsed time. Best-fit straight lines are shown, that must pass through the origin with a negative slope, from which the permeability is calculated. **136***

*Figure 5.6 Example of the raw data from constant flow rate test R6 (Table 5.1). The slope of the best-fit line gives the volumetric flow rate, from which the permeability is calculated. Total confining pressure = 9.7 MPa, Pp (up) = 2.0 MPa and Pp (downstream) = 1.0 MPa. **137***

Figure 5.7 Measured log permeability data plotted against pore pressure at constant effective confining pressures of 9 (YB03P) and 30 MPa. At pore

pressures above about 4 MPa the permeability is unaffected by variations in pore pressure. At low pore pressures (below 4 MPa) permeability is enhanced, as predicted by the gas-slippage effect. Qualitative trend lines are shown for each dataset. ***137***
Figure 5.8 Normalized permeability (permeability measured normalized by permeability at high Pp to combine both datasets YB03 in fig. 5.7. Enhanced flow (slip flow) begins at pore pressures smaller than ~ 4MPa. ***138***
Figure 5.9 Plot of normalized permeability versus reciprocal pore pressure for sample YB03P for measurements at 9 MPa and 30 MPa effective confining pressure...... ***139***
Figure 5.10 Log (gain) versus phase shift data for YB03 samples in both the core orientations parallel (triangles) and normal (circles) to layering. Plots track lines of constant ξ (pronounced Xi). Yb03N shows a much larger value of ξ does YB03P, implying that flow across the layering 'sees' a greater proportion of the total pore space than flow along the layering. (from Rutter, Mecklenburg, and Bashir, 2022)...... ***140***
Figure 5.11 Permeability of specimens YB03P and YB03N comparing permeabilities measured for flow normal to bedding and flow parallel to bedding, all at constant pore pressure (gas) = 10 MPa. In both cases the first pressure cycle corresponds to closure of pores that subsequently do not reopen. Subsequently, the pressure sensitivity normal to layering is weaker than parallel to layering. It is reasonable to expect pores parallel to layering to be more sensitive to pressure if they are of low aspect ratio oriented along the bedding, and for this to be reflected in the relative pressure sensitivity of the flow... ***141***
Figure 5.12 (a) (left) Recorded values of pore strain vs Terzaghi effective pressure for YB03P at 48.1 and 68 MPa pre pressures, with logarithmic fits. (b) Bulk modulus dry for YB03P at the same pore pressures. The curves are asymptotic to the Ko modulus at 61 GPa. (From Rutter, Mecklenburg, and Bashir, 2022). ***142***
Figure 5.13 m value for Haynesville shale versus Terzaghi effective pressure. m data from pore volumometry decrease rapidly with $Peff$. (From Rutter, Mecklenburgh, and Bashir, 2022). ***144***
Figure 5.14 Results of the constant flow rate permeability tests on the CoreTest rig using the steady state flow method at constant pore pressure difference, expressed as log permeability vs Terzaghi effective confining pressure.

Individual pressure cycles were run alternating between constant Pc and constant Pp conditions, to produce the variations in effective pressure. Details are listed in Table 5.1. All of these four samples belong to the low carbonate% group. They were tested dry on cores cut parallel to the layering. All show a first pressure cycle more permeable than the subsequent ones, which are (non-linear) elastic, and the general value of permeability (e.g., at 30 MPa $Peff$) is rather similar. ***145***
Figure 5.15 log (k) versus porosity% for carbonate-poor through carbonate-rich samples, second and subsequent pressure cycles, at the $Peff$values shown. There is no apparent correlation. ***147***
Figure 5.16 log (k) versus carbonate vol% in all samples that had a second and subsequent pressure cycle, at the $Peff$ values shown. The carbonate-rich sample YB03 appears to be substantially less permeable than the carbonate-poor samples, although YB03 was taken to higher $Peff$, which would have had the effect of lowering the permeability by about one order of magnitude. .. ***147***

Figure 6.1 Ultrasonic P-wave velocity measurements plotted against confining pressure, for successive cycles of up- and down-pressure loading. Pore pressure (Pp) = 0. Successive loading cycles show stepwise increases in velocity but by decreasing amounts, suggesting that each pressure cycle causes irreversible stiffening, probably by crack closure. Five pressure cycles without pore pressure were performed before pressure cycles were performed with the addition of non-zero pore pressures. The fourth and fifth cycles were indistinguishable, however. Arrows indicate the form of up and down pressure steps, and this pattern applies to all the cycles shown. ***151***
Figure 6.2 Ultrasonic P-wave velocity measurements plotted against confining pressure of two samples, YB01N and YB03P (2nd pressure cycle) tested dry with no pore pressure, waver direction normal to bedding and parallel to bedding, respectively. Response was hysteretical in both cases. Direction of load increase and decrease is shown for each case, but the hysteresis response is different in each case. ***152***
Figure 6.3 Up-pressure cycles (sample YB03P, dry) showing influence of increasing values of argon gas pore pressure on P-wave velocities relative to zero pore pressure behaviour, plotted against total confining pressure. The pp=0

curve is shifted progressively to the right as pore pressure is increased. The zero pore pressure data are also shown fitted by a Hill function (see text). ***154***
Figure 6.4 Up-pressure cycles (sample YB03P, dry) showing influence of increasing values of argon gas pore pressure, with Vp *plotted against Terzaghi effective pressure* $(Pc - nPp)$*, with assumed n = 1. At low pore pressure there is under-compensation whilst at higher pore pressures the pore pressure over-compensates for the confining pressure.* ***154***
Figure 6.5 Schematic illustration of the definition of n from experiments with and without pore pressure. Also shown is the effect expected (at zero pore pressure) when gas in the pore spaces is replaced by a (stiffer) liquid (the Gassmann effect).* ***156***
Figure 6.6 Plot of n and m–values against Terzaghi effective pressure for Haynesville shale YB03 in the layer parallel orientation. These parameters are both pore pressure coefficients. The upper two groups of data (n*–values) were obtained from the lateral separation of the acoustic velocity versus total confining pressure curves for* Pp *= 0 minus data at 67.7 and 48.1 MPa pore pressures (gas). The lower two groups of data (m–values) were derived from the pore volumometry data at the same pore pressures.* ***158***
Figure 6.7 Results of velocity measurements on sample YB03P after vacuum water saturation (4 pressure cycles) and compared with previous dry test (cycle #10) on the same sample. The wet tests are substantially slower than the dry test, and successive pressure cycles wet produced substantial increases in velocities...... ***161***
Figure 6.8 Plot of velocities recorded from sample YB03P at 100 MPa confining pressure versus elapsed time on the up-pressure part of the cycle. ***161***

Figure 7.1 Summary of the results of permeability measurements versus effective pressure for the specimens that were subjected to pressure cycling. These data are all from the second and subsequent pressure cycles. YB03 data are from tests on the BigRig (with effective pressure coefficient = 1.1) and the remainder from tests (to lower pressures, with effective pressure coefficient = 1.0) on the CoreTest rig. The upward concavity is evident best in the YB03 data but can also be seen in the other data. Because YB03 was taken to higher pressures, the curve has been lowered by about one order of magnitude in log(k). ***165***

Figure 7.2 Schematic illustration of the deduced dual-porosity microstructural geometry controlling flow through the shales. Networks of laterally connected but very thin pore spaces occur parallel to the layering, poorly linked to more equant and/or occluded pores that account for most of the porosity and hence total storativity..... ***168***
Figure 7.3 Permeability plotted as a function of effective pressure at a constant pore pressure of 10 MPa fitted to an exponential law and Gangi model (power law) fit.....171
Figure 7.4 log permeability versus porosity organized by lithofacies from a mixed clay-bearing carbonate-siliciclastic reservoir in Offshore Congo (Wonham et al. 2010). Observed variability in the samples of Haynesville shales reported here would fit into one of the squares on this figure, therefore it is not surprising that no trend is evident (in Fig. 5.2)..... ***173***
Figure 7.5 Re-presentation of the experimental data shown previously in Fig. 6.7, relating P-wave velocities to confining pressure. The up-down pressure cycling of the dry rock is shown for reference (red points), together with the succession of up-down pressure cycles after attempted saturation with water under vacuum. Successive pressure cycles cause the curves to be progressively displaced to higher velocities. However, all these data still lie below the curves for the dry rock. Additionally, a calculated curve is shown (labelled wet), assuming Voigt-Reuss averaging, to illustrate the faster velocities expected when the rock is fully saturated. Calculated velocities are increased by ca 250 m/s..... ***176***
Figure 7.6 Barnett shale average daily gas production rate per well in MSCF/day against time, showing the similarity of the curves (From Kenomore et al. 2018, citing Baihly et al. 2015) MSCF = million standard cubic feet; one standard cubic foot of gas is defined at as 20^{o}C and atmospheric pressure. ***178***
Figure 7.7 Schematic illustration of formation-parallel flow of gas through the rock matrix to a single hydraulic fracture (grey-shaded) draining into a horizontal production borehole. A similar flow is assumed to occur from the other side of the hydraulic fracture. This is the modelled configuration. ***180***
Figure 7.8 Plots of Permeability Factor for Haynesville (left) and Whitby (right) shales versus distance from the hydraulic fracture that drains the gas. Permfactor is the ratio of permeability at distance x divided by initial permeability (or permeability at infinite distance). Permeability decreases near

the hydrofracture because gas pressure drawdown increases the effective pressure closer to the fracture. Pwf is downhole gas pressure (psi). ***181***
Figure 7.9 Comparative production rates between Haynesville (left) shale and Whitby (right) shale, quantity of gas (scf/day) versus time (days) calculated using Gassim6 (Compare Fig. 6.6) for the first 90 days for a single hydraulic fracture (normally there are 20 or 30 per well). Pwf is the downhole pressure in psi. Gamma is the effective pressure coefficient. When gamma = 0 (blue curves) there is no effective pressure effect on permeability assumed, i.e., permeability is constant. When gamma > 0 the increasing effective pressure drives down the permeability, further reducing production rate (red curves), by about 35% in the case of Whitby shale, and by a smaller amount in the case of Haynesville shale. ***181***
Figure 7.10 Cumulative productions (millions of standard cubic feet) via a single hydraulic fracture calculated using Gassim6 for Haynesville and Whitby shales after 225 days and after 2000 days, each for the case of no permeability sensitivity to effective pressure (Gamma = 0) and with laboratory measured effective pressure sensitivity (Gamma > 0), and each as a function of downhole pressure (Pwf) held constant. The lower the downhole pressure, the greater the pressure gradient driving the gas flow, so the greater the production. The actual downhole pressure would be decided by engineering considerations. In both cases the inclusion of pressure sensitivity to the permeability has a very large effect on the cumulative production, reducing it by around 60%. ***182***

LIST OF TABLES

Table 3.1 *Samples picked for the experiments and the identifying number.* ***57***
Table 3.2 XRD mineral distributions (obtained initially as wt%) of the eight samples shown converted to vol% proportions (shown) and the principal phases were grouped into three (fig. 3.6) for the plotting of a ternary diagram to represent mineral proportions. Calculated porosities from bulk and XRD density, together with porosities obtained from helium porosimeter are presented. _ 62
Table 3.3 Haynesville Rock-Eval pyrolysis results showing the free Hydrocarbon-Carbon (S1), Hydrocarbon as a result of degradation of organic carbon (S2), hydrogen index (HI), Oxygen Index (OI) and total organic carbon (TOC). __ ***78***

Table 4.1 Sintered disc specifications ***87***
Table 4.2 The constant pressure difference, oscillatory pore pressure, and pulse transient techniques valves settings required during experiment on the core test rig when used for the permeability measurements. ***104***
Table 4. 3 Sources of errors and preventative measures taken to minimise them. ***105***

Table 5.1 summarizes the test conditions and results of permeability experiments that are described in the subsequent sections. Details of specimen locations and petrographic characterisation are provided in chapter 1. ..... ***129***
Table 5.2 Tabulation of log(k) at two effective pressures and carbonate content and porosity (data from Table 5.1). ***147***

Table 6.1 summarizes the test conditions and results of acoustic velocity experiments that are described in the subsequent sections. ***150***

Abstract

An experimental study is reported of the influence of mineralogy, microstructure, and effective pressure conditions on the permeability to argon gas and of the acoustic wave velocity in Haynesville shale, USA. Samples were prepared from slabbed core from a single well and characterized for mineralogy, porosity, density, and elastic constants. Permeabilities were measured using the steady-state flow method, the pulse transient method and the oscillating pore pressure method, and together with the acoustic wave velocities were measured over a range of confining pressures and argon gas pore pressures. Most data were collected at high effective pressures for free gas flow, while the pore pressures for the onset of slip flow (Knudsen number 10^{-2}-10^{-1}) were found to be <4 MPa.

Permeabilities were very sensitive to effective confining pressure ranging from 10^{-16} -10^{-19}. Pore volumometry was used to measure the influence of effective pressure on pore distortion and this was inferred to be responsible for the marked pressure sensitivity of porosity. The influence of confining pressure and pore pressure on both permeability and on ultrasonic acoustic wave velocities was found to follow an effective pressure law with effective pressure coefficients respectively 1.1 and 0.8. However, it was concluded that it was not possible to infer any parameters describing permeability from observations of acoustic wave velocities.

It was found that gas permeation through the shale parallel to the layering involved only a very small fraction of the total porosity and that for flow normal to layering a greater fraction of porosity was involved, but most of the porosity accounting for gas storage was inferred to lie in occluded or hard to access pores, leading to the concept of a dual porosity structure for the rock. This has implications for the applicability of laboratory measurements of permeability to the evaluation of yield of a shale gas reservoir.

Incorporation of pressure sensitive permeability into a model of a shale gas reservoir showed that if pressure sensitivity is ignored, modelling will seriously overestimate the yield and cumulative production from the reservoir. Whilst the hydrocarbon industry typically seems to ignore forward modelling of the behaviour of gas reservoirs based on laboratory data, this would be an unwise

course to take for the future used of shale-sealed conventional reservoirs for the storage of CO_2, compressed air, imported methane and hydrogen.

Declaration

No portion of the work referred to in the thesis has been submitted in support of an application for another degree or qualification of this or any other university or other institute of learning. All images used and data attributed to others is acknowledged as appropriate by reference to the published sources and are with permission of my Supervisors Dr Julian Mecklenburgh, Prof. Kevin Taylor and Prof. Ernest Rutter

Copyright

1. The author of this dissertation (including any appendices and/or schedules to this dissertation) owns any copyright in it (the "Copyright") and she has given The University of Manchester the right to use such Copyright for any administrative, promotional, educational and/or teaching purposes.
2. Copies of this thesis, either in full or in extracts and whether in hard or electronic copy, may be made only in accordance with the Copyright, Designs and Patents Act 1988 (as amended) and regulations issued under it or, where appropriate, in accordance with licensing agreement which the University has from time to time. This page must form part of any such copies made.
3. The ownership of certain Copyright, patents, designs, trademarks and other intellectual property (the "Intellectual Property") and any reproductions of copyright works in the thesis, for example graphs and tables ("Reproductions"), which may be described in this thesis, may not be owned by the author and may be owned by third parties. Such Intellectual Property and Reproductions cannot and must not be made available for use without the prior written permission of the owner of the relevant Intellectual Property and/or Reproductions.
4. Further information on the conditions under which disclosure, publication and commercialisation of this thesis, the Copyright and any Intellectual Property and/or Reproductions described in it may take place is available in the University IP Policy (see http://documents.manchester.ac.uk/DocuInfo.aspx?DocID=487), in any relevant Thesis restriction declarations deposited in the University Library, The University Library http://www.manchester.ac.uk/library/aboutus/regulations) and in The University's policy on Presentation of Theses.

Acknowledgement

My appreciation goes to each one who one way or the other impacted and supported me during this PhD journey.

Lee Paul was there for all the technical support and equipment maintenance, Dr Rochelle Taylor and Dr Mike Chandler took me through my first permeability experiment, thank you for the guidance. Dr Patrick Dowey with SEM guidance, and Dr John Waters for the XRD, thank you. Dr Lin Ma was there for guidance and support, thank you.

I would also like to express my sincere gratitude to my amazing supervisors; Dr Julian Mecklenburgh, Professor Ernest Rutter, and Professor Kevin Taylor. I am very grateful for the patience, guidance, and support throughout my PhD journey.

Dr Stefan Schroeder thank you for being my assessor for two years in a row, the grilling helped shape me. Professor Ian Lyon thank you for all the advice and support.

I would also like to appreciate BG International (now Shell) for the supply of the core samples from the Hewitt Land well. The Program was sponsored by petroleum technology and development fund (PTDF) Nigeria, I remain grateful. My appreciation also goes to my organisation Department of Petroleum Resources (DPR) for their understanding and support while running the program. I would also thank Natalie Kate Moss Trust for awarding me their scholarship, twice in row.

My G43 office mates, friends, and colleagues; Yusuf, Mala, HH, Sebastian, Tim, Clement, Ussy, Supol, Chuka, Buhari and Wunmi, and other numerous names thank you for the support.

My gratitude goes to my wife Aisha Modibbo who was part of the journey till the end. My parents Amina Waziri and my late dad Bashir Ahmed for giving me all the necessary support while growing up.

Nomenclature

λ Mean free path of a gas (m)

C Capillary radius (m)

J Fluid flux $(m\,s^{-1})$

Q Volume flow rate $(m^3 s^{-1})$

μ Fluid viscosity (Pa s)

k Permeability (m²)

P Pressure

P_p Pore fluid pressure

K_b Klinkenberg parameter

P_p Pore pressure

σij Stress tensor

σij^{eff} Effective stress tensor

X Effective pressure coefficient

P_c Confining pressure

P_{eff} Effective pressure $(p_c - p_p)$

Kn Knudsen number

K_{bolz} Boltzman constant

φ Porosity

V_b Bulk volume of the sample (m³)

V_g Grain volume of the sample (m³)

η Dimensionless permeability

ξ Dimensionless storativity

T Temperature (k)

R Gas constant

M Molecular mass (kg)

d_m Molecular diameter (m)

K_a Apparent (measured) permeability (m²)

K_∞ True (liquid) permeability (m²)

S Cross-sectional area of the sample (m²)

T Period of oscillations (s)

β_d Downstream storage $(m^3 s^{-1})$

β Sample storativity $(Pa\,s^{-1})$

A Amplitude ratio of upstream and downstream pressure waves

θ Phase shift of downstream wave relative to upstream (rad)

V_o Original sample volume (m³)

γ Permeability modulus (at constant pore pressure) (MPa^{-1})

ε Permeability modulus (at constant confining pressure) (MPa^{-1})

w Slit width (m)

V_p P-wave velocity $(m\ s^{-1})$

V_s S-wave velocity $(m\ s^{-1})$

$\mathfrak{n}$ Poisson's Ratio K Bulk modulus (GPa)

E Young's modulus (GPa) G Shear modulus (GPa)

G Shear Modulus (GPa)

V_u Volume of upstream reservoir (m³)

V_d Volume of downstream reservoir (m³)

V_p Pore volume of sample (m³)

a Ratio of pore volume to upstream volume

b Ratio of pore volume to downstream volume

K_* *defines bulk moduli

f_1 Factor to account for non-zero porosity in pulse-transient permeability measurements

Thesis Structure Summary:

Chapter One: Introduction

Chapter Two: The scientific background to the research. A) A general overview of mudstones showing petrophysical properties and burial history. B) Permeability and acoustic velocity overview and the relationship with effective stress.

Chapter Three: Characterization of the rocks studied:

Outlines the geological setting of the study area of the Haynesville-Bossier shales, with location area, selection of samples, and core plug sample preparation. The mineralogical and petrographic characterization of samples analysed using X-ray diffraction, optical and electron petrography, determination of organic carbon content and estimation of porosities.

Chapter Four: Outline of methods used in measurement of permeability, acoustic velocity, and bulk compressibility. Description of the equipment used and its calibrations with uncertainties during the measurement.

Chapter Five: Sets out the results of the measurements of permeability

Chapter Six: Sets out the results of the measurements of acoustic wave velocities and pore volumometry.

Chapter Seven: (a) Discussion and interpretation of the results of the experimental program, (b) Discussion of the experimental results within the wider framework of studies of permeability and acoustic wave velocities, and their importance in interpreting gas reservoir behaviour.

Chapter Eight: Conclusions and future research arising from this study.

Chapter 1 – Introduction

1.1 Overview

Mudrocks (shales) constitute 50-75% of the sedimentary rocks within the Earth's crust (Boggs, 2009; Bohacs et al., 2015; Lazar et al., 2012). There has been a surge of interest in mudrocks since the development of the shale gas industries in the United States in particular. Shales are the source rocks for oil and gas accumulations, but unlike conventional reservoir rocks they are typically of low permeability. Therefore, despite it being recognized that substantial quantities of natural gas can remain trapped in source rocks for hundreds of millions of years it has until 25 or so years ago feasible to exploit this resource. With the development of horizontal deviation of wells along formations, coupled with the application of hydraulic fracturing, it has become feasible to produce gas from source rocks like these. Such reservoirs are described as being unconventional.

Producing gas from an unconventional reservoir such as shale is expensive and requires a range of recently developed technologies, not only involving the deviation of wells but steering the drill string so that it remains in the productive formation (Spain & Anderson, 2010). The paradigm shift to unconventional reservoirs for hydrocarbon exploration and production increases the demand for research and development in the unconventional resources field, with the aim of maximising production. This requires ever increasing understanding of the chemistry and physics of gas flow through tight rocks such as shales.

The exploitation of shale gas has been undertaken since the 1990s and has had to contend with vocal opposition from the environmental lobby. But in more recent years, with the pressure to develop 'greener' solutions to geoenergy production, shales have continued to be rocks of extraordinary importance. The disposal by burial of CO_2 in the subsurface, the storage of produced or imported natural gas, the storage of compressed air and hydrogen all require the re-use typically of a conventional reservoir (e.g., in sandstone or carbonate rocks) together with its sealing formation. Shales can form viable sealing formations for the storage of these gases. The physics is the same in all cases, although the chemical interactions between stored gases and the rocks can be different.

In this study fundamental physical properties on one particular shale have been investigated. The rock type chosen was the Jurassic Haynesville-Bossier shale (lying between east Texas and west Louisiana, USA; Hammes 2009; Dowey and Taylor 2020). A substantial quantity of this rock was made available to us as slabbed borehole cores taken from a depth interval around 3300m by BG International (now Shell), permitting an opportunity to study aspects of a range of mineralogical and textural characteristics on physical properties.

This study has focused upon the following aspects:

1. Characterisation of a suite of samples covering a range of lithofacies, principally involving variation in the relative proportions of carbonate in rocks otherwise dominated by framework silicates (quartz + feldspar) and phyllosilicates (detrital micas and clays, plus authigenic clays). Samples were characterized mineralogically and petrographically, and in terms of porosity and organic carbon content.
2. Measurements of matrix permeability as a function of confining pressure and pore fluid (argon gas) pressure and using a range of different techniques yielding permeability and storativity.
3. Measurement of bulk moduli of some of the sample which helps in describing the permeability decrease with crack-like pore closure.
4. Measurements of acoustic wave velocity over a wide range of confining pressures and pore fluid pressures, in different orientations with respect to the sedimentary layering, with concurrent measurements of pore compressibility using the pore fluid expulsion method (as a function of changing confining pressure).

It is important to take into account the pressure-sensitivity when interpreting reservoir models. When it is ignored, there will be an overestimation of permeability, original gas in-place, and hence an erroneous estimate of gas reserve estimation (Faulkner et al., 1998; Mckernan et al., 2014). The permeability/ effective stress law is important when modelling reservoir behaviour and for improved understanding of the reservoir behaviour during production and when on routine tests especially for fluid flow within reservoirs.

The purpose in measuring the acoustic velocity and compressibility behaviour in parallel with the permeability measurements was to explore the extent to which the former might lead indirectly to estimation of the latter, given that both

properties depend upon material elasticity and the fact that they depend upon the pressure regime.

The Haynesville Shale is an upper Jurassic (Kimmeridgian) shale-gas play in the USA. It has an estimated recoverable reserve of 100 TCF, with individual wells estimated to produce 13.3MMcf of gas per day, with an initial production of about of up to 3-30MMcf / day (Hammes, 2009). The Haynesville Shale lies between east Texas and west Louisiana in the USA. It is a grey to black colour, calcareous, and organic-rich Shale (Hammes et al., 2011).

1.2 Objectives

This study will seek to address some problems observed while carrying out measurements and observations: The key difference between carrying out some of the experiments in sandstone and mudrocks. The closure of crack like pores in shales which is a direct function of the aspect ratio while measuring acoustic velocity. The experiments carried out seek to identify the following:

- Quantify the relationship between effective stress and permeability in Haynesville Shale. I will determine whether permeability in Haynesville shale shows same sensitivity to pore pressure as to confining pressure.
- Measure permeability, porosity, and acoustic velocity to characterise the stress dependence of the selected samples.
- Identify microstructural factors controlling permeability within the samples. To verify whether microstructural observations made optically can be correlated to differences in permeability in the Haynesville shale and to assess whether overall mineralogy plays a role in defining the permeability of Haynesville shale.
- Explore how the effective stress state controls fluid flow within the shale samples, and to consider whether permeability be modelled using measured poroelasticity parameters using simple pore channel models.

Chapter 2 – Background

This chapter provides a general overview of mudstones, highlighting and explaining the importance of burial, depositional environment, and their effects on physical properties. A background literature on permeability, acoustic velocity and how these are influenced by compaction behaviour is introduced, emphasising the link between pressure dependent permeability and closure of porosity.

2.1 Mudstones

Mudstones are sedimentary rocks where more than 75% of the rock is made up of grains that have a particle size of less than 63 μm. They are further subdivided into siltstones (4-63 μm) and claystones (<4 μm). Shales are fissile mudstones (Dorrik, 1981). 60-70% of marine and terrestrial basins contain mudstones, making them the most abundant sedimentary rock type on Earth (Aplin, 1999).

Due to the fine grain size of mudstones, they must have been deposited in low energy environments and initially with high porosities. The mineralogy of mudstones is very variable and will be discussed in the subsequent section. Mudstones are often rich in organic matter, making them important source-rocks for hydrocarbons. Significant diagenetic changes in mudrocks occur during burial, including significant mechanical compaction, cementation, and the maturation of the organic material to kerogens, oil and gas. Mudstones serve not only as source rocks for hydrocarbon accumulations, but also as seals and as reservoirs (the latter in the case of shale gas). They are also likely to play an important role as seals for carbon capture and storage (CCS) and gas (H_2 and compressed air) storage.

2.1.2 Mudstone (Shale) mineralogy

Mineralogy of shale is determined by sediment provenance and its modification during diagenesis. The mineralogy of mudstones is commonly represented on a ternary diagram with end members (1) quartz + feldspar + pyrite, (2) carbonates, (3) clays and detrital phyllosilicates. Fig. 2.1 shows the modal proportions of Haynesville mudstones represented in this way taken from Dowey

and Taylor (2020). Common minerals found in mudstones include carbonates (dolomite and calcite), with dominant tectosilicate (Quartz and feldspar), phyllosilicates (illites, kaolinite, smectite), oxides, sulphides, and phosphates (Ross & Bustin 2009)

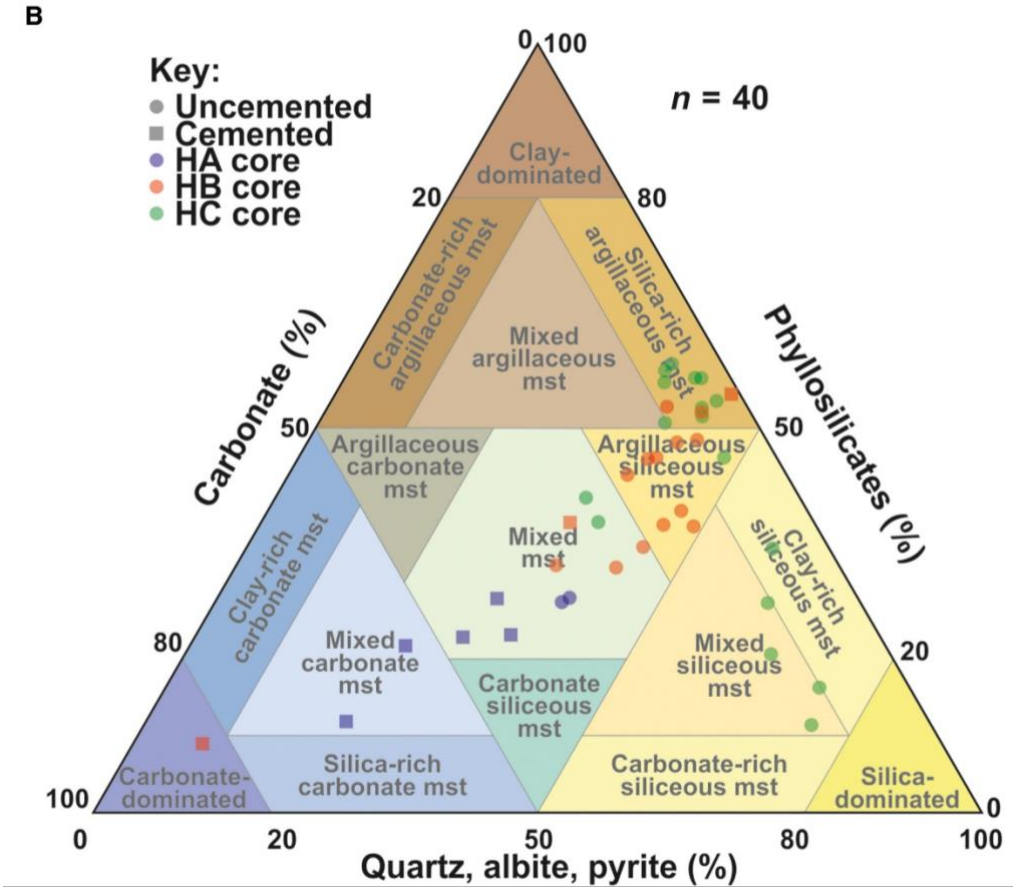

Figure 2.1 Ternary diagram for Hayneville shale from the same bore hole as the samples used in this study, taken from Dowey and Taylor (2020).

2.1.3 Depositional Environment and Diagenesis

Materials eroded from the continents as a result of both physical and chemical weathering produce quartz, feldspar, detrital phyllosilicates, and clay minerals and components in solution. Organic material such bacteria, algae, and plant debris in addition to mineralised skeletons of some organisms also contribute to the sediment load. Due to their grain size the fine particles will be held in suspension unless the flow velocity of the water is sufficiently reduced and are only deposited in relatively low energy environments. In the past this was often inferred to be correlated with a deep marine environment, but this is not always the case. The main types of sedimentary environments are glacial, alluvial fan, aeolian, fluvial (braided system), fluvial (meandering system), deltaic, shallow siliciclastic sea, shallow water carbonate, deep sea clastic and deep-water

evaporitic environments (Reading, 2001). Mudstones are either described as laminated, homogenous, structureless or massive (Lazar et al., 2012). These fine laminations represent temporal / spatial changes in environment. Detailed analysis of the fine-grained rocks reveals an extensive variety of micro-structures which show a dynamic depositional environment that may contradict the misconception of sedimentary structures having been deposited from settling only under very low energy conditions (Lazar et al., 2012; MacQuaker & Gawthorpe, 1993).

2.1.4 Burial and Diagenesis

Mudstones are deposited with porosities of up to 70%, which reduces rapidly post-burial, causing more than half the fraction of connate water to be expelled within few tens of meters of burial depth.(Cicero & Steinhoff, 2013). This is due to such a porous aggregate having almost no mechanical strength and the platy phyllosilicate grains rapidly rotate until they lie normal to the plane of compaction direction (Potter et al., 2005).

Compaction continues during the burial but at a slower pace, resulting in the progressive development of a tight framework of deformed clay and detrital phyllosilicate minerals around rigid silt grains which eventually protect the clay matrix against further compaction. The distribution of silt grains and clay matrix governs the volume, connectivity, and geometry of the remaining pore network (Day-Stirrat et al., 2011).

Grain size and mineralogy play an important role in burial. The overburden pressure controls mechanical compaction and results in fluid expulsion. The increase in temperature with burial enhances chemical changes which also depend on the grain size and mineralogy (Bjorlykke, 1999).

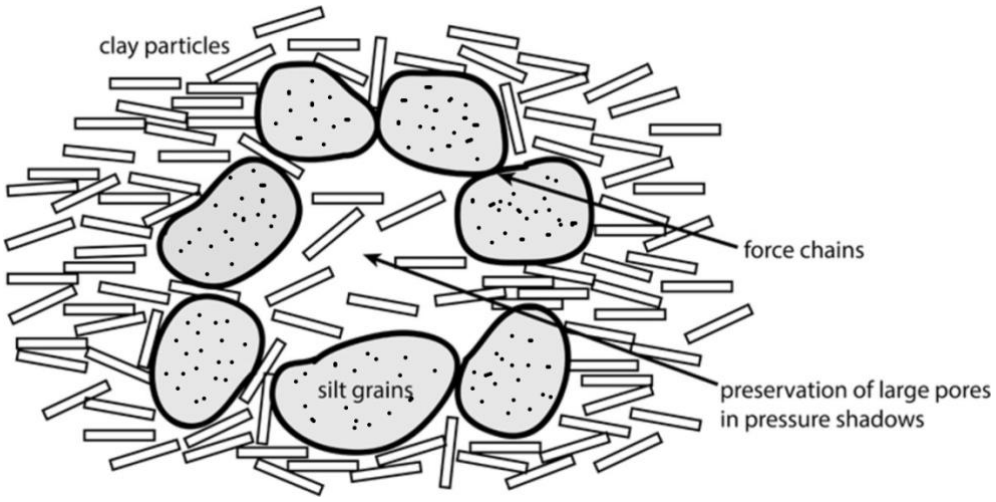

Figure 2.2 Compaction of a mixture of clays and detrital phyllosilicates around silt grains, showing development of preferred orientation of phyllosilicates platelets and residual porosity; adapted from Philipp et al. (2017)

At a depth of about 2-3km the temperature will be at about 70-95°C, and mineral dissolution and precipitation processes begin to alter the sediment, causing cementation, secondary porosity development and porosity reduction. Authigenic minerals such as quartz, clay, and sulphide minerals (pyrite) precipitate into vacant pore spaces (Lazar et al., 2012). At between 70-100°C, during the transition from smectite to illite, clay grains recrystallize with platelets growing perpendicular to the maximum principal shortening direction, thereby increasing the intensity of the fabric (Aplin, 1999). The processes occurring during original deposition, compaction, and diagenesis, change during burial and often enhance at the development of the rock texture.

The geomechanical and fluid flow properties of shales are controlled by the processes that occur during deposition burial and diagenesis. Therefore, by studying the hydraulic and mechanical properties of a variety of different mudstone lithofacies some general trends might be used to extrapolate to other mudstones.

2.2 Petrography of mudstones: pore spaces over a range of scales

The mineral grain size and microstructural characteristics of mudstones play a vital role in influencing their petrophysical properties, such as permeability, ductility, cohesion, plasticity, brittleness, and elasticity. A particularly important property is porosity, how it is hosted in the mineral framework, the distribution of pore sizes, their connectivity, and the tortuosity of the connections.

Shale is characterized by complex pore systems with ultra-low to low inter-particle permeability yet often moderate porosity (e.g., 7 to 10%). Unlike

sandstones, for which there is often a monotonic relationship between porosity and permeability, this is not true for shales, because moderate to high porosity does not necessarily point to high permeability. This conundrum was to a significant extent resolved through the seminal study of Ma et al. (2018). This study used a range of imaging techniques that permitted porosity to be studied over a wide range of scales, from micron-sized pores using optical and scanning electron microscopy, through finer pores using X-ray computed tomography, to the nanometric scale using transmission electron microscopy.

The pore space types recognized included inter-granular porosity, intra-kerogen porosity and intra-crystalline porosity within clay minerals. The pores identified were mainly categorised into mainly organic matter and mineral associated pores, which could be further divided into intra-organic and inter-organic pores, intra- and-inter mineral pores (SEM images in Figures 2.3 and 2.4, TEM and STEM images in Figure 2.5). The pore system is responsible for both storage and transportation of hydrocarbons within the shale reservoirs.

The intra-organic pores (spherical or ellipsoids) are surrounded by organic matter while the inter-organic pores (cracklike or elongate morphology) occur between the organic matter and other minerals. The smallest inter-mineral pores (elongate, lenticular or spheroid geometry) are bounded by clay minerals and other minerals and are present in most samples (Ma et al., 2018), but are smallest in size and hence account for a very small fraction of the total porosity (Figure 2.5)

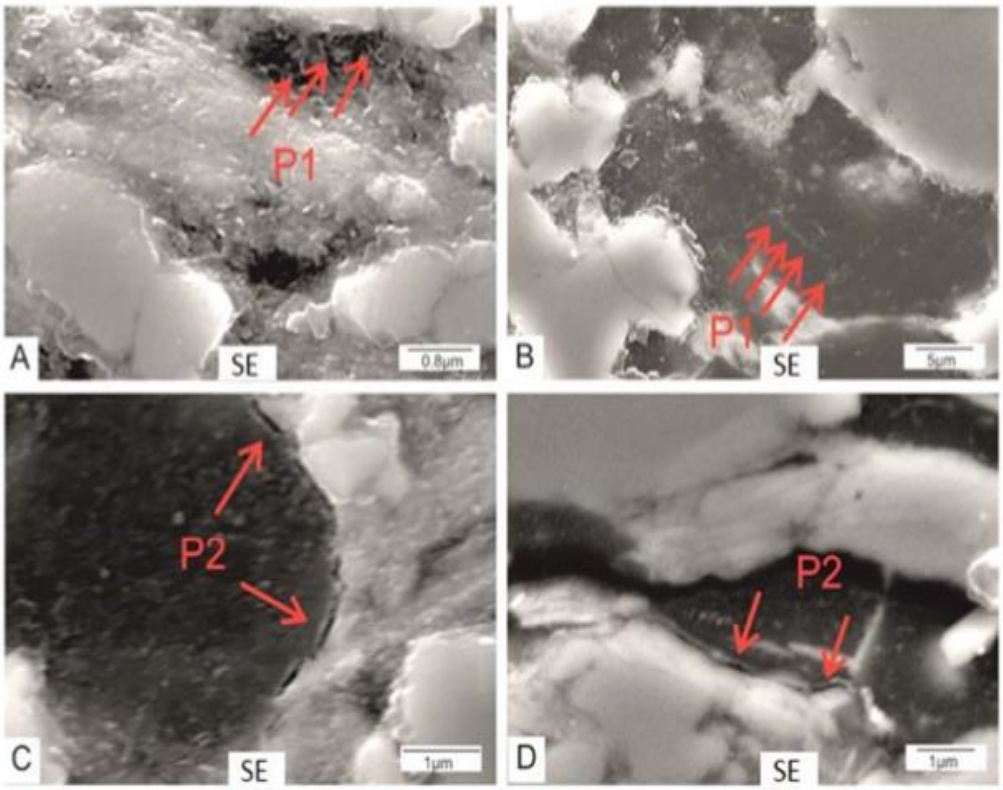

Figure 2.3 A: Intra organic pores shown in organic matter Spherical intra organic pores C & D Crack-like and intermittent pores at the interface of organic matter and other minerals (Ma et al., 2018)

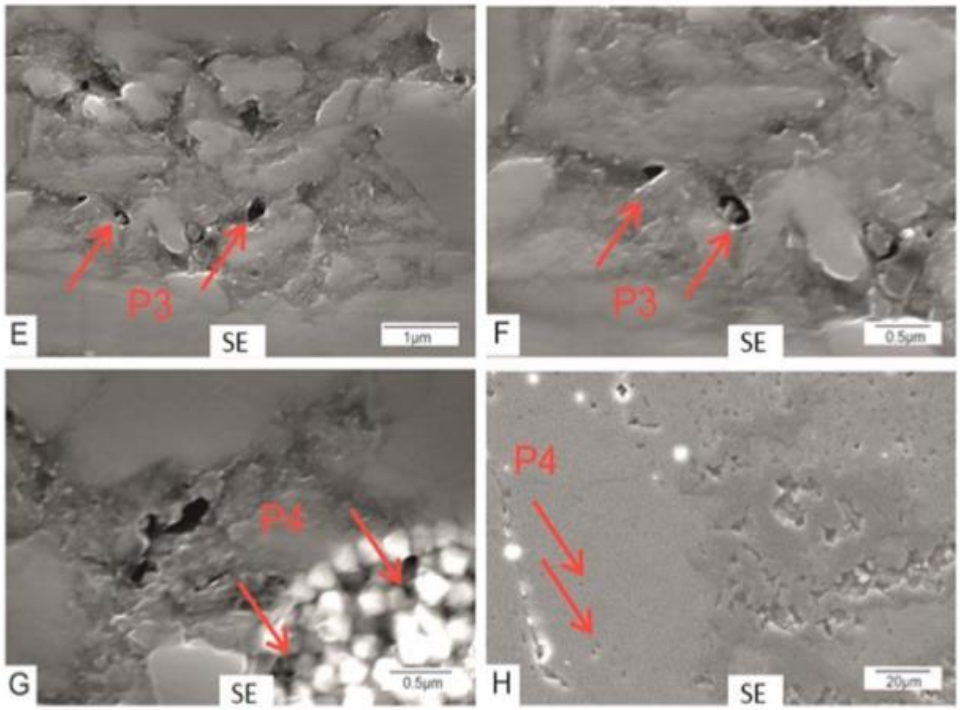

Figure 2.4 E–F: Inter mineral pores between minerals, G: irregular-shape Intra mineral pores within pyrite framboids, H: Intra mineral pores within carbonate minerals such as calcite. BSE- backscattered electron image. SE-secondary electron image. (Ma et al., 2018)

The density of natural fractures varies markedly, and pore throat n

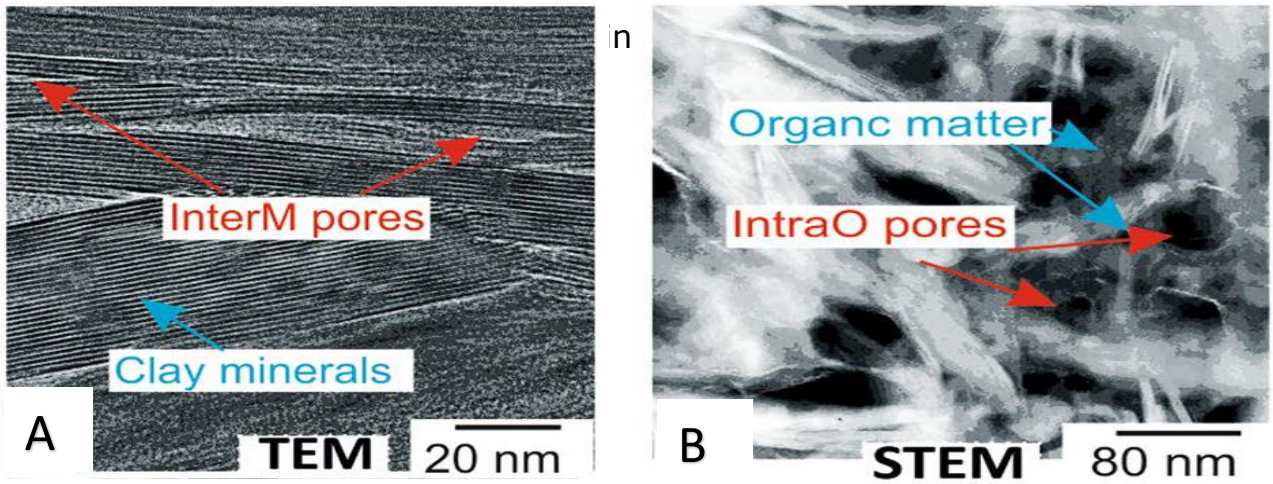

Figure 2.5 These are two transmission electron microscopy (TEM and STEM) images from the study of Ma et al. (2018) showing the nanometric-scale pores that form the connected (conductive) networks in Haynesville shale. A is a TEM image of lattice fringes in clay showing intra-mineral pores with a crack-like geometry. Scanning TEM image B shows a cluster of small clay platelets supporting 40 nm and smaller intergranular porosity.

Effective storage requires access to the largest pores, but whilst these must be connected to the conductive pore system, they can be blind ending. Ma et al. (2018) showed that only the very smallest pores (a few tens of nm in diameter) are well-connected and form a conductive pore network and can only be imaged using transmission electron microscopy (TEM). Otherwise, imagery of the larger pores using other imaging techniques gives the impression that shales are typically impermeable. This is contrary to the fact that their permeability can be measured. Ma et al. (2018) and Mckernan et al. (2017) showed that modelling of observed permeability leads to the conclusion that conductive porosity networks must be at the nanometric scale, in agreement with the multi-scale microstructural study.

These observations have implications for the applicability and utility of various techniques of petrographic study of shales. Petrographic observations using the light petrographic microscopy cannot hope to resolve the pore structure of shales to a useful degree, and cannot be expected to establish relationships between mineralogy, texture and conductive porosity. Imaging the fine structure of porosity using X-ray and TEM lies well outside the scope of the present study, therefore the petrographic characterisation of the samples used in this study (Chapter 3) is limited to textural and bulk mineralogical observations.

2.3 Permeability of Mudstones

The prime diagnostic feature of mudstones is their fine grain size, hence pore dimensions are small (10 μm or less) and as result the pore throat diameters are very small *ca*. 10nm. (Ma et al., 2016) In sandstones permeability is correlated to porosity to some degree especially when controlled by grain size and texture. In tight sandstones and mudstones this correlation starts to break down as there is a loss of connectivity between pores spaces. Porosity is also commonly localized within organic matter (isolated & laminated), between biologically precipitated calcite pellets in faecal matter, in fossil skeletal material and among abundant detrital silt grains as inter-granular porosity (Spain & Anderson, 2010). The size and distribution of pore throats and their degree of interconnectivity will control the permeability.

The hydrocarbon gases in sedimentary rocks exist in the pores, absorbed in the minerals and organic matter, and adsorbed on to mineral surfaces. This is where mudstones differ from sandstones and carbonate rock. Therefore, to produce gas from the shale, gas must flow from the pores of the rock by matrix permeation and eventually into an open fracture. Fractures are required to increase the effective surface area over which gas can flow out of formation and into a well, and thus to increase production to economic levels (Mckernan et al., 2014). But ultimately the flow of gas from a shale gas reservoir is controlled by the matrix permeability (Rutter et al. 2013).

2.3.1 Permeability Measurement

Permeability can be measured in several ways but broadly there are two main techniques used on shale.

i) The GRI (Gas research Institute) technique, that uses crushed samples and measures gas take-up into small pieces of the crushed shale over time.

ii) Standard cores of rock (usually 25 mm in diameter) are pressurised, and gas is made to flow through core of shale. When permeability from core plugs is compared to that measured from crushed samples, the crushed samples tend to have lower permeability due to presence of microfractures. (Bustin et al., 2008).

(Luffel & Guidry, 1992) used crushed samples to measure the average matrix permeabilities of shale gas and to minimize the effects of fissility in core

samples. The results show that a correlation between porosity and permeability exists despite the fact that pore networks of organic and micro-fractures in the crushed samples are significantly disrupted, yet they may be vital in fluid flow and production (Wang & Reed, 2009). Crushed sample permeability is measured with zero confining pressure and therefore higher permeability will be measured than at various reservoir conditions with overburden pressure and also depending on sample orientation, as is evident from experimental studies measuring order of magnitude variations in permeability with changes in effective pressure over expected reservoir conditions (Bustin et al., 2008; Mckernan et al., 2014).

2.3.2 Darcy's law

It was established by Darcy (1856) that slow, viscous fluid flow through a saturated porous solid is linearly proportional to the pressure gradient. Recognising that flow is also expected to be inversely proportional to fluid viscosity, we can write

$$Q_x = -A\frac{k\Delta p}{\mu \Delta x} \qquad \text{Eqn. 2.1}$$

Where Q_x is the volumetric fluid flow rate (m^3s^{-1}) in the *x* direction through an area of cross section A (m^2), k is the permeability of the medium (m^2), μ is the viscosity of the fluid (Pa s) and $\Delta p/\Delta x$ is the fluid pressure gradient in the x-direction $(P_a\, m^{-1})$. In this formulation, *k* is permeability and is a material property of the porous solid.

Applying dimensional analysis, Permeability *k* clearly has dimension of length squared and therefore has SI unit m^2. Darcy's law can also be expressed as in terms of c.g.s. units, whereby a medium with a permeability of 1 Darcy permits a volumetric flow of 1 cm^3/s of fluid (i.e., water) of viscosity 1 centipoise (1 MPa s) through an area of 1 cm^2 under a pressure gradient of 1 atm/cm (Mavko, 2009). It follows that,

$$1\ \text{Darcy} = 0.98623 \times 10^{-12} \text{m}^2 \qquad \text{Eqn. 2.2}$$

Darcy as a unit of permeability is widely used in the hydrocarbon and hydrology industry. Unconventional (mudstone) reservoirs have a permeability range of 10^{-21} - 10^{-18} m^2 while conventional reservoirs typically range from 10^{-13} m^2 to 10^{-15} m^2.

The Darcy flow is a volume flow in which the velocity is proportional to pressure gradient. The permeability relates, for a given fluid viscosity, the volumetric flow to the pressure gradient, and ultimately is dependent on the pore geometry of the reservoir rock. The principal regime of fluid flow in sedimentary rocks i.e., mudrocks for liquids is Darcian laminar flow, whereby the fluid velocity at the contact with the solid walls of a channel is zero. Gas transport within sedimentary rock at low pressures and gas density deviates from Darcy's law, as the flow of gas through the pores is no longer laminar with a viscous velocity profile and enters the slip-flow regime, where the fluid can detach from the channel walls. This is known as Klinkenberg effect (Klinkenberg, 1941) in the hydrocarbon industry, despite having been discovered much earlier (e.g., Kundt and Warburg, 1875).

2.3.3 Knudsen number and flow regimes

Permeability is related to the pore geometry of the porous medium and ideally independent of the kind of pore fluid. Permeability measured with gas should be the same as permeability measured with a liquid. However, pore apertures of the micro to nanometre scale are comparable to the mean free path of gas molecules and consequently the gas flow detachment at pore walls enhances the overall gas flow (slip-flow). This effect increases the measured permeability because the assumptions of Darcy's law have broken down as the flow can no longer be treated as a flow of a Newtonian-viscous fluid.

The transition between flow regimes, with varying gas properties and pore throat widths, are classified with the dimensionless parameter termed the Knudsen number (K_{n}) and is defined as the ratio of the molecular mean free path (λ) to some characteristics length (d) such as pore size in a system. A flow is considered as continuum (Darcy Flow) for K_{n}<0.01 while for a molecular free flow (Knudsen Flow) K_n>10. Where $K_{\mathrm{n}} = \frac{\lambda}{2c}$. The flow regime between $(0.1 < K_n < 0.001)$ is considered as transition flow regime while those between $(0.01\, K_n < 0.1)$ represents the slip flow regime (Anez et al., 2014).

where 2*c* is the channel diameter and λ is the average distance travelled by a molecule between collisions with other molecules. λ is calculated from.

$$\lambda = \frac{\mathrm{k_B T}}{\pi \mathrm{d_m^2 P}\sqrt{2}} \qquad \text{Eqn. 2.3}$$

where d_m is the molecular diameter, P is the pressure, T is the absolute temperature, and k_B is the Boltzmann constant. Figure 2.3 shows the relationship between Knudsen number, pore pressure and pore diameter.

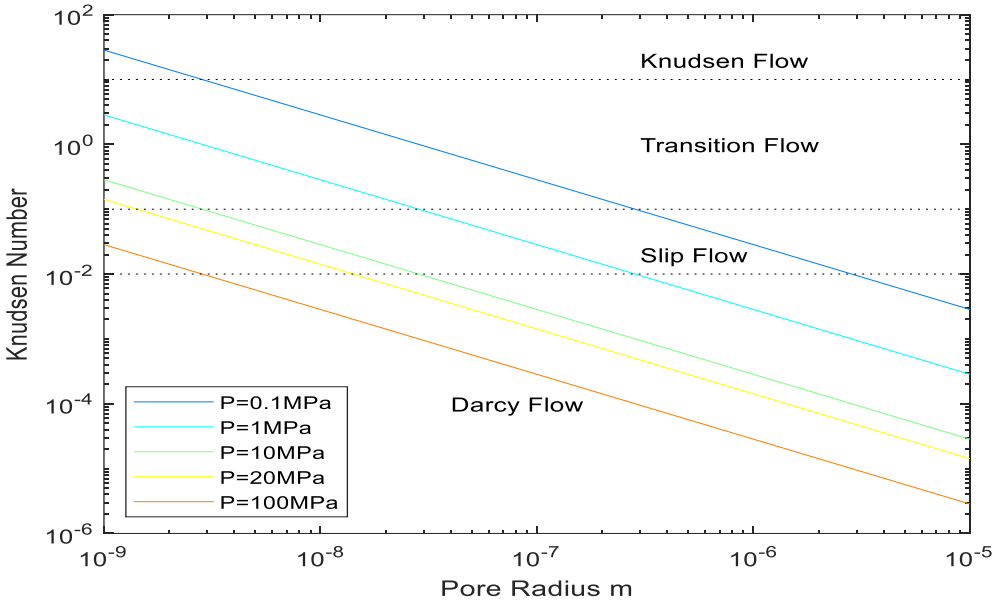

Figure 2.6 Diagram shows the relationship between Knudsen number, pore diameter and pore pressure for argon gas. For pore pressure greater than 10 MPa slip flow should only be encountered for pore throat radius less than ~30 nm.

2.3.4 Slip-flow and Klinkenberg correction

Slip-flow is favoured by narrow pore throats and low gas density i.e., low gas pressure. Klinkenberg (1941) first extended the concept from flow of gases in capillary tubes to porous rocks. When pore throats are comparable in dimension to the mean free path of the gas molecules the loss of viscous interaction between the gas molecules and the pore walls enhances flow within the pores and thereby results in an apparent increase in permeability. The assumptions are used to define permeability through Darcy's law breakdown. In reservoir models the Klinkenberg phenomenon needs to be taken into account especially in the final stages of production where drawdown has reduced the gas pressure to *ca.* 1 MPa pore pressure (Ghanizadeh et al., 2014).

In the slip flow region, permeability is found to be a linear function of $1/P$ and as pressure increases gas density increases and the Darcian flow conditions are satisfied, and the permeability asymptotically approaches a constant value. This can be represented mathematically by the following relationship:

$$k_a = k_\infty \left(1 + \frac{K_a}{P}\right) = k_\infty \left(1 + \frac{4m\lambda}{C}\right) \qquad Eqn\ 2.4$$

Where k_∞ is the permeability at high gas pressure, K_a is the gas slippage correction factor, P is the gas pressure, λ is the mean free path, C is the capillary radius and m is a proportionality constant.

2.3.5 Permeability Modelling

The theoretical modelling of permeability in terms of other physical parameters can be very sophisticated, but a simple theoretical model is the 'bundle of capillary tubes model'. Starting from the physics of viscous flow through a circular-section capillary tube, the behaviour of a bundle of such tubes, as an analogue for a porous rock, allows a simple relationship to be derived linking permeability to porosity.

The Hagen-Poiseuille law describes flow through a pipe and can be used in models relating permeability to porosity. For flow of a viscous fluid through a single capillary tube with a circular cross section under a pressure gradient $\frac{\Delta P}{x}$ the flow rate is

$$Q = \frac{\pi c^4}{8\mu}\frac{\Delta P}{x} \qquad Eqn\ 2.5$$

where, Radius = c, Length = x and Volume flow rate = $Q(m^3/s)$. For a bundle of N parallel tubes passing through a cylinder of length x with a cross sectional area S , porosity ϕ can be expressed as

$$\phi = \frac{Nc^2\pi}{S} \qquad Eqn\ 2.6$$

(Mavko et al., 2003)

Total volumetric flow = $Q_{total} = \frac{\phi S c^2 \Delta P}{8\mu x}$ $Eqn\ 2.7$

Separating out the pressure gradient and the fluid viscosity gives the sample permeability to be $k = \frac{\phi c^2}{8}$ $Eqn\ 2.8$

The above derivation takes no account of the fact that increasing hydrostatic pressure applied to the rock mass will cause elastic shrinkage of the dimensions of the pore tubes, and hence will reduce the permeability. A major part of the present thesis is to establish the influence of applied hydrostatic pressure and pore pressure on the permeability of shales.

It is to be expected that the petrophysical properties of granular rocks under pressure will be controlled by applied hydrostatic pressure P_c, also known as the confining pressure in experimental studies. Additionally, Terzaghi (1936)

proposed that the effective hydrostatic pressure is given by the applied pressure minus the pore fluid pressure P_p. Hypothetically, the pore pressure acts like a tensile stress pushing the grains apart equally in all directions. The difference between the applied confining pressure and the pore pressure, $(p_c - p_p)$, is called the Terzaghi effective pressure. Increasing the effective pressure constricts elastically the pore shapes and reduces the permeability. It also stiffens the rock mass, and therefore increases the velocity of elastic waves in the rock mass.

A more general expression of the effective pressure principle allows for the pore fluid pressure not to be fully effective, so that effective pressure is given by

$$P_{eff} = (p_c - np_p) \qquad Eqn. 2.9$$

In this case *n* is an 'effective pressure coefficient' that describes departures from a pore pressure being fully effective. *n* is usually expected to be <1 but it can also be >1 under some circumstances.

Poroelasticity is the body of theory that describes such coupled hydromechanical behaviour. Biot (1941) pioneered the theoretical development of understanding of poroelasticity. Rice and Cleary (1976) and Detournay and Cheng (1993) developed the theory further. Geertsma (1975a) and Zimmerman (1991) developed theory under conditions of hydrostatic loading which are applicable to rock mechanics and petrophysical problems.

As might be expected increasing hydrostatic pressure will not close down the pore space in a linear fashion, because with progressive compaction the porous solid will become elastically stiffer in addition to having had its porosity reduced and the dimensions of pore throats reduced. It has been common practice arbitrarily to fit by least squares methods a non-linear function to plots of permeability versus pressure. Either an exponential function or a power law function have frequently been employed.

Here we can usefully derive the parameters of an exponential law linking log permeability to pressure with the intention of using it to demonstrate in due course how it can be applied to reservoir modelling. Eqn. 2.10 shows a simple exponential relationship

$$k = ko \exp[-\gamma P_C + \propto P_P)] \qquad \textit{Eqn. 2.10}$$

This equation can be linearised by taking natural logarithms with material parameters $k_{0,}\, \gamma, and\ \alpha$. K_0 is permeability at zero P_{eff}, γ is an empirical proportionality coefficient and α is an effective pressure coefficient. Thus

$$\log_e k = \log_e k_0 - \gamma P_c + \alpha P_p \qquad \textit{Eqn. 2.11}$$

The parameters of this equation can be obtained by least squares fitting experimental data for ln *k* over a range of confining and pore pressures.

For the purposes of modelling reservoir behaviour in particular, and over the range of common reservoir pressures, it has been common to assume this relationship to be linear e.g., Bustin et al., 2008; Cui et al., 2009; Heller et al., 2014; Kwon et al., 2001; Mckernan et al., 2017). This approach has generally been considered to provide an adequate representation of the data and has been applied to the data acquired in the course of the present study. However, there is no *a-priori* reason why this description should be universal. It is also possible to apply a power law relationship (Shi & Durucan, 2016), and if the range of permeability is sufficiently small there may be little difference between the two. When there is data covering a wide range of permeabilities it is usually evident that in a plot of log *k* versus pressure the data are concave-upwards (Rutter et al., 2022), and modelling taking into account the increasing elastic stiffness of the granular framework with pressure is required to interpret it.

2.4 Dependence of permeability on effective pressure

The dependence of permeability on effective pressure is important because during production the reservoir pore pressure reduces and increases the effective pressure. Terzaghi (1923) formulated the concept of effective pressure by noting that the change in volume due to an increment of confining pressure was the same but of opposite sign to the change in volume due to the same magnitude increase in pore pressure. The concept was extended by (Biot, 1962) to account for separate dependencies for the confining pressure and the pore pressure through the inclusion of a pore pressure coefficient α. Most physical properties of porous solids are dependent on the effective pressure as defined in this way.

$$P_{\mathrm{eff}} = P_{\mathrm{C}} - \alpha P_{\mathrm{P}} \qquad \text{Eqn 2.12}$$

Where P_{eff} is the effective pressure, P_C is the confining pressure and P_P is the pore pressure and (α) is the ratio of sensitivity of a physical property l to changes

in pore pressure (P_P) to the sensitivity of the property to changes in confining pressure:

$$\alpha = \frac{\Delta l/\Delta P_{\mathrm{P}}}{\Delta l/\Delta P_{\mathrm{C}}} \qquad \text{Eqn 2.13}$$

When $\alpha = 1$, a change in pore pressure yields the same effect on *permeability* or other physical property as the same magnitude change (but opposite sign) in confining pressure. In this case the pore pressure is said to be *fully effective*. Note that the value of α is determined purely empirically. If $\alpha < 1$ the physical property is less sensitive to changes in pore pressure than to a change in confining pressure. Attempts have been made to find a physical explanation for the value of α. One qualitative explanation for this behaviour is that the pore pressure is not acting over the whole pore volume and not transmitting that pressure throughout the whole matrix. This can be compared to the effect of pore pressure on some elastic properties such as acoustic velocity. (Zoback & Byerlee, 1975) measured $\alpha \leq 1$ in sandstones.

When $\alpha > 1$ the permeability is more sensitive to changes in pore pressure than confining pressure; it is as if the pores are lined with elastically softer phase than the outer framework which transmits the applied confining pressure. This can be demonstrated clearly with the conceptual model developed by Zoback and Byerlee (1975) and Kwon et al. (2001) and shown in Figure 2.7.

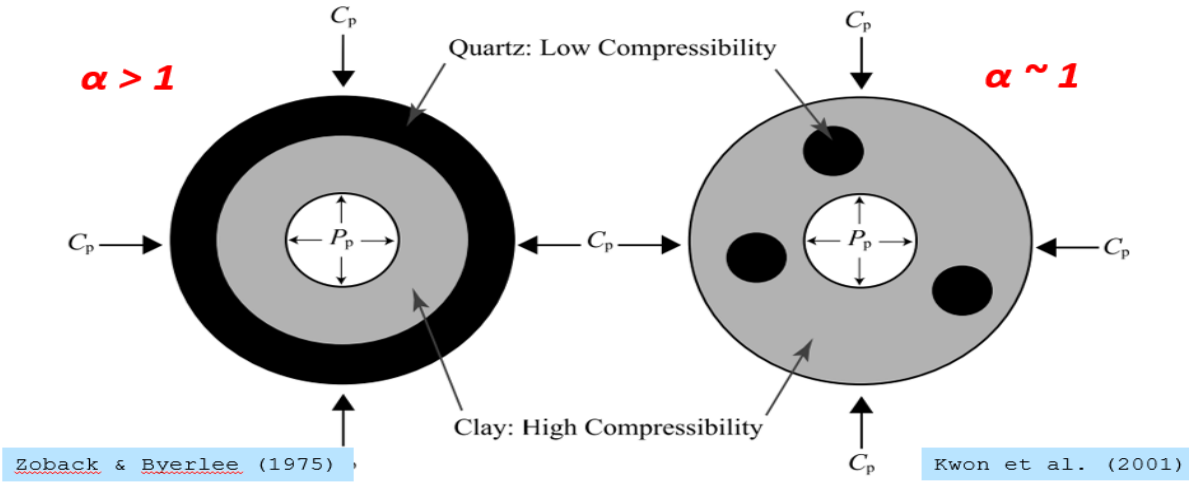

Figure 2.7 Left - Conceptual pore model developed by Zoback & Byerlee (1975), e.g., a sandstone with strong stress-supporting frame (black) and high compressibility clays (grey) lining pores (white). Right – Kwon (2001) model where clay forms a connected matrix in which flow paths reside. Given the Heller et al. (2014) observation of alpha<1, the model on the right is supported – where effective pore widths are similarly affected by changes in confining and pore pressure.

The figure 2.7 on the left shows the pore framework being lined by an elastically more compliant phase like kerogen or clays, or partially saturated by fluid whilst the outer framework is stiffer, so that increases in pore pressure tend to increase the pore diameter more than an increase in confining pressure would close up the pore throats. The pore pressure will decline as production continues, leading to consequent changes in permeability and the need to account for such changes in reservoir models. It should not necessarily be assumed that $\alpha = 1$. Whilst this qualitative explanation for variations in α is attractive there has been no physically based proposal for predicting α in the case of permeability.

2.5 Elastic pore closure

Deformation of the porous framework associated with gas production can lead to reservoir compaction and thereby cause reduction in permeability and porosity. Rocks generally contain a range of different pore shapes from nearly spherical to low aspect ratio, crack-like pores. The different pore shapes will have different resistances to closure by the externally applied confining pressure. Equidimensional pores are much stiffer than crack like pores. Therefore, with effective stress increases during pore pressure drawdown, the more ellipsoidal, oblate pores will be the first to close whereas the more spheriodal ones will never completely close elastically. The pressure at which a pore closes (P_{close}) as a function of its aspect ratio R is given by:

$$P_{\mathrm{close}} = \frac{E_{\mathrm{m}}\pi R}{4(1-v_{\mathrm{m}}^2)} \qquad \text{Eqn 2.14}$$

(Walsh, 1965) where E_{m} is the young's modulus of the supporting matrix and v_{m} is the matrix Poisson's ratio. In mudstones the highly non-linear relationship seen between permeability and effective pressure (e.g., (Mckernan et al., 2017) is largely due to the progressive closure of differently shaped pores.

Partial elastic closure of pores is expected progressively to reduce permeability with effective pressure. Nur and Byerlee (1972) proposed an exact effective pressure coefficient for the elastic *deformation* of a porous aggregate

$$m = 1 - \frac{K_{dry}}{K_o} \qquad Eqn\ 2.15$$

in which *m* is the pore pressure coefficient, K_{dry} is the bulk modulus of the porous rock and K_{o} is the bulk modulus of the pore-free aggregate of grains. This pore pressure coefficient is expected to exert control on the effect of pressure on

permeability through its influence on the dimensions of the pore spaces. Nur and Byerlee (1972) took care to explain that this effective pressure coefficient is **not** the same as α, which describes *empirically* the influence of effective pressure on permeability and includes effects other than just the change in dimensions of the pore spaces. Neither is it the same as the effective pressure coefficient describing effective pressure on rock strength, nor is it the same as the influence of effective pressure on acoustic wave velocity. As will be shown later in this thesis, these different effective pressure coefficients can be separately measured.

2.6 Seismic velocities, porosity, and permeability

The seismic velocity (= acoustic wave velocity or elastic wave velocity) of a material can be calculated from the elastic moduli and the density. For example, the shear wave velocity V_s can be calculated from the shear modulus G and the density ρ.

$$V_s = \sqrt{\frac{G}{\rho}} \qquad \text{Eqn 2.16}$$

Both the density and the modulus are affected by the porosity. Density is a linear function of porosity whereas elastic modulus can be a highly non-linear function of porosity and is not only dependent on the magnitude of the porosity but also its shape and geometry. Hence the increase in velocity associated with the reduction in density is overwhelmed by the reduction in velocity associated with the reduction of stiffness due to the inclusion of porosity. There are many models for calculating the elastic properties and hence seismic velocities of porous rocks. It is beyond the scope of this thesis to discuss them in detail, but a review of the different modelling approaches can be found in Mavko et al. (2009).

As set out above, the pressure at which pores close is a direct function of their aspect ratio. Ultrasonic velocities of rocks, measured in the laboratory, are found to increase with increasing confining pressure. This is due to the progressive stiffening of the rock through closure of crack-like pores. Hence it is possible to invert for the distribution of pore aspect ratios responsible for the observed changes in seismic velocity during increasing confining pressure (Mckernan, 2017).

Commonly, hysteresis in the seismic velocity variation with pressure is observed, with slightly different behaviour on the loading and unloading cycles. During unloading, velocities are typically slightly higher due to the rock being stiffer on the down pressure part of the cycle. It is also commonly observed that the velocity does not reduce precisely to its initial value on the reduction of the pressure but may be a little faster. A similar behaviour is also observed with the measurement of permeability (Mckernan et al., 2017; Rutter and Mecklenburgh, 2018) whereby there is a non-recoverable fall in permeability during the first pressurisation cycle. This permanent increase in velocity can be compared to the observed permanent fall in permeability after each successive pressure increment because they are a consequence of the same elastic pore closure (Birch, 1961). Velocity hysteresis is attributed to irreversible partial or fully closure of crack like pores, and compaction of pore spaces in highly compressible clay matrix (Jones & Wang, 1981). The qualitative commonality of the origins of the observed relationships between seismic velocities and pressure, and permeability and pressure, and the role of porosity in both behaviours suggests that quantitative relationships might exist between these two types of petrophysical property. Previous studies on sandstones have found such relationships (Bourbie and Zinzner, 1985; Gomez et al., 2010).

2.7 The effective pressure coefficients

In the above, the influence of pore pressure on permeability has been described by reference to a single effective pressure coefficient *n*. However, it is well known that the pore pressure coefficient does not take the same value nor vary in the same way with confining pressure for different physical properties (Seeburger and Nur, 1984). In the same way that increasing pore pressure at constant confining pressure causes permeability to increase, in the case of acoustic velocities an increasing pore pressure at constant confining pressure causes velocity to decrease. The pore pressure coefficient for shales, for example, $n(P_p)$ for permeability and $\alpha(p_p)$ for acoustic wave velocities, take different values and display different pressure sensitivities for the same rock. They are empirically determined coefficients and there is no model available to predict them theoretically. A pore pressure coefficient of different value again (approximately unity) describes the influence of pore pressure on rock failure.

In contrast, and as mentioned above, Biot and Willis (1957), Skempton (1960), and Nur and Byerlee (1971) derived an exact effective pressure law applicable to the description of the *elastic distortion of the porous framework* of a granular rock. The pore pressure coefficient *m* (also called the Biot coefficient) is given by

$$m = 1 - \frac{K_{dry}(p_c)}{k_o} \qquad Eqn. 2.17$$

In which K_{dry} is the bulk modulus of compressibility of the porous framework of the rock in the absence of pore pressure (and is a function of pressure) and k_o is the average bulk modulus of the minerals of the rock (without porosity). Each of these pore pressure coefficients is unique to the physical process which it describes and can vary in very different ways with pressure. Thus, normally we expect that *m* is initially close to 1 and decreases with pressure. At extreme pressures, when the porosity closes elastically (depending on pore shape) or collapses inelastically, k_{dry} might approach K_0 (for which porosity is zero), hence *m* should decrease towards zero, or flatten off to an asymptote.

Interpreting the volumometry data in this way, it is implied that a large amount of pore collapse takes place with increasing pressure. However, the pore volumometry data tells us that only a small amount of porosity loss is occurring, from the small amount of gas expelled. Further, the steep rise of the volumometry curves, with apparently high values of K_{pore} and K_{dry}, implying near-total pore collapse, is not consistent with the small amount of volume loss relative to the starting porosity. It is therefore inferred that it is only the small amount of conductive porosity that is being closed down, and the bulk of the porosity remains filled with pressurized gas. The *m*-value for the volumometry is therefore likely to be more relevant to the permeability of the rock than to the acoustic wave propagation properties and can be used as a basis for estimating the *expected* influence of confining pressure on permeability, independently of the actual permeability measurements. Hence it is unsurprising that the two methods of measuring *m* are inconsistent – because they relate to different physical processes.

The study in this thesis as highlighted in Chapter one will quantify the relationship between effective pressure and permeability in Haynesville Shale, measure acoustic velocity and its relationship to effective pressure, and consider the extent to which these properties are related. We shall seek to identify the

extent to which mineralogical factors might be expected to control the permeability of the samples and finally to explore the implications of pressure-dependent permeability for shale gas production.

Chapter 3-Characterization of Test Materials

This chapter describes the geological setting of the Haynesville-Bossier shale and the selection of the 8 core samples chosen, from which a subset was subjected to petrophysical study. The mineralogy and microstructure of the suite of samples is described, based on X-ray diffraction analysis and optical and electron microscopy. Characterization of the organics present in the rocks is presented, and the methods used for the determination of porosity are described.

3.1 Haynesville Shale Geological setting

This study was carried out on samples of the Haynesville Shale which, combined with the overlying Bossier shale, it is a formation of upper Jurassic (Oxfordian through Tithonian) age. It is an important shale-gas play, lying between East Texas and west Louisiana in the USA, at more than 3048 meters below the surface. The Haynesville and associated shales are amongst the most actively explored and developed shale gas investment prospects in the history of North America (Hammes & Gale, 2013).

Haynesville Shale is a grey to black, organic- and carbonate-rich mudrock, underlying the Gulf coast region of the USA. Fig. 3.1 illustrates the stratigraphy of the Haynesville and adjacent formations and the location of the productive interval at depth is also shown on Fig. 3.1. The depositional system consists of backstepping facies in the western part while a contrast in the east with progradational stacking patterns mainly consists of siliciclastic facies assemblages. The Haynesville Shale Formation lies stratigraphically above the carbonate shelves of Smackover limestone Formation. A calcareous interval which occurs at the bottom of the Haynesville Shale Formation is the Gilmer lime member, which is informally referred to by workers as the Haynesville Lime (Hammes et al., 2011). The Bossier Shale formation overlies the Haynesville Shale Formation and is also a potential shale gas prospect. It is divided into three (3) members, upper, middle, and Lower Bossier members.

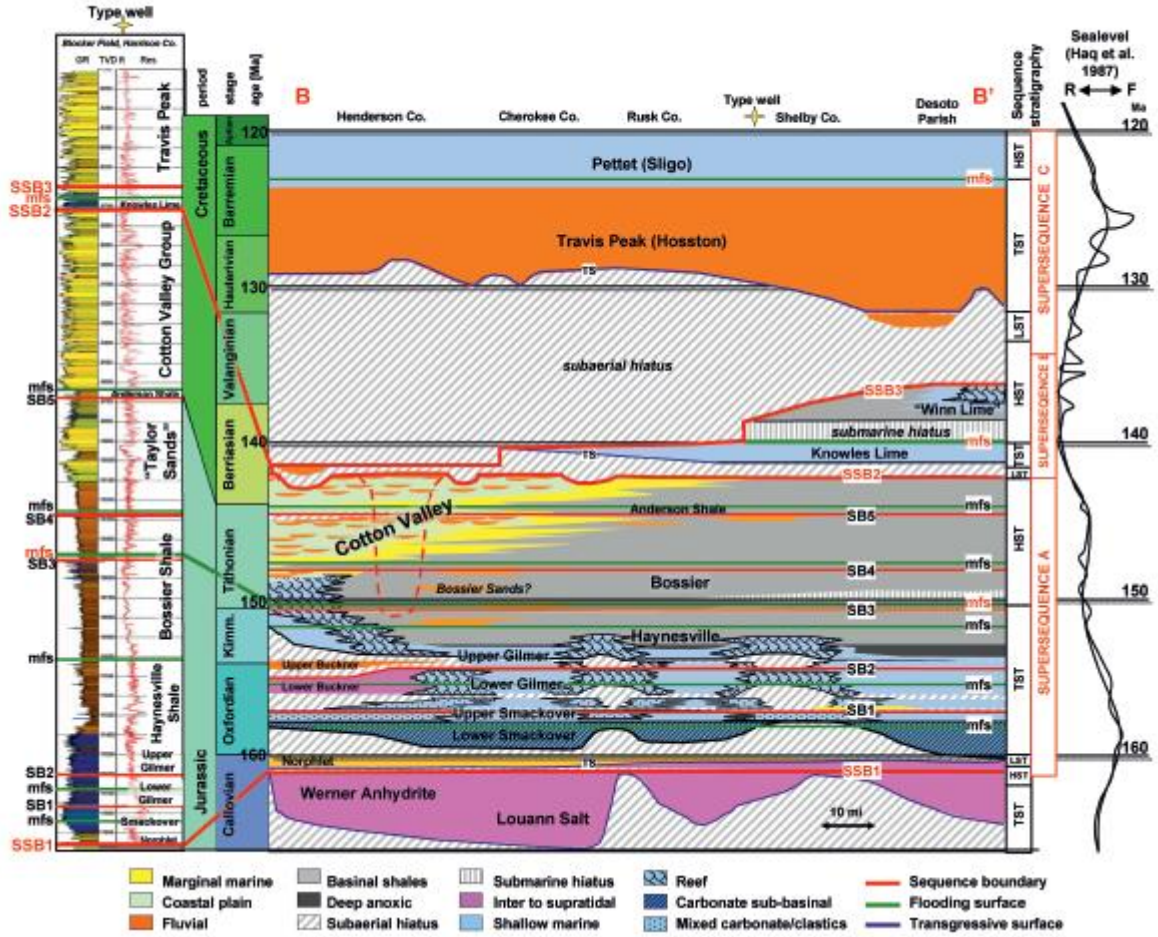

Figure 3.1 Strike-Oriented Chronostratigraphic diagram including a type well, sequence stratigraphy, ages and eustatic sea level curves. Adapted from (Hammes, 2009).

The Kimmeridgian and Berriasian Haynesville and Bossier shales collectively supply more than 8% of the USA (EIA, 2011) total gas production. It has estimated to represent a recoverable reserve of 2 trillion m^3 (at normal temperature and pressure) with individual wells estimated to produce between 84 million-169 million m^3, with an initial production of about of up to 769000 to 847000 m^3. The play has a thickness of 99m-121m in western Louisiana and 60m-99m in eastern Texas (Wang et al., 2013).

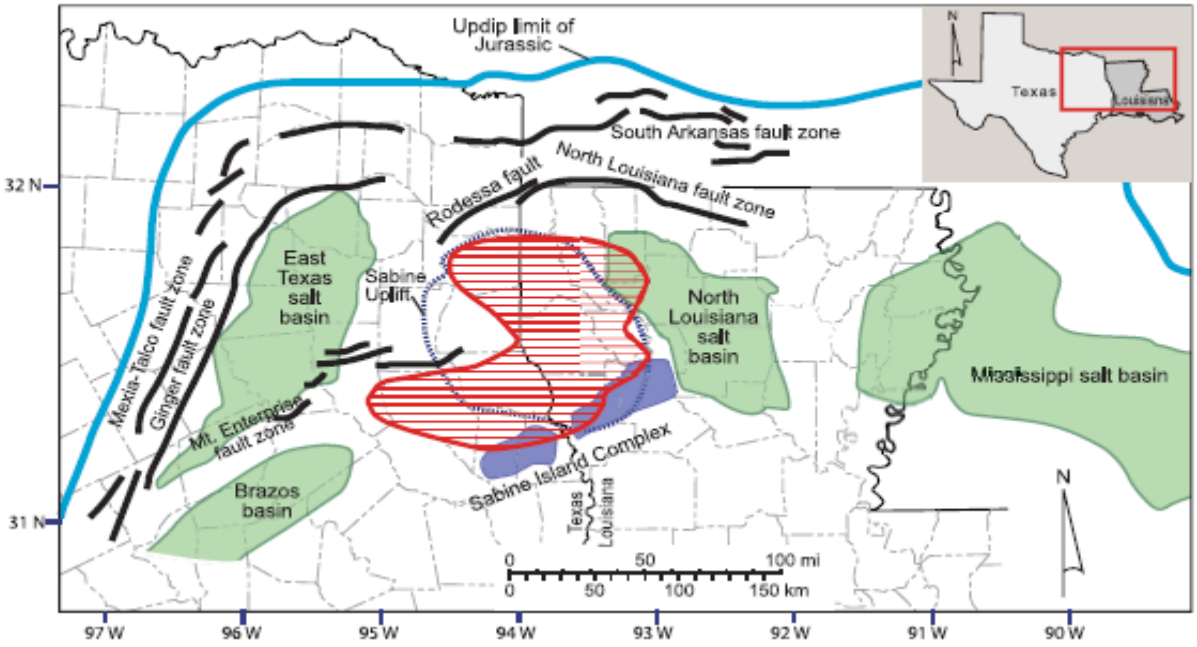

Figure 3.2 Map of Study area showing Late Jurassic structural elements and the red striped area is the Haynesville Shale productive area. The structures are controlled by the opening of early Gulf of Mexico basin that controlled the Haynesville deposition in east Texas and West Louisiana. Areas in blue and red crosses are highs while the green are basins. Image from (Hammes et al., 2011)

3.2 Haynesville Core and Log

This study analysed only samples taken from the Hewitt-Land LLC4 well from the Haynesville-Bossier Shale. The well is located in the Caspian Field under the De Soto parish, Louisiana, United States (Fig 3.2). Fig. 3.3 shows a paleogeographic map of the area. The rock samples used in this study were taken from core boxes provided by BG International (now Shell). The core boxes had been collected from the interval containing the thick, dominantly carbonate and organic-bearing Haynesville-Bossier Shale, but the interval also contains carbonate-poor, clay-rich silty mudstones.

The well log personally sketched by me, showing the stratigraphic levels from which, the 8 selected samples (YB01 to YB08) were taken, is shown in Fig. 3.4 and the tabulation of depths is shown in Table 3.1. A visual representation of the sedimentary features shown in the log is presented in fig. 3.4, which covers the depth range 11372ft- 11808ft (3446 to 3578 metres). Planar lamination is present in the upper and lower parts of the sampled core, otherwise the rocks selected appear homogeneous in hand specimen. The finely laminated sections of the core were not suitable for petrophysical studies on account of their extreme friability, which prevents core sampling. In this respect the samples

selected cannot be considered representative of the whole depth interval. Images of the sampled core intervals are shown in Fig. 3.5. A detailed petrographic study of samples from this core section has been presented by Dowey and Taylor (2020), and Ma et al. (2018, 2019) described details of the pore structures using high resolution SEM and TEM imagery.

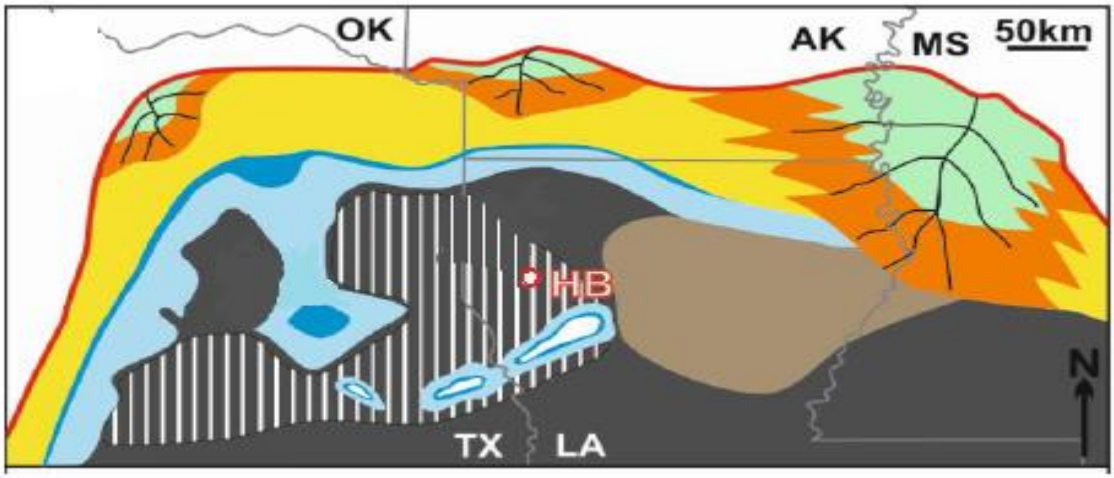

Figure 3.3 Paleogeographic Map of Jurassic Haynesville Shale deposition (after Hammes et al., 2011) with the Hewitt Land core sample location (HB).

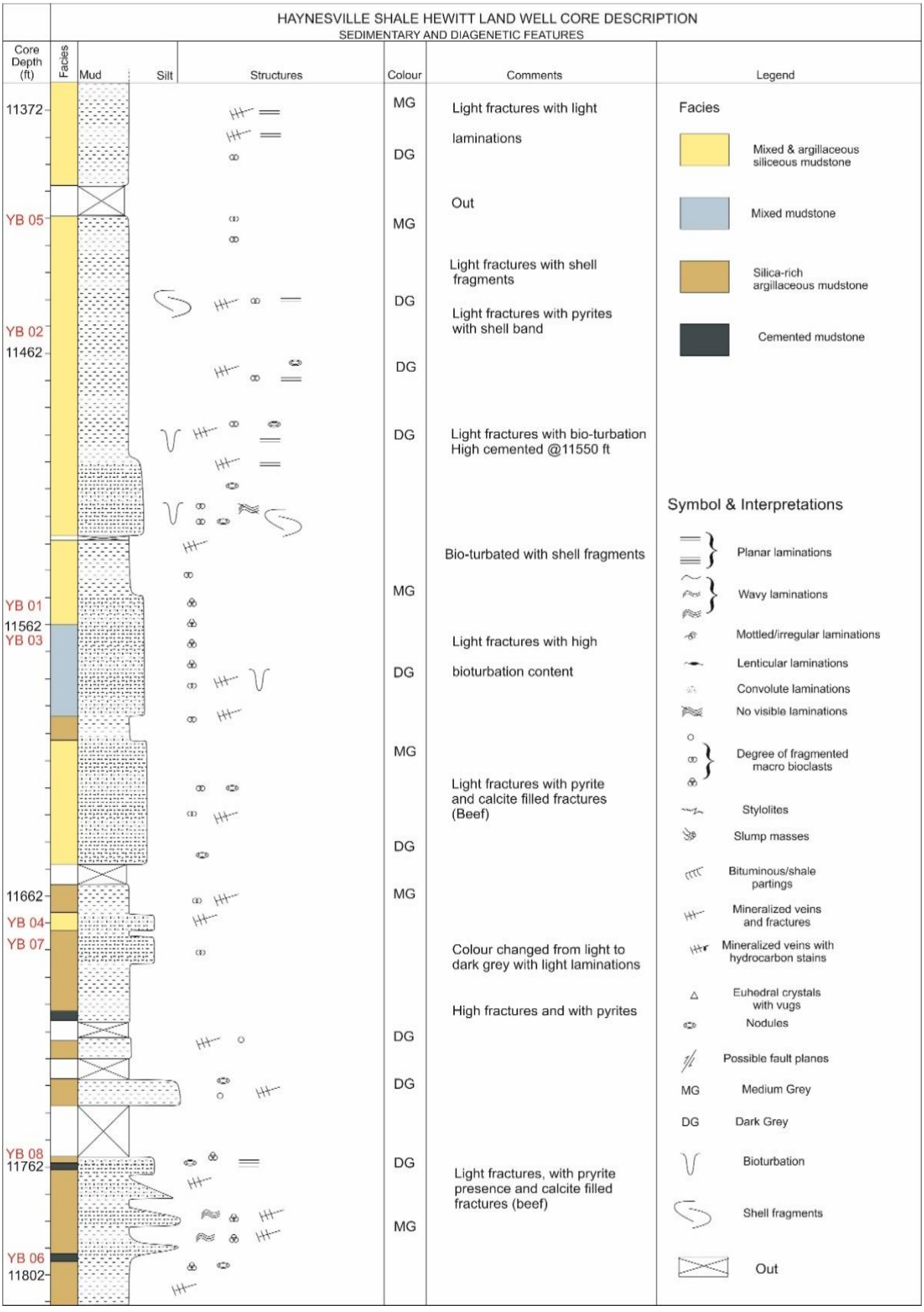

Figure 3.4 Core description of Hewitt land LLC 4 Well, highlighting sedimentary features, and horizontal lines on log represent mineralized veins. The facies column shows grainsize, mineral and textural observations noted during the core logging and thin section studies. The core is dominated by shell fragments, light fractures, and bioturbation. Produced by Yusuf Bashir

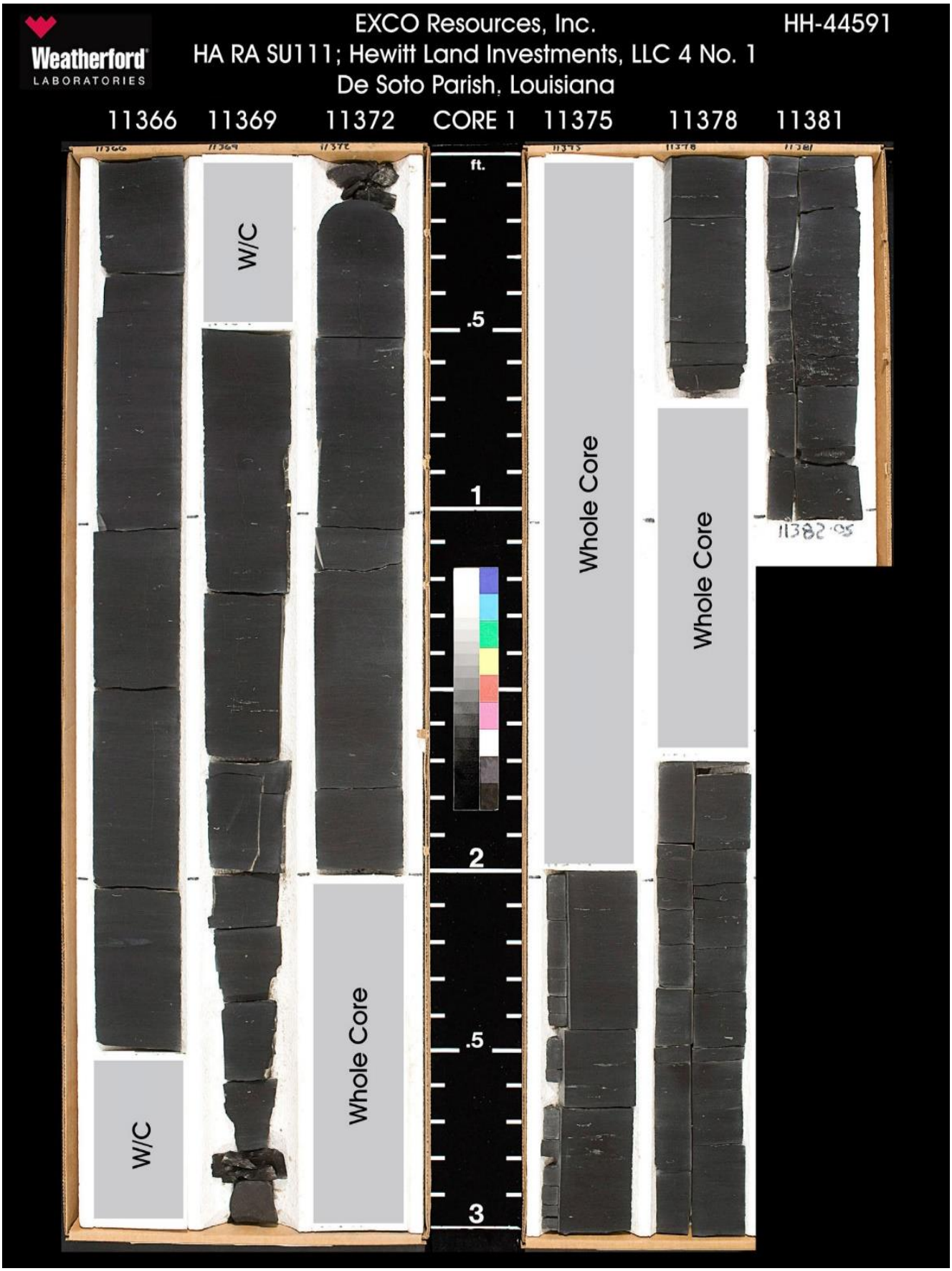

Figure 3.5 The slabbed core used for the analysis, ranging in depth in between 11372 -11802 ft. The image is courtesy of Weatherford laboratories. The empty slots are slabs in other school laboratories.

3.3 Mineralogy and petrography of the samples studied.

Eight samples were chosen for study, and the prefix YB were used for all the 8 samples. Cores were cut oriented either parallel or normal to bedding, or both. The samples were chosen to provide a range of lithofacies, characterized by different combinations of microstructure and mineralogy, with the intention to provide a basis for examining the influence of these features on permeability. While there is representation of the minerals in all the samples, the Hewitt Land core samples are mainly argillaceous siliceous mudstone and silica-rich argillaceous mudstone (Dowey & Taylor, 2019).

S/N	Sample	Orientation	Depth (m)	Nos of sample
1	YB 01	Parallel & Normal to bedding	3521.8	3
2	YB 02	Parallel to Bedding	3499.1	1
3	YB 03	Parallel & Normal to bedding	3525.1	3
4	YB 04	Parallel to Bedding	3558.5	1
5	YB 05	Parallel to Bedding	3481.9	1
6	YB 06	Parallel to Bedding	3595.2	2
7	YB 07	Parallel to Bedding	3559.2	1
8	YB 08	Parallel to Bedding	3584.4	1

Table 3.1 Samples picked for the experiments and the identifying number.

Samples YB03 and YB06 differ principally in terms of carbonate content relative to framework silicates plus phyllosilicates, and this is weakly linked to the degree of development of mineralogical layering and the development of a planar fabric produced by post-depositional Compaction. Samples were therefore regarded as comprising two groups: the carbonate rich samples comprise YB06 and YB03, whilst the remainder are relatively carbonate poor and silicate rich.

3.3.1 Petrographic Study

Sixteen (16) Polished thin sections ($30\mu m$ thickness) were prepared from the samples, oriented both parallel and perpendicular to the layering of the samples. An optical polarizing microscope was used to identify the microstructural

features i.e., primary depositional and diagenetic. Samples were examined under both plane polarized light and between cross polars.

To improve the visibility of low-contrast sedimentary features, where appropriate the images acquired were manipulated with Adobe Photoshop® i.e., hue, tone, saturation, brightness, and contrast.

A small number of samples were studied by scanning electron microscope (SEM), Images were obtained using the FEI Quanta 650 field emission microscope at the University of Manchester on polished thin sections after carbon sputter coating. Although the images proved useful in identifying mineral phases, the data are not presented here because the images obtained were too few in number due to time constraints.

3.3.2 X-ray diffraction (XRD)

Powder XRD measurements were performed to determine the mineralogy of the samples. The samples were taken from cut-off ends of cored samples and crushed to a powder of less than 10 microns using a ceramic mortar and pestle. The measurements were made on a Bruker D8 diffractometer using CuKα radiation produced at 40 kV. Counting time was 4 s per step of 0.02°. 2θ diffractograms were recorded from 2° to 92° 2θ. Mineral identification was quantified by the Rietveld refinement (RR) method using the BGMN program for mineral structures (Doebelin & Kleeberg, 2015). The precision achieved from analysis of the sample was estimated to be approximately $\pm 1\ wt\%$ for phases with concentration above $2\text{wt}\%$.

3.4 Petrographic Characterisation

Image photomicrographs analysis of Haynesville samples (YB01, YB02, YB03, YB04, YB05, YB06, YB07, and YB08) using the polarising microscope are presented showing the dominant textures and grains sizes, bearing in mind the limitations on image resolution in these fine-grained rocks. Table (3.2) shows the results of the XRD analyses $(\text{as wt}\%)$ for the samples used in this study. The XRD data were converted into vol% via the published density data for individual phases (engineering toolbox). In terms of total phyllosilicate, samples that are particularly rich are YB05 (39%), YB02 (40%), YB04 (45%), YB08 (39%) and YB01 (29%) and can be classified as phyllosilicate-bearing or -rich silty mudstones and most samples contain 9 or 10 wt% albite (Table 3.2). The XRD data from the eight (8) samples show range of minerals within the Haynesville

Shale and form the basis for classifying individual samples into carbonate-rich and carbonate poor, phyllosilicate-bearing silty mudstones (Dowey & Taylor, 2019) A ternary diagram is plotted (fig 3.6A) showing the end members in terms of the volume percentages of quartz+feldspar+pyrite, total carbonate, and clay minerals+organics of a wide range of shales from different geographic locations, and this aids in visualising the relative compositions of the eight samples studied here (fig. 3.6B) in a global context.

The total organic content of the shale samples shown in Table 3.2 were separately determined (Chapter 4). They are shown as wt% and average around 2 wt%. Given the typical range of densities of maceral particles the volume% will be greater. Methods of determination of organic content are describe in Section 3.3.7.

Sample #	Minerals	Vol. %	TOC wt%	He Porosity	Porosity % from Bulk and XRD Density
YB 05	Albite	11.12	1.3	7.97	7.97
	Ankerite Fe0.55	0.16			
	Calcite	13.90			
11423.5 ft	Clinochlore IIb-2	11.40			
	Gypsum	0.10			
	Muscovite 1M	15.05			
	Pyrite	1.50			
	Quartz	35.62			
	Siderite	0.48			
	Orthoclase	8.17			
	organic	2.49			
	Total	100.00			
Sample #	**Minerals**	**Vol. %**	**TOC wt%**	**He Porosity**	**Porosity % from Bulk and XRD Density**
YB 02	Albite	7.54	1.27	8.16	8.16
	Ankerite Fe0.55	0.03			
	Calcite	10.00			
11480ft	Clinochlore IIb-2	12.29			
	Gypsum	0.19			
	Muscovite 1M	17.97			
	Pyrite	1.47			
	Quartz	38.28			
	Siderite	0.34			
	Orthoclase	9.45			
	organic	2.43			
	Total	100.00			
Sample #	**Minerals**	**Vol. %**	**TOC wt%**	**He Porosity %**	**Porosity % from Bulk and XRD Density**
YB 06	Albite	8.35	0.99	2.55	3.07
	Ankerite Fe0.55	34.18			
	Calcite	20.10			
11795.4ft	Clinochlore IIb-2	4.94			
	Gypsum	0.76			
	Muscovite 1M	8.66			
	Pyrite	0.86			
	Quartz	17.09			

	Siderite	0.25			
	organic	4.82			
	Total	100.00			
Sample #	**Minerals**	**Vol. %**	**TOC wt%**	**He Porosity %**	**Porosity % from Bulk and XRD Density**
YB03	Albite	10.73	1.29	7.61	9.27
	Ankerite Fe0.55	4.07			
11565.3ft	Calcite	46.48			
	Clinochlore IIb-2	3.79			
	Muscovite 1M	9.26			
	Pyrite	0.68			
	Quartz	18.86			
	Siderite	0.32			
	Orthoclase	3.36			
	organic	2.46			
	Total	100.00			
Sample #	**Minerals**	**Vol. %**	**TOC wt%**	**He Porosity %**	**Porosity % from Bulk and XRD Density**
YB04	Albite	11.56	1.75	10	10
	Ankerite Fe0.55	0.11			
11675ft	Calcite	6.37			
	Clinochlore IIb-2	10.26			
	Muscovite 1M	20.34			
	Pyrite	1.50			
	Quartz	44.59			
	Siderite	0.59			
	organic	4.67			
	Total	100			
Sample #	**Minerals**	**Vol. %**	**TOC wt%**	**He Porosity %**	**Porosity % from Bulk and XRD Density**
YB07	Albite	10.18	1.94	8.3	11.54
	Ankerite Fe0.55	0.68			
11677.3ft	Calcite	17.41			
	Clinochlore IIb-2	9.78			
	Muscovite 1M	16.77			
	Pyrite	0.88			
	Quartz	31.50			
	Siderite	0.51			

	Orthoclase	8.63			
	organic	3.65			
	Total	100			
Sample #	**Minerals**	**Vol. %**	**TOC wt%**	**He Porosity %**	**Porosity % from Bulk and XRD Density**
YB01	Albite	10.51	2.48	2.55	7.43
	Ankerite Fe0.55	2.45			
11554.5ft	Calcite	13.09			
	Clinochlore IIb-2	8.48			
	Muscovite 1M	9.57			
	Pyrite	1.68			
	Quartz	42.57			
	Siderite	0.40			
	Orthoclase	9.34			
	organic	1.90			
	Total	100			
Sample #	**Minerals**	**Vol. %**	**TOC wt%**	**He Porosity %**	**Porosity % from Bulk and XRD Density**
YB08	Albite	6.63	**1.91**	**7.23**	**9.71**
	Ankerite Fe0.55	0.16			
	Calcite	13.12			
	Clinochlore IIb-2	11.70			
	Muscovite 1M	18.57			
	Pyrite	1.09			
	Quartz	34.88			
	Siderite	0.71			
	Orthoclase	9.53			
	organic	3.61			
	Total	100			

Table 3.2 XRD mineral distributions (obtained initially as wt%) of the eight samples shown converted to vol% proportions (shown) and the principal phases were grouped into three (fig. 3.6) for the plotting of a ternary diagram to represent mineral proportions. Calculated porosities from bulk and XRD density, together with porosities obtained from helium porosimeter are presented.

Petrographic features of samples YB01 through YB08 are described below.

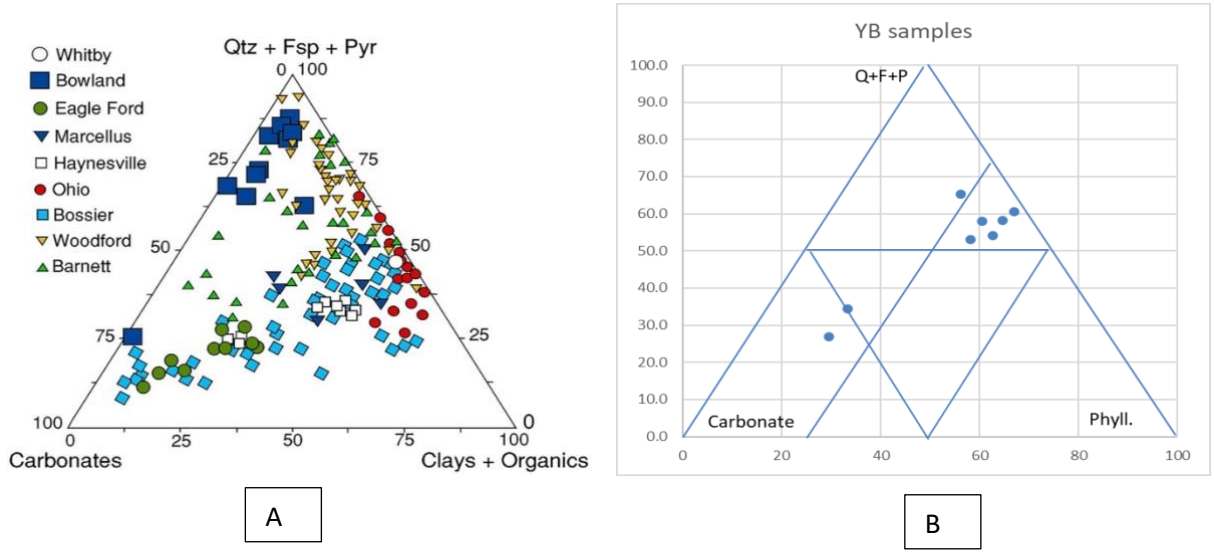

Figure 3.6 A shows a ternary diagram that characterizes the modal composition of shales on the basis of (qtz + fsp + pyrite), (phyllosilicates, i.e. detrital mica + clays, and organic (maceral) particles and (total carbonate) for a wide range of shales of different origins (from Rutter et al., 2017), including previously published compositional information for Haynesville shale (Hammes, 2009; Sone & Zoback, 2013). B shows the corresponding data for the samples used in the present study. With respect to carbonate content, YB03 is particularly calcite-rich (47 wt%) and YB06 is particularly rich in dolomite (38.3wt %) plus calcite (20 wt%). The remainder contain less than 18 wt% total carbonates.

3.4.1 Mineralogical and microstructural observations of the samples

The following section describes in outline the eight samples initially selected for study, although owing to the pressures of time not all were eventually selected for full programmes of petrophysical testing using permeametry and acoustic velocity measurements. The most important samples in this respect are indicated following the sample petrographic descriptions.

YB01 A phyllosilicate-rich, carbonate-poor silty mudstone.

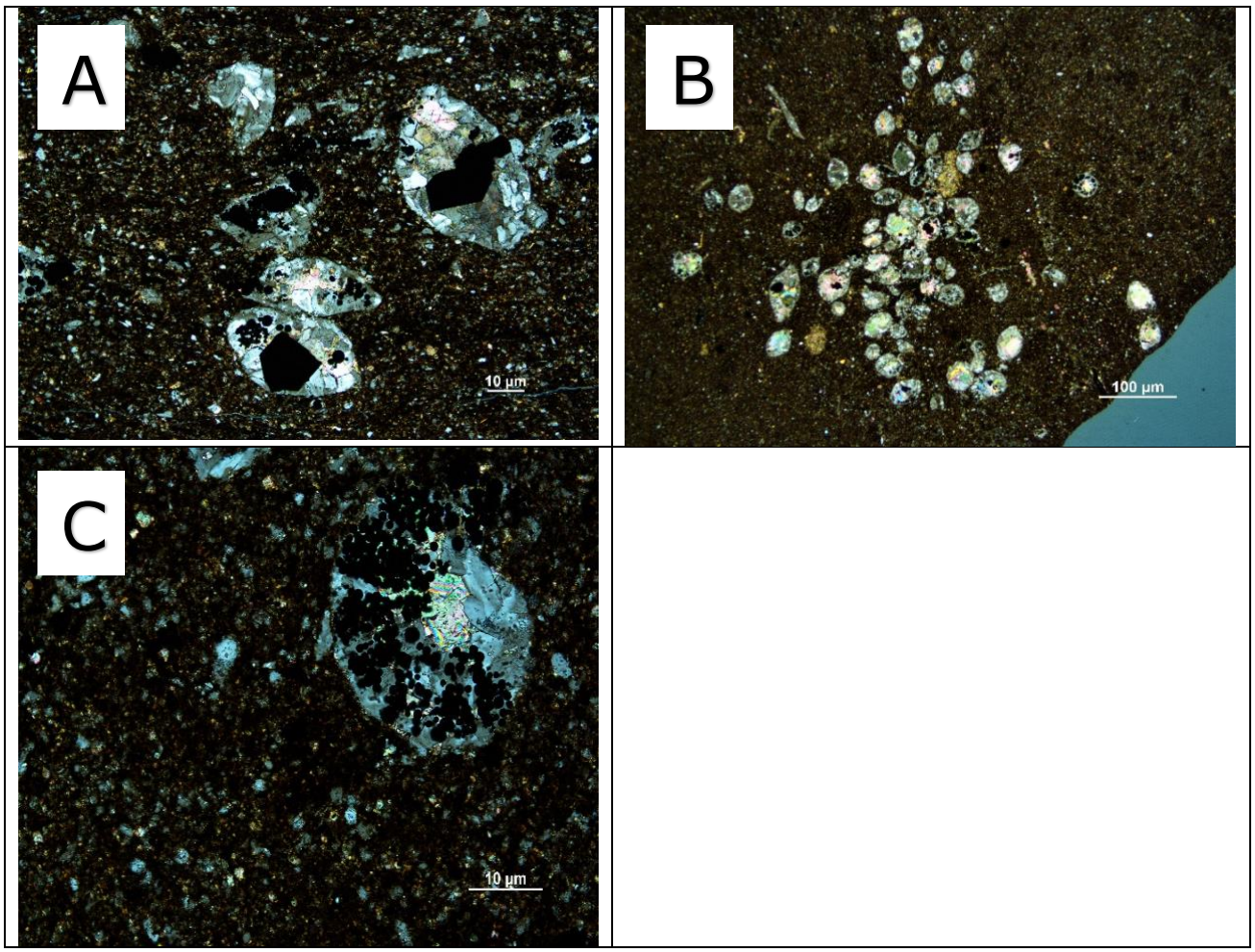

Figure 3.7 Thin section photomicrographs of sample YB01. This sample is rich in phyllosilicate (XRD analysis shows 29wt% phyllosilicate and 13wt% calcite. Diagenetic pyrite is also present within the samples. The sample recorded the highest total organic carbon of all samples (2.48 wt% TOC). (A) Clusters of microfossils with cavities filled with secondary calcite, in a finer matrix of fine-silt sized quartz and phyllosilicate grains (crossed polars; thin section normal to foliation). (B) Cluster of microfossils with cavities filled with secondary sparry calcite, leaving residual occluded voids in their centres, in a finer matrix of fine-silt sized quartz and phyllosilicate grains (crossed polars, normal to foliation). (C) Microfossil (foraminiferid) with cavities filled with secondary sparry calcite, and partially with spheroids of pyrite, in a finer matrix of fine-silt sized quartz and phyllosilicate grains. (Crossed polars, thin section normal to foliation).

YB01 thin section photomicrographs (Fig 3.7) show the sample is rich in phyllosilicate. XRD analysis show 29wt% phyllosilicate and 13wt% calcite with diagenetic pyrite present within the samples (Table 3.2). Calcite content is represented by clusters of body fossils of pelagic foraminifera, with cavities filled by sparry calcite and some occluded porosity (figure 3.7). The sample recorded the highest total organic carbon of all samples (2.48 wt% TOC). It yielded good core samples and was used for acoustic velocity measurements (wave propagation direction normal to foliation). The helium porosity is 2.55%, which is a relatively low value compared with other samples. (Table 3.2)

YB 02 A phyllosilicate-rich, carbonate poor silty mudstone.

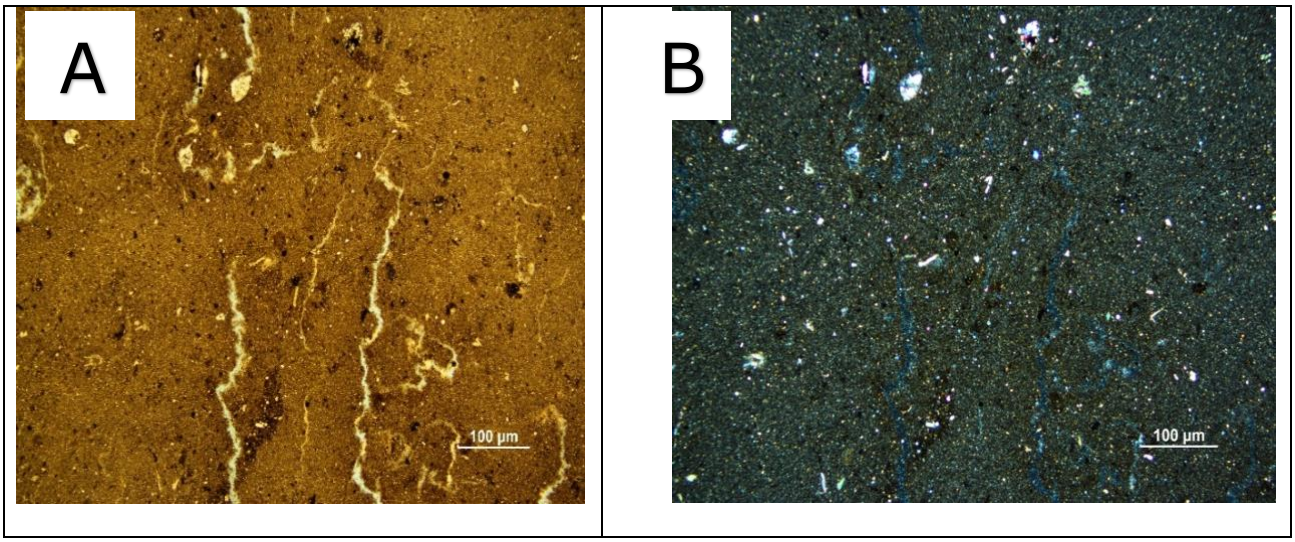

Figure 3.8 Thin section photomicrographs of sample YB 02 which is rich in phyllosilicate (XRD 30%) Both imaged are of the same field (PPL and XP) and viewed normal to foliation. The sample belongs to the group that are carbonate-poor and contain similar proportions of framework silicates and phyllosilicates and is relatively well foliated. YB 02 is fine grained with similar average concentrations of sand and silt size grains. The sample He porosity is 8.16% which is relatively termed 'porous'. Thin section view (A) shows fine silt-sized detrital grains in a phyllosilicate-rich matrix, with sinuous calcite veins. View (B) shows more clearly the fine-silt sized detrital grains in a phyllosilicate-rich matrix.

YB02 thin section photomicrographs (Fig 3.8 viewed normal to foliation) show fine-silt sized detrital silicate grains in a phyllosilicate-rich matrix, with sinuous calcite veins cross cutting the foliation. XRD analysis showed 40% vol phyllosilicate with 1.27 wt% TOC. (Table 3.2).

YB03 A calcite-rich mudstone with similar proportions of quartz+ feldspar and phyllosilicates.

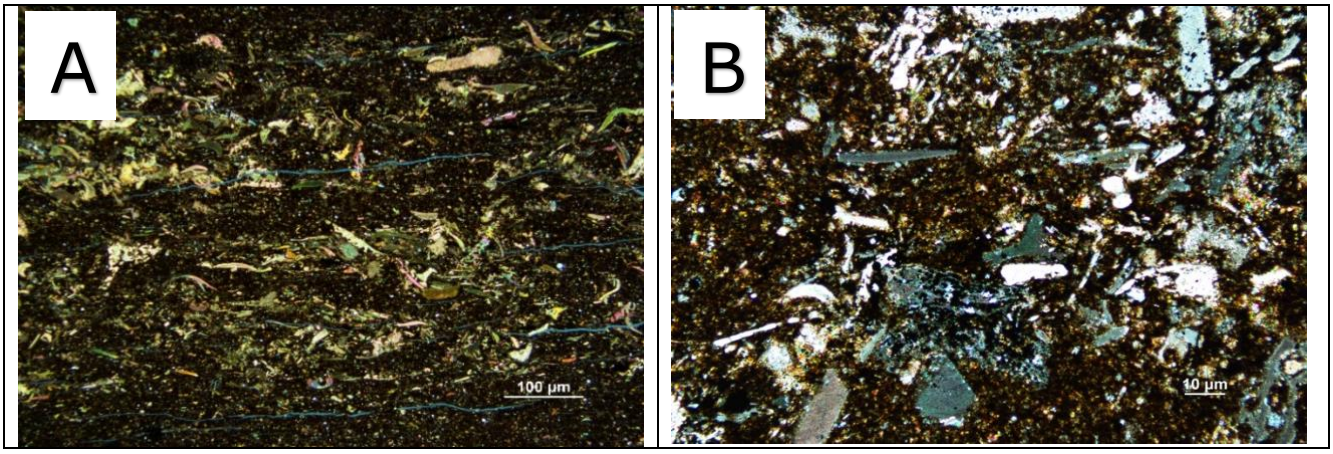

Figure 3.9 Thin section photomicrographs of YB 03 (views along foliation) showing remarkable bioturbation which has destroyed continuity of layering. The sample rock is only weakly banded but fissile with calcareous fossil fragments in matrix of finer-grained clays and detrital micas and silicates. (fine silt-sized) A) Optical micrograph, crossed polars, view parallel to foliation showing cracks. Compared to the relatively carbonate-poor samples, the foliation is not very evident from the orientation of elongate particles, but cracks have opened during the sectioning process, and these have become filled with blue impregnation resin. These have formed parallel to bedding. There is a large proportion of calcareous fossil debris, together with secondary calcite cement, and a matrix of fine silt-sized clastic grains and a phyllosilicate matrix. B) shows similar image (Optical micrograph, crossed polars), view normal to foliation.

YB03 (Fig 3.9) displaysa remarkable degree of bioturbation which destroys continuity of layering. The sample rock is only weakly banded but nevertheless fissile with calcareous fossil fragments in matrix of finer-grained clays, detrital micas and framework silicates. The XRD analysis showed YB03 to be particularly calcite-rich (47 wt%) with 1.29 wt% TOC. (Table 3.2). YB03 sample was selected as a representative of the carbonate rich group for both permeametry and acoustic velocity measurements because of its richness in carbonate (Rutter et al., 2022) and by far the greatest number of such measurements were carried out on this sample.

YB04 A carbonate-poor, phyllosilicate-rich silty mudstone.

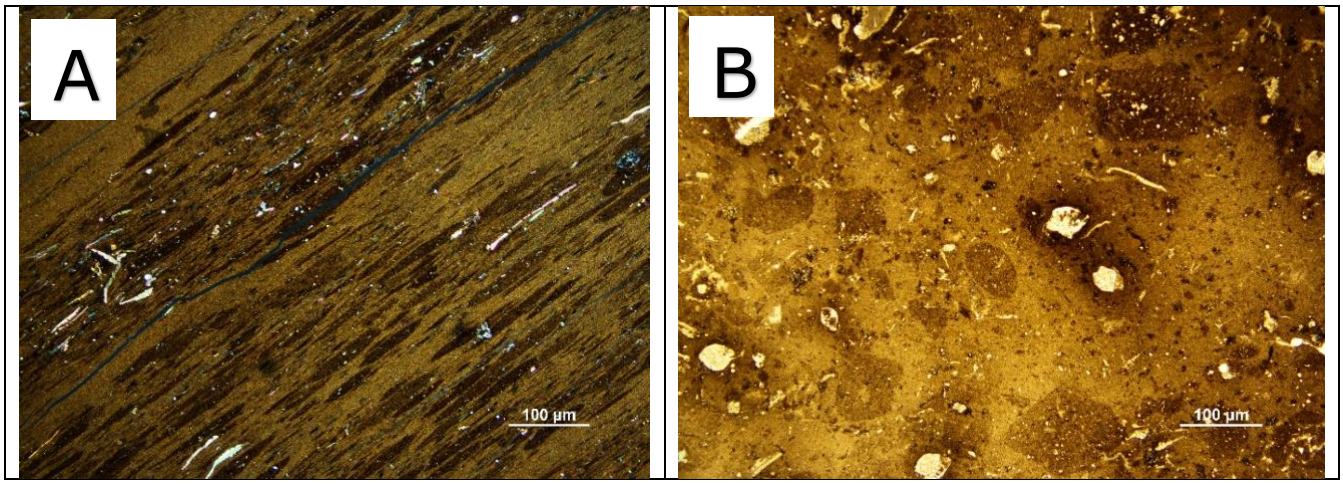

Figure 3.10 YB04 A) view parallel to bedding XPL Optical micrograph, cut normal to layering, showing silt and smaller-sized clastic grains in a phyllosilicate matrix. Ellipsoidal particles are strongly flattened rip-up clasts (intraclasts) that may have had a strong shape factor before they were redeposited. The rock contains a small proportion of shelly fossil debris. B) view normal to foliation, plane-polarized light, view onto plane of layering. The lithic rip-up clasts that appear as strongly flattened ellipsoids in the previous picture here display an equant shape, supporting the view that this rock displays a transversely isotropic fabric.

YB04 thin section photomicrographs (Fig 3.10) shows silt and smaller-sized clastic grains in a phyllosilicate matrix. Ellipsoidal particles are strongly flattened rip-up clasts (intraclasts) that may have had a strong shape factor before they were redeposited. The sample belongs to the carbonate-poor group which contains a small proportion of shelly fossil debris with XRD analysis showing 45vol% phyllosilicate with 1.75 wt% TOC. (Table 3.2) YB04 (A) sample shows a marked flattening fabric parallel to the bedding lamination which is in contrast with the less-well foliated phyllosilicate rich YB01 sample.

YB05 A carbonate-poor, phyllosilicate-rich silty mudstone

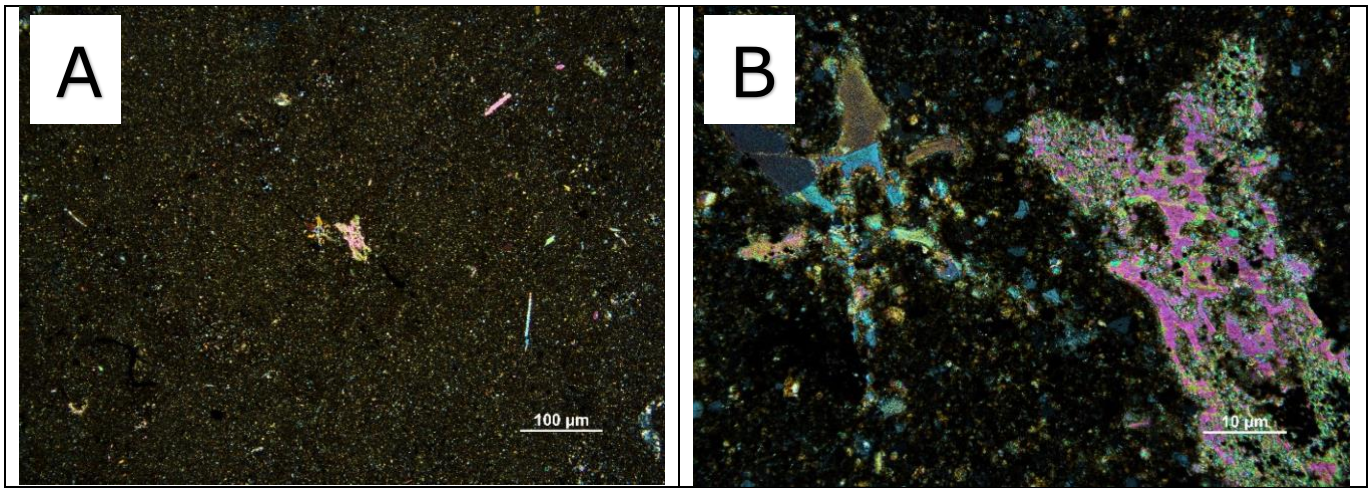

Figure 3.11 Sample YB05 A) Optical micrograph, crossed polars, view onto plane of layering, showing uniform arrangement of fine silt sized clastic grains in a phyllosilicate matrix with shelly calcite fragments. B) Larger magnification image of the central part of the previous image, showing calcareous fossil fragments in fine silt sized clastic grains within a phyllosilicate matrix.

YB05 Thin section photomicrographs (Fig 3.11) shows a uniform arrangement of fine silt sized clastic grains in a phyllosilicate matrix with shelly calcite fragments. The sample belongs to the carbonate-poor group with few calcareous fossil fragments. The XRD analysis shows 39 vol% phyllosilicate with 1.3 wt% TOC. (Table 3.2)

YB 06 A Dolomite+Calcite-Rich silty Mudstone

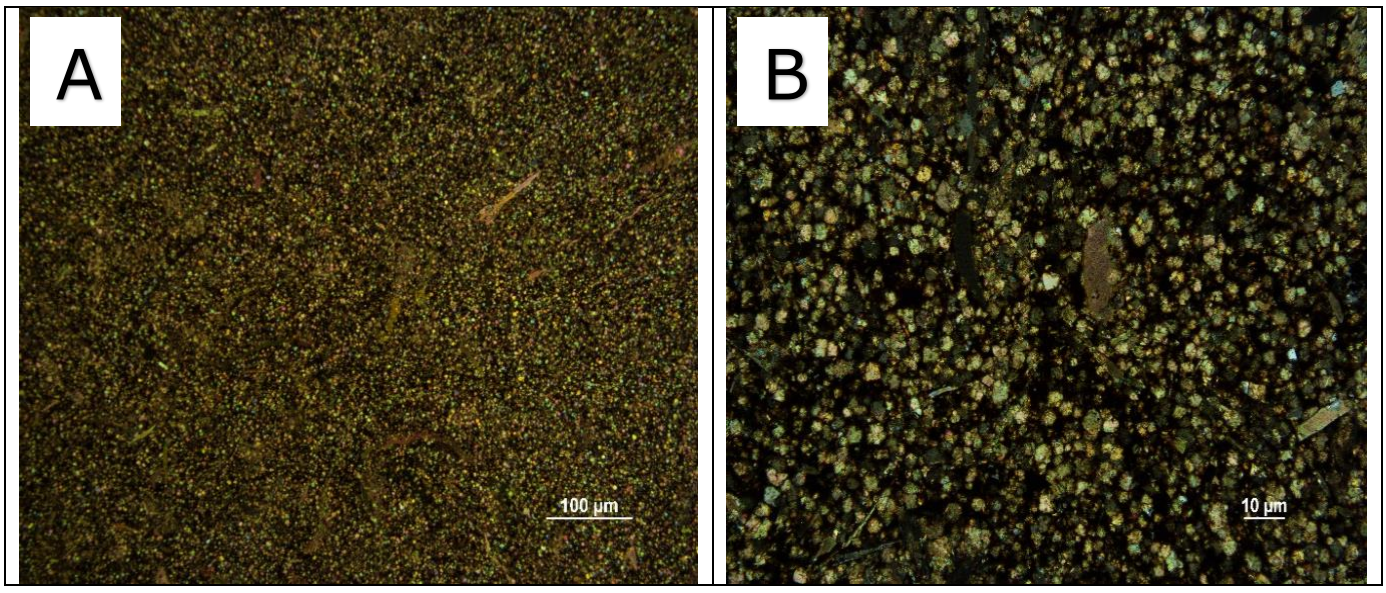

Figure 3.12 Thin section photomicrographs of YB06. There are two images of similar fields but different magnifications, A) PPL, B) XP, both showing a view onto plane of layering, with a uniform granular texture of carbonate grains (ferroan dolomite and calcite carbonate mud) in a matrix of finer framework silicate and phyllosilicate grains.

YB06 Thin section photomicrographs (Fig 3.12) shows a uniform granular texture dominated by carbonate grains (dolomite and calcite carbonate mud) in a matrix of finer framework silicate and phyllosilicate grains. The XRD analysis shows the sample is rich in dolomite with 0.99 wt% TOC. (Table 3.2). Energy Dispersive X-ray (EDX) scans of dolomite concretions within the Haynesville samples carried out by Dowey & Taylor (2019) showed both non-ferroan and ferroan chemistries in similar samples. The carbonate content impacts strongly on the overall microstructure and cementation of the sample. Therefore, it was suspected that carbonate content might correlate strongly with a low permeability for the sample. Despite its granular appearance the rock still displays a significant fissility in hand specimen.

YB07 A phyllosilicate-rich, moderate carbonate, silty mudstone

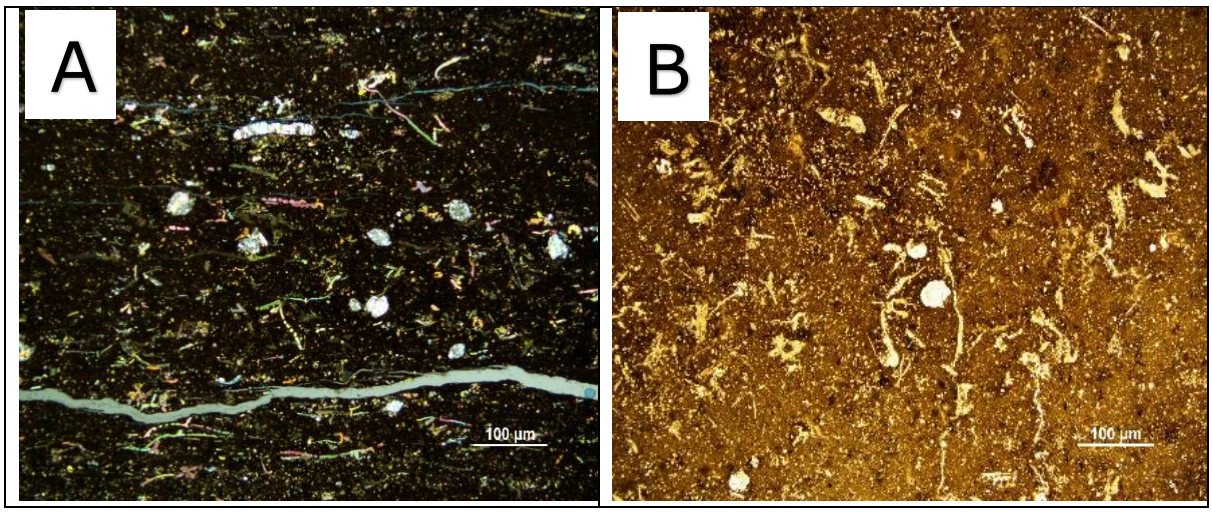

Figure 3.13 Thin section photomicrographs of YB07. In A) the sample is viewed along the foliation (crossed polars) and is better foliated than YB03 owing to the smaller carbonate content and greater phyllosilicate content. B) is a plane polarized light optical image viewed normal to the plane of foliation. Fossil debris and sinuous carbonate veins can be seen in an apparently isotropic clastic matrix.

YB07 thin section photomicrograph (Fig 3.13 A, viewed along the foliation) shows that the sample is microstructurally similar to YB03, but with much less carbonate, which results in if being better foliated, owing to the smaller carbonate and higher phyllosilicate content. The XRD analysis shows the sample to be relatively poor in carbonate with 1.94 wt% TOC (Table 3.2). Sinuous carbonate veins and fossil debris can be seen within the thin section sample (B) viewed normal to foliation.

YB08 A framework silicate-rich, phyllosilicate-bearing, carbonate-poor mudstone

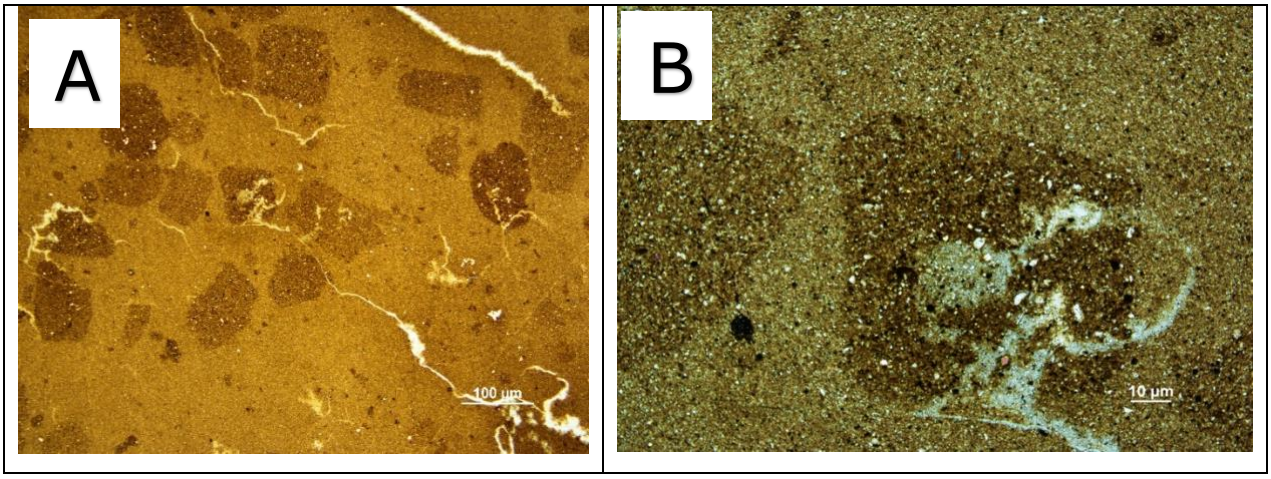

Figure 3.14 Thin section photomicrographs of Sample YB08. A) is viewed normal to the foliation. This rock shows in this view apparently equant rip-up clasts set in an extremely fine matrix of flattened and oriented silt-sized clasts and phyllosilicate matrix. B) similarly oriented but higher magnification (Cross polars), this image displays the extremely fine granularity of the rock.

YB08 thin section photomicrographs (Fig 3.14) shows it is microstructurally and mineralogically similar to YB04. The XRD analysis shows the sample is rich in phyllosilicate (39%) vol with 1.91 wt% TOC (Table 3.2). Viewed normal to foliation it shows apparently equant rip-up clasts set in a finer matrix of flattened and oriented silt-sized clasts.

3.5 General observations concerning mode of occurrence of key minerals.

(a) Detrital minerals

Calcite: Detrital calcite is present in carbonate bioclasts, often recognizable as shelly fossil fragments and even whole bivalve shells. Peloids and micro fossils are common within the detrital minerals. Large calcareous fossil fragments disrupt the formation of a planar compaction fabric and render the rock less fissile than it otherwise would be.

Dolomite: There is possible occurrence of detrital dolomites present, sometimes as rhomboids, but also as primary grains as also shown by Dowey & Taylor (2019)

Quartz: silt-sized and fine-silt-sized grains are present in all samples (e.g., in YB01, Fig.3.7a), often uniformly distributed but also as lenses.

Muscovite and clay minerals: Relatively large (>10 micron) well-oriented detrital muscovite grains appear to be generally detrital but the fine matrix grains probably consist of a mixture of detrital and authigenic grains.

(b) Diagenetic Minerals

Authigenic growths are major components of the mineralogy of Haynesville-Bossier shales (Dowey and Taylor, 2020). Common authigenic minerals observed in the samples include calcite, dolomite, pyrite, authigenic quartz and phyllosilicates.

Calcite: Calcite is the most common authigenic mineral within the Haynesville-Bossier Shale. The Hewitt land (HB) well displays secondary calcite mineralization as an intergranular cement phase within some of the analysed samples. Evident from the samples are calcite cemented fractures.

Dolomite: Authigenic dolomite occurs in form of ferroan and non-ferroan dolomite grains (Dowey and Taylor 2020). Dolomite (results from XRD) makes up a large proportion of sample YB06 (Fig. 3.7f), which is a carbonate mudstone. Dolomite has been found in the same samples but the scope of observation for this study did not afford the distinguishing of Fe- and non-Fe-rich dolomite.

Pyrite: Pyrite is present in all the eight (8) samples but at lower concentration and not more than 3.1wt % in any samples and owing to its high density the volume fractions are even smaller as shown by the XRD. They display euhedral, anhedral and framboidal features. The pyrite granular clusters are present as spherically closely packed, loosely packed or non-spherical unevenly spaced. Equant clusters typically cut across the planar bedding/compaction fabric, which demonstrates their post-compaction origin.

Quartz: The average percentage in total is about 32 vol% of quartz in the observed samples, comprising both detrital and diagenetic quartz. Quartz overgrowths are present in the cement phase and have been suggested to arise from silica released during illitization of early smectites (Dowey and Taylor, 2020).

Feldspars: There are undoubtedly detrital feldspar grains present but they cannot easily be distinguished from authigenic grains (Dowey & Taylor, 2019). Albite and orthoclase (sanidine) are usually chemically distinctive because, as a result of their formation at low temperatures on the feldspar solvuses, they have very pure end-member compositions (Dowey & Taylor, 2019). From this study, no attempt was made to investigate systematically the feldspar compositions.

Clay minerals: The average percentage for clay minerals present is about 35.3 vol%. Dowey and Taylor (2020) reported a range of clay minerals arising from diagenetic changes in these rocks, such as illitization of early smectites, releasing silica, alumina and cations to be available for the formation of framework silicate cement phases. This was also observed in this study of the Haynesville samples.

3.6 Relationship Between Rock Fabric and Mineralogy

Whereas no direct correlation could be established between constituent mineralogy and porosity, the observed mineralogical differences might be expected to be correlated with their dominant fabric types, i.e. degree of development of macroscopic foliation. As might be expected, the carbonate-poor samples displayed marked planar fabrics characterised by lithic clasts interleaved with phyllosilicate-rich layers and flattened in the plane of the foliation. In the plane of the foliation, polycrystalline clasts appeared near equant in shape, indicating the deformation was primarily by diagenetic flattening normal to the plane of the bedding, so that the overall shape fabric of the rock appears to be transversely isotropic.

The relatively carbonate-rich sample show higher proportions of primary (fossil debris) carbonate and secondary minerals (diagenetic replacement and intergranular cement). This prevents the formation of a marked planar flattening fabric, but these skeletal, debris-rich rocks are also more affected by bioturbation. It was considered that these gross mineralogical differences (carbonate poor versus carbonate-rich), reflected in morphological fabric types seen in thin section, would be likely to result in marked differences in petrophysical characteristics, particularly with respect to the orientation of bedding (foliation). It might also be noted that owing to a relatively poor planar fabric development in carbonate-rich samples, it might be easier to obtain core samples, from YB03 for example, than from the more strongly foliated types.

Surprisingly, even the more massive, carbonate-rich specimens possessed a 'latent' fissility in hand specimen, such that there was little difference in the difficulty of obtaining successful core samples without splitting across the whole range of samples.

3.7 General observations of samples pertaining to experimental methods employed

Physical observation of the core-slab samples showed the samples YB05, YB02 and YB08 displayed visible laminations. YB04 showed mineralized veins with hydrocarbon stains. YB02, YB08 and YB03 showed visible carbonate-filled, lighter-coloured fractures (veins) within the core-slab samples.

Of the 8 samples selected for this study, only YB03 and YB06 were rich in carbonate (over 50 vol%), while the remainder fell into the carbonate-poor category. The YB 03 sample was selected for both permeability and acoustic velocity measurement as a

representative of the carbonate-rich group. The carbonate content evidently impacts strongly on the overall microstructure and cementation of these rocks. (Dowey and Taylor 2020). Therefore, it was suspected that carbonate content evidently might correlate strongly with the permeability. The samples YB 06 and YB 01 show remarkably low porosity, A pulse transient decay permeability test, better suited to lower permeability materials, was therefore planned for these samples.

The constant flow rate permeability tests on the CoreTest rig using the steady state flow method at constant pore pressure difference were planned on YB05, YB08, YB02 and YB04 cores, with individual pressure cycles to be run alternating between constant P_c and constant P_p conditions, to produce the variations in effective pressure by different routes. These four samples belong to the low carbonate% group sand would be tested dry on cores cut parallel to the layering.

3.8 Conductive Porosity

As pointed out in Chapter 2 (section 2.2) the microstructural features of porosity that contribute to fluid flow in shales can only be observed with TEM (Ma et al., 2017). This is a specialist technique that lay outside the scope of the present study. Table 3.2 shows that with the exception of sample YB01, the total accessible porosity of the Haynesville shales studied here lies in the range 7 to 10%. In porous sandstones, this level of porosity is typically associated with high permeabilities, and all the porosity can be expected to contribute to the permeability. Combined with the effects of grain size (d) in sandstones in particular, permeability in sandstones has been shown to be proportional to $\varphi^3 d^2$ (Bourbie and Zinsner, 1985), i.e., there is a systematic relationship between porosity and permeability.

In shales such as studied here, on the other hand, the low values of permeability typically encountered and which will be described later suggest that most of the porosity is in the form of partially occluded 'storage' pores, with only about 1% of the porosity contributing to the permeability, hence no simple correlation between porosity and permeability can be expected (Rutter et al., 2022). Porosity, and the extent to which it is connected, could not be observed in the optical thin section observations made on Haynesville shale as described above because the small grains sit on top of each other in the thin sections, and also the conductive channelways between them lie beyond the scale of optical resolution.

Whilst standard petrography cannot image conductive porosity, correlations between bulk petrographic and mineralogic features, such as total carbonate content, and

measured permeability can potentially be established, and this possibility is explored in subsequent chapters.

3.9 Samples selected for permeability and velocity measurements.

Based on the mineralogy and microstructural features of the above samples the following were selected for velocity and permeability measurements. It was clear that samples fell into two broad groups based on mineralogy (Fig. 3.6b), (a) carbonate-rich and relatively phyllosilicate poor (YB03 and YB06, both of which contain over 50% volume carbonate), and (b) carbonate poor but relatively phyllosilicate and framework silicate rich (i.e., all other samples, although of these YB07 contains an intermediate proportion ~20% vol. carbonate).

From the more phyllosilicate-rich samples it was not always possible to obtain suitable core samples for both velocity and permeability measurements because the slabbed samples supplied possessed a minimum dimension of only about 4 cm. YB01, which is similar to other samples that have been cored few meters apart from one another, was used for acoustic velocity measurements (wave propagation direction normal to foliation). YB05 was selected for permeability measurements.

3.10 Sample preparation for high pressure testing.

The selected Haynesville Shale samples (YB 01, YB 02, YB 03, YB04, YB 05, YB 06, YB 07 and 08) slabbed cores were sub-cored, using tap water as drill coolant, to make 25 mm or 26 mm nominal diameter cylindrical samples cored both parallel and normal to foliation (bedding). Core sample lengths ranged from 8mm to 30mm. Several diameters of each sample were measured and averaged to an overall accuracy of within 0.01mm using a digital calliper after using a saw to trim the ends, followed by gentle grinding with fine carborundum paper to make them flat and parallel. The mass of each freshly prepared sample was also measured to an accuracy of 0.001g.

All of the samples measured for this study were tested in an oven-dried state. It is to be expected that partial saturation of samples with water will lead to reduction in permeability and potentially have an effect on acoustic wave velocities. Testing in the dried state was therefore considered to be the 'reference state'.

The samples were oven dried at 60°C until constant mass was achieved (Table 3.2, Fig. 3.15.a & 3.15.b). At or below 60°C organic particles do not alter, nor is there dehydration of swelling clay minerals (Bush & Jenkins, 1970). Constant mass was attained typically after about 160 hours of drying, or fewer, according to sample size,

but drying was usually continued for more than 200 hours. Samples were stored in desiccators after removal from oven before testing. Sample weights were further checked before putting in the testing rig.

There is likely to have been some uptake of pore water during the core drilling, especially into cracks, thus the overall loss of weight during drying can be used to estimate the amount of water initially in the samples. The weight loss in grams is equal to the volume of water (in ml) lost from the sample. Thus, after determination of the dry pore volume, the water volume loss during drying can be expressed as a percentage of the pore volume and is a measure of the initial saturation of the sample. Fig. 3.15 shows examples of weight loss curves obtained during drying.

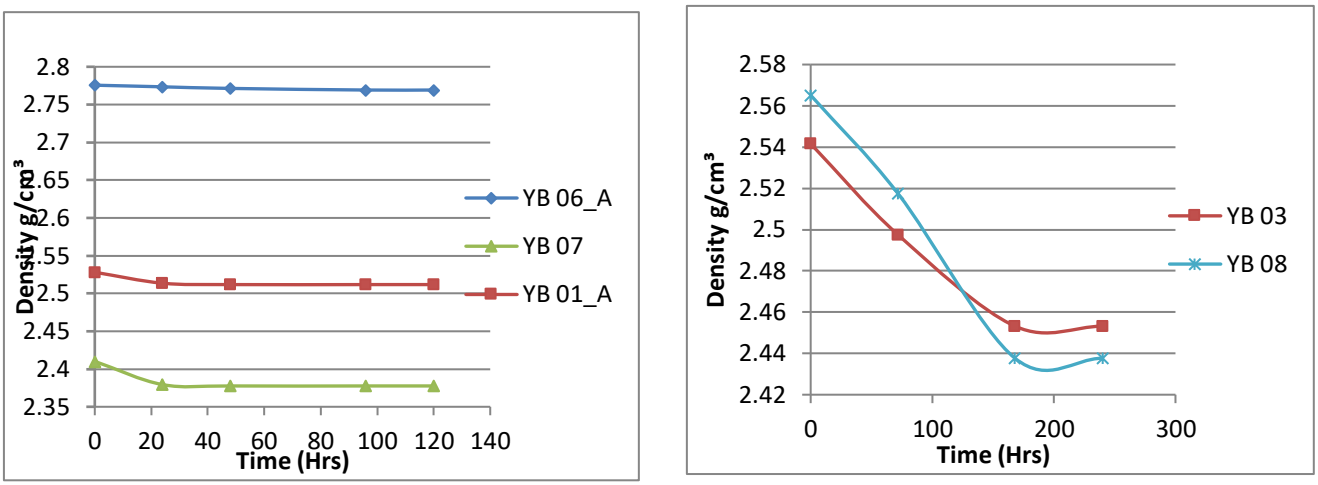

Figure 3.15 A & B Graphs showing weight loss data during oven drying expressed as changes to the densities of samples YB03, YB08, YB06, YB07 and YB01. The densities became constant after 240 hours of drying. The oven was controlled at 60° to inhibit dehydroxylation of swelling clays and thermal damage to organic matter particles.

3.11 Organic Carbon Analysis

(a) Total organic carbon (TOC)

TOC analysis was carried out by **Applied Petroleum Technology** AS in Norway. The TOC measures the total organic content of a rock. TOC analyses were carried out on a LECO SC-632 instrument equipped with an Infra-Red detector to analyse the released combustion products of **CO_2 and CO.** Crushed samples 220-260 grams were first washed with diluted HCl to remove any inorganic carbon (e.g., as carbonate) prior to analysis. Hence organic carbon was the only carbon left within each sample after acidification. The samples were washed and dried to remove excess acid prior to the analysis. The samples were heated in air in an oven to 720°C hour for the complete combustion of the organic carbon, thereby converting it to CO_2. The CO_2 released is

directly proportional to TOC. This was measured and reported as TOC of the sample (Steiner et al., 2016).

(b) Rock Eval Pyrolysis

Rock-Eval pyrolysis is one of the alternative methods for TOC measurement which is also carried out by the **Applied Petroleum Technology AS** Company in Norway. Here, the sample is subjected to temperature stepwise pyrolysis. During Rock-Eval pyrolysis a continuous monitoring is made of CO_2 and CO released during both combustion and pyrolysis (Fig. 3.16).

A Rock-Eval 6 instrument was used for these measurements. A sample of Jet-Rock 1 (the reference standard used) was run for every tenth sample and checked against the acceptable range given in the Norwegian Industry Guide to Organic Geochemical Analyses (NIGOGA). For pyrolysis, the samples were crushed to a fine particle size ranging between 0.125-0.25 mm & 100 mg samples were loaded and heated to 300 °C for 3 minutes to release the so-called **free carbons (S1)** present within the rock sample (Fig. 3.17). Each sample was then gradually heated to 650 °C and held for 20 minutes, resulting in vaporisation of **heavier hydrocarbons and cracking of both bitumen and kerogens**, thereby producing lighter hydrocarbon which is measured as S2. (Fig. 3.17) During the analysis any hydrocarbon released passes through the flame ionizing detector (FID); the FID response is proportional to the content of hydrocarbons present in the samples (Fig 3.17)

This generation of apparatus is equipped with a combustion oven for the rock residue after pyrolysis. This residue also potentially contains carbon, and the oven is also fitted with an infra-red cell to ensure the continuous monitoring of CO_2 and CO release during both combustion and pyrolysis. (Fig 3.17) The final phase of the method is to oxidise the residual rock recovered after pyrolysis by heating to 850°C, in an atmosphere composed of 80% of N_2 and 20% of O_2.

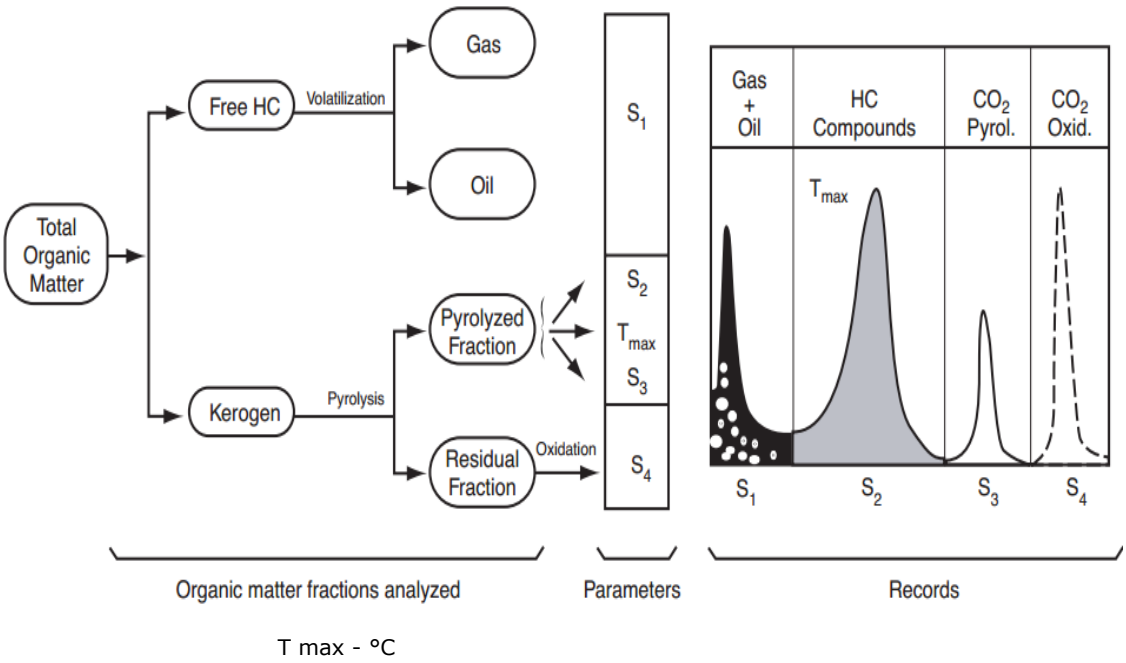

Figure 3.16 General diagram showing the different fractions of the total organic matter of analysed rocks, the corresponding parameters and their recording (Lafargue et al., 1998).

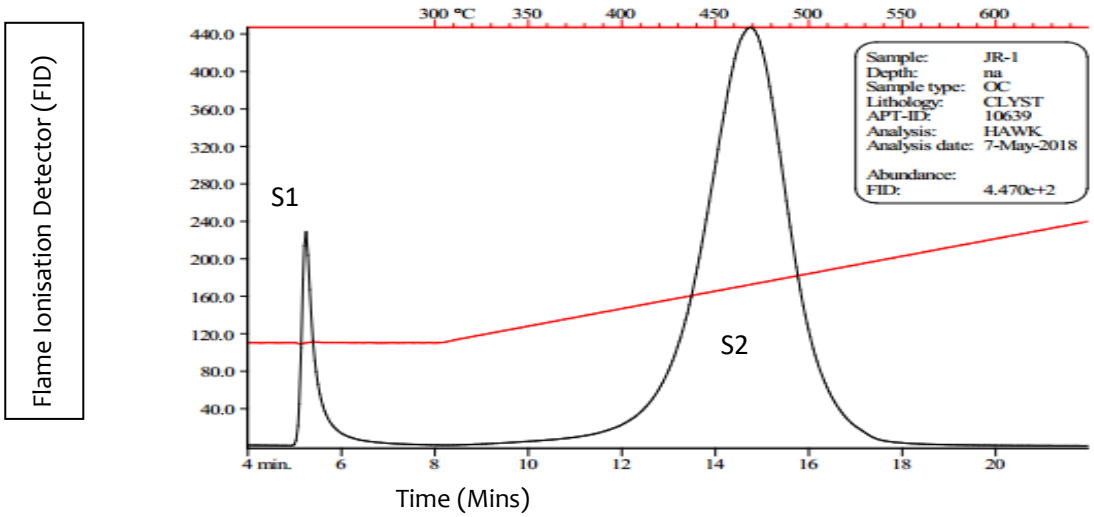

Figure 3.17 The first and second Flame Ionisation Detector (FID) stages are named S1 and S2 respectively. S1 is amount of Hydrocarbon (HC) already present in the sample and it also represents thermally vaporised free hydrocarbon contained in the rock while S2 is the amount of hydrocarbons generated by degradation of OC during between 350°C & 650°C it represents hydrocarbon produced from the cracking of sedimentary organic matter.

(c) Total organic carbon (TOC) and Rock-Eval pyrolysis results

A total of 8 samples were analysed (Table 3.3). The TOC in the selected samples ranges between 2.48 and 0.99%, with sample YB01 recording the highest while YB06 the least. The TOC result generally suggests that the Haynesville Shale samples used for this analysis are organic-lean.

Sample Name	Lower Depth (ft)	S1 (mg/g)	S2(H) (mg/g)	S3(Co_2) (mg/g)	Tmax (°C)	PP (mg/g)	PI (wt ratio)	HI (mg HC/g TOC)	OI (mg CO2/g TOC)	TOC (wt%) *
YB 05	11423.5	0.05	0.1	0.55	598	0.15	0.33	8	42	1.3
YB 02	11480.0	0.09	0.1	0.76	289	0.19	0.47	8	60	1.27
YB 06	11795.4	0.13	0.08	0.39	609	0.21	0.62	8	40	0.99
YB 03	11565.3	0.3	0.11	0.52	285	0.41	0.73	9	40	1.29
YB 04	11675.5	0.07	0.09	0.57	609	0.16	0.44	5	33	1.75
YB 07	11677.0	0.07	0.11	0.61	609	0.18	0.39	6	31	1.94
YB 01	11554.5	0.06	0.09	0.59	608	0.15	0.4	4	24	2.48
YB 08	11760.0	0.08	0.1	0.7	607	0.18	0.44	5	37	1.91

Table 3.3 Haynesville Rock-Eval pyrolysis results showing the free Hydrocarbon-Carbon (S1), Hydrocarbon as a result of degradation of organic carbon (S2), hydrogen index (HI), Oxygen Index (OI) and total organic carbon (TOC).

S1 is amount of hydrocarbon already present in the sample and it also includes thermally vaporised free hydrocarbon contained in the rock. **S2** is the number of hydrocarbons generated by degradation of organic carbon during between 350°C & 650°C. It represents the hydrocarbon produced from the cracking of sedimentary organic matter.

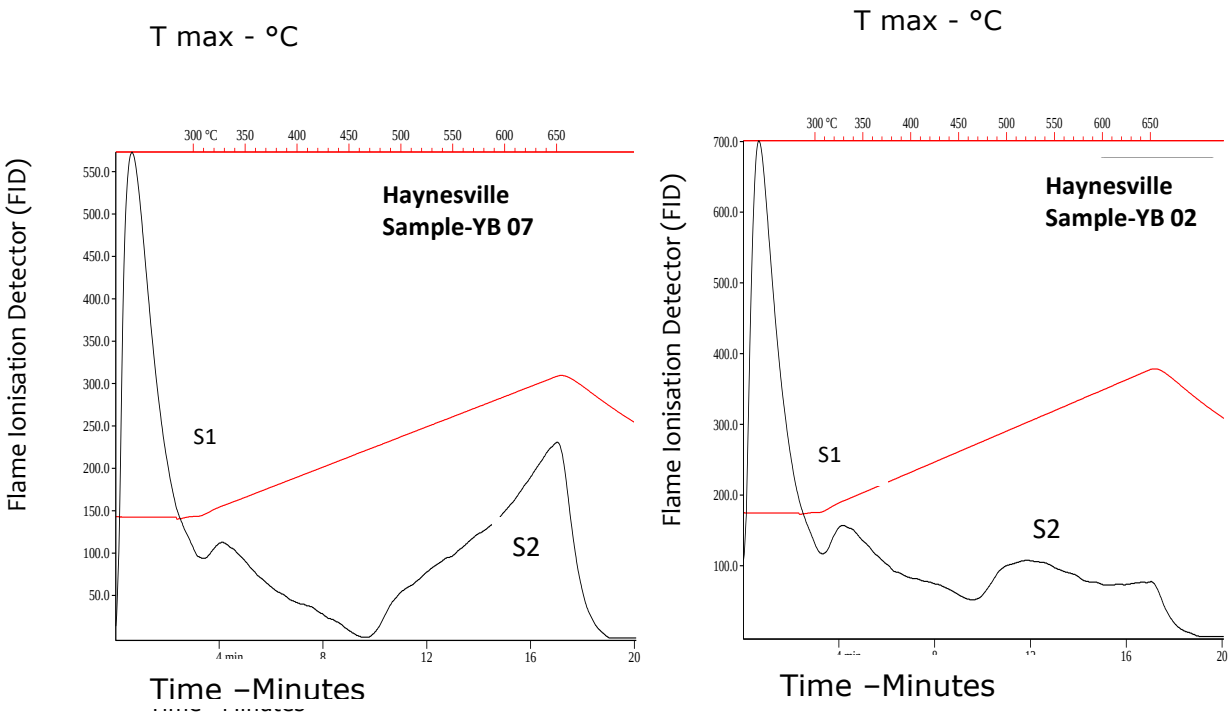

Figure 3.18 Examples of pyrograms for Haynesville YB 07 and YB 02 samples showing the S1 and S2 peaks.

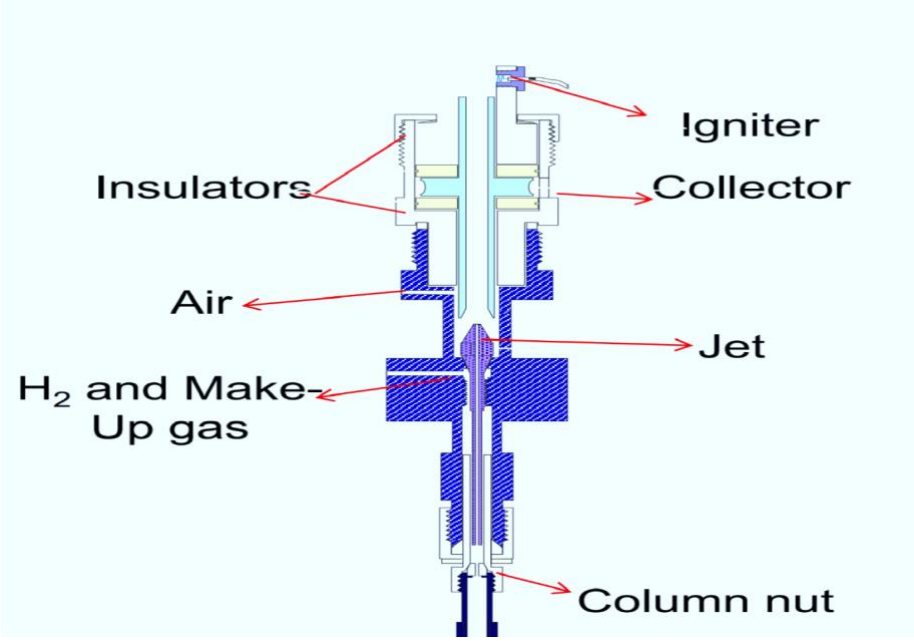

Figure 3.19 FID column within the instrument, the Flame Ionisation Detector detects the hydrocarbon within the samples.

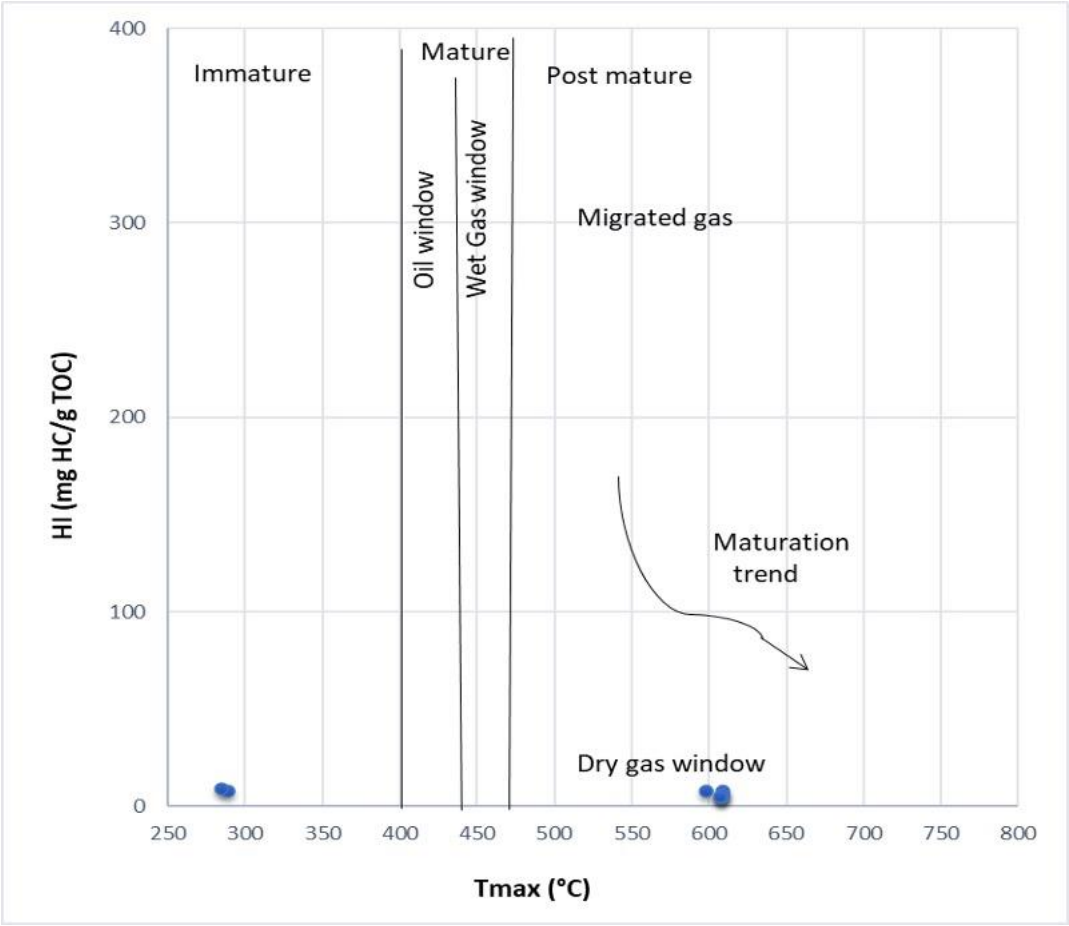

Figure 3.20 HI (hydrogen index) vs Tmax cross plot: the plot shows the kerogen type and maturity range of the samples.

The maturation of samples is poor to fair which is sufficient for gas generation. Most of the samples fall in the post-matured zone (Figure 3.20), and has generated gas in some of the intervals. The maturation increases with depth, the samples falls within the dry

gas window, meanwhile Haynesville formation has some producible dry gas within some intervals in other locations.

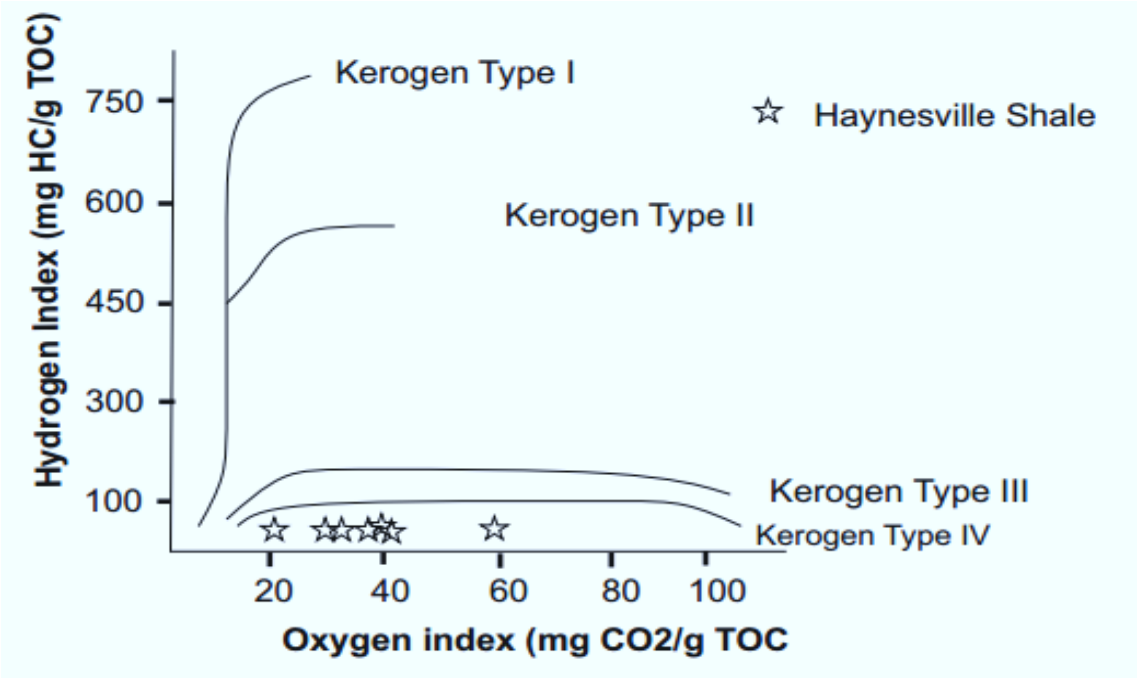

Figure 3. 21 Van Krevelen diagram of the Haynesville samples, it shows they all fall within the type IV of the kerogen types, which is the gas-prone section.

Analysed data from this study shows all the samples from this Haynesville core fall within type IV Kerogen (Figure 3.21). It is composed of < 20 hydrogen index (HI) which is poor and difficult to distinguish from type III kerogen. The kerogen type falls within the type IV with poor hydrocarbon constituents. It is an inert gas which falls within the end member on the hydrocarbon generative spectrum.

3.12 Porosity of the starting material

a) Gravimetry combined with quantitative XRD.

Total porosity of shale samples can be estimated by gravimetry, that is by measuring the bulk density ρ_b of a dried cylindrical sample from its weight and volume, and by measuring the grain density, ρ_g. Porosity ϕ is then given by.

$$\phi = 1 - \frac{\rho_b}{\rho_g} \qquad Eqn\ 3.1$$

The grain density can be measured using a specific gravity (SG) bottle, in which a sample is finely crushed to break down the pore spaces. However, this is particularly difficult for shales because the particle size must be very small to break down the pore spaces, especially any sealed or isolated pore spaces. This results in a tendency for the small particles to become suspended in the water (despite containing a drop of

detergent per 200 ml to break down surface tension) added to the SG bottle, and/or for surface tension forces to prevent ingress of water into all of the very small spaces, hence the apparent grain density can be smaller than the true grain density. For this reason, this method was not used in this study.

An alternative approach to estimation of the grain density is to use modal proportions and published densities of the principal mineral phases present, as determined from XRD, and to sum their contributions to the overall grain density. This approach was used in the present study and the results obtained are given in Table 3.2. This approach yields the *total* porosity of the rock because it is not dependent upon a fluid (liquid or gas) accessing the rock pores.

These results can be compared with those from porosity determination using helium pycnometry (section (b) below), the results of which are also shown in Table 3.2.

(b) Helium Method

Helium pycnometry measures the total volume of solid grains in a dried regular cylindrical sample. Together with the bulk density of the sample (assuming the pore spaces to be empty), the grain density and hence the porosity can be obtained. The grain density together with the bulk density of the sample can be used to determine the porosity using the equation (Eq. 3.2) given above.

Determination of the grain density depends on measuring the volume of helium gas that penetrates the sample, hence what is measured is the *effective* porosity, i.e. that proportion of the total porosity accessible to gas flowing in from the outside. For high porosity rocks the total porosity and effective porosity are approximately equal, but for a low porosity rock, or one that is fine-grained, or one with occluded or isolated pores, the effective porosity may be less than the total porosity. However, helium gas is highly fugitive and can be expected to penetrate connected pores of even atomic dimensions, thus the measured porosity can be close to the total porosity. Any intragranular, sealed pores will remain inaccessible, however. It is implicit in the application of the helium method that there is no significant proportion of the gas selectively adsorbed onto grain surfaces.

The experimental method is based on an empirical application of Boyle's law. The apparatus used (RESLab^{TM} DHP-100 digital helium porosimeter) is shown in Fig. 3.24.

The porosimeter (figure 3.24 A) has two chambers; the sample cell (of volume V_c) and the reference cell (of volume V_1), which can be connected or isolated from each other by a valve whose operation does not affect the total volume. The chamber V_c typically can accommodate a cylindrical sample 25 mm diameter and up to 100 mm long. The temperature of the chambers is measured continuously and must remain constant throughout the experiment, so that nRT (n-number of moles of gas, R-gas constant & T -Temperature) of the gas remains constant. The measurements are carried out at low pressure, less than 1 MPa, so that the behaviour of the gas can be assumed to be ideal. The gas pressure measurement transducer (with a resolution (and precision) of 0.0001 MPa) is connected to volume V_1 (Figure 3.23B) and with the interconnecting valve closed helium is admitted to V_1 until a pressure rises (from atmospheric) on the order of 0.7 MPa is attained, V_1 is then isolated. V_c remains at atmospheric pressure of air. When the interconnecting valve is opened, the new, larger volume is V_1/V_c, hence the pressure falls to P_2. The system is calibrated by measuring the pressure ratio P_1/P_2 following the introduction of each of a series of steel discs (or a combination of discs) of known volume into the sample chamber. A plot of P_1/P_2 vs disc volume is a straight line, such as illustrated in Fig. 3.22. The pycnometer is provided with switches that make small changes to the amount of the reference volume; therefore, it is essential that the same reference volume is used for calibration and for all measurements on rocks.

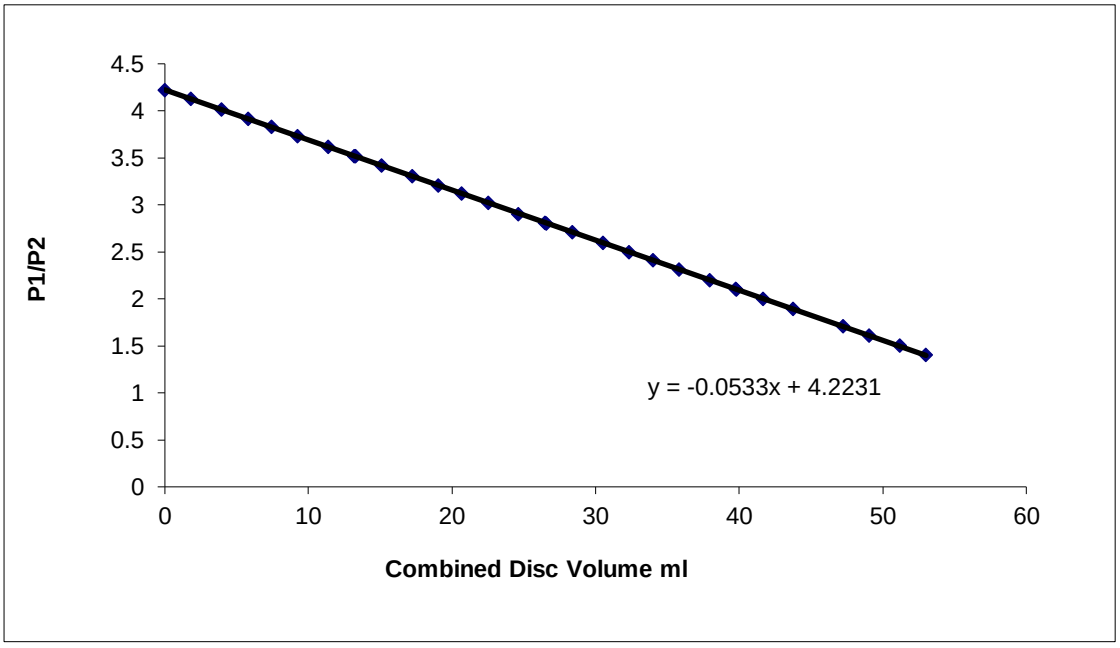

Figure 3.22 Example of a calibration of the helium porosimeter, showing how P1/P2 varies as the volume of steel discs in the sample chamber is increased.

Errors of measurement can be estimated from the parameters of the linear regression.

A straight line fit to the data is obtained, hence by measuring P_1/P_2 with an unknown cylindrical porous specimen in the sample chamber, the solid phase volume (i.e., grain volume) of the sample can be calculated using the linear fit obtained in the calibration procedure, and hence the porosity can be calculated. To ensure confidence in the results, the user should carry out his or her own calibration at the start of each programme of measurements. Also, the measurement relies on the setup being at a constant temperature therefore differences in laboratory temperature will affect the calibration. Because the *ratio* of two pressures is measured, this obviates errors arising from a small degree of long-term instrumental drift in the pressure measurements. Precision is more important than accuracy. The only volumes that are required to be known accurately are the calibration disc volumes.

The method depends on the effective permeation of the helium into all the pore space until a constant pressure P_2 is attained. Enough time is required for such permeation to occur, and for the transient adiabatic temperature change to dissipate. This typically takes a few seconds to one or two minutes. Before the unknown specimen is used, the system must be checked for leaks (slow pressure decay). If a continuous pressure decay occurs with a specimen volume in place it may imply time-dependent adsorption of gas into organic grains in the specimen, for example. With care, porosities can be measured by this method to better than 0.1% of the measurement.

A

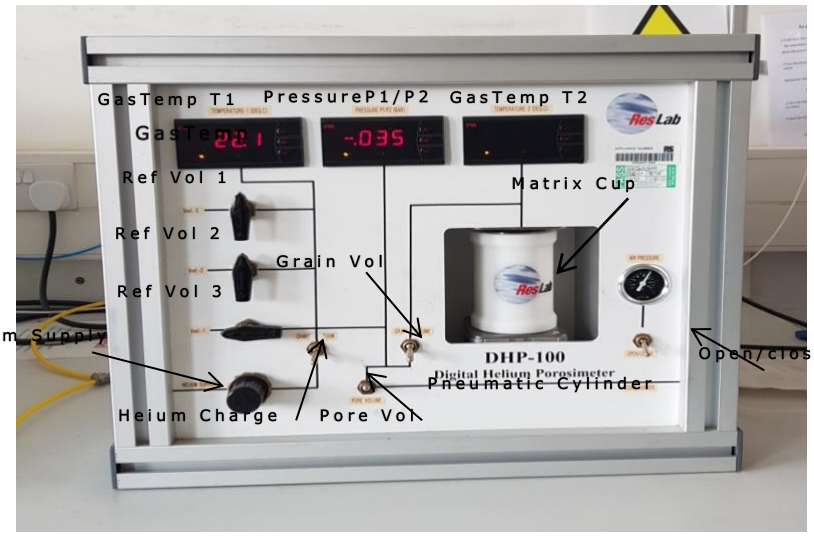

B

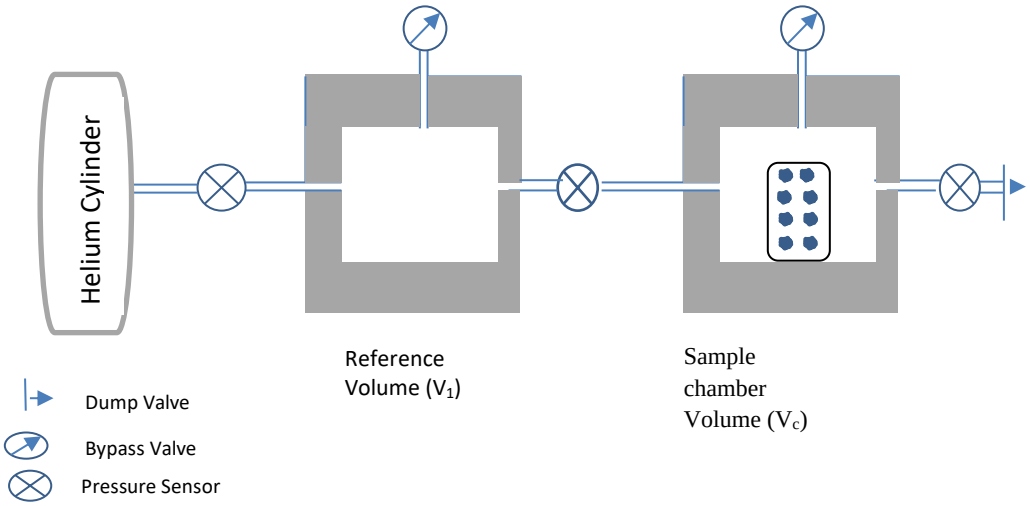

C

Figure 3.23 A) External photographic view of the Res Lab Porosimeter B) A schematic diagram showing the layout of the Porosimeter, with a representation of a porous rock cylinder inside volume V2 C) Specimen vessel (volume V2) and calibration disc set provided with the Porosimeter.

(c) Comparative porosities from Helium and XRD measurements

Table 3.3 shows the values of porosities obtained by the two methods, and these are compared graphically in Fig. 3.24. Total porosities obtained using the XRD method tend to be higher than those estimated using helium porosimeter. This is to be expected if there are occluded pores that are inaccessible to gas introduced from outside, whereas the XRD method is sensitive to all of the porosity in the sample, whether externally accessible or not.

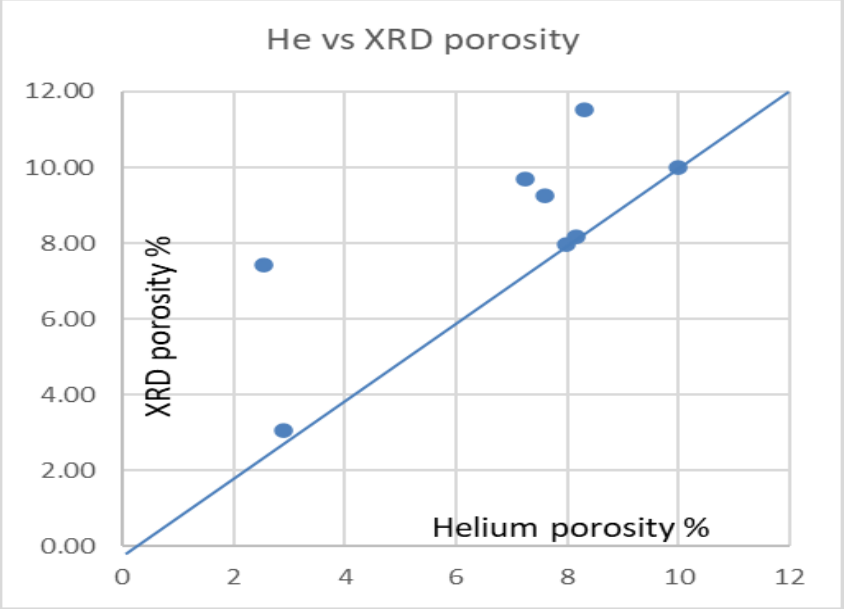

Figure 3.24 Comparative porosities estimated from the XRD and helium imbibition methods. The XRD results are equal to or greater than the helium porosities, suggesting that in some samples there has been incomplete flooding of the pore spaces with helium.

Chapter 4 – Experimental Methods for Permeability and Acoustic Velocity Measurements.

4.1 Introduction

After specimen characterization, the principal aim of the laboratory testing part of this research has been to measure (a) the permeability of Haynesville Mudstone under a range of high confining and pore pressures and (b) acoustic wave velocities and pore compressibilities under high pressures and pore pressures, and (c) to determine the interrelationships between these data as part of the research aim. In this section are described the experimental apparatus used, calibrations and methods of use.

4.2 Permeability measurement

Permeability measurements on cylindrical core plugs from conventional reservoir rocks are commonly made using steady-state pressure difference conditions, so that permeability can be obtained directly from the definition of permeability as expressed in Darcy's law. Either a constant flow-rate condition can be imposed, eventually resulting in a constant difference in fluid pressure at either end of the sample, which is then measured, or in an alternative approach a constant pore pressure difference is imposed at the ends of the sample and the resulting flow rate is measured (Zolotukhin, 1997).

In very low permeability rocks (<1 md or $<10^{-18}$ m^2) it can take a long time to establish a steady state condition, therefore it can be better to use a non-steady state (transient flow) method, such as the pulse transient method (Brace et al., 1968) or the oscillating pore pressure method (Bernabé et al., 2006; Fischer, 1992; Kranz et al., 1990). The pulse transient method is much easier to apply, but issues can arise from the fact that only a small amount of fluid is displaced through the sample. Variation of pore pressure in these sample with time means that the pressure-sensitive compressibility of the pore fluid must be known and the pressure sensitivity of pore fluid viscosity. Even small temperature fluctuations can affect the data, as can the possibility of even minor pore pressure leaks. To overcome the impact of temperature fluctuations and (small) pore pressure leaks the oscillatory pore pressure method can be employed. However, when measurement of extremely low permeabilities ($< 10^{-20}$ m^2) is required, or for measurements at low pore pressure, or if there is partial liquid saturation of the pore spaces that can lead to capillary entry pressures, the pulse transient method has been previously identified as a better approach (Mckernan et al., 2017).

For the samples tested here, the oscillatory pore pressure method, the pulse transient (decay) method and constant pressure difference method have all been used on various samples, owing to the variability within the selected sample set.

4.3 Apparatus and calibration

Measurements were carried out on two equipment items: the CoreTest rig and the 'BigRig'. The CoreTest rig was modified from an original piece of equipment manufactured by CoreTest® and intended for experiments under hydrostatic pressure conditions. The BigRig was built in-house additionally to permit 'triaxial' testing both in extension and in compression. It allows measurements over a wider range of pore pressure and confining pressure values than the CoreTest rig. It was also used specifically to measure permeabilities in physically the same samples for which acoustic velocity measurements had been carried out or were going to be carried out.

4.3.1 The CoreTest rig.

For the CoreTest rig, samples of 25mm nominal diameter with varying lengths were used for the experiments. A sintered stainless-steel porous disc was placed at both ends of the sample in order to spread the pore fluid uniformly over each end of the sample and were connected respectively to the upstream and downstream reservoirs. The sintered discs (GKN type SIKA R5AX) have a porosity of 31.5% (table 4.1),

Porosity	Filter Grade	Permeability Coefficient		Grade Efficiency	Bubble point pressure ΔP	Shear Strength
		α [10^{-12} m^2]	β [10^{-7} m]	[µm]	[mbar]	[N/mm^2]
31.5%	SIKAR-R 5 AX	0,08	0,3	1,3	89	350

Table 4.1 Sintered disc specifications

Samples were jacketed in a heat shrink rubber and placed in a 53 cm long high-pressure vessel with a maximum confining pressure rating of 70 MPa. (Figure 4.2) Samples was assembled and hydrostatically pressurized by water in the vessel. The confining pressure is measured using a Haskel 10,000 psi (70 MPa) rated pressure transducer with accuracy of ± 0.1%. All the experiments were carried out at ambient temperature (21°C). It was established by using a solid steel dummy specimen that no short-circuit flow of pore fluid took place between the jacket and the specimen cylindrical surface.

For the pore pressure, argon gas was used as the permeant fluid. This gas has a viscosity at one atmosphere pressure of 2.23 x10^{-5} Pa s (Michels et al., 1954) and does

not interact with clay chemically (Faulkner & Rutter, 2010). The gas is supplied to the permeameter via a compressed air-driven gas booster pump through a valve (labelled Gas-In in Figure 4.2).

Whilst the confining pressure was held constant during each experiment, the pore pressure sinusoidal waveform (typically 1 MPa amplitude) used in the oscillating pore pressure tests was generated using a small pressure intensifier driven via a mechanical screw, in turn driven from a stepper motor, and controlled by the data logging and control computer. The data logging and control was carried out using the Labview® software, which recorded the confining pressure, the upstream and downstream pore pressures, and the displacement of the piston of the pore pressure intensifier. The latter was measured by a Linear Variable Differential Transformer (LVDT) The calibration procedures for the various measurement devices is given in the following section.

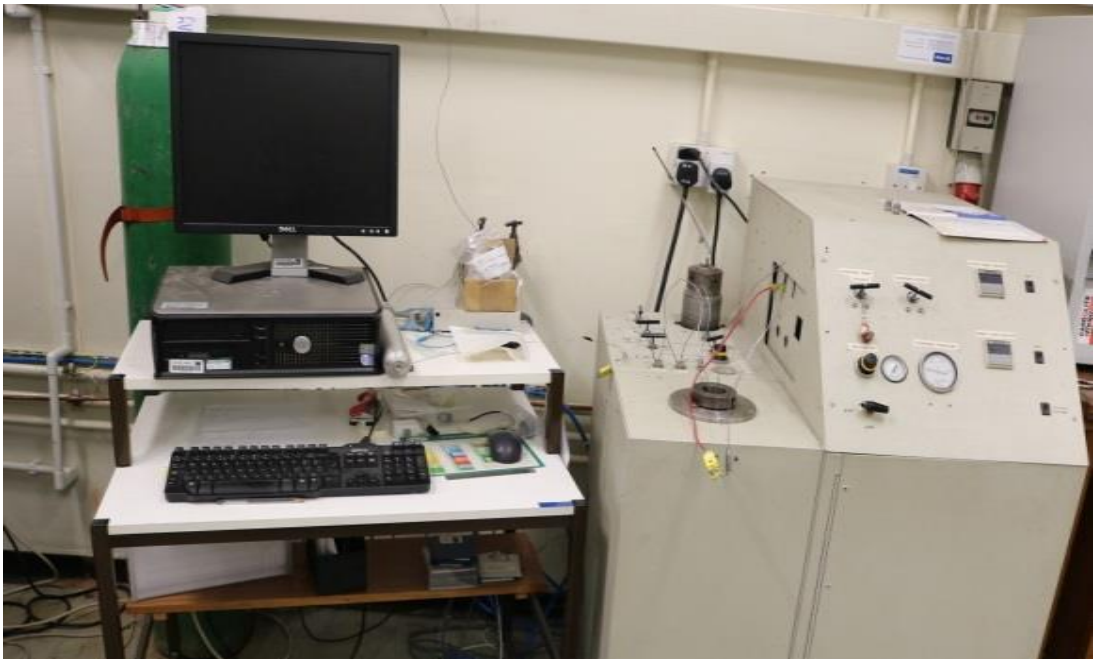

Figure 4.1 The CoreTest rig used for permeability measurements.

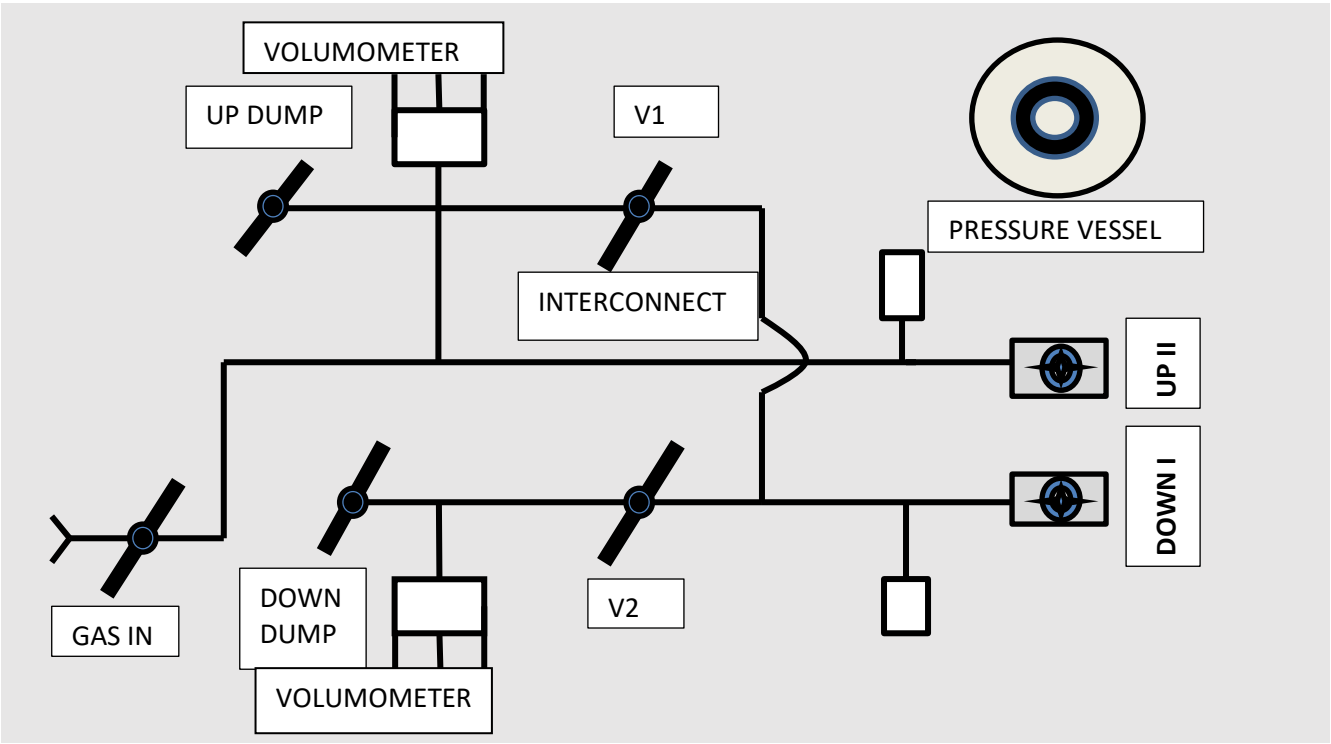

Figure 4.2 CoreTest Permeameter plumbing outline showing the valves and interconnections. The pore pressure connections to the sample ends are labelled DOWN I and UP II.

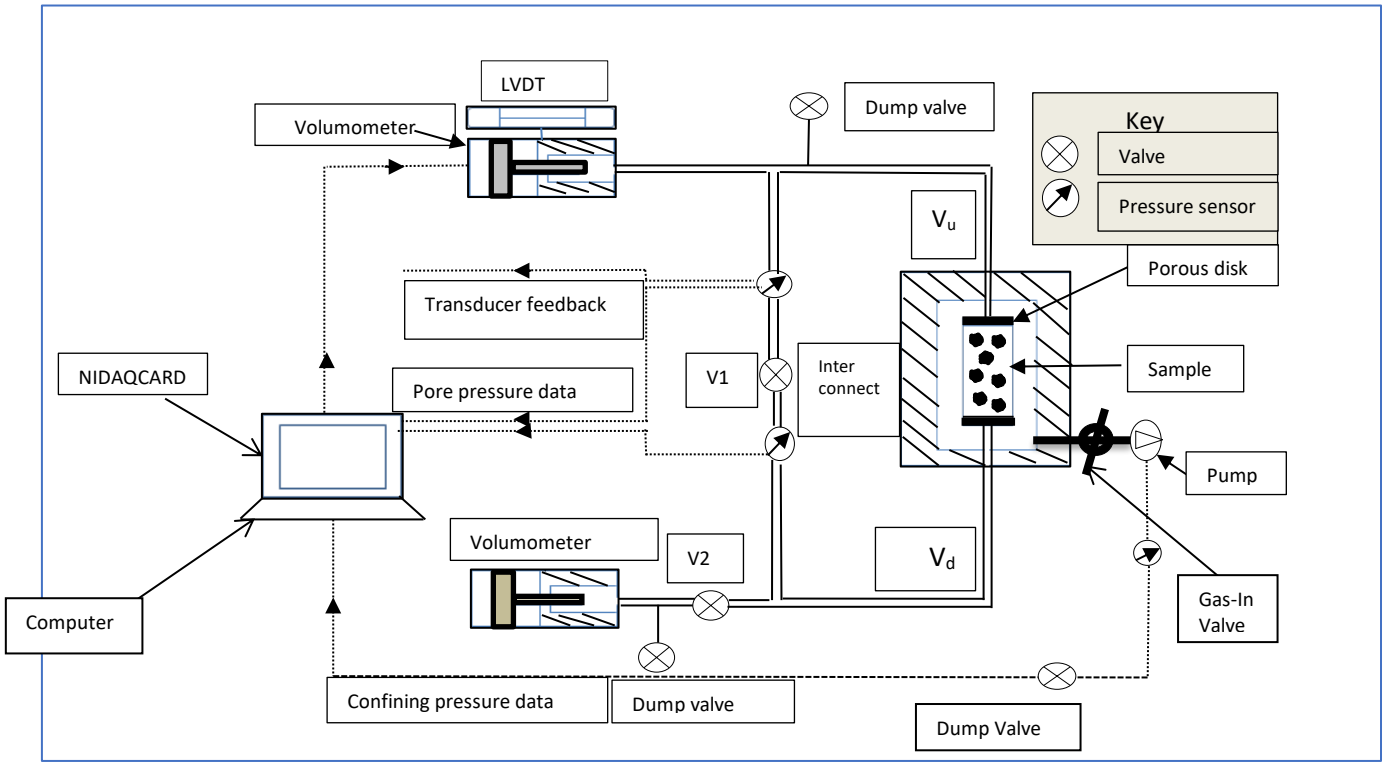

Figure 4.3 A schematic diagram of the CoreTest permeameter data-logging arrangements as used for permeability measurements.

4.3.2 Pressure Transducers Calibration

The confining pressure (CP), upstream and downstream pore pressure transducers (output is in Volts) were calibrated against a Heise Bourdon Tube pressure gauge. The very similar calibrations of each of the three transducers are shown in Fig. 4.3.

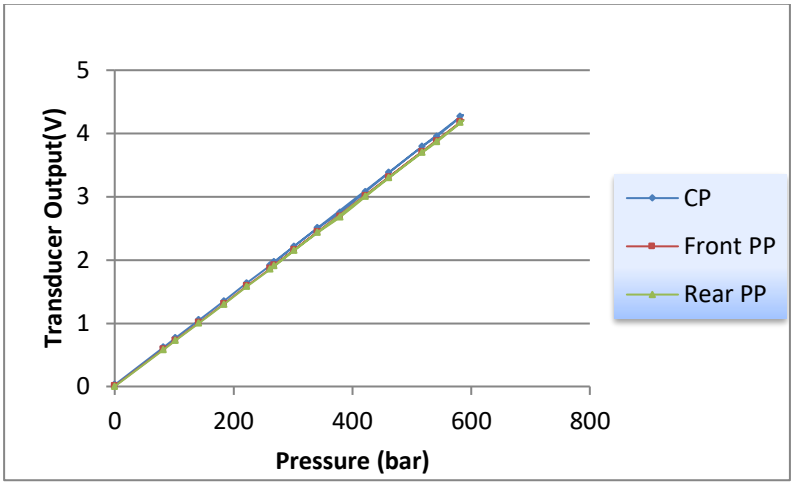

	CP	Front PP	Rear PP
slope	0.0073	0.0072	0.0071
intercept	0.0182	0.0041	0.0104

Figure 4.4 a) Plot displaying the calibrations and illustrating between the transducers' voltage outputs and pressure measured using a Bourdon tube gauge. b) The regression analysis table for the confining pressure (Cp), upstream and downstream pressures.

Pore Volumometer Calibration

The volume swept out by the movement of the piston on one of the pore pressure generators was measured using a Linear Variable Differential Transformer (LVDT). Note that owing to the compressibility of the pore fluid, this is only a measurement of volume change in the sample pore spaces if the pore pressure is kept constant. The voltage output was calibrated against the distance moved, so that the piston displacement times its cross-sectional area measures the volume displaced. A 150mm length digital Calliper with resolution of 0.01 mm was used for the displacement measure, with an accuracy of ±0.01 mm. The plot showing the calliper position versus the voltage output is shown in Fig. 4.5.

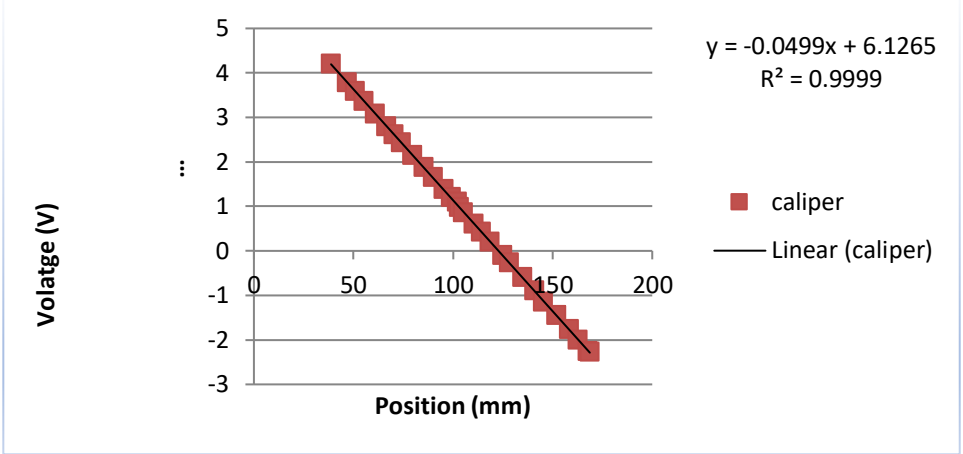

Figure 4.5 Plot illustrating the caliper position and the corresponding voltage output from the LVDT on the pore Volumometer.

Downstream Reservoir Volume

The downstream reservoir volume has to be known in order to measure permeability using transient pressure methods. It was determined with a steel plug in place of a rock sample to prevent communication between the upstream and downstream reservoirs. The measurement was carried out at a pore fluid and confining pressures typical of a permeability experiment. The reservoir volume is expected to be almost independent of pore pressure, owing to the high elastic stiffness of the steel components. The method of measurement is based on Boyle's Law.

Procedure

1. Pull back volumometer piston to allow maximum displacement for travel.
2. Set the desired gas pressure in the pore pressure system and close the interconnect valve (= bypass valve) which connects the upstream and downstream reservoirs.
3. Vent downstream to a lower pressure, keeping the interconnect valve closed.
4. Displace the volumometer piston to raise the pore pressure back to the value before the venting of gas pressure. Allow the adiabatic temperature rise to dissipate and make a final adjustment to the piston (keeping the direction of travel always the same, to avoid backlash) until the pressure is what it was before venting.
5. The displacement volume of the piston required to restore the downstream pressure will be equal to the volume of the downstream reservoir, including the pore volume of the downstream steel filter plate. The total downstream volume of the core test rig was found to be 750 mm^3, with an estimated uncertainty of +/- 3 mm^3.

4.3.3 The BigRig

The BigRig is shown in Fig. 4.6, the sample configuration is essentially the same as in the CoreTest rig. The confining and pore pressure handling capabilities are much greater, however, and for this study the maximum confining pressure used was extended to 100 MPa. There is a single pore pressure intensifier/volumometer, but there is additionally a servo controlled confining pressure control capability. The axial loading facility was not used in the present study.

The pore pressure and confining pressure transducers arrangements were the same as for the CoreTest rig. They were calibrated against a Heise Bourdon tube gauge with an accuracy of better than 100 psi (0.6 MPa). The resolution of the downstream pressure transducer was 0.03 MPa. The pore volumometer was calibrated in the same way as for the CoreTest rig and the volume resolution was 0.3 mm^3. Data logging and control was carried out using an Acorn RiscPC running the RISC-OS 5 operating system and program ROCDEF. The downstream volume was determined in the same way as for the CoreTest rig, to be 450 mm^3, including the pore volume in the sintered disc on the downstream side.

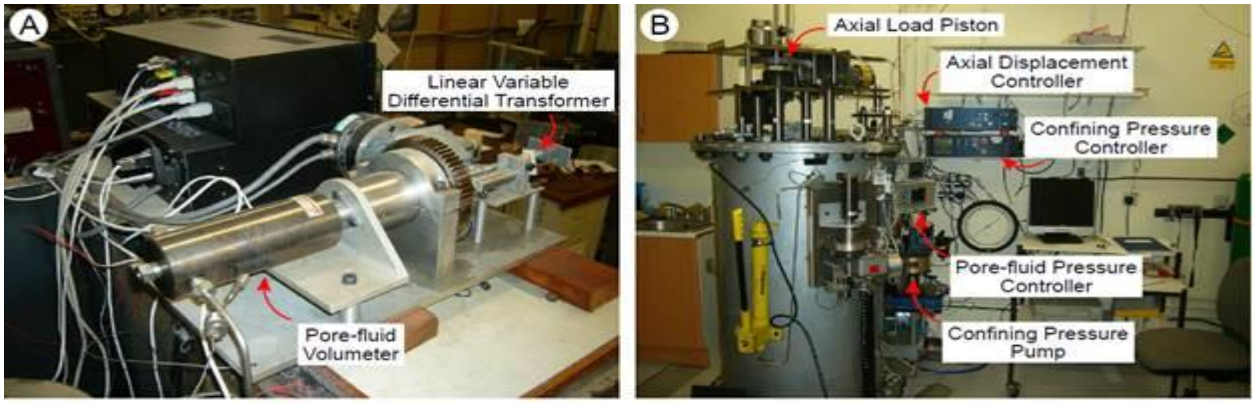

Figure 4.6 Images of the big rig. (a) shows a pore volumometer and its control unit, and in (b), which shows an image of the whole rig, the pore volumometer can be seen mounted in the right front side of the cylindrical safety shield around the pressure vessel.

4.4 Oscillating pore pressure method

The oscillating pore pressure technique as presented by (Bernabé et al., 2006; Fischer, 1992; and Kranz et al., 1990) was the preferred method of measuring permeability for this study because of its noise cancellation and elimination of systematic error sources such as pore pressure leaks, fluctuations in temperature or transient behaviour. A sinusoidally oscillating gas pore pressure with a fixed frequency is applied at the upstream side. As the pore pressure wave passes through the sample the downstream pressure signal is attenuated in amplitude and phase shifted. The downstream pressure

signal can be easily detected because its period is the same as the upstream signal (Figure 4.7).

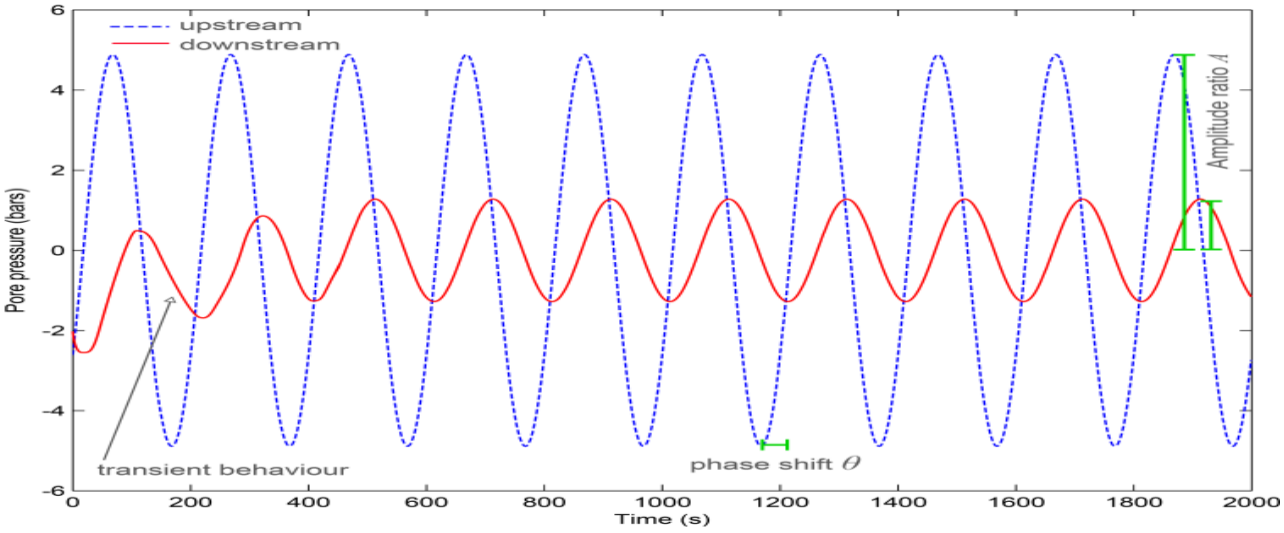

Figure 4.7 Sinusoidally oscillating upstream pressure (blue) and the downstream response recorded (red), with decreased amplitude and phase shifted (Mckernan et al., 2014).

Permeability is determined from the ratio of the upstream to downstream signal amplitudes, and sample storativity is determined primarily by the amount by which the downstream signal is phase-shifted. Processing of several cycles of data (approximately 10 cycles) allows for noise cancellation and elimination of systematic error sources such as pore pressure leaks, fluctuations in temperature or transient behaviour arising from initially non-uniform pressure distribution in the sample, leading to the system settling for the first few cycles (Bernabé et al., 2006; McKernan et al., 2017).

The transmission of a pore pressure oscillation through a rock sample is analogous to the behaviour of an electrical low-pass filter, comprising a series resistance followed by a shunt capacitor (David et al., 2018). This single stage filter corresponds to the rock sample being of near zero storativity (or at any rate much less than that of the downstream reservoir). The resistance is analogous to the permeability of the sample, and the capacitor is analogous to the storage capacity of the downstream reservoir (David et al., 2018). The complexity introduced by a rock storativity that is not negligibly small (i.e., a relatively more porous rock) corresponds to the behaviour of a multi-stage, or cascaded filter network. The theoretical basis of the two systems is identical.

Practicable analyses of the problem were developed by Kranz et al. (1990) and (Fischer, 1992), permitting extraction of the permeability and specimen storativity. Bernabé et al. (2006) re-analysed the oscillating pore pressure method in such a way

as to separate the parameters that define permeability and storativity. Their solution to the transport equation is expressed as.

$$A = exp(-i\theta)\left(\frac{1+i}{\sqrt{\xi\eta}}sinh\left[(1+i)\sqrt{\frac{\xi}{\eta}}\right] + cosh\left[(1+i)\sqrt{\frac{\xi}{\eta}}\right]\right)^{-1} \qquad \text{Eqn 4.1}$$

The real and imaginary parts of the function A exp (-$i\theta$) are respectively the amplitude ratio of downstream to upstream wave amplitudes A (gain) and the phase shift θ. The latter two terms are the values that are experimentally measured. The two dimensionless parameters ξ and η are given by:

$$\xi = \frac{SL\beta}{\beta_D}, \quad \eta = \frac{STk}{\pi L\mu\beta_D} \qquad \text{Eqn 4.2}$$

in which ξ is dimensionless storativity, and η is dimensionless permeability. S is specimen cross-sectional area (m^2), L is specimen length (m), β is specimen storativity (Pa^{-1}), β_D is downstream storage (m^3 Pa^{-1}), T is oscillation period (s), k is permeability (m^2), and μ is fluid viscosity (Pa.s). Equation 3.2 may be solved iteratively by searching for values of ξ and η that satisfy the measured values of A and θ (Figure 4.7) The region of valid solutions is delimited by the lines $\xi = 0$ & $\xi = \infty$, any value outside this region is not physically realistic. When ξ is close to zero, obtaining a value for ξ is not certain, but dimensionless permeability η can be obtained accurately. There is a relationship between A and η where $\xi \approx 0$ because around that region lines of constant η are almost horizontal. This means that dimensionless permeability η can be calculated directly from Equation 4.3 (Bernabé et al., 2006).

$$\eta = \frac{2A}{\sqrt{1-A^2}} \qquad \text{Eqn 4.3}$$

When $\xi \neq 0$, i.e., when the pore volume is commensurate with the downstream volume, permeability determination requires also the parallel determination of ξ from the solution to eq. 4.2. Because ξ is constant and related to the rock porosity, It is expected (and observed, e.g. McKernan et al., 2017; Rutter et al., 2022) that data from a suite of tests covering a wide range of gain and period will lie along a curve of constant ξ. Because of the convergence of the constant ξ and constant η contours at high gains, the resolution of the two parameters becomes poorer. It is best to target oscillation periods that will result in gains smaller than about 0.5, for maximum resolution of permeability.

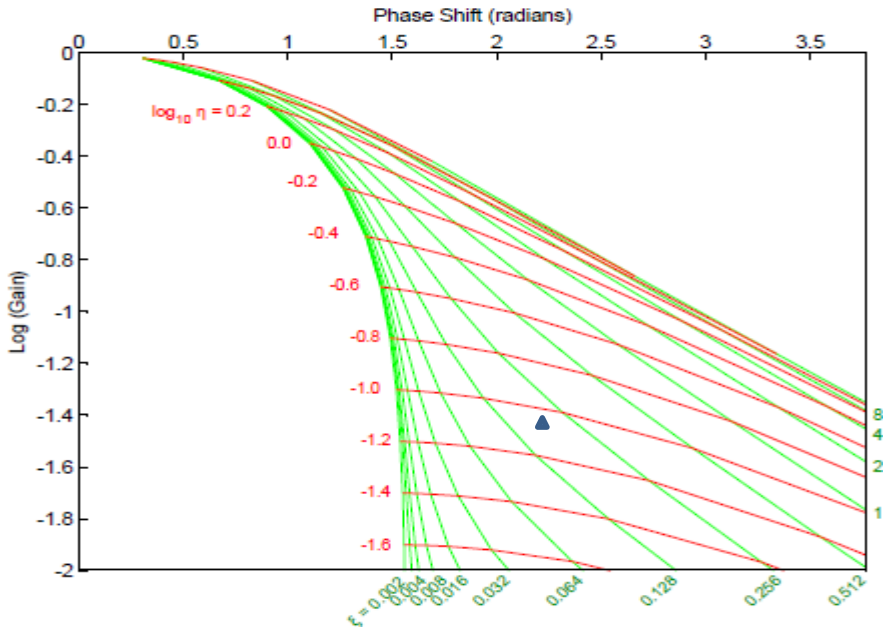

Procedure

(a) Measure wave amplitude ratio (Gain) and phase shift by curve fitting.

(b) Solve solution to transport eq. iteratively for dimensionless ratios ξ and η.

(c) Solve for permeability k and sample storativity β.

Figure 4.8 Solution space showing the region in which physically meaningful values of A and θ can be found, delimited by the iso- ξ lines $\xi = 0$ & $\xi = \infty$. Storativity (ξ) is directly proportional to porosity. The gain and phase shift coordinates of the typical point shown also correspond to coordinates defined by the intersection of lines of constant ξ and η.

4.5 Pulse transient (decay) method

The pulse decay method is used to measure flow properties of rock with very low permeability and was developed by Brace et al. (1968). To measure some of the impermeable samples of the Haynesville Shale, a cylindrical sample of porosity (φ), length (L) and cross-sectional area (S) is connected at each end to fluid reservoirs of

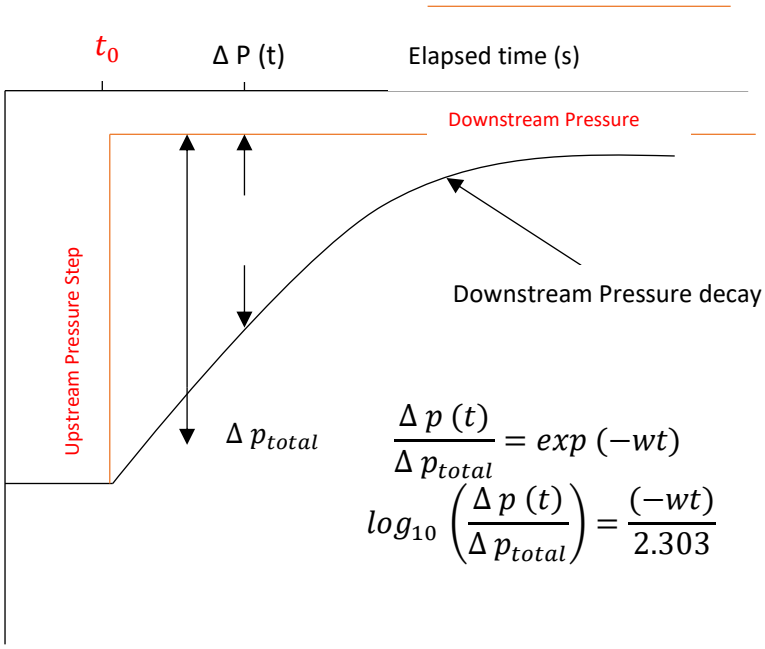

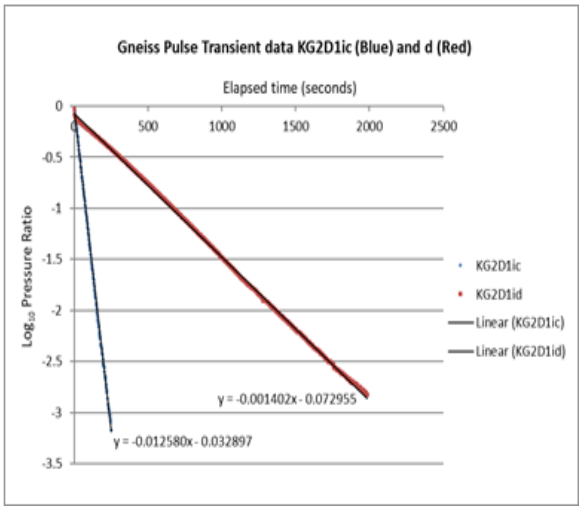

Figure 4.9 a) Schematic plot of data displayed in a pulse transient experiment, here upstream pressure is red, while downstream pressure is black. b) Plot of log of the time-decaying pressure ratio, in this case for samples of gneiss of two different permeabilities; the permeability is measured from the gradient of the fitted line (ω) (data of Rutter, pers.Comm.2020)

volumes V_u (upstream) and V_d (downstream). To begin with, pressures in the upstream (P_u) and downstream (P_d) reservoirs are equal. The two reservoirs are isolated from one another by closing the interconnect valve so that the only route for fluid to flow between them is through the sample. A sharp pore pressure increase (ΔP_{total}) is imposed at the upstream end. The pressure pulse propagates through the sample and the differential pressure ($\Delta P(t)$) between upstream and downstream reservoirs gradually diminishes to zero at a rate dependent on permeability (k).

Brace et al. (1968) demonstrated, by analogy with a resistor-capacitor low-pass filter circuit, that in response to a suddenly applied pore pressure transient between the upstream and downstream reservoirs, the differential pressure (ΔP) will decay exponentially with time (t) according to:

$$\Delta P\,(t) = \Delta P_{total} \exp(-\omega t) \qquad Eqn\ 4.4$$

Where t is time, ΔP_{total} is the initial pressure step amplitude and ω is a dimensionless term related to permeability (k) by:

$$\omega = \left(\frac{kS}{\mu C f L}\right)\left(\frac{1}{Vu} + \frac{1}{Vd}\right) \qquad \text{Eqn } 4.5$$

where S is sample cross-sectional area and length L, μ is fluid viscosity and C_f is fluid compressibility. V_u & V_d are respectively the upstream and downstream volumes. k can therefore be determined by plotting $\log(\Delta P(t)/\Delta P_{total})$ [dimensionless] against time t to obtain the gradient ($-\omega$) as shown in fig. 4.9b. In the present work, the transient pulse decay method of Brace et al. (1968) has been applied only to the most impermeable samples of Haynesville shale.

Although the initially different upstream and downstream pressures can be allowed to decay towards a common value, dependent on the relative values of the upstream and downstream reservoir volumes, it is a useful practical modification of the procedure whereby the pore pressure control system is used to maintain a constant upstream pressure. This corresponds to an apparent infinite upstream volume V_u, so that $1/V_u$ in eqn. 4.5 becomes zero (Zoback & Byerlee, 1975) (Fig. 4.9 a). The benefits of the constant upstream pressure are that leaks in the upstream system become unimportant, and it is easier to recognize the end of the pressure decay because the two pore pressures approach a constant value that is known in advance. This approach also makes it possible to determine permeability when there is a capillary pressure in

the sample arising from partial saturation. Partial liquid saturation due to capillary pressure can make the oscillating pore pressure method impossible to employ.

Although it seems straightforward to apply, it must be noted that this method relies on the assumption that specimen porosity (φ) is small enough to neglect the influence of specimen storage on the calculation of permeability. While this assumption is expected to be valid for crystalline rocks with porosity <1%, sedimentary rock pore volumes can be comparable in magnitude to downstream reservoir volumes and can no longer be ignored. (Dicker & Smits, 1988) studied the influence of relative pore volume and reservoir volume on the pressure decay curve. It is implicit in the application of equation 4.5 that specimen pore volume is much less than the downstream reservoir volume. However, by defining parameters *a* and *b* as follows.

$$a = \frac{Vp}{Vu} \quad , \quad b = \frac{Vp}{Vd} \qquad \text{Eqn 4.6}$$

Where V_p is pore volume, Cui et al. (2009) derived a factor (f_1) which can be used to calculate permeability when V_p is not negligibly small, thus:

$$k = \frac{\omega \mu C_f L}{f_1 S(1/V_d)} \qquad \text{Eqn 4.7}$$

Where $f_1 = \frac{\theta_1{}^2}{a+b}$ and θ_1 is the first solution to the transcendental equation,

$$tan\theta = \frac{(a+b)\theta}{\theta^2 - ab} \qquad \text{Eqn 4.8}$$

From the pressure decay curves measured during the present work, permeability was calculated using both the methods of (Brace et al., 1968) and Cui et al., (2009). The results previously obtained in this laboratory are compared in below.

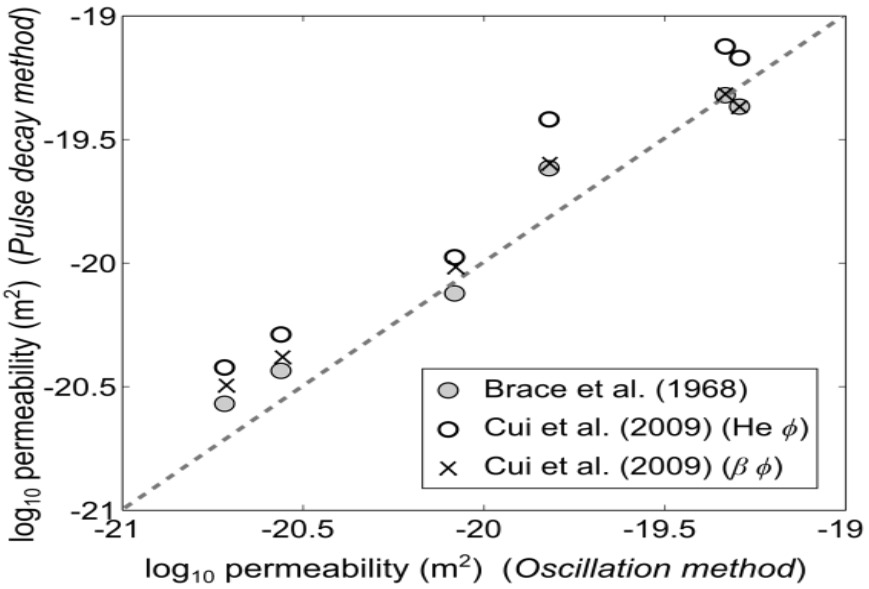

Figure 4.10 Comparison of permeabilities measured using the oscillating pore pressure method (Bernabé et al., 2006) *and the transient pulse decay method* (Brace et al., 1968) *Transient pulse decay measurements were processed using both equation 6* (Cui et al., 2009) *(grey circles) and equation 7* (Cui et al., 2009) *which takes porosity into account. Data for Whitby shale, after McKernan et al., (2017).*

4.6 Permeability measurement under steady state conditions; The constant pressure difference technique.

A minor variation was introduced to the CoreTest permeameter procedure used in this study to measure the permeability of the samples. This involved the use of a constant argon gas pore pressure difference of 1, 1.5, -1 and -1.5 MPa maintained between the upstream and downstream pore pressures. While also keeping the V2 valve opened (Fig. 4.2) and the bypass (interconnect) valve closed, while closing the downstream dump valve.

Permeability measurements using the constant pressure difference using liquids and gases are carried out in a similar way. The major difference concerns dealing with the mean compressibility of the flowing fluid.

The original Darcy equation (Eq. 2.1) assumes the pore fluid (a liquid) to be incompressible. When an incompressible fluid flows through a core sample of uniform cross section, the flux Q/A along the flow path remains constant because the volume occupied by a given mass of fluid does not change. However, when gases are used along the flow path the pressure drop results in gas expansion, which increases the volumetric flux. Therefore, gas flux is not constant along the flow path and requires modification of the Darcy equation for the permeability calculation (Dandekar, 2013). The product of inlet and outlet flow rate *(Q_1 and Q_2),* pressures (P_1 and P_2) are equated by using Boyle's law.

$$Q_1 P_2 = Q_2 P_2 (Temperature\ constant) \qquad \text{Eqn 4.9}$$

These can also be represented by average gas flow rate and average pressure.

$$Q_1P_2 = Q_2\,P_2 = Q_{avg}P_{avg} \qquad \text{Eqn 4.10}$$

To account for gas expansion Darcy equation can then be expressed in terms of the average gas flow rate.

$$Q_{avg} = \frac{kA(P_1 - P_2)}{\mu L} \qquad \text{Eqn 4.11}$$

Flow rate of gas normally measured at the outlet of the core plug; Q2 Therefore, equation is rearranged as.

$$\frac{Q_2P_2}{((P_1 + P_2)/2)} = \left(\frac{kA(P_1 - P_2)}{\mu L}\right) \qquad \text{Eqn 4.12}$$

or

$$Q_2 = \frac{kA({P_1}^2 - {P_2}^2)}{2\mu LP_2} \qquad \text{Eqn 4.13}$$

Permeability therefore is –

$$k = \frac{2Q_2\mu LP_2}{A({P_1}^2 - {P_2}^2)} \qquad \text{Eqn 4.14}$$

1. Q_2 = is the gas flow rate measured at the outlet of the sample in m^3/s
2. k is the permeability in m^2
3. A is the cross-sectional area m^2
4. P_1 and P_2 are the inlet and out pressure in N/m^2 (Pascals)
5. μ is the average gas viscosity (Ns/m^2) (Pa s) along the flow path.
6. L is the length of the sample m.

Equation 4.14 was used for the permeability calculation for constant flow rate tests on specimens of YB 02, YB 03, YB 04, YB 05, and YB 08. (Oscillatory pore pressure method was used for sample YB 03).

4.7 Experimental procedures

As outlined above, the three main techniques used for the permeability measurements were the oscillating pore pressure method, pulse transient decay method and constant pressure difference technique. In all cases pore pressures (P_p) and confining pressure (p_c) were raised in increments to realize the desired effective pressure (P_{eff}) during the initial pressurisation, whilst ensuring that the desired effective pressure was not exceeded in case it caused permanent permeability decrease. The permeability measurements were made under total confining pressure ranging from 20 MPa - 110 MPa, at pore pressures ranging between 10 MPa – 80 MPa.

4.7.1 Oscillatory Pore Pressure measurements

Confining pressure is raised to a desired pressure; pore pressure is introduced via the gas in valve (Fig. 4.2). During each experiment, time was always allowed for pore pressure to stabilise along the sample length. This could require several minutes for low permeability samples (10^{-18} m^2). Thereafter the interconnect valve was closed to apply sinusoidal pore pressure wave to the upstream, while the downstream settles slowly at steady wave amplitude and phase shift. (Fig. 4.7) The oscillation cycle periods applied could range from 100 to 12000 seconds and amplitudes from 0.4-1.5 MPa depending on the sample dimensions and permeability to be measured. The oscillation amplitude was always made 10% or less than the mean pore pressure. Each experiment was run for an average of 6-10 cycles to ensure that the downstream signal had settled to a uniform waveform. (Bernabé et al., 2006)

Data Processing

The data were processed using a MATLAB® program following these steps.

1. Sample dimensions i.e., length, diameter and downstream volume were entered and then the desired raw datafile was selected. The elapsed time, upstream pore pressure, and downstream pore pressure was extracted from the file, and pore pressures were plotted against elapsed time.

2. The timeframe in seconds within which the signals were to be processed was selected manually. Any poor data arising from bad data transmission was eliminated by a data-cleaning algorithm. The wave period was entered manually.
3. The Fast Fourier Transform (FFT) program in MATLAB® was used to determine the both the amplitude ratio and phase offset between in upstream and downstream waveforms. It converts the data stream from the time to the frequency domain and the discrete Fourier transform of the chosen signal was found. The extracted upstream and downstream pore pressure amplitude ratio and phase shift were calculated as

   Amplitude ratio $A = \frac{Upstream\ Amplitude}{Downstream\ Amplitude}$ &

   Phase shift $\theta = Downstream\ phase - Upstream\ phase$

Calculating Permeability and Storativity

1. Equation 4.1 was solved iteratively using the Fsolve algorithm in MATLAB® to find dimensionless parameters ξ & η.
2. The Fsolve uses a minimisation routine to find solutions to an equation that cannot be rearranged by separating variables. By starting with initial guesses, then iterating through an array of values for ξ & η we obtain values for amplidude and phase shift that are minimally different from the measured values. From the optimal values obtained for ξ & η the values of permeability *k* and specimen storativity β were calculated using equation 4.2.

4.7.2 Pulse Transient (Decay) measurements

The CoreTest rig was used for these experiments. After initial application of desired confining and pore pressures, with the pore pressure bypass valve open the pore pressure system was set at the desired constant upstream pressure. The bypass valve was then closed to isolate the reservoirs (Figure 4.2). Knowing that these pressures are initially the same, if there is any apparent difference in the pore pressures implied by the measured transducer voltage outputs between the two reservoirs, a correction was applied during the processing of the data. A small amount pore pressure (between 5-10%) increase is applied to the P_U reservoir so as to make negligible change to the fluid properties viscosity and compressibility. The controller maintains the upstream pressure, and the data is recorded until the downstream pore pressure rises to become equal to the upstream pressure (Figure 4.9).

Data Processing

1. Sample dimensions (length and diameter), porosity (∅) and downstream volume (V_d) were entered manually and then the desired raw data file was selected. The time, upstream pore pressure and downstream pore pressure were extracted from the file and pore pressure signals were plotted against time.
2. If there was any difference between the upstream and downstream pore pressures at the start of the experiment, a correction was applied to correct this difference in the complete data set.
3. The downstream decay curve was displayed in the time window which is manually selected during the processing.
4. The pore pressure difference as a function of time difference $\Delta P(t)$ was determined by subtracting the instantaneous downstream pore pressure (P_d) from the upstream pore pressures (P_u). Log $(\frac{P(t)}{\Delta P_{total}})$ was then plotted against time (t) and fitted to a straight line of slope (ω) (Fig. 4.9). ΔP_{total} is the difference between upstream and downstream pore pressures at t = 0.
5. To calculate f_1 in equation 4.7 (Cui et al., 2009) to account for the pore volume of the sample, parameters *a, b* and *θ* must be determined. To find *a* & *b*, the upstream, downstream volumes and porosity were used while equation 4.8 is used to find *θ*. Recall that *a* = 0 for a test in which the upstream pore pressure is held constant.
6. Finally, is f_1 used with the gradient of the fitted line ω to determine the permeability k together with equation 4.7.

4.7.3 Constant Pressure Difference test (steady-state flow)

The CoreTest rig is set at constant pressure difference mode. A pore pressure of about 10 MPa is introduced to the sample with the bypass valve closed while V1 valve which connects the two volumometer is left open and while the downstream dump valve is closed (Fig. 4.2). A set point of 1-1.5% is applied to initiate a pressure difference between the downstream and upstream pore pressure. The confining pressure is set at about 20 MPa at the start of the experiment with the controller keeping the pressure difference constant while data is recorded during the experiment. The confining pressure is increased incrementally to obtain various effective pressures while keeping the pore pressure constant.

Data Processing

1. Sample dimensions (length (l), diameter (d), and downstream volume (V_d) were entered manually and then the desired raw data file was selected. The elapsed time (s), upstream pore pressure (P_u), downstream pore pressure (P_d) and volume flowed as a function of time V(t) were extracted from the file. Flowed volume was plotted versus elapsed time to verify that it was linear.
2. The Darcy equation of flow $Q_2 = \frac{kA(P_1^2 - P_2^2)}{2\mu L P_2}$ was used to calculate the permeability k. which is presented as $k = \frac{2Q_2\mu L P_2}{A(P_1^2 - P_2^2)}$
3. The exported data is displayed on a spreadsheet,
   - where the flow Q_2 = is the gas flow rate measured at the outlet of the sample in m^3/s.
   - A is the cross-sectional area of the sample in m^2
   - P_1 and P_2 are the inlet and out pressure in Pa.
   - L is the length of the sample in m.
   - μ is the gas viscosity of argon at the mean value of the pore pressure. The National Institute of Standards and Technology (NIST) chemistry webbook was used to obtain the viscosity for pressure in MPa.

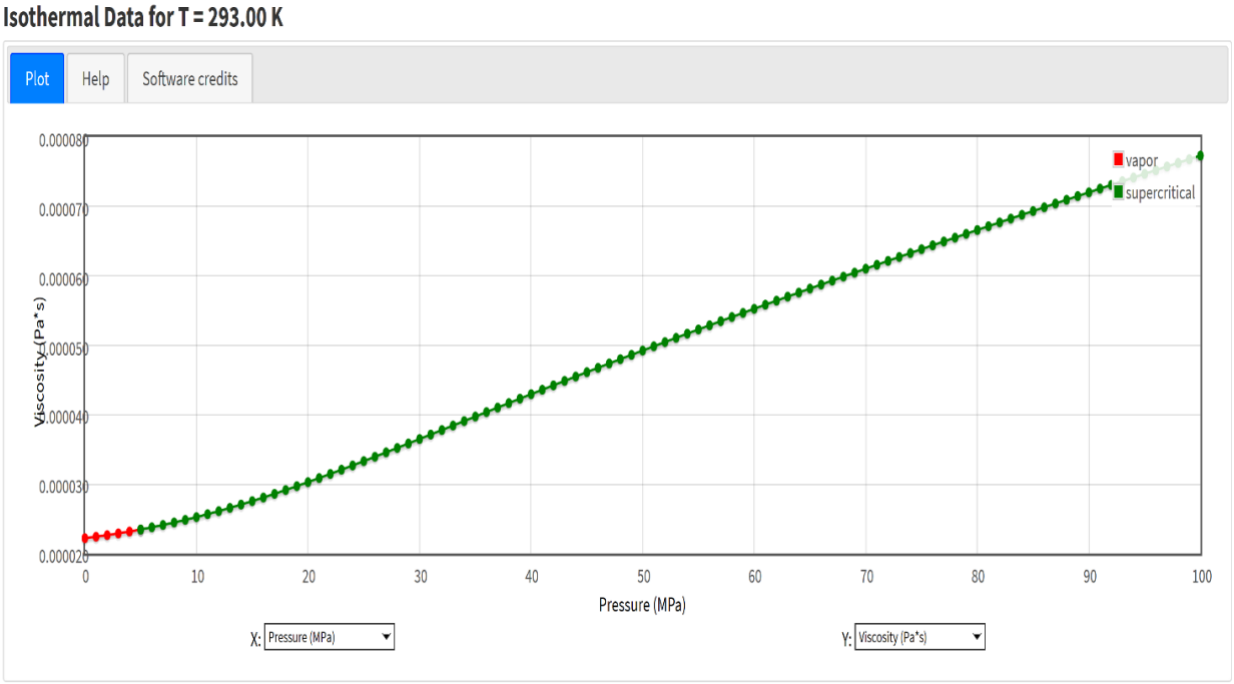

Figure 4.11 Graph showing the National Institute of Standards and Technology (NIST) chemistry webbook page used for the correction of viscosity for pressure.

4. Finally, the permeability (k) was calculated for each test and plotted against effective pressure to show the relationship between the effective pressure and permeability in m^2.

Valve	V1	V2
Constant pressure diff	Close	Open
Oscillatory	Close	Close
Pulse transient	Close	Close

Table 4.2 The constant pressure difference, oscillatory pore pressure, and pulse transient techniques valves settings required during experiment on the core test rig when used for the permeability measurements.

4.8 Testing Darcy's law for the flow of argon gas through shale

Darcy's law, as defined by the equation $J = \frac{-k}{\mu}\frac{\Delta p}{\Delta x}$ implies that the steady-state flow rate of the pore fluid will be linearly proportional to the pressure gradient across the sample. A simple experimental test of the validity was made of Darcy's law for the conditions of the present experiments.

The law states that fluid flow within a porous medium is proportional to the pressure drop across the length of the sample in the oscillatory pore pressure method, the maximum pressure gradient in the sample is proportional to the amplitude of the upstream wave. Thus, Darcy's law can be tested using the oscillatory pore pressure method of permeability measurement. Permeability was measured using a range of driving waveform amplitudes whilst keeping all other parameters constant. A constant value of permeability obtained over a range of wave pressure amplitudes implies that Darcy's law is followed.

The sample YB 03 from Haynesville shale was used for the test on the Big Rig. Four pore pressure wave amplitudes were used 0.17, 0.33, 0.66 and 1.0 MPa during the permeability measurements. The mean pore pressure was maintained at 10 MPa, with a constant total confining pressure of 18.7 MPa. The period was 200 sec, log rate at 1.5 s. These parameters were maintained throughout the experiments with different amplitudes. Figure 4.12 shows permeability plotted against driving pressure waveform amplitude. Permeability remained constant within experimental uncertainty, implying that under these experimental conditions' permeability is independent of pressure gradient, therefore Darcy's law is satisfied.

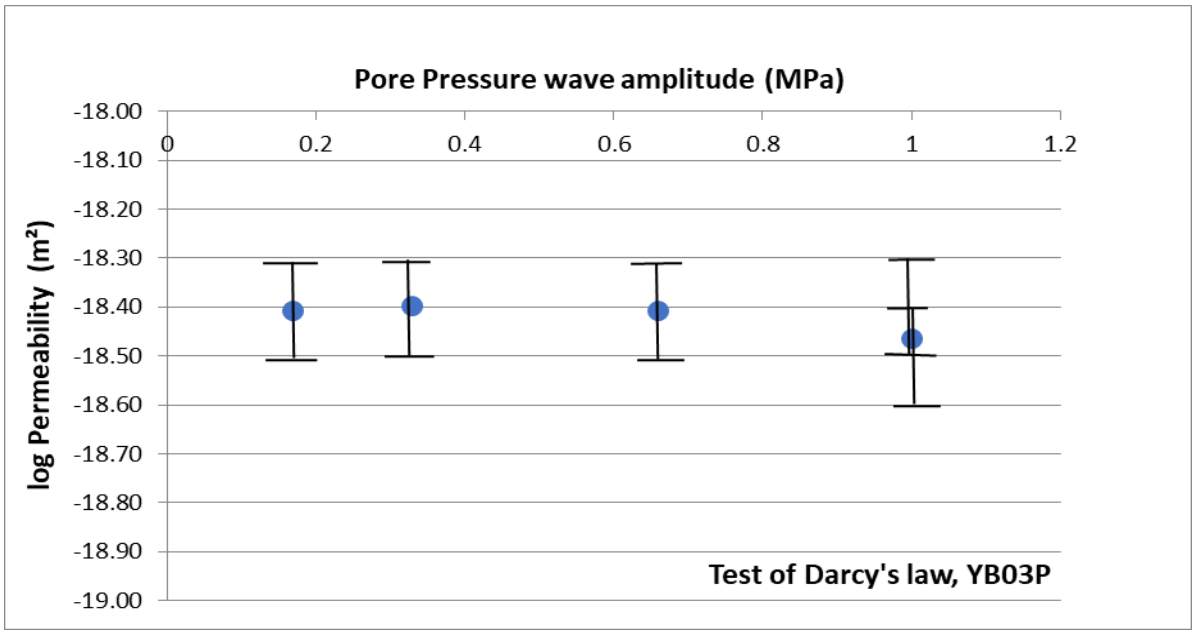

Figure 4.12. Oscillatory pore pressure technique of permeability measurement with a constant period of 200 sec, constant confining pressure of 18.2 MPa, in order to test the validity of Darcy's law. The results plotted as log permeability against a six-fold change in pore pressure wave amplitude show that the permeability remains unchanged within experimental error (estimated to be ± 0.1 log units), hence Darcy's law is followed within experimental error.

Factors limiting the quality of the data.

During permeability experiments, there are factors which may compromise the quality of data. These factors are addressed and tabulated in table 4.3.

Source of Error	Preventative action	Results affected
Temperature fluctuations	The lab temperature is controlled, and all exposed pipes are insulated by foam.	Pore pressure
Oblique cylindrical Core plug	Drill bit will be well maintained, core slowly and use the take care squaring the ends.	Sample dimensions
Residual water in pore space after drying.	Oven dry to constant weight at 60°C.	Permeability and porosity
Rehydration	Samples were stored in desiccators with dehydration agent added.	Permeability and porosity
Pore pressure leaks	Check for leaks before any experiment, minimise number of valves except where necessary.	Pore pressure
Sample jacket leaks	A heat shrink sleeve is used to jacket specimen. The heat was evenly distributed around the jacket.	Permeability
Downstream P-cycles	Sufficient number of cycles until data judged satisfactory.	Downstream volume

Table 4. 3 Sources of errors and preventative measures taken to minimise them.

4.9 Acoustic Velocity measurements.

Measurements of the compressional (P) wave velocities from Haynesville shale samples over a wide range of confining and pore pressures were made as part of this study. Some constraints on the bulk elastic properties of specimens can be obtained from such measurements. During these measurements pore volumometry was used to obtain the pore bulk compressibility of the samples as a function of effective confining pressure.

The longitudinal and shear wave velocities are dependent on both the density and elastic moduli, which in turn are dependent on the petrological characteristics of rock samples. The latter include mineral composition, pore structure, texture, and orientation-dependent anisotropy. In homogeneous and isotropic elastic media wave velocities for P and S waves are related to the shear modulus (G), Poisson's ratio (v) and density (ρ) as follows (Mavko, 2009).

$$V_p = \sqrt{\frac{K + \frac{4}{3}G}{\rho}} \qquad \text{Eqn 4.15}$$

$$V_s = \sqrt{\frac{G}{\rho}} \qquad \text{Eqn 4.16}$$

For isotropic solids, there are only two independent elastic moduli, whereas four are usefully defined, bulk modulus, Young's modulus, shear modulus and Poisson's ratio. Thus, if any two are known the other two can be calculated. (Fig 4.13)

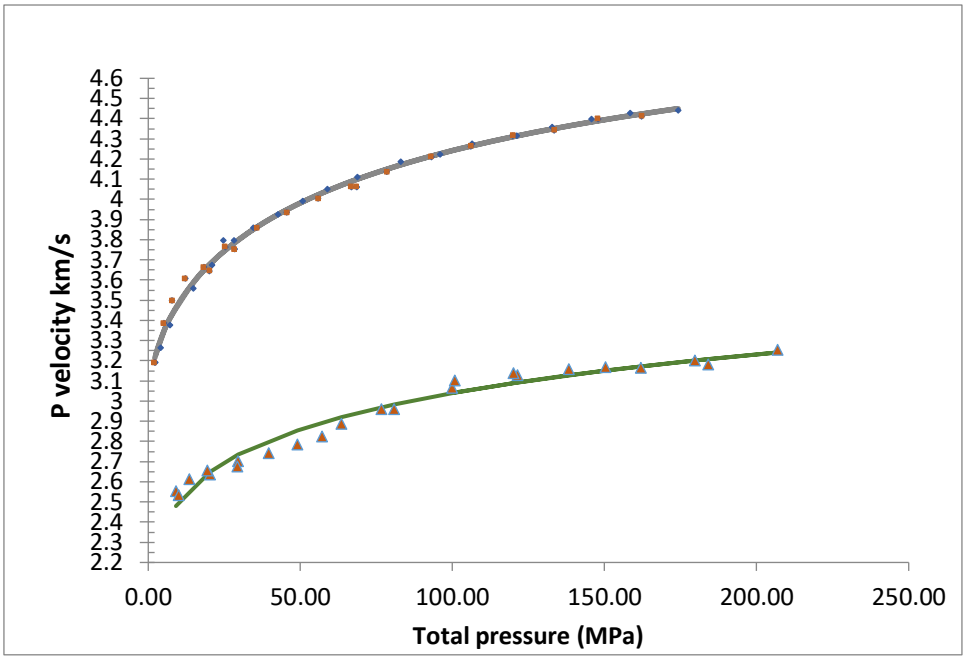

Figure 4.13 Example of the influence of confining pressure on P and S wave velocities, zero pore pressure, dry, for Darley Dale sandstone (Rutter, pers. Comm. 2020). S velocities are lower than P velocities and typically the curves diverge to higher confining pressures.

When pressure is raised during compressional velocity measurements of jacketed samples, velocity increases. This is attributable to the stiffening of the rock matrix due to pore and crack closure with increasing pressure (Birch, 1960). The effect of stiffening with pressure is much greater than the small concomitant increase in density with pressure, which would otherwise tend to decrease velocity. The pore shape has significant effect on the velocity sensitivity to stress during low pressure measurements. Crack-like pores (low aspect ratio) close easily with applied hydrostatic pressure relative to more equant primary pore spaces (high aspect ratio), which are less non-compliant under applied pressure (Walsh, 1965).

Velocity versus pressure curves rise most rapidly at low pressures (Birch 1960; Brace et al., 1968; Jaeger et al., 2007), and the rate of increase progressively decreases, tending towards linear at high pressures (fig. 4.13). This observation can be attributed to the progressive initial closure of thin microcracks (low aspect ratio), which markedly increase elastic moduli whilst having little effect on density, until cracks become largely closed. Beyond this point the slower, linear rate of velocity increase is due to the progressive stiffening of mineral structures with increasing pressure. Although unimportant for the present study, temperature causes decrease of acoustic velocities as a result of thermal expansion and elastic stiffness reduction.

Porosity (more equant voids) reduces both density and, more so, elastic stiffness, hence reduces velocity. Pore spaces behave like the addition of an extra mineral phase but of

zero density and stiffness. Many theoretical approaches to the analysis of the influence of porosity on elastic velocities have been made, that are well summarized in in the literature, e.g., (Han et al., 1986; Jaeger et al., 2007; Mavko, 2009; Wyllie et al., 1956)

4.10 Influence of elastic anisotropy

Elastic anisotropy markedly affects elastic wave velocities and is particularly important in shales, on account of their marked bedding-parallel fabric, produced as a result of compaction. In terms of properties arising from elasticity, such as elastic wave velocities, shales are normally expected to be transversely isotropic. That is, they are isotropic in the plane of the layering (P-wave velocities are the same for any direction in the plane of the layering) but are uniquely different (usually slower) in the direction normal to the layering. This causes transversely isotropic materials to require 5 independent elastic constraints to describe them fully, unlike isotropic materials that require only two (Mavko, 2009; Sayers, 2013) .

It is beyond the scope of the present project to consider the full anisotropic elastic properties of shales, because only P wave velocities have been measured, although for wave propagation directions both normal and parallel to the layering. However, through the use of pore volumometry it has been possible to measure the bulk moduli of compressibility of these rocks. Application of hydrostatic pressure results in volumetric compaction and distortion of the shape of pore spaces, and it is this which leads to the effect of pressure on permeability, hence it is relevant to the interpretation of the results of permeability measurements reported herein.

Bulk modulus is an isotropic property, because it measures the volume change arising from the application of hydrostatic pressure to the rock. This does not mean that the elastic strains normal and parallel to layering will be the same in response to hydrostatic loading; they will not be. Thus, the distortion of pore shapes will not be isotropic. On the other hand, Nur & Byerlee (1971); Seeburger & Nur (1984); Sprunt & Nur (1980); and Walsh (1965) show that in an isotropic matrix, pores of different shapes undergo the same volumetric strains in response to hydrostatic loading, and Andrews (1978) showed that this is true even when inequant pores show a preferred orientation.

4.11 Bulk Moduli

Porous rocks display three bulk moduli, according to the definitions and nomenclature scheme proposed by Zimmerman (1991) and employed by Mavko et al. (2003). Isothermal compressibility is the inverse of bulk modulus and defined in the following way (Zimmerman 1991).

The compressibility C_{pc} of the pore space is defined as the fractional change in pore volume v_p in response to a change in confining pressure P_c at constant pore pressure p_p . It is the reciprocal of the dry pore space bulk modulus $K_\emptyset$:

$$C_{pc} = \frac{1}{K_\emptyset} = \frac{1}{v_p}\left(\frac{\partial v_p}{\partial P_c}\right)_{Pp} \qquad \text{Eqn 4.17}$$

V_p is related to the total sample volume V_b (which includes the pore space) by $V_p = \emptyset\ v_b$. K_{dry} is the bulk modulus of the porous aggregate. Its reciprocal, compressibility C_{pc}, the bulk volume change in response to a change in confining pressure at constant pore pressure and is defined by.

$$C_{bc} = \frac{1}{K_{dry}} = \frac{1}{V_b}\left(\frac{\partial V_b}{\partial P_c}\right)_{Pp} \qquad \text{Eqn 4.18}$$

The zero-porosity bulk modulus of the constituent mineral aggregate is defined as K_o. The dry bulk modulus k_{dry} (= k_{bc}) is given (Mavko et al., 2009) by

$$\frac{1}{K_{dry}} = \frac{1}{K_o} + \frac{\phi}{K_\phi} \qquad Eqn\ 4.19$$

A change in pore pressure at constant confining pressure also produces a bulk volume strain, because the pore spaces are inflated by the pore pressure. This is characterized by the compressibility C_{bp}, which for direct measurements requires strain gauges to be glued to the outside surface of the rock sample. It is defined as

$$C_{bp} = \frac{1}{K_{bp}} = \frac{1}{V_b}\left(\frac{\partial V_b}{\partial P_p}\right)_{Pc} \qquad Eqn\ 4.20$$

Hasanov et al. 2019; 2020) described experiments in which volumetric strains were measured both in this way and by pore fluid volumometry. But Mavko et al. 2009 show that k_{bp} can also be obtained from

$$\frac{1}{K_{bp}} = \frac{1}{K_{bc}} - \frac{1}{K_o} \qquad Eqn\ 4.21$$

thus, determination of all four bulk moduli can be obtained from knowing only the pore compressibility C_{pc} measured by pore fluid expulsion volumometry and K_o . K_o can be calculated from an averaging scheme, such as the Voigt-Reuss-Hill (V-R-H) average elastic moduli, which requires published V-R-H moduli for individual minerals (Healy et al., 2020) and their relative volume proportions obtained from quantitative XRD. This is the approach adopted in the present study (Table 4.3).

4.12 Pore pressure and effective pressure

As well as making permeability and velocity measurements over a range of confining pressures, the influence of large variations in pore pressure on both physical properties was also measured. The only constraint is that pore pressure must always be less than the confining pressure, so that the heat shrink rubber jacket is not inflated away from the specimen. Additionally, for permeability measurements a minimum pore pressure must be applied, so that argon gas can be made to flow through the specimen. For most of the tests carried out the pore pressure was 10.0 MPa, with further tests with pore pressures ranging up to 90 MPa, but always with the confining pressure greater than the pore pressure. To investigate specifically the effect of pore pressure magnitude on permeability, some tests were carried out to pore pressures as low as 2 MPa.

When using the pore volumometer to control pore pressure, the magnitude of pore pressure impacts the pore pressure controller behaviour, because the compressibility of gas decreases with increasing gas pressure. It also influences the data processing of permeability data.

The compressibility of an ideal gas is given simply by

$$c_f = \frac{1}{P_f} \qquad Eqn\ 4.22$$

Argon is close to ideal at room temperature for pressures up to about 20 MPa (Gosman et al., 1969). But deviates strongly by application of pressures as high as 90 MPa. More generally, gas compressibility is given by

$$C_f = \frac{1}{C_f} + \left(\frac{1}{Z}\right)\left[\frac{d_z}{d_{pf}}\right]_T \qquad Eqn\ 4.23$$

Where C_f is the compressibility factor while z is the gas deviation factor (describing departures from ideal behaviour). Thus, departures from ideality cannot be ignored for processing permeability data.

Figure 4.14 shows the variation of the gas deviation factor Z (from Gosman et al., 1969) as a function of pressure described by a polynomial, and the derived ratio of real/ideal compressibility with a polynomial approximation up to 1000 bars (100 MPa). This function can be used in processing permeability data over a range of pore pressures.

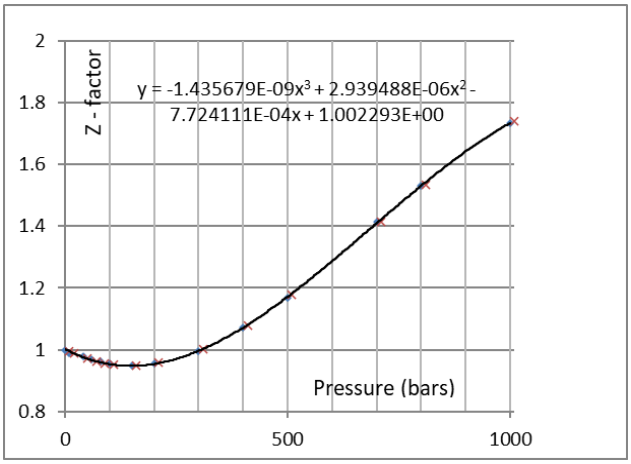

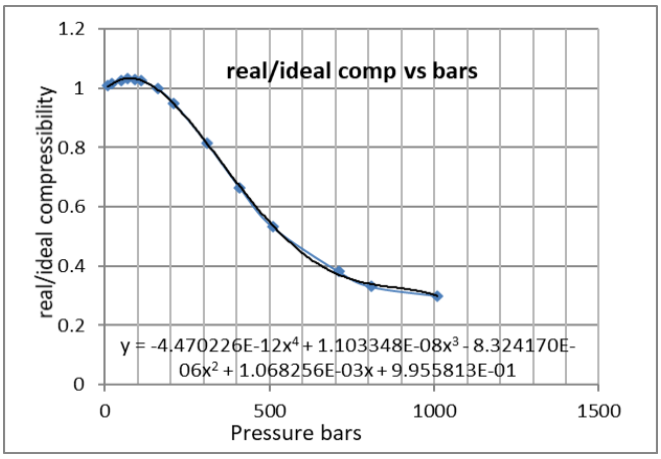

Figure 4.14 (a) shows the variation of the gas deviation factor z for argon gas as a function of pressure in bars (data of Gosman et al., 1969), with a polynomial fit. (b) shows the derived curve of real gas/ideal gas compressibility ratio for argon gas with a polynomial fit y=-4.470226E-12x^4 + 1.103348E-08x^3 - 8.324170E-06x^2 + 1.068256E-03x + 9.955813E-01 (where y is the compressibility ratio and x is pressure in bars) valid up to 1000 bars (100 MPa). Ideal gas compressibility is taken as $\frac{1}{p_{gas}}$

Pore pressure reduces the effective confining pressure by an amount mp_p , where *m* is called the pore pressure coefficient and p_p is the pore pressure. According to Terzaghi (1923) pore pressure reduces the effective confining pressure by the amount of the pore pressure, so that *m* = 1. Thus, we can define the *Terzaghi* effective pressure as (P_c – P_p), where P_c is the total confining pressure.

The value of *m* has engendered much discussion. (Biot & Willis (1957); Geertsma (1957); Nur & Byerlee (1971); and Skempton (1960) investigated the influence of pore pressure on rather specifically the elastic distortion of a porous rock and obtained

$$m = 1 - \frac{K_{dry}}{K_o} \qquad Eqn\ 4.24$$

so that effective pressure $P_{eff} = (P_c - mP_p)$. *m* is here called the Biot-Willis coefficient.

As well as elastic constants, pore pressure is known to influence several rock petrophysical properties, including rock strength, permeability, acoustic wave velocities and electrical conductivity. These properties depend, in various ways on the elasticity of the rock, but their respective effective pressure coefficients are not necessarily the same, as emphasized by Nur & Byerlee (1971) and Seeburger & Nur (1984). In this study, as a result of performing tests over a range of pore fluid pressures, we obtain values for m from permeability measurements and acoustic velocity measurements, but only the value calculated from the pore volumometry measurements is expected to correspond to the Biot-Willis coefficient.

4.13 Experimental Methods

Measurement of ultrasonic acoustic velocities were made on heat-shrink rubber-jacketed cylindrical samples via the determination of the time-of-flight of an acoustic pulse, in the manner developed by Birch (1960). A piezoelectric transducer (lead-zirconium-titanate, PZT) was mounted in the steel supporting pistons at each end of the cylindrical sample. One transducer acts as a driver and the other as a receiver. The receiving transducer generates an electrical pulse across its faces when the acoustic signal arrives, and both the driving and received signals are displayed on a 300 MHz digital oscilloscope. The total time taken for the sound waves to travel across the sample to the receiver can be used to calculate the wave velocity. The driving voltage was 70 V with the capacity to be increased to 150V.

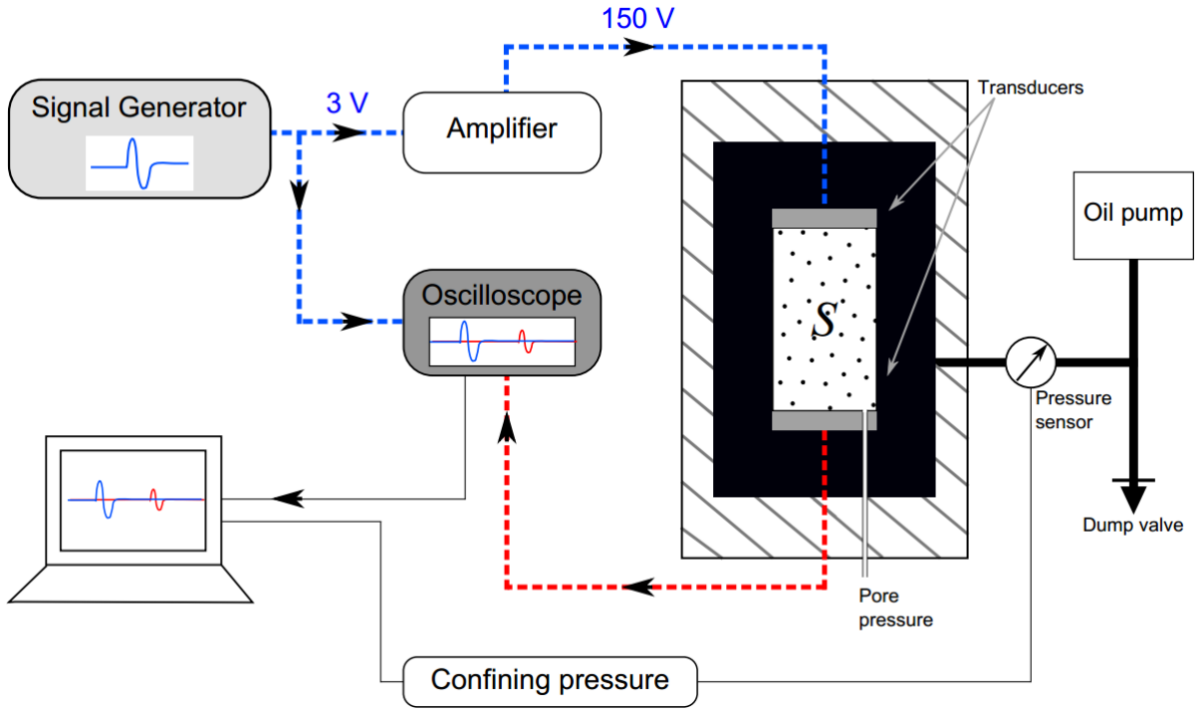

Figure 4.15 A schematic diagrams showing the ultrasonic velocity experimental setup.

The apparatus configuration is shown schematically in Figure 4.15. The total time of flight includes the time for passage of the pulse through the specimen but also the time to pass through the steel pistons between the transducers and the ends of the samples (the 'dead time'). The dead time varies with confining pressure and must be determined experimentally by measuring time of flight versus pressure without a rock specimen in position. The dead time is shown in Figure. 4.16, and must be subtracted from the total time measured at each confining pressure when a sample is present. The dead time measured at zero confining pressure was 11.214 μs. The value reduces slightly with pressure as the apparatus stiffens with loading. The variation was represented satisfactorily by the power law.

$$td(\mu s) = 11.214\, P^{-8E-4} \qquad Eqn\ 4.25$$

where pressure *P* is in MPa.

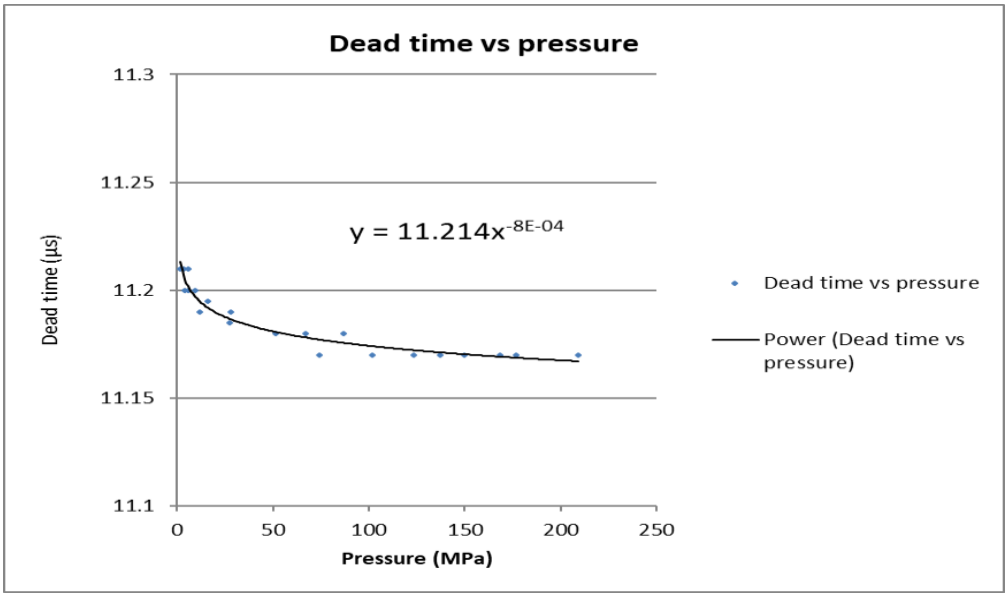

Figure 4.16 Dead time vs pressure in microseconds. The dead time was measured without the sample in the assembly, confining pressure was increased and time of flight of the waves was measured.

Two Haynesville shale samples YB01 (Normal to bedding) and YB03 (cores both parallel and normal to bedding) were measured. The YB03 samples were physically the same samples that were used for permeability measurements on the BigRig. This was to eliminate the influence of specimen variability between these tests. This can be significant, given that the mineralogy and microstructure of shales can vary over centimetric distances along the same core. Ideally a core for velocity measurements should be relatively long (e.g., 7 cm), to increase the time of flight and hence accuracy, whilst the ideal core length for permeability measurements is only about 3 cm, to increase hydraulic transmissivity. On the other hand, for velocity measurements with pore pressure the ideal core length is short (3 cm), to facilitate equilibration of pore pressure inside the sample in response to confining pressure changes.

These conflicting requirements are exacerbated further, because using short samples relative to diameter results in significant deviations from hydrostatic pressure within the sample, as a result of the frictional forces that arise from the elastic mismatch between the ends of the specimen and the steel end pistons.

Despite being forced to use short samples for velocity measurements, a short, 1.5 mm diameter hole was drilled into the ends of the specimen to facilitate pore fluid movements and equilibration, even when the pore fluid was gas. Although the low

permeability of shales even to gas means that care must be taken to allow sufficient time for the effects of induced pore pressures as a result of increments or decrements in confining pressure to dissipate, such induced pore pressure transients are expected to be negligibly small for gas pore pressures, although that may not be true when liquids are used.

Acoustic velocity measurements were carried out over a range of confining pressures from <2 MPa to 206 MPa with fixed argon gas pore pressures of 10.3, 34.5, 46.1 and 67.7 MPa. The low permeability of the shale samples, leading to difficulties with uniform saturation of pore spaces, precluded the use of pore pressure tests using liquid pore fluids.

Apparatus used for Acoustic Velocity Measurements

The apparatus used for the acoustic velocity measurements is known as the Green Rig (Figs. 4.17 and 4.18). This is similar to the BigRig but is only used for hydrostatic pressure work. As with the BigRig, synthetic oil (Reolube-DOS) is used as confining medium with argon gas as the pore fluid. The apparatus is equipped with two pore pressure volumometer/controllers, for use with either gas or liquid pore fluids. The acoustic measurements were made using a TENMA 72-8710A oscilloscope, a pulse amplifier (constructed in-house), a programmable digital signal generator (Thurlby-Thandar TG-1304), a stabilized high voltage supply (for the pulse amplifier) and a dedicated sample assembly (Figure. 4.18).

Pore pressure system and pore volumometry

Samples could be tested over the full range of confining pressures whilst a constant pore pressure of argon gas was applied to one end of the specimen via a capillary pressure pipe. A small diameter (1 mm) hole through the upper piston gave access of the pore fluid pipe to the end of the specimen. To enhance gas flow coupling and reduce the chance of blockage of the hole in the piston, the hole was extended into the specimen for about 10 mm by drilling a 1.5 mm diameter hole into the end of the specimen.

The pore pressure is generated and controlled by a servo-controlled DC motor-driven pressure generator (identical to that used on the BigRig) rated at 400 MPa. There are two; one of these is dedicated to gas and the other is for use with water. The displacement of the piston on the pressure generator is measured by an axially-mounted LVDT. The volume measurement resolution is 0.3 mm^3. The volume swept out

by the pressure generator whilst the pore pressure is kept constant equals pore volume change in the sample, such as can be produced by confining pressure change or inelastic pore collapse.

As the confining pressure is changed whilst holding the pore pressure constant with the servo-control system, the pore volume changes by a small amount, forcing gas to flow either into or out of the specimen. The movement of the pressure generator piston required to hold the pressure constant measures the pore volume change. When the pore deformation is recoverable and elastic, a complete confining pressure cycle produces no net change in volume. However, the elastic volume change is not necessarily linear, because the pore compressibility tends to decrease with increasing confining pressure.

During progressive increase in confining pressure, as pore spaces shrink elastically, fluid is expelled at constant pore pressure maintained by the withdrawal of the pore volumometer piston. The displacement rate times the volumometer piston area measures the pore volume reduction rate. The reverse happens during confining pressure reduction, leading to expansion of the pore spaces and recharge with pore fluid. It is important that during an up or down pressure cycle the piston always moves one direction, to avoid 'noise' through inevitable backlash through the servo-motor gearing or changing in the compression direction of the 'O' ring seals. Volumetric strains were measured at different pore fluid pressures. Owing to the relatively small specimen size used (on account of the small size of the slabbed cores available together with the hazard of losing a specimen through fracturing during machining), only a few volumetric measurements could be made, and the effect of the low resolution of the data was exacerbated by the small size of the samples.

Phase shift and storativity during measurements using the oscillating pore pressure method.

In the application of the oscillating pore pressure method, data analysis yields the dimensionless permeability parameter η and the dimensionless storativity parameter ξ

$$\xi = \frac{SL\beta}{\beta_D}, \quad \eta = \frac{STk}{\pi L \mu \beta_D} \qquad Eqn. 4.26$$

The pore volume in the sample is related to the downstream storage volume V_d and ξ, which is a dimensionless ratio (the pressure terms in the storativities cancel out). Thus ξ= 1 when the volume of the sample pore spaces = the downstream volume, = 435 mm^3 as measured in the case of the BigRig. It is to be expected that experimental data

for a single sample on a plot of log A vs phase shift ϕ will lie along a line of constant ξ , from which the effective pore volume fraction that contributes to permeation can be calculated. It might be expected that if the pore spaces are well-connected, such as in a porous sandstone for example, the conductive pore volume would correspond to the total pore volume.

As the sample pore volume becomes very small, the ratio sample pore volume/downstream volume approaches zero, hence ξ approaches 0. Log *A* vs ϕ therefore lie along the bounding tangent curve $\xi = 0$. This corresponds to the electrical analogue of a first order RC low-pass filter and can be used to calculate how the phase shift varies with gain. This is represented by the equation (David et al., 2018).

$$A = \frac{1}{\sqrt{1+ tan^2\phi}} \qquad \text{Eqn. 4.27}$$

where ϕ is asymptotic to 90° as amplitude A tends towards zero.

Figure 4.17 The Green Rig apparatus used for the acoustic wave velocity measurements. The green panels are the steel plates that provide safety screening for the user. The left-hand side has the electrical system used for control functions and for monitoring the data. The vessel uses oil as a confining medium while argon gas is used as pore fluid. The pore pressure volumometer for argon is mounted behind the apparatus and is identical to the pore volumometer dedicated for use with water that can be seen to the left of the Heise pressure gauge.

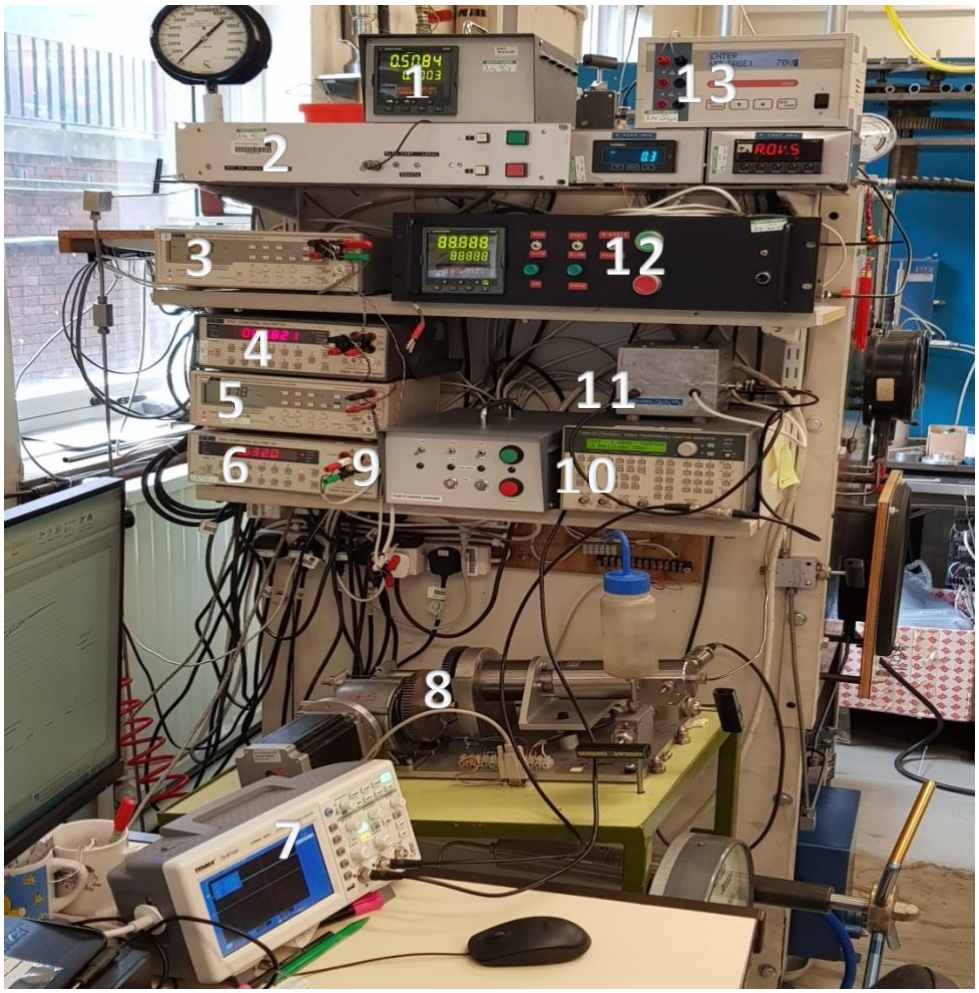

1. Gas pore pressure meter/controller
2. Gas Volumometer servo-control driver
3. Pore volume displacement meter
4. Multimeter#1 reading confining pressure
5. Multimeter#2 reading confining pressure
6. Multimeter reading downstream pore pressure
7. Oscilloscope
8. Pore Water Volumometer
9. Water system stepper motor controller
10. Thurlby Thandar TG 1304 Pulse generator
11. Pulse Amplifier (-35v and 70v)
12. Pore water servo-control driver

Figure 4.18 Electrical control and signal handling system used for monitoring and data recording during experiments on the Green Rig. The digital multimeters read confining pressure, pore pressure and pore volumometer displacement. Other items drive the acoustic signals and provide measurement and control for the pore pressure servo-controllers.

Experimental procedure

As with the permeability measurements, 25 mm diameter samples were jacketed in heat-shrink rubber tubing that was sealed to the pistons via 'O' rings and a pair of cable ties at each end to clamp the rubber tubing against the 'O' rings. When 20 mm diameter samples were used (smaller diameter than the steel pistons, a length of silicone-rubber tubing, cut to the same length as the specimen, was placed over the specimen to make up the difference in diameter. The finished assembly is shown in Fig. 4.19, prior to insertion into the pressure vessel. The connection to the pore pressure system was made, and the electrical connections to the sending and receiving acoustic transducers. The desired confining pressure was applied, and velocities were measured with confining pressures increments from <2 MPa to 206 MPa during loading and again during offloading with zero pore pressure. The loading and offloading were repeated

three (3) times to determine whether there were permanent changes during the first cycle, perhaps induced by compaction.

Figure 4.19 A sample assembly for acoustic velocity experiments, with the 25 mm diameter specimen inside the (black) heat-shrink rubber tubing, between the two transducer housings. At the right hand end is the closure plug that seals the top end of the pressure vessel.

Running experiments involving pore pressure, and pore volumometry.

After the first pressure cycles at zero pore pressure, a sequence of up-down confining pressure cycles was carried out at each of a sequence of pore pressures. At each pore pressure, the initial confining pressure must be at least 2 MPa greater than the pore pressure, otherwise the excess pore pressure will inflate the jacket and probably burst the end seals around the specimen. This will lead to contamination of the pore pressure system with oil, and likely lead to loss of the specimen itself as a result of oil contamination.

When experiments are carried out with pore pressure, the servo-control system is employed to keep the pore pressure constant, thus the piston in the pore pressure controller is moved by the control system to maintain constant pore pressure. Hence by logging the displacement of the piston (read by an LVDT) a record of pore volume change in the specimen at constant pore pressure can be made. It is important to try to ensure that the controller piston is always displaced in the same sense, to avoid the inevitable backlash in the gears and in the piston's moving pressure seal that would cause a 'dead band' to appear in the displacement record.

Data Acquisition and Processing

The first break of the travel time of the transmitted *P* waves from the oscilloscope was manually recorded on a spreadsheet after each small step (about 7 MPa) of loading and offloading. Picking of the first break was straightforward and consistent throughout each experiment. Each confining pressure reading was taken directly from the Heise pressure gauge (Fig, 4.17) in psi and also read off on the digital multimeter in millivolts. The output from the electrical pressure transducer had been calibrated against the Heise

gauge. The time of arrival of the transmitted P-waves was also recorded from the oscilloscope and the dead time subtracted from the arrival time in μs. The sample length (distance) is divided by time of flight to obtain velocity (km/s). Finally, the velocity was plotted against pressure in MPa prior to further analysis.

Effect of confining pressure on elastic length of sample

Changing the confining pressure causes elastic compaction, which in turn reduces the length of the sample with progressive pressurization, and this impacts upon the measured velocity. The minimum value for the bulk modulus of shale is on the order of 5 GPa, therefore a hydrostatic pressure on the order of 100 MPa will induce a volume strain of 2×10^{-2}, hence a longitudinal strain on the order of 7×10^{-3}. This would cause a maximum error in the estimation of velocity of ~ 1%, and more typically a much smaller amount, which was considered negligible compared to the uncertainty in picking the time of flight.

4.14 Reservoir Modelling

Whilst it is of intrinsic interest to explore experimentally the petrophysical properties of shales for their own sake, the value of the data is enhanced if it is applied to understanding the behaviour of a shale gas reservoir, and in particular the way that changes in pore pressure as a result of gas pressure drawdown influences rate of flow and ultimately gas yield. Results of modelling of linear gas reservoir flow will be described as part of the discussion of results in in chapter 7. The textbook on Gas Reservoir Engineering by Lee and Wattenbarger (1996) provided computer code for gas reservoir modelling. A full description of the methods used is provided in the book, together with a listing of the original version of the code. The late Robert Wattenbarger kindly made available the latest version of his code (Gassim6) to this laboratory, including the modifications for incorporating the pressure sensitivity of permeability. Industry field units (psi pressure, distances in feet) are used because these are the units used in modelling.

The power law or an exponential law describes the reservoir behaviour. The equation below was used.

$$k = ko \exp -\gamma(P_C - nP_P) \qquad Eq.4.26$$

The description is empirical and is valid within the range of the experimental data. It shows the effect of ignoring the influence effect of pressure sensitivity of permeability when one estimates the economics of production in the early stages of field development.

The transport equation 4.27 (Rutter et al., 2013) is evaluated by Gassim 6 at mean drainage area pressure. Solutions are gas pressure as a function of time.

$$\nabla^2 m'(p) = \frac{\emptyset \mu c_t}{k_i} \frac{\partial m'(p)}{\partial t} \qquad Eq. 4.27$$

in which *m'*(p) is a 'pseudofunction' of gas pressure (Al-Hussainy et al., 1966), *k* is permeability (a function of effective pressure), μ is gas viscosity, and c_t is the summed compressibility of the fluid and the porous matrix of the rock. *t* is time. The GASSIM program obtains the finite difference numerical solutions to Eq. 4.27 for appropriate initial boundary conditions and simulates formation-parallel linear flow. (Al-Hussainy et al., 1966)

Chapter 5: Experimental Results 1-Permeability and Bulk Modulus Measurement

This chapter describes the results of the experiments performed to investigate the influence of confining pressure and pore pressure on the permeability of Haynesville shale, and the influence of flow path relative to the planar anisotropy. Most tests were carried out at pore pressures too high for the effects of slip flow to be seen, and above the level of saturation of adsorbed gases in the pore spaces, so that only viscous flow of gas was of importance. However, tests were conducted at low pore pressures to allow the permeability-enhancing effects of slip flow to be seen. Perhaps inevitably, the range of specimen petrographies that could be investigated in the available time frame was limited, and this impacts on the extent to which the question of the influence of carbonate content on permeability could be investigated.

Uncertainty values are given in the main text.

Table 5.1a Summary of test identifiers

Tests on BigRig			* Identifies tests forming part of slip flow test sequence	

Downstream volume (all tests) 445 mm^3

Results of permeability measurements using the oscillating pore pressure method.

YB03P		(Parallel to layering)			len.(mm)	18.94	dia. (mm)	24.69		
Test #	Pc (MPa)	Pp (MPa)	Period (s)	Gain	Phase shift	eta	Xi	log (k m^2)	P eff MPa	**Comment**
					(degrees)				Terzaghi	
kb	34.48	9.7	80	0.57	52	1.387	0	-18.47	24.78	first cycle
kc	51.72	9.7	80	0.105	91	0.2118	0.0711	-18.33	42.02	first cycle
kd	68.97	9.7	150	0.032	100	0.0641	0.0381	-19.13	59.27	first cycle
Le	17.24	9.7	200	0.19	84	0.387	0	-18.47	7.54	first cycle
ke	86.21	9.8	250	0.02	120	0.0424	0.0701	-19.53	76.41	first cycle
kf	103.45	9.8	500	0.01	122	0.0211	0.036	-20.13	93.65	first cycle
Ma *	17.24	9.7	200	0.23	75	0.473	0	-18.38	7.54	
Mb	34.48	9.8	500	0.195	79	0.398	0	-18.86	24.68	
Mc	51.72	9.8	500	0.064	94	0.128	0.048	-19.35	41.92	
Md	68.97	9.8	1000	0.058	98	0.117	0.066	-19.69	59.17	
Me	86.21	9.8	1000	0.034	103	0.069	0.052	-19.92	76.41	
Mf	103.45	9.8	1000	0.02	105	0.04	0.033	-20.16	93.65	
Na	103.45	9.8	1000	0.016	115	0.033	0.045	-20.24	93.65	
Nb	86.21	9.8	1000	0.022	112	0.045	0.055	-20.11	76.41	
Nc	68.97	9.7	1000	0.021	115	0.044	0.06	-20.11	59.27	
Nd	51.72	9.7	600	0.02	105	0.04	0.033	-19.93	42.02	
Ne	34.48	9.7	500	0.05	99	0.101	0.06	-19.45	24.78	
Nf *	17.24	9.8	200	0.161	88	0.326	0	-18.55	7.44	

Nf2 *	17.24	9.7	200	0.182	76	0.37	0	-18.49	7.54	
R3b	60.00	9.7	300	0.021	105	0.042	0.035	-19.61	50.30	
R4a	60.00	9.7	600	0.041	109	0.085	0.095	-19.61	50.30	
R5a	17.24	9.7	200	0.2	94	0.456	0.374	-18.40	7.54	
R5b	17.24	9.7	200	0.197	94	0.447	0.361	-18.41	7.54	
R5c	17.24	9.7	200	0.18	92	0.391	0.248	-18.47	7.54	
R5d	17.24	9.7	200	0.2	90	0.447	0.314	-18.41	7.54	
Ye	40.00	10	200	0.029	107	0.059	0.0568	-19.30	30.00	
Yd	30.00	10	200	0.0495	95	0.0984	0.0374	-19.07	20.00	
Pd	28.70	19.6	800	0.455	65	1.02	0	-18.46	9.10	
R3a	60.00	19.6	800	0.057	99	0.115	0.0713	-19.41	40.40	
Yb	40.00	20.0	800	0.09	94	0.183	0.0828	-19.04	20.00	
Yc	30.00	20.0	800	0.15	89	0.303	0	-18.82	10.00	
Za	86.21	20.0	800	0.035	110	0.0726	0.0834	-19.91	66.21	
zb	103.45	20.0	300	0.022	105	0.0445	0.037	-20.13	83.45	
R2a	60.00	29.3	300	0.17	89	0.345	0	-19.08	30.70	
Ya	40.00	30.0	200	0.23	80	0.473	0	-18.78	10.00	
Rb	60.00	37.2	200	0.036	105	0.0731	0.0641	-18.86	22.80	
Xf	50.00	40.0	600	0.053	107	0.1107	0.1156	-18.76	10.00	
Xe	86.21	40.0	600	0.175	93	0.381	0.256	-19.70	46.21	
Xd	103.45	40.0	300	0.35	75	0.747	0	-19.85	63.45	
Ra	60.00	40.6	200	0.322	75	0.68	0	-18.79	19.40	
Xa	60.00	50.0	600	0.072	98	0.157	0.0899	-18.71	10.00	
Xb	86.21	50.0	600	0.055	99	0.111	0.068	-19.40	36.21	
Xc	103.45	50.0	400	0.44	68	0.98	0	-19.73	53.45	
Azd	70.00	60.0	300	0.46	70	1.036	0	-18.82	10.00	
Aze	86.20	60.0	200	0.105	92	0.213	0.083	-19.30	26.20	
Azf	105.00	60.0	400	0.05	93	0.0991	0.0273	-19.72	45.00	
R7 *	16.2	7.4	300	0.203	85	0.45	0	-18.49	8.8	For slip flow
Va	10	2.0	600	0.135	92	0.281	0.136	-18.51	8.00	
Vb	9.50	1.5	600	0.11	93	0.225	0.104	-18.49	8.00	
Pa *	12.21	4.90	200	0.079	88	0.156	0	-18.63	8.60	
Pb *	11.20	2.60	600	0.15	86	0.303	0	-18.58	8.02	

Pc *	15.52	7.50	400	0.305	72	0.641	0	-18.47	9.10	
Pd *	28.70	19.60	300	0.455	65	1.02	0	-18.46	9.00	
fz1 *	39.93	9.63	500	0.027	103	0.055	0.043	-19.80	30.30	
fz2 *	35.81	4.71	500	0.014	107	0.029	0.027	-19.79	31.10	
Gz1 *	33.06	2.26	1333	0.035	115	0.077	0.115	-19.50	30.80	
Gz2 *	31.42	1.12	3000	0.046	133	0.115	0.299	-19.38	30.30	
YB03N					len.(mm)	9.29	dia. (mm)	20.00		
Test #	Pc (MPa)	Pp (MPa)	Period (s)	Gain	Phase shift	eta	Xi	log (k m^2)	**P eff MPa**	
		(Normal to layering)			(degrees)				Terzaghi	
Na	20.17	9.59	80	0.248	96.1	0.6769	0.8214	-18.04	10.59	first cycle
Nb	39.87	9.59	80	0.107	120.6	0.2818	0.6082	-18.42	30.29	first cycle
Nc	60.06	9.58	80	0.022	173.5	0.0766	0.4169	-18.98	50.48	first cycle
Nd	80.19	9.60	200	0.020	167.1	0.0643	0.3130	-19.46	70.59	first cycle
Ne	80.22	9.59	199	0.017	178.0	0.0605	0.3475	-19.48	70.63	first cycle
Nf	99.90	9.60	499	0.027	156.5	0.0785	0.3237	-19.77	90.30	
Ng	80.54	9.60	399	0.023	163.3	0.0717	0.3304	-19.71	70.95	
Nh	60.62	9.60	401	0.044	146.5	0.1243	0.4404	-19.47	51.02	
Nj	40.14	9.59	300	0.061	132.6	0.1590	0.4280	-19.24	30.55	
Nk	20.18	9.58	200	0.133	107.9	0.3240	0.4716	-18.75	10.60	
NL	60.30	9.60	399	0.060	128.7	0.1511	0.3657	-19.39	50.71	
Nm	80.18	9.60	400	0.030	153.1	0.0862	0.3362	-19.63	70.58	
Nn	99.91	9.58	500	0.025	159.4	0.0728	0.3139	-19.80	90.33	
Np	40.13	9.59	300	0.052	137.3	0.1360	0.4009	-19.31	30.54	
Test of Darcy Law using variable pore pressure wave amplitudes (Flow parallel to layering)										
YB03P	Pc (MPa)	Pp (MPa)	Period (s)	Gain	Phase shift	eta	Xi	log (k m^2)	**P eff MPa**	Pp wave
										ampl. (MPa)
R5a	17.2	9.7	200	0.2	94	0.408	0	-18.40	7.3	0.33

R5b	17.2	9.7	200	0.197	94	0.402	0	-18.41	7.3	0.66
R5c	17.2	9.7	200	0.18	92	0.366	0	-18.47	7.3	1
R5d	17.2	9.7	200	0.2	90	0.408	0	-18.41	7.3	0.17
Ma, Nf and Nf2 tests (above) also used for Darcy law verification										
Permeability results using the steady state method (constant pressure difference, flow parallel layering)										
	(for slip flow tests)									
YB03P					Volumetric					
		Pp(up)	Pp(down)		flow rate Qv		Mean	gas		
	Pc (MPa)	(MPa)	(MPa)	Peff (MPa)	mm^3/s		Pp (MPa)	visc.Pas	log(k)	
R6 *	9.7	2	1	9.1	0.4392		1.5	0.0000224	-16.82	
S *	11.7	3.05	1	10.2	0.4858		2	0.00002282	-17.08	
Pulse transient tests(corrected for gas compressibility, viscosity and Cui function) for slip flow tests										
YB03P		Pp(up)			Gas	Compr.	Compr.			
	Pc (MPa)	(MPa)	Peff MPa	slope	visc.Pas	muliplier	1/MPa	log(k)		
yb03Tc *	10.2	2.05	8.15	0.0033	2.364E-05	1.01307	0.00494	-18.19		
yb03Ua *	10.0	2	8	0.00149	0.0000236	1.01266	0.050633	-18.35		
YB03Ub *	11.0	3	8	0.00198	0.0000244	1.02007	0.034002	-18.39		
YB03Uc *	12.0	4	8	0.00292	0.0000252	1.02589	0.025647	-18.33		
YB03Ud *	13.0	5	8	0.00385	0.000026	1.03019	0.020604	-18.29		
YB03Ue *	18.0	10	8	0.00741	0.00003	1.03135	0.010313	-18.24		
Hz *	31.30	1.30	30	6.555E-05	0.0000224	1.01266	0.769231	-19.55		
Jz *	30.90	0.90	30	0.001018	2.205E-05	1.01266	1.111111	-18.16		
Kz *	31.10	1.10	30	0.0001422	2.204E-05	1.01266	0.909091	-19.13		
Tests on CoreTest Rig										

Downstream volume (all tests)750 mm^3										
Sample orientation: all samples cored along bedding (P-orientation)										
Results of permeability measurements using the oscillating pore pressure method.										
Test #	Pc (MPa)	Pp (MPa)	Period (s)	Gain	Phase shift	eta	Xi	log (k m^2)	**P eff MPa**	**Comment**
					(degrees)				Terzaghi	
YB07		len.(mm)	10.72	dia. (mm)	25.64					
a	63.6	9.9999599	100	0.4211369	64.88	0.934436	0.002689	-17.994854	53.6	Const. Pc,
b	63.6	21.499014	100	0.7046208	44.61	2.038244	0	-17.899285	42.1	& vary Pp
c	63.6	29.998142	100	0.847548	31.47	3.153948	0.060533	-17.815782	33.6	"
d	63.6	39.994889	50	0.8343703	32.56	3.076309	0.123104	-17.658885	23.6	"
Permeability results using the steady state method (constant pressure difference, flow parallel layering)										
					Volumetric					
		Pp(up)	Pp(down)		flow rate Qv		Mean	gas		
	Pc (MPa)	(MPa)	(MPa)	Peff (MPa)	mm^3/s		Pp (MPa)	visc.Pas	log(k)	**Comment**
YB04		len.(mm)	18.18	dia. (mm)	24.79					
a1	20.7	7.5	7.462147	13.2	2.47E-10		3.750	0.00	-15.74	const Pp
a2	30.8	7.7	7.160906	22.9	2.47E-10		3.850	0.00	-16.35	1st cycle
a3	40.5	7.5	7.466467	32.6	2.47E-10		3.750	0.000028	-16.71	"
a4	47.7	7.5	7.465071	40.7	2.46E-10		3.750	0.000028	-17.26	"
b1	51.8	7.5	7.462147	43.3	2.46E-10		3.750	0.000028	-17.71	const Pc
b2	59.4	29	28.15455	30.5	3.63E-12		14.500	0.0000452	-17.23	2nd P-cycle
b3	59.5	37	35.97565	21.9	2.17E-12		18.500	0.0000516	-16.86	"
b4	59.5	45	43.43566	14.7	2.59E-14		22.500	0.000058	-16.37	"
c1	20.6	7.5	7.407645	13.6	3.10E-10		3.750	0.000028	-16.43	const Pp
c2	31.2	7.5	7.411097	23.3	3.10E-10		3.750	0.000028	-16.96	3rd P-cycle
c3	40.8	7.5	7.409741	33.7	3.10E-10		3.750	0.000028	-17.44	"

c4	51.4	7.5	7.408315	43.6	3.10E-10		3.750	0.000028	-17.80	"
d1	61.8	7.5	7.408381	38.8	3.10E-10		3.750	0.000028	-17.62	const Pp
d2	35.5	7.5	7.412702	27.8	3.10E-10		3.750	0.000028	-17.19	4th P-cycle
d3	20	7.5	7.408692	12.7	3.10E-10		3.750	0.000028	-16.37	"
								0.000022		
YB05		len.(mm)	18.6	dia. (mm)	24.88					
a1	29.9	5.6	5.833929	15.4	2.67E-10		2.800	0.00002648	-15.93	const Pp
a2	33.1	5.6	5.798073	27.1	2.66E-10		2.800	0.00002648	-16.10	1st cycle
a3	44.3	5.6	5.770205	38.2	2.65E-10		2.800	0.00002648	-16.36	"
a4	56.6	5.6	5.749444	51.2	2.64E-10		2.800	0.00002648	-16.90	"
b1	56.6	5.6	5.729153	51.2	2.63E-10		2.800	0.00002648	-17.07	const Pc
b2	60.9	12	12.90356	37.7	6.47E-10		6.000	0.0000316	-16.91	2nd P-cycle
b3	50.3	22	24.00786	27.9	8.94E-10		11.000	0.0000396	-16.71	"
b4	22.4	34	34.80788	15.7	9.40E-10		17.000	0.0000492	-16.60	"
c1	22.4	7	6.697878	15.7	8.02E-10		3.500	0.0000276	-16.58	const Pp
c2	36.4	7	6.694421	29.7	8.17E-10		3.500	0.0000276	-16.73	3rd P-cycle
c3	46.3	7	6.701591	39.2	8.33E-10		3.500	0.0000276	-16.90	"
c4	58.1	7	6.702358	51.1	8.48E-10		3.500	0.0000276	-17.09	"
YB08		len.(mm)	12.91	dia. (mm)	24.88					
a1	20.2	9.5	9.597122	10.6	6.32E-09		4.750	0.0000296	-15.56	const Pp
a2	31.5	9.5	9.595151	21.1	7.17E-09		4.750	0.0000296	-16.08	1st cycle
a3	43	9.5	9.587298	33.5	8.02E-09		4.750	0.0000296	-16.41	"
a4	55.3	9.5	9.588496	46.7	8.86E-09		4.750	0.0000296	-16.50	"
b1	55.3	19.8	19.97092	35.8	1.90E-09		9.900	0.00003784	-16.73	const Pc
b2	55.3	25	25.84304	29.2	6.95E-09		12.500	0.000042	-16.60	2nd P-cycle
b3	55.3	38	38.07824	17.6	2.47E-09		19.000	0.0000524	-16.47	"
b4	55.3	42.5	43.14282	12.2	1.35E-09		21.250	0.000056	-16.15	"
c1	20.4	9.7	9.547195	10.7	1.94E-08		4.850	0.00002976	-16.24	const Pp
c2	31.7	9.7	9.555372	21.6	1.99E-08		4.850	0.00002976	-16.50	3rd P-cycle
c3	44.2	9.4	9.562224	34.7	2.04E-08		4.700	0.00002952	-16.73	"
c4	61.1	9.4	9.568301	52.3	2.08E-08		4.700	0.00002952	-16.83	"
d1	61.1	24.2	24.56574	37.4	-1.36E-08		12.100	0.00004136	-16.77	const Pc

d2	61	33	33.89494	28.6	-6.94E-09		16.500	0.0000484	-16.69	4th P-cycle
d3	61	42	43.08677	19.0	1.26E-08		21.000	0.0000556	-16.47	"
d4	61	48	48.94546	13.8	-6.29E-09		24.000	0.0000604	-16.22	"
YB02		Len. (mm)	18.52	dia. (mm)	25.29					
a1	25.1	9	8.985213	15.9	-3.81E-10		4.500	0.0000292	-16.18	const Pp
a2	38.3	9	8.982745	29.3	-3.57E-10		4.500	0.0000292	-16.58	1st cycle
a3	50	9	8.985537	40.9	-3.33E-10		4.500	0.0000292	-17.36	"
b1	50	9	8.985243	40.8	-3.08E-10		4.500	0.0000292	-17.49	const Pc
b2	37.5	8	8.985973	31.9	-2.84E-10		4.000	0.0000284	-17.37	2nd P-cycle
b3	26.8	8	8.987401	17.9	-2.60E-10		4.000	0.0000284	-16.82	"
c1	49	32	32.4665	18.3	1.95E-08		16.000	0.0000476	-16.81	const Pp
c2	49	16	16.24431	28.7	1.50E-08		8.000	0.0000348	-17.18	3rd P-cycle
c3	49	8	8.985973	40.5	-3.33E-10		4.000	0.0000284	-17.49	"
d1	49	8	8.987401	40.5	-3.08E-10		4.000	0.0000284	-17.51	const Pc
d2	49	16	16.24344	32.6	1.49E-8		8.000	0.0000348	-17.32	4th P-cycle
d3	49	32	32.46915	16.6	1.94E-08		16.000	0.0000476	-16.85	"
Pulse transient tests (corrected for gas compressibility, viscosity, and Cui function)										
YB01		len.(mm)	10.89	dia. (mm)	25.4					
		Pp(up)			Gas	Compr.	Compr.			
	Pc (MPa)	(MPa)	Peff (MPa)	slope	visc.Pas	muliplier	1/MPa	log(k)		
a1	58.1	10.9	47.2	3.64E-06	3.07E-05	0.9928	0.091912	-21.41		
a2	57.9	11.7	46.2	2.09E-05	3.135E-05	0.9928	0.085543	-21.38		
a3	57.5	12.0	45.5	1.59E-05	3.158E-05	0.9928	0.083542	-22.44		
YB06		len.(mm)	9.25	dia. (mm)	25.42					
a1	20.3	10.3	10.0	3.12378E-06	3.07E-05	0.9928	0.09739	-22.24		

Table 5.1 summarizes the test conditions and results of permeability experiments that are described in the subsequent sections. Details of specimen locations and petrographic characterisation are provided in chapter 1.

5.1 Permeability Measurements

5.1.1 Influence of pressure cycling at constant pore pressure.

Most permeability measurements were carried out at a low argon gas pore pressure of nominally 10 MPa. This allows the widest accessible range of effective pressure to be accessed, and to be able investigate the influence of repeated pressure cycling on permeability. Most experiments in this respect were carried out on sample YB03P (cored parallel to layering and oven dried, Table 5.1).

Fig. 5.1 shows the variation of log *(k)* with total confining pressure over seven pressure cycles at a constant nominal pore pressure of 10 MPa. The first pressure cycle shows log*(k)* decreasing rapidly with total confining pressure (from an initial 20 MPa total pressure, so that Terzaghi effective pressure was 10 MPa). Subsequent depressurization shows a lower rate of increasing log*(k),* which is largely replicated in a recoverable manner in subsequent up/down pressure cycles. Thus, the first pressurization steps are inferred to close permanently some of the conductive pathways, that may have opened since initial coring, depressurization and retrieval from depth, and subsequent pressure cycles display elastic opening and closing of connected porosity in response to pressure. The elastic response is non-linear, tending to be concave upwards, although the depressurization part of an up/down cycle tends to be more concave (i.e., displays some hysteresis). This is to be expected, as the elastic compressibility of pore spaces is expected to decrease with increasing pressure. There is also a weak tendency to displace the curves downwards, which is interpreted to be due to second-order closure of some porosity, perhaps through time-dependent creep.

Even in the region of non-linear elastic behaviour, the range of permeability values is noteworthy, from log*(k)* = -18.5 to -20.5; that is 2.0 log units. This is substantially larger than the 0.75 log units that was observed for Whitby shale (Mckernan et al., 2017) and tends to emphasise the upward-concave curvature of the data. As anticipated the absolute values of permeability are also low, in the nanodarcy to microdarcy range.

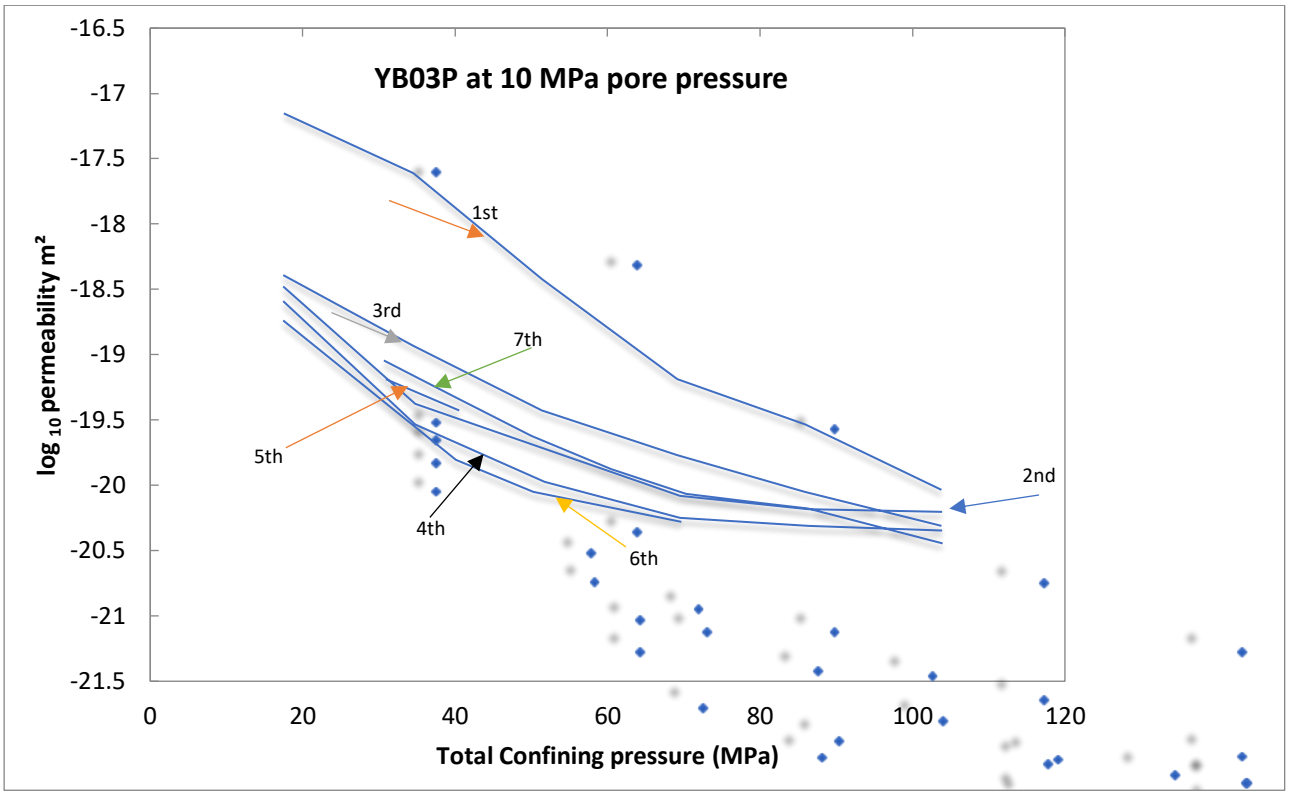

Figure 5.1 Sensitivity of log permeability to confining pressure shown at constant pore pressure of 10 MPa, seven pressure cycles were measured (labelled). Estimated uncertainty in permeability values is ±0.1 log units. The first pressure increment shows non-recoverable permeability loss, whereas subsequent pressure cycles showing nearly non-linear elastic behaviour.

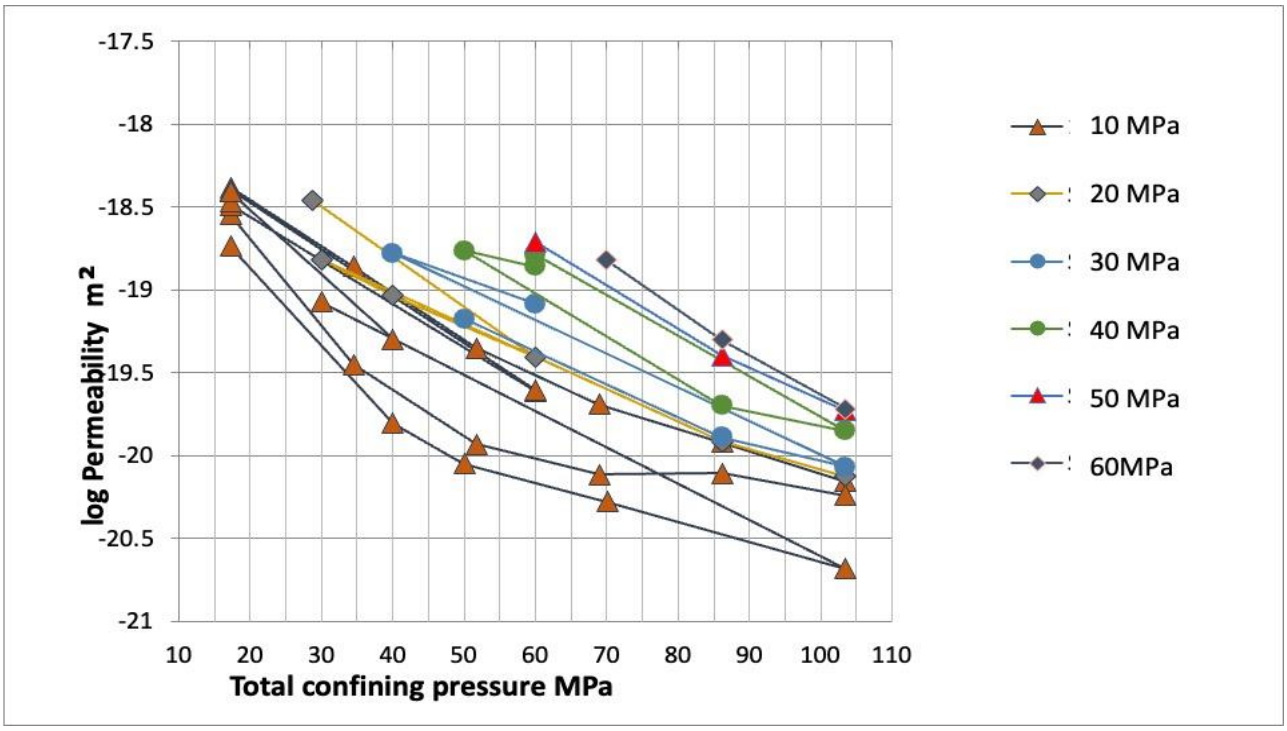

Figure 5.2 YB 03P log Permeability plotted as a function of confining pressure at 10MPa, 20 MPa(series4), 30 MPa (series5), 40 MPa (series6), 50 MPa (series7) and 60 MPa (series14) pore pressure. It shows the movement of the data points towards the right as the pore pressure is increased, in accordance with the principle of effective pressure.

The observation of the marked permanent reduction of permeability in the first pressure cycle demonstrates the importance of pressure cycling shales to a pressure corresponding to the depth from which they were retrieved before relying on obtaining meaningful values of permeability from laboratory tests.

5.2 Influence of different constant pore pressures on permeability

The previous experiments on sample YB03P at constant 10 MPa pore pressure were extended to encompass a range of constant values of pore pressures. These were 20 MPa, 30 MPa, 40 MPa, 50 MPa and 60 MPa over the range of confining pressures from 20 MPa to 100 MPa (Fig. 5.2). The sensitivity to pore pressure was measured at each pore pressure over a sequence of cycles of total confining pressure, to demonstrate reproducibility. Data are presented in Table 5.1.

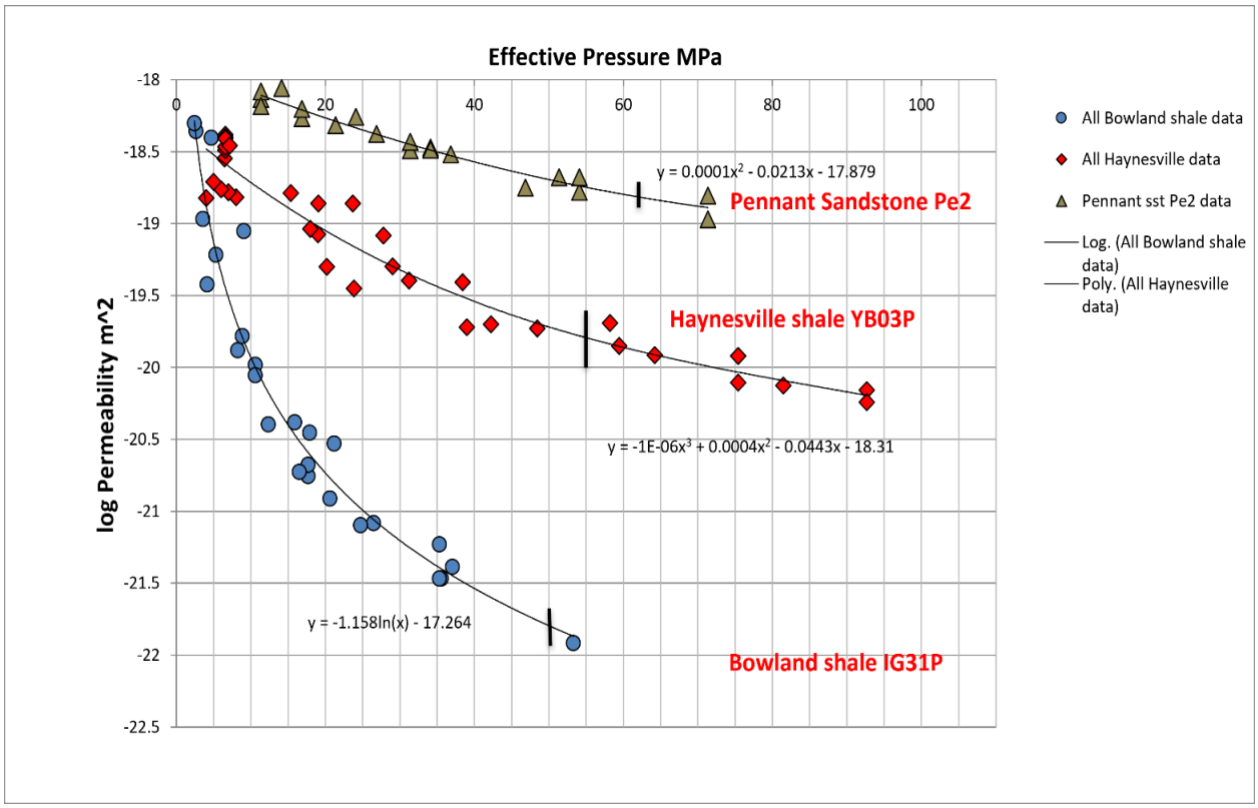

Figure 5.3 Analysis of permeability data for three tight rock types tested over a range of pore pressures, all on the BigRig, to demonstrate the effective pressure principle applied to permeability (from Rutter, Mecklenburgh, and Bashir, 2022). In the equations for best-fit curves, y = log(k) and x = Pc – n Pp. Pore pressures for Pennant sandstone (a tight gas sandstone) were 10, 30 and 50 MPa, with n = 0.86, for Haynesville shale were 10, 20, 30, 40, 50 and 60 MPa with n = 1.1, and for Bowland shale were 10, 25, 40 and 50 MPa with n = 1.1 but increasing in value with effective pressure. All curves are concave upwards and diverge with increasing effective pressure, so that permeability differences are most pronounced at highest effective pressures.

Fig. 5.2. shows how the data are shifted to the right as the pore pressure is increased. The data can alternatively be plotted as log *(k)* against effective pressure $P_{eff} = P_c - nP_p$.

This is done in Fig 5.3, in which the best fit value of *n* has been found by least squares analysis, to maximise the correspondence between the data at different pore pressures. The fit is a test of the effective pressure principle applied to permeability data. It also allows the upward concavity of the collective data to be appreciated. Other previously unpublished data for other rock types collected in this laboratory by E. Rutter and J. Mecklenburg are also shown for comparison. For each dataset, a best-fit polynomial or power function has been shown to represent the data, and in practice the least squares procedure to find *n* involved minimising the sum of the squared deviations between the log(k) values in the dataset and the representative curve. For the Haynesville shale data, the best-fit value for *n* using this procedure was *n* =1.1.

For each of the three rock types in Fig. 5.3 the upward-concave curvature of the plots is evident and is most evident where the range of log*(k)* is greatest.

It has been common to ignore the decreasing slope of log permeability versus confining pressure as pressure is increased and, for the purposes of modelling reservoir behaviour, to assume this relationship to be linear e.g., Bustin et al. (2008); Cui et al. (2009); Heller et al. (2014); Kwon et al. (2001) and Mckernan et al. (2017). It is also possible to apply a power law relationship (Shi & Durucan, 2016), but if the range of permeability is sufficiently small there may be little difference between the two.

Here we can usefully derive the parameters of an exponential law between permeability and pressure with the intention of using it to demonstrate in due course how it can be applied to reservoir modelling.

Fig. 5.4 shows the permeability-pressure data fitted to an exponential law for sample YB 03P.

$$k = ko \exp -\gamma(P_C - nP_P) \qquad \text{Eqn. 5.1}$$

This equation can be linearised by taking natural logarithms permeability which gives parameters $k_{0,}\ \gamma, and\ n$ where

$$\log_e k = \log_e k_0 - \gamma\, P_c + \alpha P_p \qquad \text{Eqn. 5.2}$$

And $\alpha = \gamma n$. This is a linear equation in terms of dependent variable $\log_e k$ and independent variables P_c and P_p and constants k_o, γ and α. Note that the values of these parameters change by a factor 2.303 if the fit is made using $\log_{10}$.

The data was fitted using multiple linear regression analysis. In fig 5.4 the $\log_{10}$ of permeability versus confining and pore pressure is shown. The parameters $k_{0,}\gamma$ and $\alpha\gamma$ are the intercept on permeability axis and the two gradients $\left|\frac{\partial \log_e k}{\partial P_c}\right|_{P_p}$ and $\left|\frac{\partial \log_e k}{\partial P_p}\right|_{P_c}$ respectively.

When $n > 1$ permeability is more sensitive to changes in pore pressure than confining pressure, and is less sensitive to pore pressure when $n < 1$. In the case where the effect of both pore pressure and confining pressure on permeability are equal, $n=1$. From this fit the value of n in these experiments is 1.05 within experimental error (Table 5.1) meaning the pore pressure is fully or slightly more than fully effective.

$$\log k = -18.73 - 0.02002P_c + 0.02097P_p$$

$$\gamma = 0.02002 \quad ; \quad n = 1.0474$$

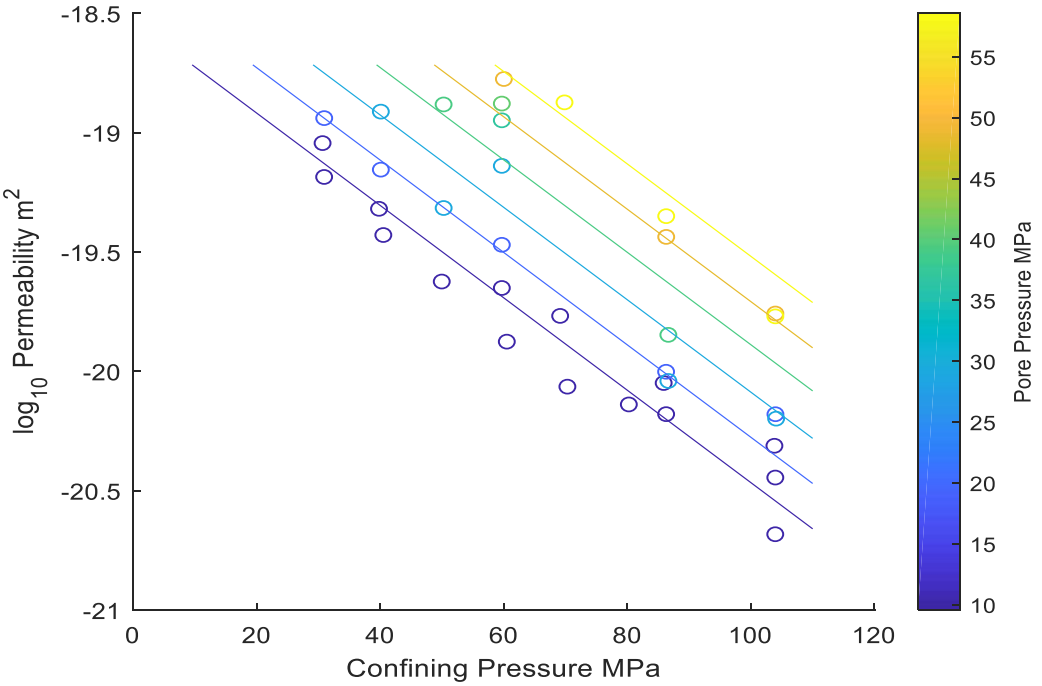

Figure 5.4 Data for YB 03 sample showing log permeability variation with confining and pore pressure using equation 5.2. Here, total confining pressure is used for the horizontal axis and contoured for pore pressure. The pore pressure is presented in a colour bar, while the sample $\log_{10}$ permeability is presented with the coloured circles and fitted lines at constant pore pressure.

Within the limits of the range of experimental conditions, the exponential function describes moderately well a relationship between permeability and effective stress (Eqn.5.1), hence the description can be used a basis for modelling evolution of fluid flow in a shale gas reservoir with time, as the gas pore pressure is drawn down, emphasising again that this applies only within the limits of the pressure conditions used.

The non-linear relationship shown in Fig. 5.2 can also be used for reservoir modelling and should yield more precise results, where:

$\log(k) = -2.21E\text{-}6(P_c - nP_p) + 4.91E\text{-}4(P_c - nP_p) - 4.83E\text{-}2\ (P_c - nP_p) - 18.82$
and $n = 1.1$. *Eqn*. 5.

5.3 Permeability at low pore pressures –slip flow

As outlined in section 2.3.3, at relatively high pore pressures the pore fluid flow is dominated by viscous effects, hence a pressure gradient develops with distance away from the pore walls, with zero fluid velocity adjacent to the pore walls. At progressively lower pore pressures the lower fluid density leads to a longer mean free path of gas molecules and detachment of the fluid from the pore walls. This is slip flow, which leads to the Klinkenberg effect. It leads to an anomalous increase in measured permeability with decreasing pore pressure and facilitates gas production at low pore pressures when otherwise viscous flow would result in progressively decreasing gas flow with pressure drawdown.

In this study, slip flow was investigated for sample YB03P via a set of experiments in which the Terzaghi effective pressure was kept close to constant (between 7 and 9 MPa) whilst the gas pore pressure was allowed to vary from about 20 MPa down to the minimum manageable, about 1.5 MPa. It was not possible to use the oscillating pore pressure method at such low pore pressures therefore the pulse transient and steady state fluid flow methods were used. These are highlighted in Table 5.1 by an asterisk beside the test identifier. To illustrate their form, Figs. 5.5 and 5.6 show data examples of some of the pulse transient tests (YB03U series) and a steady-state flow test (R6). The pulse transient test raw data takes the form of the following.

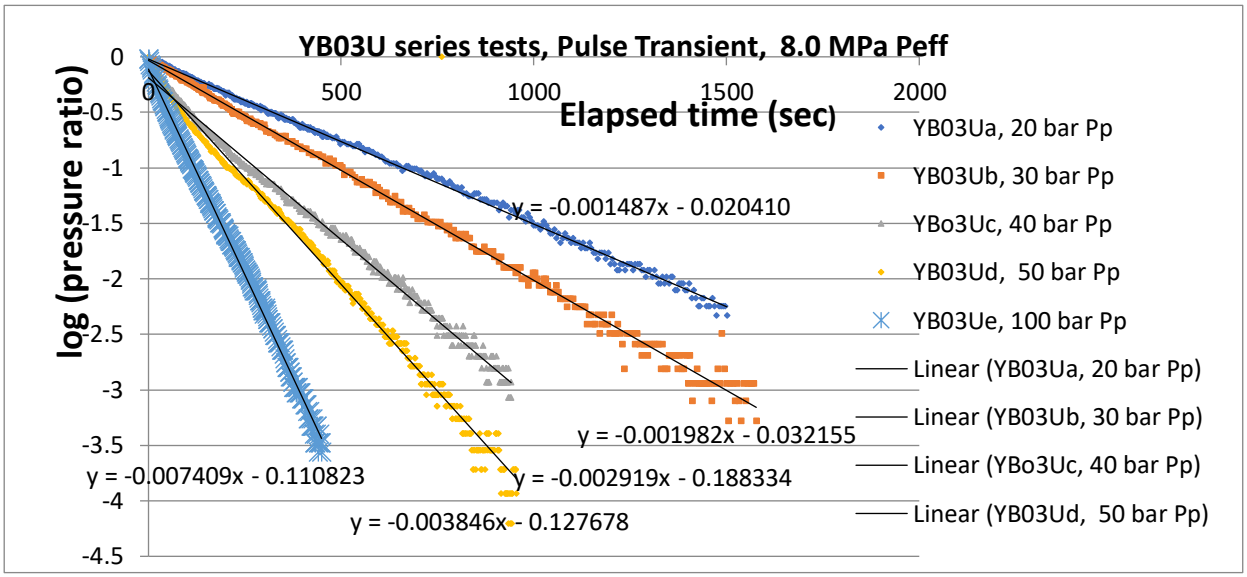

Figure 5.5 Pulse transient tests from series YB03U (table 5.1). The log of ratio of instantaneous pore pressure to the whole pore pressure step range is plotted against elapsed time. Best-fit straight lines are shown, that must pass through the origin with a negative slope, from which the permeability is calculated.

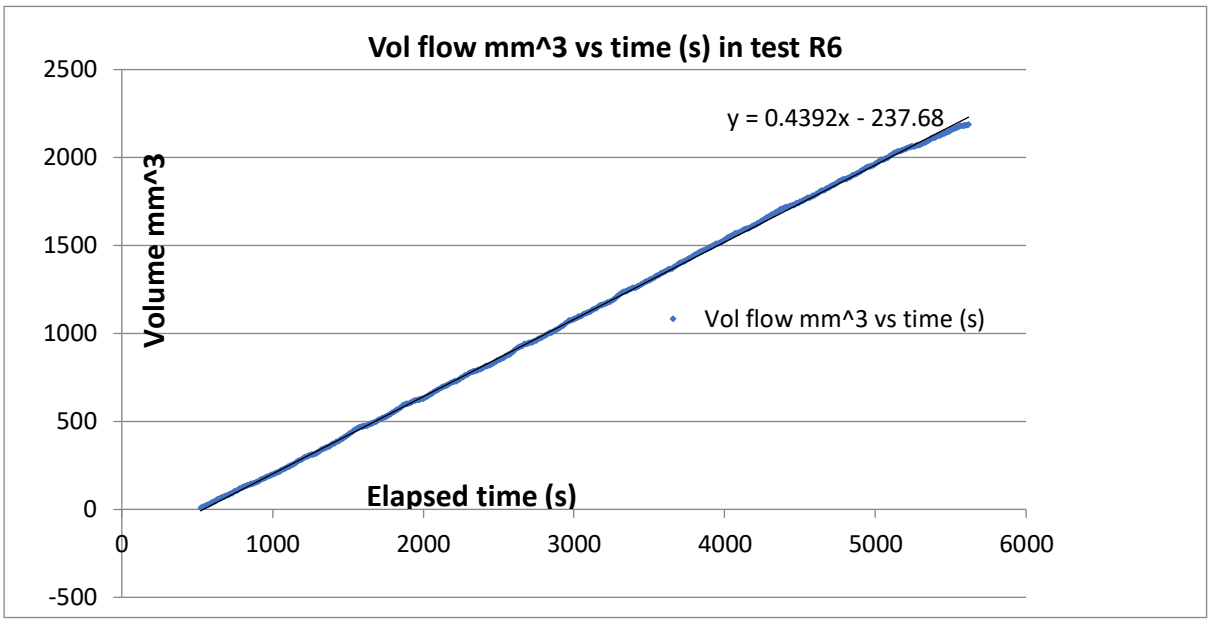

Figure 5.6 Example of the raw data from constant flow rate test R6 (Table 5.1). The slope of the best-fit line gives the volumetric flow rate, from which the permeability is calculated. Total confining pressure = 9.7 MPa, Pp (up) = 2.0 MPa and Pp (downstream) = 1.0 MPa.

A second set of tests was carried out for sample YB03P, now keeping the Terzaghi effective pressure constant at 30 MPa and varying the pore pressure over the same range as above. These two sets of results are shown in Fig. 5.8. and in fig. 5.9 after normalization of the permeability by the value at high pore pressures, beyond the range where the permeability enhancement begins to take effect.

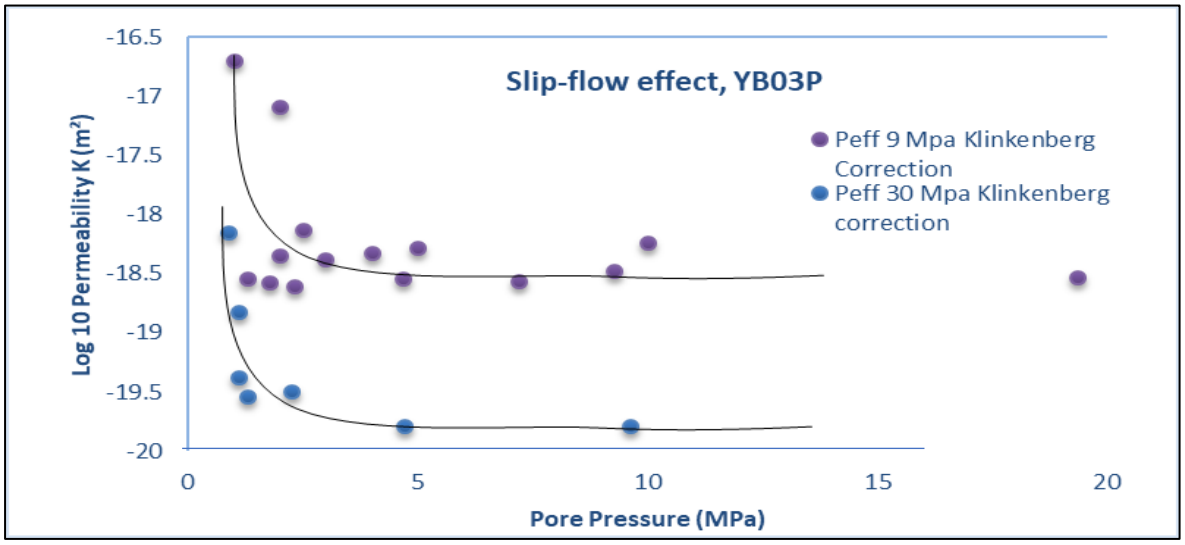

Figure 5.7 Measured log permeability data plotted against pore pressure at constant effective confining pressures of 9 (YB03P) and 30 MPa. At pore pressures above about 4 MPa the permeability is unaffected by variations in pore pressure. At low pore pressures (below 4 MPa) permeability is enhanced, as predicted by the gas-slippage effect. Qualitative trend lines are shown for each dataset.

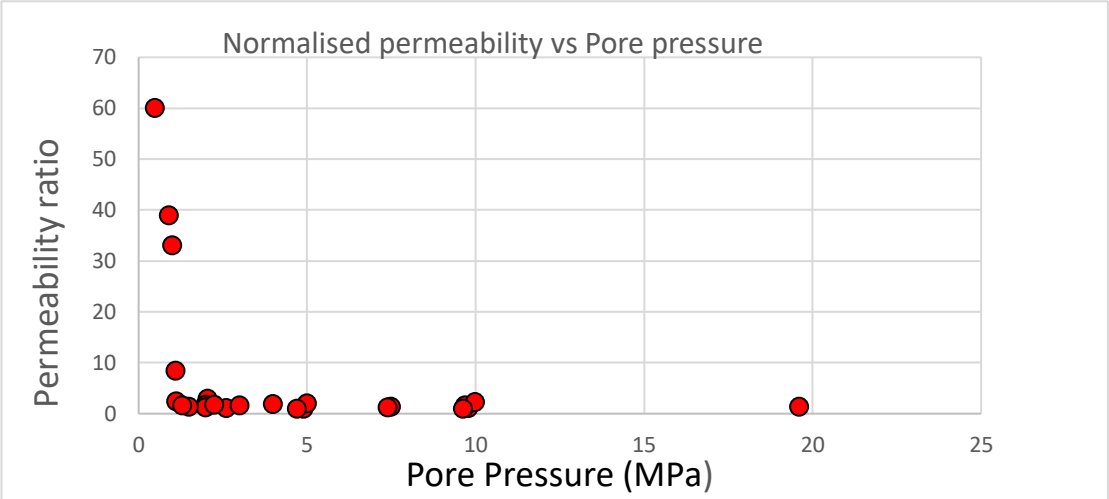

Figure 5.8 Normalized permeability (permeability measured normalized by permeability at high Pp to combine both datasets YB03 in fig. 5.7. Enhanced flow (slip flow) begins at pore pressures smaller than ~ 4MPa.

To incorporate the enhancement of permeability at low pore pressures, Eq. 5.3 can be modified by a multiplier $(1 + \frac{P_K}{P_p})$, where P_K is called the Klinkenberg parameter (dimensions are pressure)

$$\log_e k = k_0 \ \exp\left(-\gamma\left(P_c - \alpha P_p\right)\right)\left(1 + \frac{P_K}{P_p}\right) \qquad Eqn. 5.4$$

P_K can be estimated from a plot of normalized permeability (which measures deviations from the high pore pressure permeability trend) against $\frac{1}{P_p}$. According to Eqn. 5.4 the plot should be linear, and at high pore pressures $\frac{1}{P_p}$ approaches zero and normalized permeability approaches one (fig. 5.9). The data on the right-hand side of fig 5.9 shows an extremely large scatter and the slope is very poorly constrained at 20 MPa.

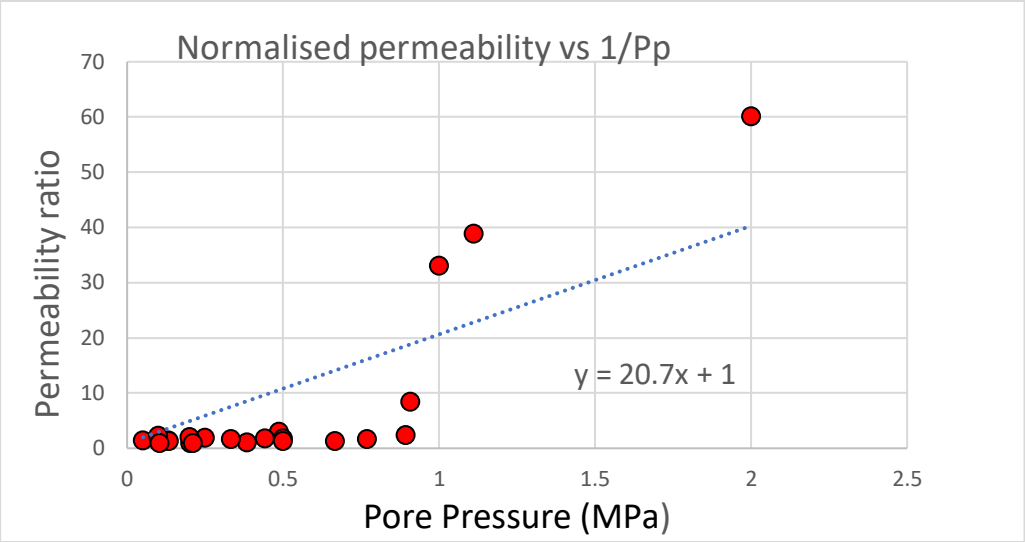

Figure 5.9 Plot of normalized permeability versus reciprocal pore pressure for sample YB03P for measurements at 9 MPa and 30 MPa effective confining pressure.

Following Heller et al. (2014) it is possible to interpret the Klinkenberg parameter in terms of the width (w) of the crack-like pores based on the Poiseuille equation for flow of a gas of viscosity μ and molar mass *M* through a parallel-sided channel. They obtained:

$$w \sim \left(\frac{20\mu c}{P_K}\right)\sqrt{\left(\frac{RT}{M}\right)} \qquad Eqn.\,5.5$$

where *c* is an empirical constant of order 1, R is the gas constant and T is the temperature (K). Evaluating Eqn. 5.5 for P_K = 20 MPa gives w = 6 nanometres, which is roughly the order of size expected for flow through crack-like pores in a shale.

A plot of amplitude ratio (gain) *A* vs phase shift ϕ from the oscillating pore pressure tests on sample YB03P and YB03N are presented in Fig. 5.10, showing the observations of $\log A$ and ϕ and the solutions, for constant dimensionless permeability η (roughly horizontal lines) and constant dimensionless storativity ξ (roughly vertical lines), of equation 4.1 (Bernabé et al., 2006). The data for YB03P lie along the line for dimensionless storativity factor ξ line approximately equal to 0.032. which implies storativity in the sample YB 03 is small relative to the downstream storage of the apparatus. The expected storativity factor for the total porosity of 9.3% is ξ= 1.9, thus implying that the fraction of the porosity used in flow

parallel to bedding is 0.03/1.9 ~ 2% of the available pore space. In contrast, for flow normal to layering, $\xi = 0.3$ corresponding to 0.3/1.9 ~ 16% of the total pore space.

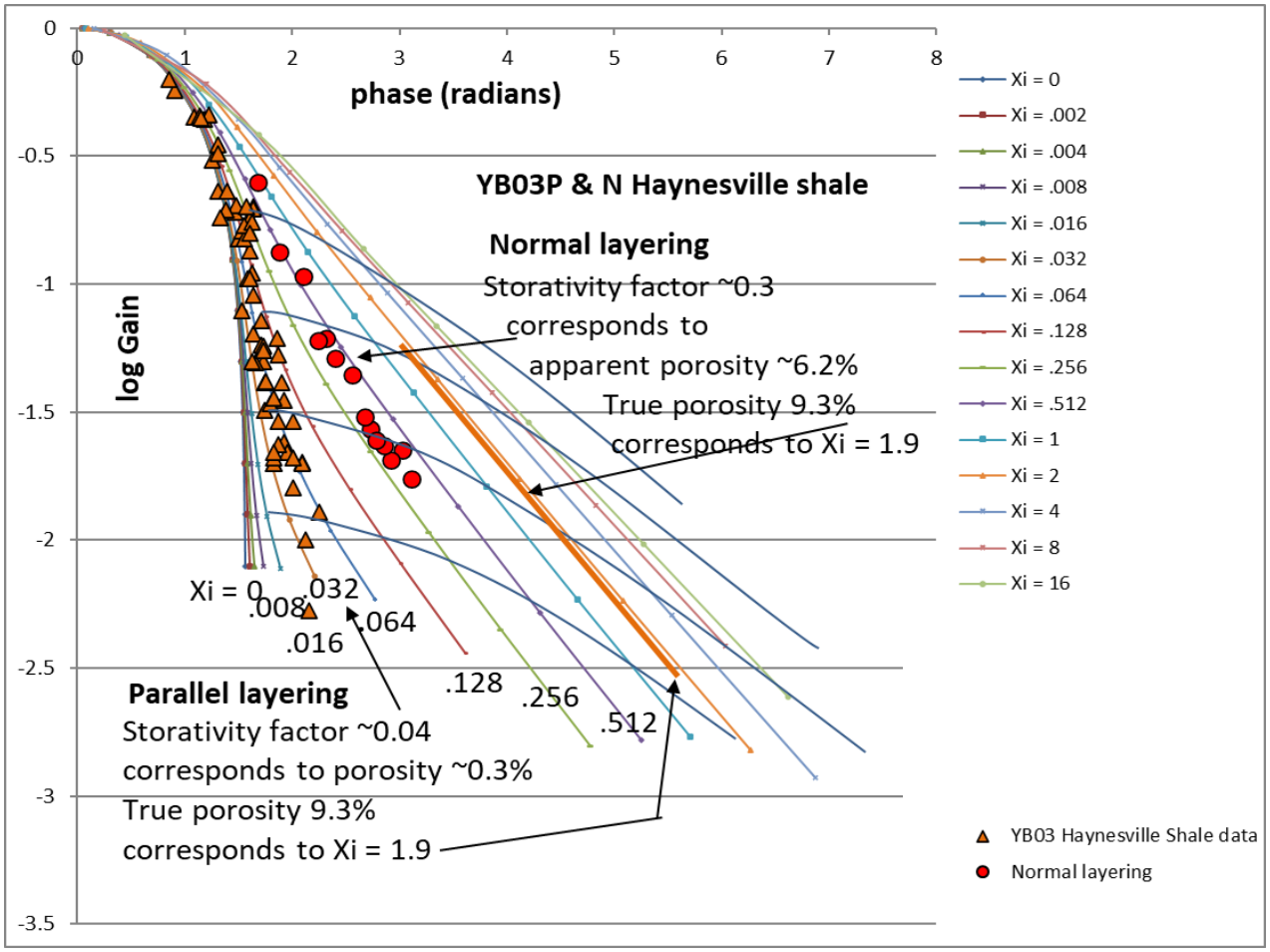

Figure 5.10 Log (gain) versus phase shift data for YB03 samples in both the core orientations parallel (triangles) and normal (circles) to layering. Plots track lines of constant ξ (pronounced Xi). Yb03N shows a much larger value of ξ does YB03P, implying that flow across the layering 'sees' a greater proportion of the total pore space than flow along the layering. (from Rutter, Mecklenburgh, and Bashir, 2022).

Haynesville shale is similar to other shales, in which conductive porosity is a small fraction of total porosity, such as Bowland shale and Whitby shale (Mckernan et al., 2017). In contrast, for the higher permeability but nevertheless relatively tight Pennant sandstone, the conductive porosity was found to be almost equal to the total porosity (Rutter, Mecklenburgh, and Bashir, 2022). The finding that shales such as the Haynesville shale have conductive porosities that are but a small fraction of the total has implications for the behaviour of shale gas reservoirs (and also for gas storage reservoirs). The total production (or storage) potential is determined by the total

porosity, whereas the rate of production (or rate of filling) is determined by the permeability. These implications will be discussed in further later in chapter 7.

5.4 Permeability Anisotropy

Two samples of YB 03 which are physically different were used for this experiment (Table 5.1). The samples were cored next to each other, thereby minimizing the effects of sample heterogeneity. The two samples were cored in perpendicular directions, parallel and normal to bedding. Permeability for flow normal to bedding is commonly lower than for flow parallel to bedding, perhaps reflecting better connectivity of pores in that orientation.

The sample oriented for flow parallel to bedding displayed greater reduction of permeability with pressure than the sample normal to bedding as shown in figure 5.11, although the numeric values of permeability were not greatly different.

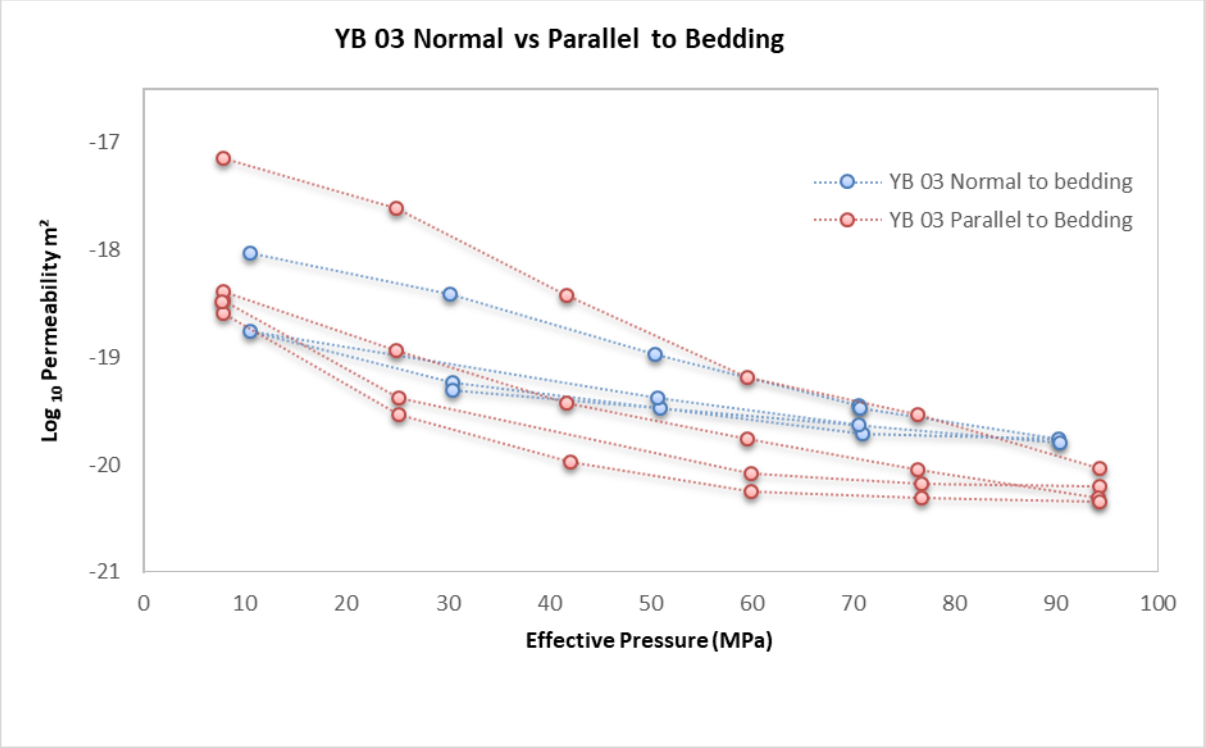

Figure 5.11 Permeability of specimens YB03P and YB03N comparing permeabilities measured for flow normal to bedding and flow parallel to bedding, all at constant pore pressure (gas) = 10 MPa. In both cases the first pressure cycle corresponds to closure of pores that subsequently do not reopen. Subsequently, the pressure sensitivity normal to layering is weaker than parallel to layering. It is reasonable to expect pores parallel to layering to be more sensitive to pressure if they are of low aspect ratio oriented along the bedding, and for this to be reflected in the relative pressure sensitivity of the flow.

5.5 Pore Volumometry

Pore volume changes were measured for sample YB03P (Table 5.1) at the same time as acoustic wave velocities were measured on these samples. Obtaining bulk moduli as a function of pressure helps with the interpretation of the influence of pressure on permeability, and potentially acoustic wave velocities also.

Fig. 5.12 a shows plots of volumetric strain change versus Terzaghi effective pressure. Each measurement was taken at a point at which a corresponding velocity measurement was taken.

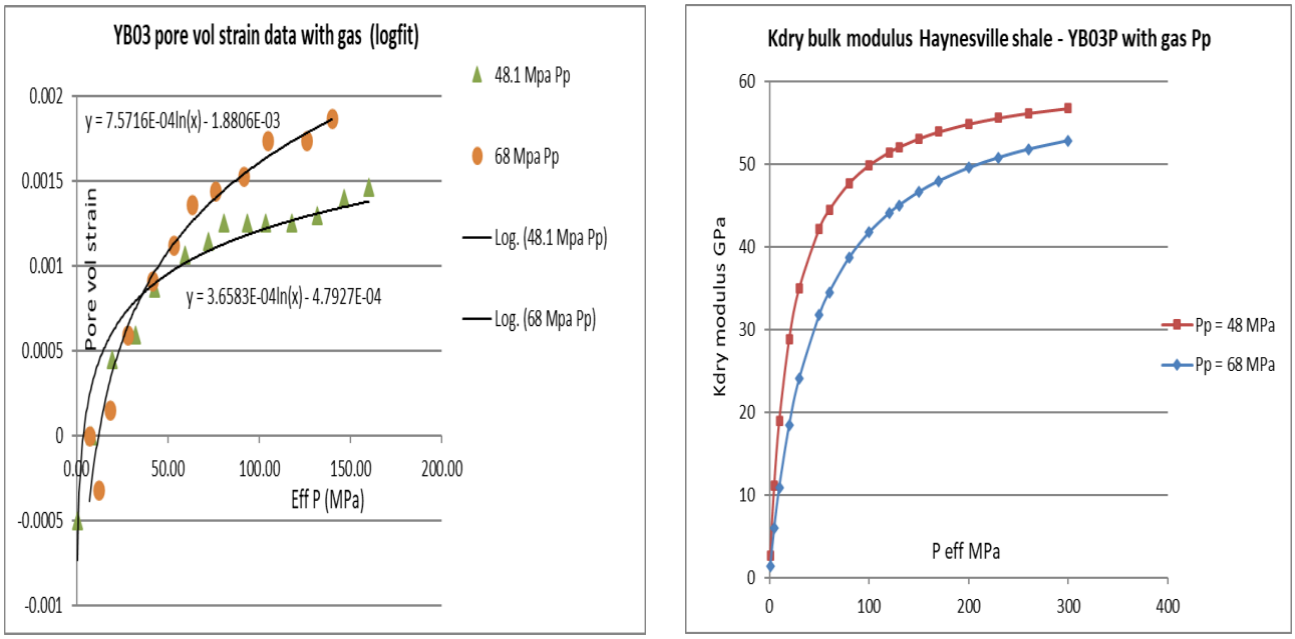

Figure 5.12 (a) (left) Recorded values of pore strain vs Terzaghi effective pressure for YB03P at 48.1 and 68 MPa pre pressures, with logarithmic fits. (b) Bulk modulus K_{dry} for YB03P at the same pore pressures. The curves are asymptotic to the K_o modulus at 61 GPa. (From Rutter, Mecklenburgh, and Bashir, 2022).

These data were fitted to logarithmic curves as shown. At any point, the gradient of the up-pressure volumetric strain curve with respect to effective pressure is obtained by differentiation of the strain/pressure curve $(for\ y = In\ (X), \frac{dy}{dx} = \frac{1}{X})$ and is the compressibility of the pore spaces C_{pc}, whose reciprocal is $K_{\emptyset}$.

The down-pressure hysteretical behaviour implies that no gas is being drawn into the pore spaces until most of the pressure had been released, after which the volume strain would rapidly expand back to start point. Thus overall, there was no permanent volume strain through a pressure cycle.

Knowing the V-R-H grain modulus (=61 GPa) from the XRD data, we can find the bulk modulus k_{dry} of the porous aggregate from

$\frac{1}{K_{dry}} = \frac{1}{K_o} + \frac{1}{K_\emptyset}$, and this is plotted in Fig. 5.12b for the same two pore pressures. As pressure rises the pores stiffen and $\frac{1}{K_\emptyset}$ approaches zero, thus the k_{dry} curves are asymptotic to K_o.

k_{dry} versus Terzaghi effective pressure describes how the dimensions of pore spaces reduce elastically with increasing pressure, and it is this which causes permeability to decrease with pressure, as shown in Fig. 5.3, at an ever-decreasing rate as the porous framework stiffens. Seeburger & Nur (1984), following Walsh (1965) and Mavko & Nur (1978) showed that the bulk modulus k_{dry} of a solid of unit volume containing a population of *N* penny shaped crack-like pores elliptical cross section, Poisson's ratio ν and semi-major axis $2c$ is given by.

$$\frac{1}{K_{dry}} = \left(\frac{1}{K_o}\right) + \left(\frac{1}{K_o}\right)\left\{\left(\frac{16\,Nc^3}{9}\right)\frac{(1-V^2)}{(1-2V)}\right\} \text{ or } \left(\frac{K_o}{K_{dry}} - 1\right) = \left\{\left(\frac{16\,Nc^3}{9}\right)\frac{(1-V^2)}{(1-2V)}\right\} \qquad \text{Eqn. 5.8}$$

The results for different pore configuration geometries only affect the results by a numerical constant. Recalling the Biot-Willis effective pressure parameter m (Chapter 4.12), that describes how effective pressure influences the elastic properties of porous solids.

$$m = 1 - \frac{K_{dry}}{K_o} \qquad Eqn. 5.9$$

and $P_{eff} = (P_c - nP_p)$. Note that the left-hand side of eq. 5.8b above is $\frac{m}{(1-m)}$. The value $m(P_{eff})$ is therefore an indicator of the sensitivity to pressure of processes that depend on the elastic volume strain of a porous solid. It derives directly from the plot of $K_{dry}\,(P_{eff})$ and is plotted in fig. 5.12 for the two pore pressures considered above.

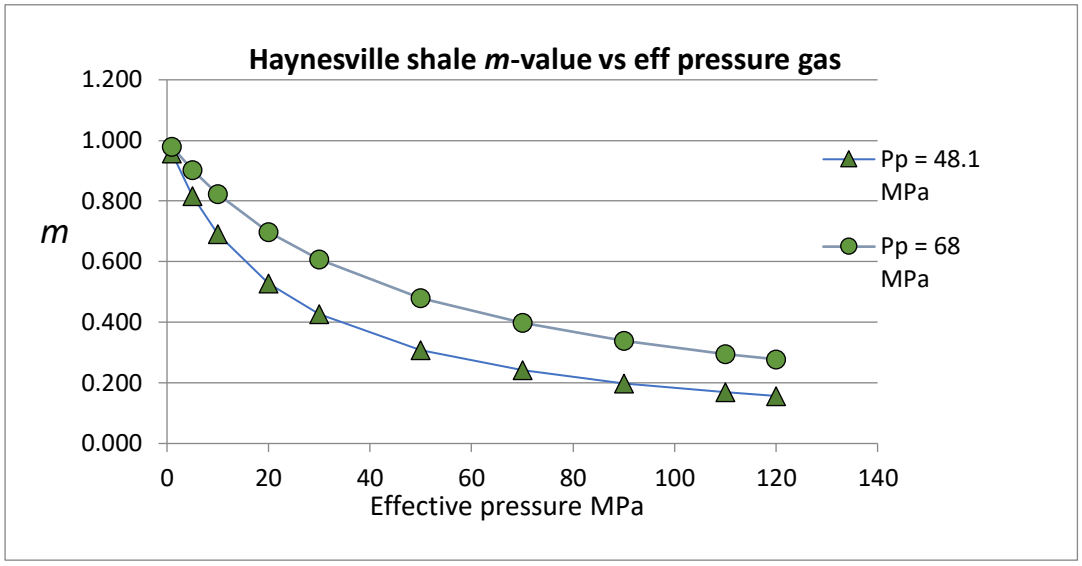

Figure 5.13 m value for Haynesville shale versus Terzaghi effective pressure. Experimental m data from pore volumometry decrease rapidly with P_{eff} . (From Rutter, Mecklenburgh, and Bashir, 2022).

m will be revisited later in the chapter 6 in the context of the influence of pore pressure on acoustic wave velocities and in the discussion of effective pressure laws for different petrophysical properties.

5.6 Permeability measurements using the CoreTest Rig.

A number of permeability measurements were made using the CoreTest rig, and these are listed in table 5.1. all samples were tested dry and with the core cut parallel to layering. The maximum confining pressure attainable on the CoreTest rig was only 60 MPa, therefore except for the first cycle of increasing pressures they are not directly comparable to the results from the BigRig, for which specimen YB03 was taken to 110 MPa total confining pressure.

Four measurements were made on sample YB07 using the oscillating pore pressure method. This sequence of four measurements were made at a constant confining pressure of 64 MPa and successively increasing pore pressures of nominally 10, 20, 30 and 40 MPa.

Measurements were made using the constant flow rate method on samples YB05, YB04, YB08 and YB02, with alternating pressure cycles at constant P_c and then constant P_p, stepwise varying the effective pressure. The results from these tests are shown in Fig. 5.14. Each of these samples belongs to the group that are carbonate-poor and contain similar proportions of framework silicates and phyllosilicates and are relatively well foliated. All the samples measured were parallel

to foliation. Perhaps as a consequence they display similar magnitudes and patterns of permeability versus pressure behaviour. Each of the samples shows an initially high range of permeability, with subsequent effective pressure cycles showing less pressure sensitivity and lower overall permeabilities, but their mean values after the first pressure cycle are quite similar and high, e.g., at *ca* log (k) ~ -17.0. Whether effective pressure is varied using pore pressure or confining pressure, permeabilities are unaffected, thus the materials follow the effective pressure law with n~1.

A small number of pulse transient decay tests were made on samples YB01 and YB06. There are too few tests to see trends, however, but the recorded permeabilities are rather low, at *ca* log(k) ~ -21 to -22.

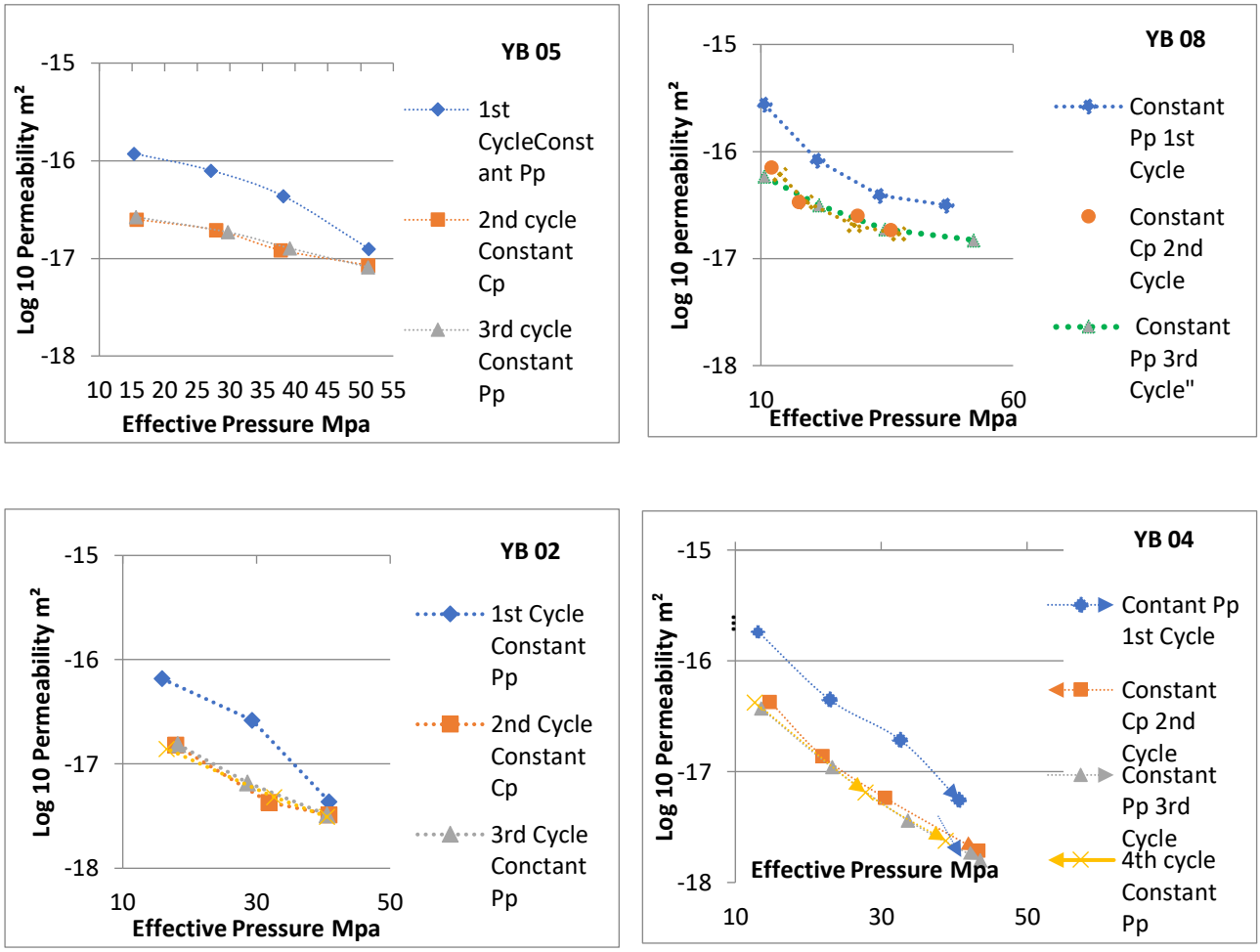

Figure 5.14 Results of the constant flow rate permeability tests on the CoreTest rig using the steady state flow method at constant pore pressure difference, expressed as log permeability vs Terzaghi effective confining pressure. Individual pressure cycles were run alternating between constant Pc and constant Pp conditions, to produce the variations in effective pressure. Details are listed in Table 5.1. All of these four samples belong to the low carbonate% group. They were tested dry on cores cut parallel to the layering. All show a first pressure cycle more permeable than the subsequent ones, which are (non-linear) elastic, and the general value of permeability (e.g., at 30 MPa P_{eff}) is rather similar.

5.7 Influence of Mineralogy and Porosity on Permeability

As shown in fig. 3.6, Haynesville-Bossier shales tend to contain similar proportions of phyllosilicates to framework silicates, and a wide variation in total carbonate content, such that the carbonate content can be taken to provide a first-order descriptor of the mineralogy of this group of rocks. In the 8 samples selected for this study, only YB03 and YB06 were rich in carbonate (over 50 vol%), while the remainder fell into the carbonate-poor category. The carbonate content impacts strongly on the overall microstructure and cementation of these rocks. Therefore, it was suspected that carbonate content might correlate strongly with the permeability.

A further factor that might be expected to impact upon permeability is porosity. Combined with the effects of grain size (d) in sandstones in particular, permeability has been shown to be proportional to $\phi^3 d^2$ (Bourbie and Zinsner, 1985). When comparing permeability with other factors it is important that the samples have had similar pressure histories, as has been done here. The following Table 5.2 extracts $\log_{10}(k)$ taken from the second and subsequent cycles of pressure cycling at 30 and 50 MP Terzaghi effective pressures, together with porosity and carbonate vol%, from which the figures 5.15 and 5.16 have been drawn. Fig. 5.15 shows that there is no clear correlation between permeability and porosity. This is perhaps unsurprising, given the mineralogical and microstructural complexity of shales. Fig. 5.16 shows the same permeability data plotted against carbonate vol%. Whilst there is a cluster of data at high permeabilities corresponding to the carbonate-poor data, unfortunately only one sample (YB03) was investigated in sufficient detail to provide data of sufficient quality, and this sample is substantially less permeable that the carbonate-poor cluster. One caveat is that whereas the carbonate-poor samples were taken to only 50 MPa effective pressure, the carbonate-rich sample was taken to 100 MPa effective pressure, which would have caused log(k) at 50 MPa P_{eff} to be the observed -19.7 instead of ~-18.3. Nevertheless, the carbonate-rich sample YB03 would still have been significantly less permeable than the carbonate-poor samples.

Sample#	log(k) 30 MPa	log(k) 50 MPa	Carbonate vol%	Porosity%
YB3	-19.24	-19.7	52.2	9.3
YB4	-17.15	-17.9	7.4	10
YB5	-15.8	-17.05	15	7.97
YB8	-16.7	-16.8	14.5	9.7
YB2	-17.2	-17.5	10.7	8.2

Table 5.2 Tabulation of log(k) at two effective pressures and carbonate content and porosity (data from Table 5.1).

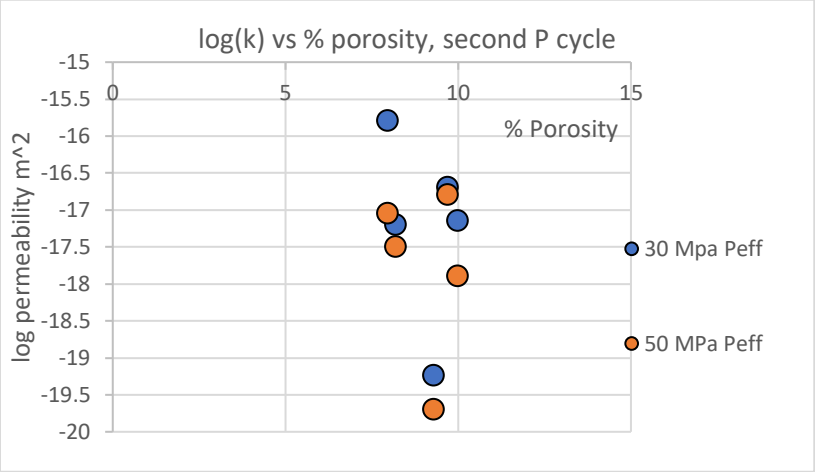

Figure 5.15 log (k) versus porosity% for carbonate-poor through carbonate-rich samples, second and subsequent pressure cycles, at the P_{eff} values shown. There is no apparent correlation.

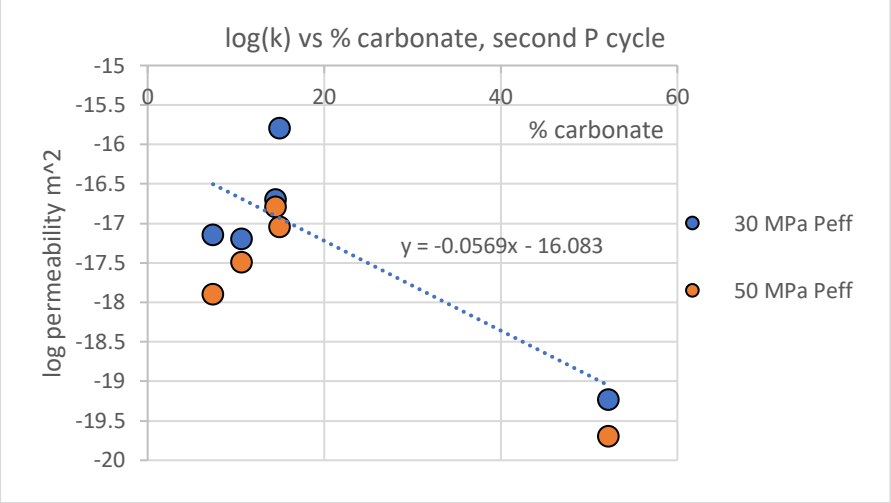

Figure 5.16 log (k) versus carbonate vol% in all samples that had a second and subsequent pressure cycle, at the P_{eff} values shown. The carbonate-rich sample YB03 appears to be substantially less permeable than the carbonate-poor samples, although YB03 was taken to higher P_{eff}, which would have had the effect of lowering the permeability by about one order of magnitude.

Chapter 6: Experimental Results 2-Acoustic velocity measurements.

Experiments are described here to investigate the effects of confining and pore pressure on acoustic wave velocities, and at the same time to measure the compressibility of the porous aggregate and how effective pressure affects it. The aim is that these data will allow some investigation of the extent to which measurements of petrophysical characteristics related to acoustic velocities can be used to constrain and interpret permeability data.

6.1 Acoustic Velocity Measurements

Compressional (P) wave ultrasonic velocities were measured for Haynesville shale sample YB03P (parallel to foliation) and YB01N (normal to foliation) to total confining pressures 200 and 150 MPa, respectively. Measurements were made with air-filled porosity for both rocks and also for YB03P at a sequence of pore pressures of argon gas in order to evaluate the applicability of the effective pressure law. Measurements were also made with sample YB03P vacuum-saturated with water at atmospheric pressure in order to evaluate the Gassmann fluid replacement effect. The apparatus used for these experiments is described in Chapter 4.13. The conditions for each experiment performed are summarized in results table 6.1.

Tests on Green rig - acoustic velocities and pore volumometry										
All tests on YB03P and YB01N - YB03P (dry parallel layering) and YB01N (dry normal layering)										
YB03Psat is YB03P now saturated with water.										
	len.(mm)		dia. (mm)							
YB03P	18.94		24.69							
YB01N	29.6		23.68							
Individual measurement cycles are in time sequence.										
	Min. conf	Max conf	Pore Press	cycle #	Pore Vol	*Hill fit parameters - up-pressure*				
YB03P	press MPa	Press MPa	MPa			*V1 (km/s)*	*V2 (km/s)*	*k*	*s*	
YB03Pa	1.5	208.8	0	1	No	3.745	9.352	7628.00	0.711	
YB03Pb	**rapid P-cycle - not measured**			2	No					
YB03Pc	**2.2**	298.2	0	3	No					
YB03Pd	**rapid P-cycle - not measured**			4	No					
YB03Pe	2.7	210.3	0	5	No	4.200	8.300	1752.00	0.604	
YB03Pf	40.0	207.0	34.5	6	Yes					
YB03Pg	74.9	207.4	67.7	7	Yes					
YB03Ph	54.3	207.9	48.1	8	Yes					
YB03Pi	14.5	208.2	10.3	9	Yes					
YB03Pj	2.3	210.3	0	10	No	4.489	9.360	1752.00	0.696	
YB03Pk	38.7	212.5	34.5	11	Yes					

YB01Na	2.5	139.8	0	1		1.339	10.522	1226.00	0.444	
YB03Nb	rapid P-cycle - not measured			2						
YB03Pn	2.5	140.3	0	3						
Tests on YB03P water saturated										
	Min. conf	End conf	Pore Press	cycle #	Pore Vol	*Hill fit parameters - up-pressure*				
YB03Psat	press MPa	Press MPa	MPa			*V1 (km/s)*	*V2 (km/s)*	*k*	*s*	
YB03satA	1.3	141.3	0	1	No					
YB03satB	1.9	96.3	0	**2**	No					
YB03satC	2.4	143.6	0	3	No					
YB03satD	2.5	193.0	0	4	No	4.013	7.389	1752	0.419	

Table 6.1 summarizes the test conditions and results of acoustic velocity experiments that are described in the subsequent sections.

6.1.1 Measurements on dry samples without pore pressure

Fig. 5.17 shows the results of P-wave velocity measurements as several up-pressure and down-pressure cycles. The tendency for successive pressure cycles to shift the velocities upwards in stepwise fashion was noted (Fig. 5.17). This implies that successive pressure cycles are causing stiffening, perhaps arising from increments of permanent microcrack crack closure. In contrast, increasing pressure is not expected to produce significant change in sample density. Recall in chapter 5, the comparable tendency for permeabilities to decrease slightly with successive pressure cycles. After 5 pressure cycles little further change was noted.

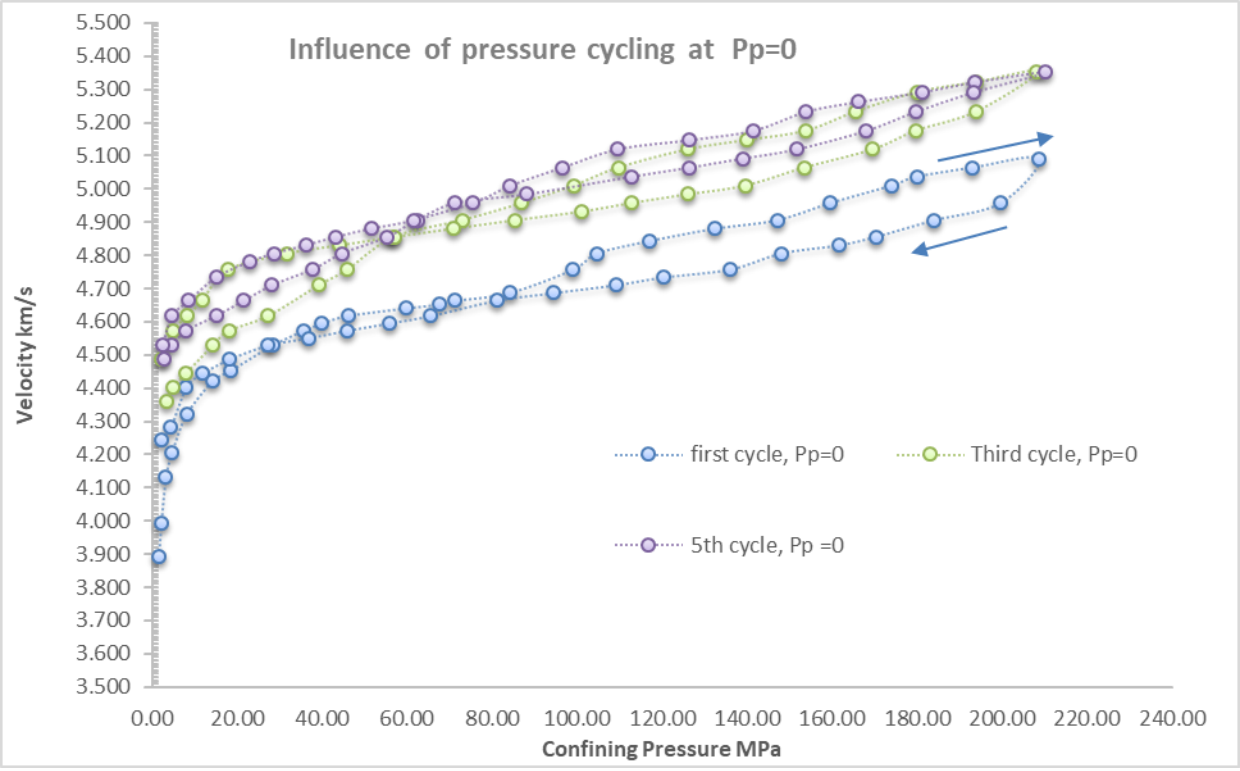

Figure 6.1 Ultrasonic P-wave velocity measurements plotted against confining pressure, for successive cycles of up- and down-pressure loading. Pore pressure (P_p) = 0. Successive loading cycles show stepwise increases in velocity but by decreasing amounts, suggesting that each pressure cycle causes irreversible stiffening, probably by crack closure. Five pressure cycles without pore pressure were performed before pressure cycles were performed with the addition of non-zero pore pressures. The fourth and fifth cycles were indistinguishable, however. Arrows indicate the form of up and down pressure steps, and this pattern applies to all the cycles shown.

It is not uncommon for acoustic wave velocities to display hysteresis between up and down pressure cycles. The down pressure cycle typically displays higher velocities than the up-pressure cycle because frictional forces tend to keep cracks closed until part of the pressure has been released. YB03P displays significant hysteresis, but with an unusual pattern. At the start of the pressure release, velocity is lower than during the last part of the up-pressure cycle. This behaviour is reproducible (Fig. 6.1). After about 50% unloading the down-pressure curve crosses over with the up-pressure curve, and from this point until complete unloading the velocity is higher than during the up-pressure cycle. Thus, the velocity pressure path traces a figure-8 pattern.

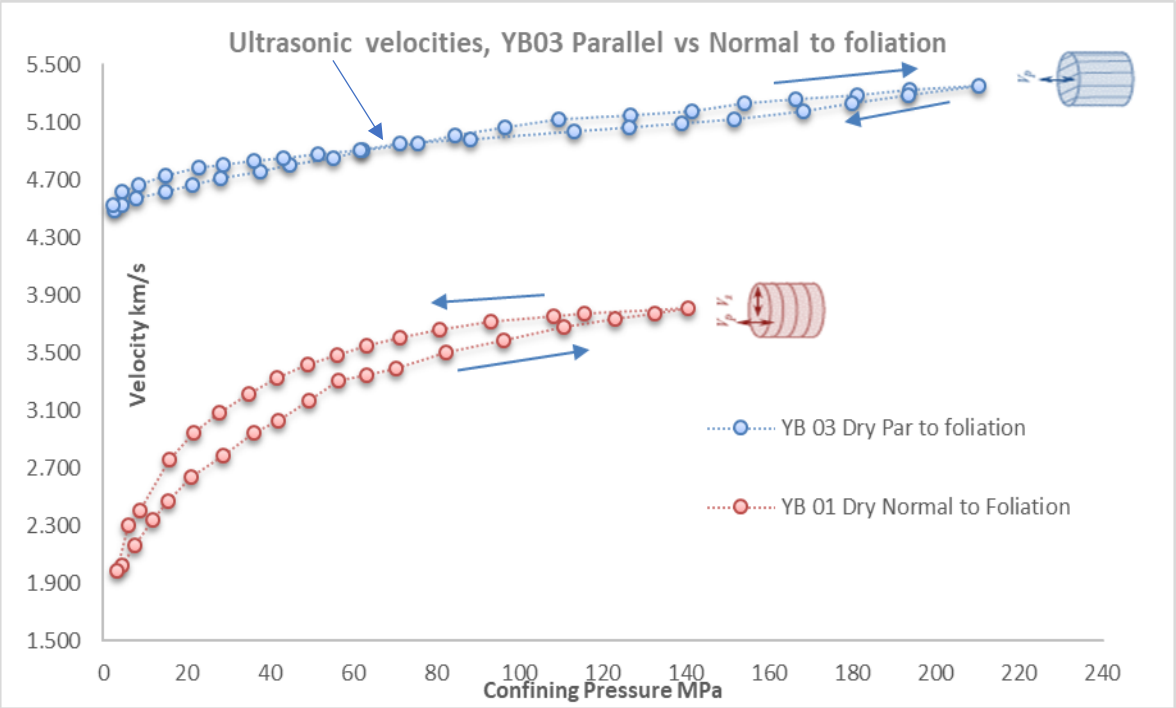

Figure 6.2 Ultrasonic P-wave velocity measurements plotted against confining pressure of two samples, YB01N and YB03P (2nd pressure cycle) tested dry with no pore pressure, wave direction normal to bedding and parallel to bedding, respectively. Response was hysteretical in both cases. Direction of load increase and decrease is shown for each case, but the hysteresis response is different in each case.

This behaviour of YB03P (a carbonate-rich shale) is in contrast to that of YB01N (a clay-rich shale) (Fig. 6.2). The latter displays much slower velocities, spread over a larger range than YB03P. This is typical of foliated rocks, for which normal-to-foliation velocities are slower, are particularly affected by oriented cracks parallel to layering, and a larger range of pressure is required to close cracks and cause stiffening. Wave propagation along foliation is relatively uninfluenced by cracks parallel to layering.

Hysteresis is different too. Unlike YB03P, the pattern of behaviour is typical of other rocks, with the offloading curve displaying higher velocities over the whole pressure range.

6.1.2 Pore Pressure effect on V_p

After the initial multiple measurements of YB03P at zero pore pressure, cycling five times over the full range of total confining pressures, measurements were made at a succession of increasing argon gas pore pressures, until pressure cycle #10 was again at zero pore pressure. An 11th cycle was performed at 34.5 MPa pore pressure also. Pressure cycle #5 was the same as #10 within experimental error.

Use of gas as a pore fluid minimises problems that might arise with a more viscous and less compressible pore fluid such as water, in which pore volume changes during pressure cycling might induce pore pressures if the fluid cannot flow into or out of the specimen during the time scale of the experiment. Gas pore pressures of 10.3 MPa, 34.5, 48.1 MPa, and 67.7 MPa were used, with confining pressures ranging up to 200 MPa. Both up-pressure and down-pressure velocity data were recorded with each constant value of pore pressure in the sample. The sequence of pore pressure conditions is listed in Table 6.1, but for ease of reference the first 11 cycles are re-stated here:

Pressure cycle #	Pore pressure (MPa)	Pressure cycle #	Pore pressure (MPa)
1	0	6	34.5
2	0	7	67.7
3	0	8	48.1
4	0	9	10.3
5	0	10	0
11	34.5		

Application of pore pressure shifts the curve of velocity vs total confining pressure to the right, shown in Fig. 6.3), as expected according to the principle of effective pressure. Only the up-pressure parts of each cycle are shown in this figure for ease of comparison. Pore pressure is expected to reduce effective confining pressure by all or part of the amount of the pore pressure, thus the pore pressure in the sample tends to counteract the confining pressure effect.

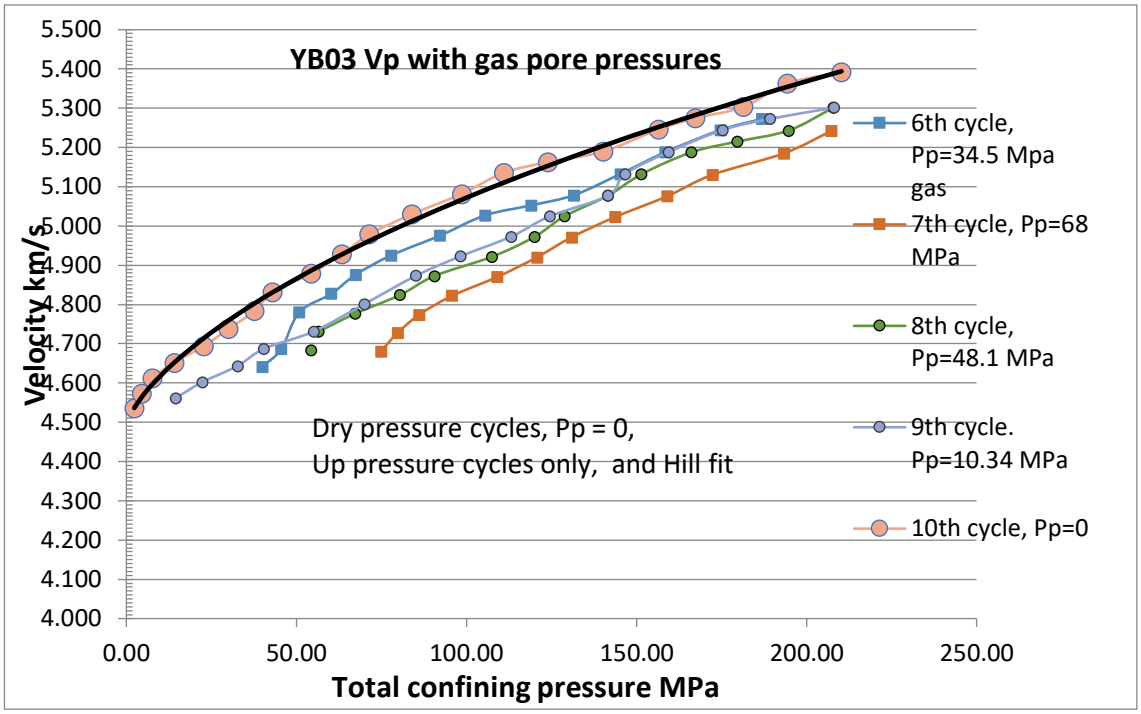

Figure 6.3 Up-pressure cycles (sample YB03P, dry) showing influence of increasing values of argon gas pore pressure on P-wave velocities relative to zero pore pressure behaviour, plotted against total confining pressure. The p_p=0 curve is shifted progressively to the right as pore pressure is increased. The zero pore pressure data are also shown fitted by a Hill function (see text).

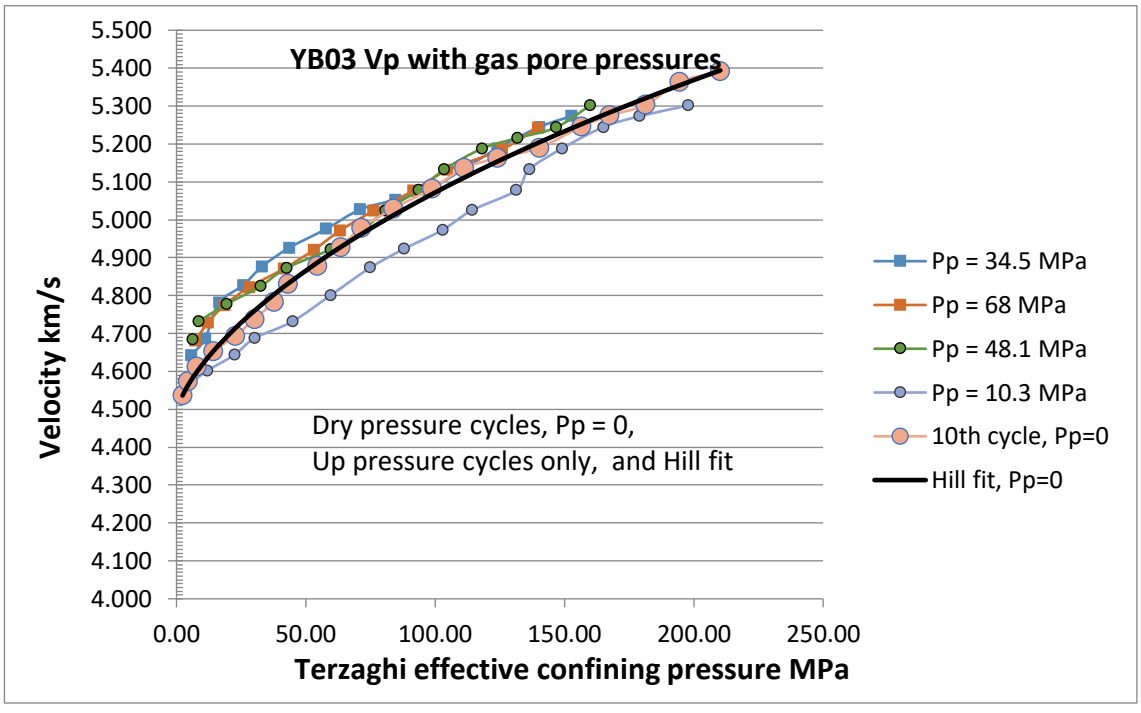

Figure 6.4 Up-pressure cycles (sample YB03P, dry) showing influence of increasing values of argon gas pore pressure, with V_p plotted against Terzaghi effective pressure $(P_c - nP_p)$, with assumed n = 1. At low pore pressure there is under-compensation whilst at higher pore pressures the pore pressure over-compensates for the confining pressure.

Fig. 6.4 shows the same data as in fig.6.3 but plotted against Terzaghi effective pressure. If the pore pressure rule $P_{eff} = (P_c - nP_p)$ applies with n = 1 all the curves should overlie one-another. However, the pore pressure undercompensates in the case of the 10 MPa P_p data (which appear anomalous) and overcompensates in the case of the other pore pressures. As pointed out in Chapter 4, the anomalous pore pressure unlikely to arise from pore pressure fluctuations arising from elastic expansion or compression of pore spaces due to changes in confining pressure during pressure cycling, owing to the high compressibility of the gas pore fluid.

6.1.3 Analysis of the pore pressure effect on P-velocities

The experimental data above show that increasing pore pressure shifts the velocity $= f(P_{total})$ curve to the right and suggests that the effective confining pressure takes the form.

$$P_{eff} = (P_{total} - n^* P_p) \qquad Eqn. 6.1$$

(Geertsma, 1957; Skempton, 1960), so that velocity = $f(P_{eff)}$. n^* is a number on the order of 1 which describes the extent to which the effective confining pressure is reduced. When n^* = 1 Eqn. 6.1 becomes the Terzaghi effective pressure law, but in detail n^* itself may depend on effective pressure. The value of n^* is also expected to depend on the physical process being described. It may be different for describing elastic strains, rock failure and frictional sliding, for permeability and for elastic wave velocities. Many descriptions of the effect of pore pressure on elastic wave velocities have been offered (Christensen, 1984; Eberhart-Phillips et al., 1989; Mavko & Vanorio, 2010; Todd & Simmons, 1972). Mavko and Vanorio (2010) have shown that n*<1 can arise from the effects of frequency-dependent dispersion, which has the effect of raising ultrasonic velocities relative to velocities at low (seismic) frequencies. The aim of this section is to describe how the observed value of the pore pressure coefficient n^* varies with effective pressure for these velocity measurements on Haynesville shale.

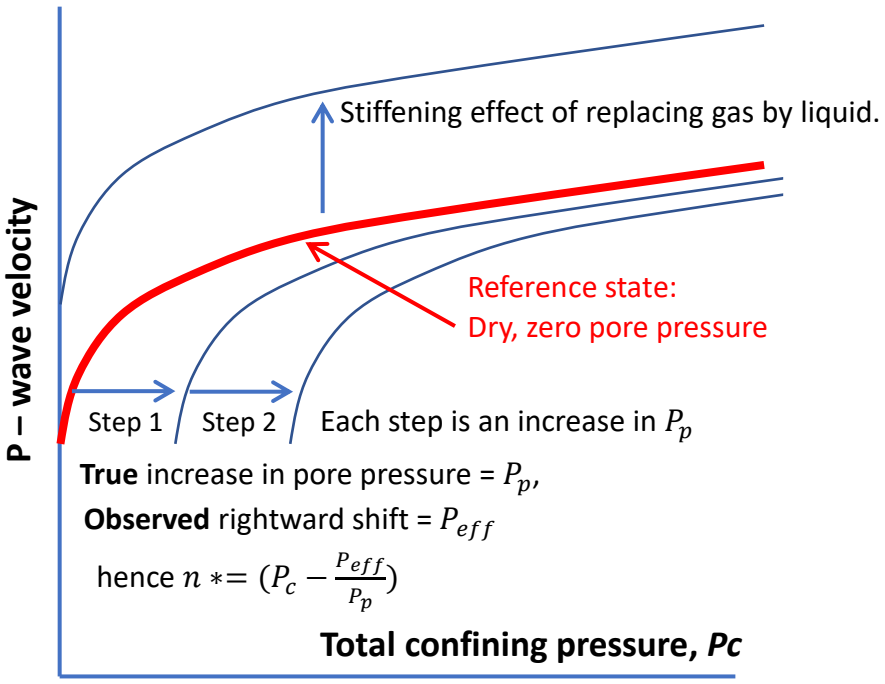

Figure 6.5 Schematic illustration of the definition of n from experiments with and without pore pressure. Also shown is the effect expected (at zero pore pressure) when gas in the pore spaces is replaced by a (stiffer) liquid (the Gassmann effect).*

From $n^* = (P_c - \frac{P_{eff}}{P_p})$ where $P_c - P_p$ is the Terzaghi effective pressure and P_{eff} is the *apparent* effective pressure. P_{eff} is equal to the measured lateral separation of the velocity curves for P_p=0 and for the applied P_p at the same ultrasonic velocity. To obtain P_{eff}, therefore, the values of the separation pressure of the two curves must be measured at the same velocity (Fig. 6.5). This requires interpolation between the discrete points of $V_{p=}f(P_c)$ measured at zero pore pressure. If the data are not too scattered, this can be done by linear interpolation between data points, or it can be done by fitting a continuous function to the P_p = 0 velocity data.

Simple functions such as logarithmic or power functions cannot adequately describe the variation of curvature of $V_p = f(P_c)$ typical of data for real rocks, but the Hill equation is an empirical relationship devised originally for 4-parameter description of drug uptake kinetics (Somvanshi & Venkatesh, 2013). It is also well-suited to describing velocity as a function of pressure data (Taylor et al., 2015)

$$V(P) = V1 + \left[\frac{(V2 - V1)s}{(k^s + P^s)}\right] \qquad Eqn.6.2$$

V1 = Ordinate intercept (V at *P* = 0): Note: *k* is not the same as permeability.

P = total pressure; V2, k and s are parameters to be determined.

k = *P* at V = (V2 + V1)/2

Rearranging eqn. 6.2, we obtain an alternative expression, with *P* as independent variable:

$$P = \left[-k^s \frac{(V-V1)}{(V-V2)}\right]^{1/s} \qquad \text{Eqn. 6.3}$$

Acoustic velocity data tend to show monotonically decreasing curvature with increasing pressure, and good fits can usually be obtained. However, the 10th cycle at zero pore pressure provides the most reproducible curve (Figs. 5.19 and 5.20). The Hill fit represents the data well, and although the data residuals are not perfectly randomly distributed about the best-fit curve, the scatter is far less than the variability of the data points in the higher P_p datasets.

The Hill fit can conveniently be made by non-linear least squares fitting using the Solver add-in in MS Excel, or via other data analysis packages, such as in MATLAB or in Origen. The best-fit parameters obtained here are:

V1	4.489 km/s
V2	9.360 km/s
k	1752
s	0.697

Standard error of fit on velocity (km/s) = ±0.003

This is the formulation required for determination of the pressure-separation of the P_p = 0 and P_p > 0 velocity curves, with each pair of points at the same value of velocity. Recall that by definition $n^* = (P_c - \frac{P_{eff}}{P_p})$. $P_c - P_{eff}$ is the separation of the velocity curves for P_p =0 and P_p >0, therefore from the Hill fit at P_p = 0 and the data for a particular pore pressure at the same velocity, we can plot *n** as a function of either total P_c or Terzaghi effective pressure. This is done in fig. 6.2 for Haynesville shale YB03p, in the layer-parallel orientation, using velocity data at two pore pressures, 67.7 and 48.1 MPa. Data from the velocity curves at P_p= 10.34 and 34.5 MPa are not shown, because pressure difference measurements at low pore pressures are smaller and hence very susceptible to scatter in the data. Errors of measurement become less significant as P_p increases.

The *n** value is approximately 0.8 across the whole range of effective pressures, thus the behaviour is as if the pore pressure is not fully effective. (Fig. 6.2). This

representation of the data is simply a way to describe what is observed. There is no physical theory involved.

Fig. 6.2 also shows the variation of *m,* with Terzaghi effective pressure over the same range. Recall that *m* is the pore pressure parameter derived (Walsh, 1965 and Mavko & Nur, 1978) to describe how the elastic distortions of a porous solid vary with pore pressure (Eqn.5.9, Chapter 5.6). This parameter decreases strongly with effective pressure and displays a clearly quite different behaviour to *n**.

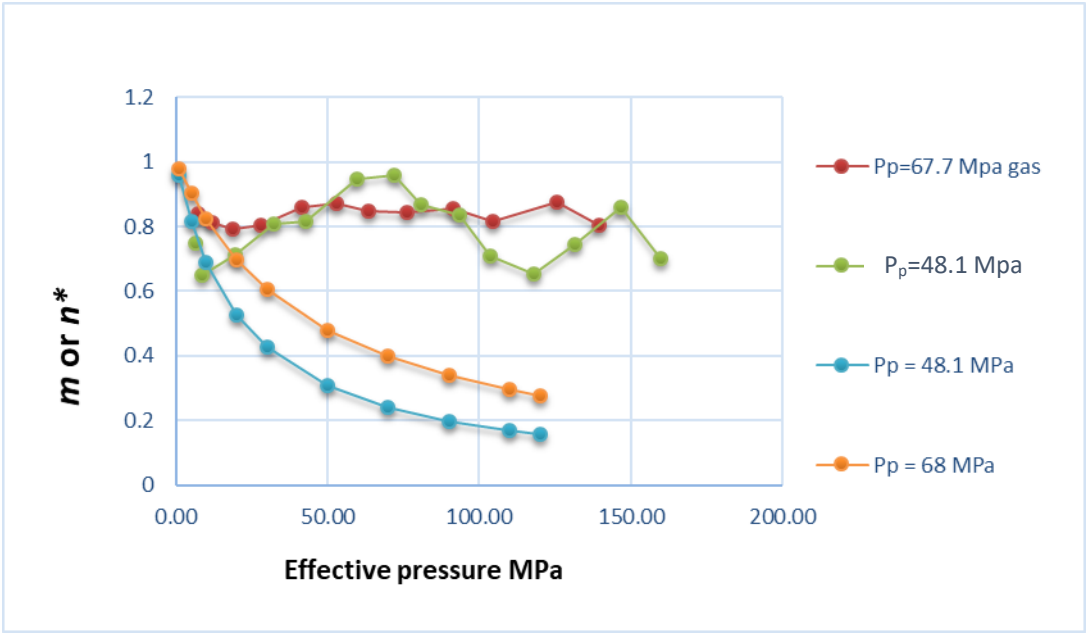

Figure 6.6 Plot of n and m–values against Terzaghi effective pressure for Haynesville shale YB03 in the layer parallel orientation. These parameters are both pore pressure coefficients. The upper two groups of data (n*–values) were obtained from the lateral separation of the acoustic velocity versus total confining pressure curves for P_p = 0 minus data at 67.7 and 48.1 MPa pore pressures (gas). The lower two groups of data (m–values) were derived from the pore volumometry data at the same pore pressures.*

6.2 Three different pore pressure coefficients – summary so far.

The above experimental results, investigating the role of pore pressure on the pressure sensitivity of permeability and acoustic velocities, have demonstrated three different pore pressure coefficients, acting as multipliers of pore pressure, and taking different numerical values. These are:

a) Parameter *n*, (Chapter 5.2. eq. 5.1) which describes how increasing pore pressure influences permeability via its influence on the effective stress state in the rock. Its value for Haynesville shale (specimen YB03P) is 1.1 and it does not appear to vary with Terzaghi effective pressure.

b) Parameter *m*, which describes how pore pressure affects the elastic bulk modulus of a porous solid, and hence how the shapes of pores change with pressure. This was obtained from pore volumometry measurements and is very sensitive to Terzaghi effective pressure.
c) Parameter *n**, which describes how pore pressure influences the stiffness of the rock matrix and hence how it transmits elastic waves. It does not appear to be sensitive to the magnitude of effective pressure.

It was initially suspected that there might be commonality between these parameters, and hence that, for example, measurements of the elastic wave velocities in porous rocks might facilitate computation of the permeability of a rock and its pressure sensitivity. The implications of the experimental results for this question will be addressed in the Discussion, Chapter 7.

As pointed out earlier, Geertsma (1957) & Skempton (1960) proposed the following relationship between the effective pressure coefficient *m* and the bulk moduli $k_{dry}\ and\ K_o$

$$m = \left(1 - \frac{K_{dry}}{K_0}\right) \qquad Eqn.6.4$$

for the description of the poroelastic behaviour of porous rocks, and this was shown to be exact by Nur & Byerlee (1972). K_o would be expected to be relatively insensitive to confining pressure, but k_{dry}, which incorporates the compression of the pore space would be expected to be initially small and to increase with pressure as the porous matrix becomes stiffer.

6.3 Influence of liquid saturation on V_p

After the V_p measurements had been made on the dry rock, and also the argon gas pore pressure measurements, the *same* Haynesville shale YB 03P sample was vacuum saturated with water for 3 weeks in order to determine the effect of water saturation on V_p.

From the initial volume of the sample and the weight gain on vacuum saturation, the water take-up into the sample was estimated to have been ~80% of the pore space volume.

Because shales often tend to expand and disaggregate on wetting, the sample was held in a section of heatshrink sleeving. The pressurisation was taken to about 140

MPa confining pressure. It was observed V_p was substantially decreased when compared to the dry sample results. (Fig 6.2). This observation was *strongly counter* to what was expected as a result of replacing the gas in the pore spaces with stiffer water. According to the Gassman effect (see discussion below), replacing pore-filling gas by a liquid should raise bulk modulus and hence velocity. However, it was also noted that V_p appeared to increase with time. Therefore, the sample was left at 97 MPa confining pressure for 100 hours whilst monitoring V_p. The V_p increased rapidly at first (fig 6.7) and then more slowly, rising from 4.35 km/s to 4.72 km/s, which is commensurate with the V_p of the dry sample.

Fig. 6.7 shows the effect of the pressure cycles on V_p of the water saturated sample. With each subsequent pressure cycle the velocity increased markedly. Additionally, each cycle was markedly hysteretical, with the down pressure steps markedly faster than the up-pressure part of the cycle.

The observed behaviour seems to imply that fluid within the pores initially could not escape as a result of pore pressure generated by elastic compaction of the pore/crack space. As we have seen with the effective pressure effect data described above, generation of pore pressure should decrease V_p. Yet we see an increase in velocity with time as the excess P_p is dissipated. Thus, it is inferred that these effects are due to the progressive and cumulative expulsion of pore water from the sample, progressively reducing the capacity for generation of pore pressure with each increase and decrease cycle of confining pressure. This implication of these results is that it is near-impossible to carry out experiments on a tight rock such as shale involving liquid pore pressure in a reasonable period of time.

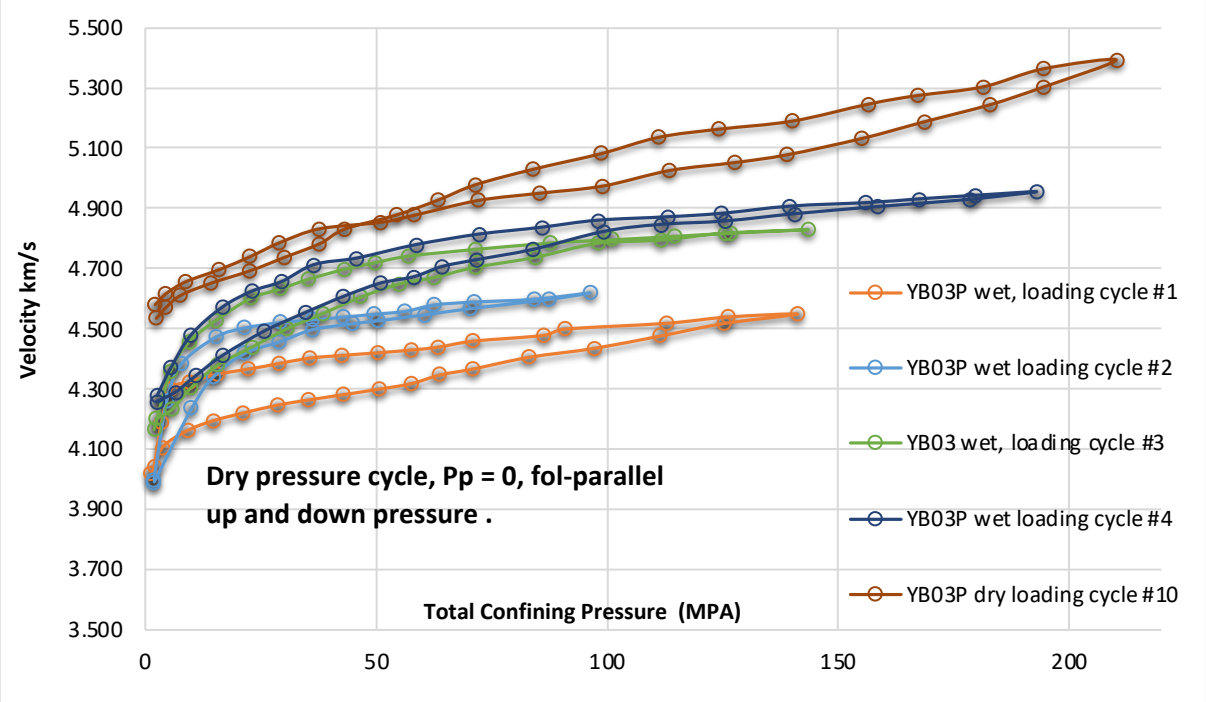

Figure 6.7 Results of velocity measurements on sample YB03P after vacuum water saturation (4 pressure cycles) and compared with previous dry test (cycle #10) on the same sample. The wet tests are substantially slower than the dry test, and successive pressure cycles wet produced substantial increases in velocities.

All of the above experiments on seismic velocity measurements on Haynesville shale were carried out on the dry rock both without and with pressurized argon gas in the pore spaces. The final runs on sample YB03P were carried out with the pore spaces saturated with water (Fig.6.7 and listed in Table 6.1)

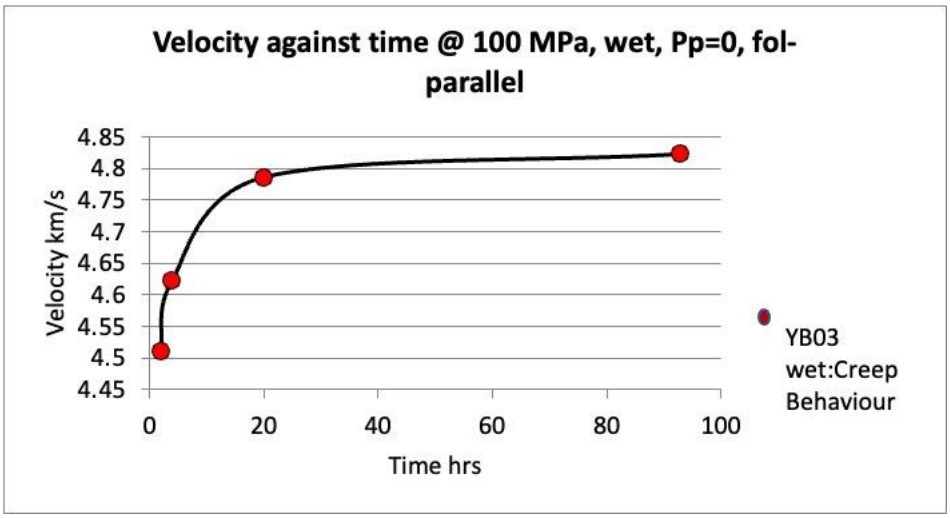

Figure 6.8 Plot of velocities recorded from sample YB03P at 100 MPa confining pressure versus elapsed time on the up-pressure part of the cycle.

The sample used was physically the same one as had been used for all previous dry and with argon pore pressure tests. It had been subjected to 11 pressure cycles. Water saturation would render the sample useless for any drier tests therefore was left until last. The sample was evacuated in a desiccator for one day, and the vacuum was broken under water. The sample was left to soak for three weeks thereafter. The take-up of water was measured to be 0.077 g, representing only 0.85% of the rock volume, or only about 10% of the total porosity. This is perhaps not surprising given the low permeability of this rock and the viscosity of water. Saturation of clay-bearing rocks like shales also typically leads to swelling by the opening of microcracks, and in extreme cases disaggregation of the rock can occur, although this sample did not fail in this way.

Fig. 6.7. shows the behaviour of the wetted rock through 4 pressure cycles, and is compared with the behaviour of the dry rock reported previously. The velocities are substantially reduced, the pattern of up- down- hysteresis changes to the more 'normal' type (down-pressure velocities are always faster), and the rate of increase of velocity with total pressure is much less than when tested dry. To emphasise the effect of successive pressure cycles after different amounts of time Fig. 6.8 shows velocity at 100 MPa confining pressure plotted for the four successive pressure cycles, and hence after different elapsed times. Velocity appears to 'settle' at about 3.86 km/s, although this is much less than at the equivalent pressure for the dry rock.

Replacing gas in the pore spaces by a liquid, which is much less compressible, is normally expected to cause an increase in P-wave velocity because the fluid contributes to the overall bulk modulus of the rock (the Gassman effect, Han & Batzle, 2004). In this case, however, the poor uptake of water into the pore spaces implies that little if any velocity increase might be seen. The observed substantial reduction in velocity is considered attributable to reduced bulk modulus arising from the swelling of the rock on wetting. There may also be a contribution from the generation of internal pore pressure as pore compaction occurs. This would be favoured by the low compressibility of water combined with its high viscosity, making drainage difficult in the time frame of the experiment (Zimmerman, 1991). The low rate of increase of velocity with pressure suggests that some degree of pore pressure generation may be occurring, thereby reducing velocity, although this is speculative. There may also be enhancement of stiffness through progressive expulsion of water from pore spaces

as a result of pressure cycling. The form of the velocity versus time plot (Fig. 6.8) is also suggestive of time-dependent creep occurring, increasing the bulk modulus through compaction enhanced by the chemical interaction between water (a polar liquid) and clay minerals, which carry free surface charges.

These experimental results point to the difficulty of carrying out meaningful experiments on tight rocks such as shales with a liquid pore pressure, or even simply liquid saturated. Further study of this point lies beyond the scope of this thesis.

Chapter 7 – Discussion

The purpose of this chapter is to discuss points arising from (a) the programme of experimental studies themselves and (b) to explore the wider implications of these results.

Permeability – Exact permeability-stress relationships for a shale gas reservoir in mudstone are best obtained using core plugs of the mudstone tested in a high-pressure apparatus. In this study the in-situ conditions were successfully simulated in the laboratory using such equipment. Sensitivity of permeability to both pore and confining pressure at depth can be measured after an initial pressure cycle to 'repair' the damage through microfracturing incurred during core recovery and preparation for testing.

For unconventional reservoirs, where the pore throat diameters are sub-micron in size, changes in effective pressure demonstrated herein can have an exceptionally large effect on permeability because the pore throats are easily closed by effective pressure. It is important to take into account the pressure-sensitivity when interpreting reservoir models. When it is ignored there will be an overestimation of permeability, original gas in-place, and hence an erroneous estimate of gas reserve estimation (Rutter et al., 2013b; Mckernan et al., 2014). The permeability/ effective stress law is important when modelling reservoir behaviour.

In the lifetime of any reservoir, from first oil to peak production, pressure drawdown increases effective pressure, leading to a decrease in permeability, depending on the drive mechanism of the reservoir. The sensitivity of the rock to confining pressure and pore pressure will determine how rapidly the drawdown occurs. If the rock is more sensitive to pore pressure than confining pressure, then the draw down will be faster than would be predicted from a simple Terzaghi effective stress law. In the case of Haynesville shale, the rock is equally sensitive to both confining pressure and pore pressure as shown in results chapter 5.

7.1 Influence of effective pressure on permeability of Haynesville shale

7.1.1 Comparison of data within the Haynesville shale dataset

The permeability of four specimens of carbonate-poor shale (YB 02, 04, 05 and 08) were measured over a range of Terzaghi effective pressures up to 50 MPa, and one specimen of carbonate-rich shale (YB 03) was studied in rather greater detail up to 100 MPa effective pressure. In all cases the first cycle of increasing effective pressure was followed by a reproducible pattern of variation of log*(k)* with effective pressure, implying elastic constriction and reopening of pore spaces through successive pressure cycles. Fig 7.1 shows this behaviour.

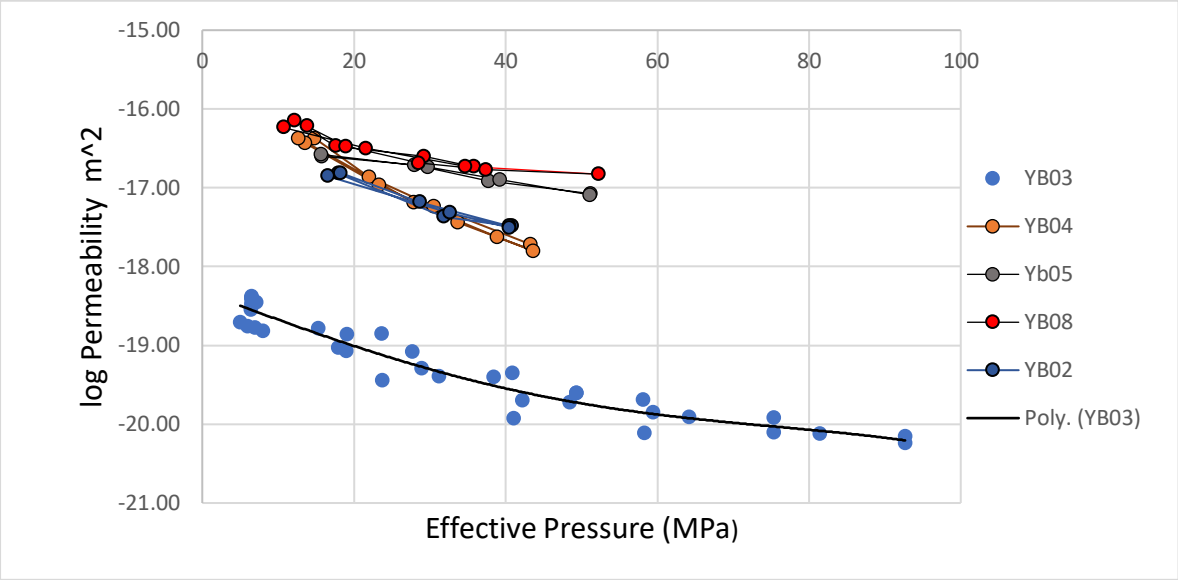

Figure 7.1 Summary of the results of permeability measurements versus effective pressure for the specimens that were subjected to pressure cycling. These data are all from the second and subsequent pressure cycles. YB03 data are from tests on the BigRig (with effective pressure coefficient = 1.1) and the remainder from tests (to lower pressures, with effective pressure coefficient = 1.0) on the CoreTest rig. The upward concavity is evident best in the YB03 data but can also be seen in the other data. Because YB03 was taken to higher pressures, the curve has become lowered by about one order of magnitude in log(k).

Sample YB03 (Parallel to bedding) displays data over the wider pressure range available on the BigRig, but the upward concavity in the data is apparent in all data. YB03 is a carbonate-rich sample, compared to the others that are carbonate-poor. The YB03 data will have been reduced to lower log*(k)* values by about one order of magnitude as a result of being exposed to a higher-pressure range, but it would still have displayed a lower overall permeability than the carbonate-poor rocks.

It was suspected that through its cementing qualities (i.e., YB 06), carbonate-rich shales within the Haynesville shales might be systematically tighter than carbonate-poor shales. The above results are consistent with that pre-supposition, but data coverage turned out to be poorer than initially expected, therefore it is impossible to offer this as a general conclusion within the experimental time frame.

YB04 and YB05 show a lower rate of decrease of permeability with increasing effective pressure than YB02 and YB08, which are comparable in this respect to YB03. There is no immediately apparent reason for this in their mineralogical compositions. It should be reflected in their respective pore compressibilities, but unfortunately such data was only obtained for YB03.

Permeability Anisotropy

Permeability anisotropy is a measure of the relative ease of flow along the layering compared to across it. The sample oriented for flow parallel to bedding displayed greater reduction of permeability with pressure than the sample normal to bedding as shown in figure 5.11, although the numeric values of permeability were not greatly different. One aspect of anisotropy reported is the apparent substantial difference between the amount of porosity in the two orthogonal orientations. This may negate the influence of differences in the lengths of flow paths between the two orientations. One contributing factor to behavioural differences is the sample length, a shorter sample was used in the layering-normal orientation, thereby reducing the effective mean pressure by 20% relative to the applied confining pressure, as a result of frictional stresses induced at the sample/piston interfaces. The short sample mean stress will be less than the applied hydrostatic stress, leading to a potentially higher flow this reason in the longer sample, perhaps tending to reduce the apparent anisotropy.

7.1.2 Implications of the range of permeabilities observed with effective pressure variation.

The YB03 data shows a variation of 2 orders of magnitude in permeability over the range of effective pressures likely to be encountered in a shale gas reservoir, and this also applies to the range of pressures that might be encountered in the cap rocks over reservoirs to be used for gas storage, whether of CO_2, compressed air, or hydrogen.

Other shales show different degrees of sensitivity of permeability to effective pressure. Fig, 5.3 shows for comparison a very large degree of pressure sensitivity displayed by a rock from the Bowland shale sequence, with 3.5 orders of magnitude in log(*k*) over the range of reservoir pressures (~80 MPa). In contrast, Pennant sandstone (a tight gas sandstone with intergranular spaces filled by clay minerals), data for which is also shown in Fig.5.3, displays only about 0.75 order of magnitude variation in log permeability over the same pressure range. Open textured sandstones tend to display least pressure sensitivity (Hasanov et al., 2019). It is noteworthy that with increasing effective pressure, permeabilities tend to diverge, so that initially small permeability differences at low pressures become extremely pronounced at higher pressures.

Fig. 5.12a shows for sample YB03 the accumulation of volume strain of the pore spaces with effective pressure, from pore volumometry measurements. From these measurements, the variation with pressure of the bulk modulus of the whole rock K_{dry} was obtained. K_{dry} rapidly increases with pressure, then more slowly, and should asymptotically approach the value of the bulk modulus of the grains as it would be if there were no porosity present (61 GPa, from V-R-H averaging based on the elastic moduli of the constituent minerals). Volumetric strains measured are ~0.002 at *ca* 140 MPa effective pressure applied. This corresponds to only *ca* 2% of the total pore space, which is in turn 9% of the total volume of the rock, and results in apparent K_{dry} rising to a high fraction of K_0. When $K_{dry} \rightarrow K_0$ it implies total collapse of the pore space has occurred, but in the case of the shale this is far from happening because the pressure cycling behaviour is elastically recoverable and because the amount of fluid expelled is such a small fraction of the total volume of the pore space.

As pointed out in section 5.6, the parameter $m = (1 - \frac{K_{dry}}{K_0})$ determines the stiffness of the pores in a rock and hence how they constrict elastically under applied hydrostatic pressure (Walsh, 1965; Mavko & Nur, 1978), and this in turn is expected largely to determine the pressure sensitivity of permeability. A rapid decrease in *m* with effective pressure, such as is shown by YB03, results in sufficient constriction of the width of the crack-like pores lying parallel to layering to produce a large reduction of permeability without a large reduction in porosity. It is striking that virtually all the permeability data plots presented herein show upward concavity, and that this is in

accord with the progressively decreasing rate of change of K_{dry} with higher effective pressures.

Although accompanied by a large amount of experimental uncertainty, a pore width of only a few nanometres is required to explain the characteristics of slip flow in this rock (Chapter 5, section 5.7). (Ma et al., 2018), working on Haynesville shales sampled from the same core section as used in this study, was able to image for the first time, using scanning/transmission electron microscope tomography, the connected pore arrays on the order of only 10 nm diameter. In contrast, larger pores in shales, accounting for most of the porosity, generally tend to appear isolated or poorly connected.

7.1.3 Pore space storativity and pore volumometry

An important result of this work using the oscillating pore pressure method to measure permeability arises from the determination of storativity of the specimen, and the fraction of the pore space volume that it represents (chapter 5, fig. 5.10). (from Rutter, Mecklenburgh and Bashir, 2022) The storativity shows a directional dependence and is greater for flow normal to the layering than for flow parallel to layering. Both measures of the volume fraction involved in the flow are, however, small compared to the total porosity. For flow parallel to the layering the storage volume corresponds to only 3% of the pore volume (fig. 5.10), and to 18% of the pore volume for flow normal to the layering. Thus, only a small fraction of the pore space is connected for through-flow, although the remainder is probably blind-ending but is accessible for gas storage (Fig. 7.2). Fundamentally the same model for a dual-porosity structure of shales was deduced by Mckernan et al. (2017) as shown in fig. 5.10.

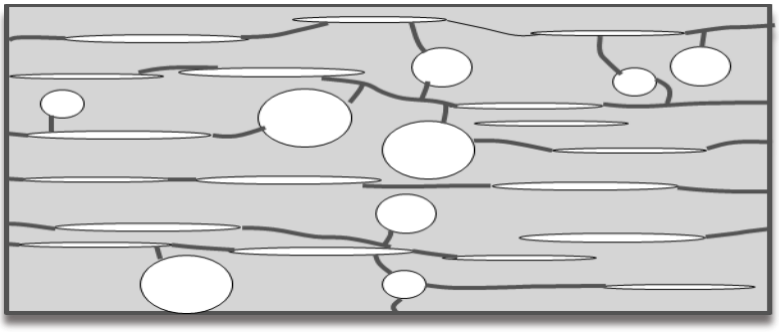

Figure 7.2 Schematic illustration of the deduced dual-porosity microstructural geometry controlling flow through the shales. Networks of laterally connected but very thin pore spaces occur parallel to the layering, poorly linked to more equant and/or occluded pores that account for most of the porosity and hence total storativity.

From the above it must be inferred that the pore volumometry as measured in this study may only measure the compressibility of the fraction of the pore space that takes part in the transport of the fluid into and out of the specimen, and that the derived K_{dry} is an *apparent* value. With full connectivity of the pore space, K_{dry} measured via pore volumometry should correspond to the bulk stiffness of the rock measured externally to the specimen, for example via strain gauges (Hasanov et al., 2019). Therefore, future work must test the extent of this correspondence for shales. Whilst measurements of the characteristics of permeability in shales results in the conclusion that only a small amount of porosity is involved in pore fluid flow, this cannot be true for acoustic velocity measurements. The passage of elastic waves through a specimen 'sees' all of the pore space because collectively it determines the bulk stiffness characteristics of the specimen. The velocity of *P*-waves through an isotropic specimen is related to density (ρ) and stiffness by

$$V_p = \sqrt{\frac{K + \frac{4}{3}G}{\rho}} \qquad Eqn.\,7.1$$

Where K is bulk modulus (K_{dry}) and *G* is shear modulus. Unfortunately, in this study, because S-wave velocities were not measured there is no basis for determination of elastic moduli from velocity measurements. Further, given the issues identified with the measurement of bulk modulus by pore volumometry, it is possible that this bulk modulus may not correspond precisely to bulk modulus measured from outside the specimen.

7.2 The effective pressure law and the relationship between permeability and acoustic velocity data

In section 5.8 it was shown that three different pore pressure multipliers in the expression for effective confining pressure could be identified in the present study. All of these parameters appear in the expression for effective pressure $P_{eff} = (P_c - MP_p)$, where *M* is the relevant pore pressure multiplier (below).

Parameter *n* (Chapter 5.2, eq. 5.1) describes how pore pressure reduces the effective confining pressure and hence permeability of porous rocks (Zoback and Byerlee, 1975; Kwon et al., 2001; Mckernan et al., 2017). The value of this parameter can vary from less than one to more than one. Zoback and Byerlee (1975) interpreted the variation in terms of the pore structure and relative compressibilities of the various

minerals in the rock. For pure quartz sandstones or any single-phase aggregate $n \leq 1$, whereas for a rock consisting of a strong framework of contiguous quartz or carbonate but with the pores lined with more compressible clay minerals the pore sizes may be more sensitive to the compression of the clays by the pore fluid that to the elastic constriction of the granular framework by the effective confining pressure, such that $n > 1$. Sample YB03P in this study returned a value $n = 1.1$, whereas for the other samples YB02, 04, 05 and 08, for which values were obtained, n was close to 1 (fig. 7.1). the value of n does not appear to vary with effective pressure, i.e. it is an independent parameter.

Parameter $m = (1 - \frac{K_{dry}}{K_0})$ is the pore pressure coefficient that describes how the elastic *distortion* of a rock is affected by pore pressure, and hence how the shape and size of pores are affected. Because it depends on K_{dry}, which increases with pressure, it is pressure sensitive. It was shown to be an exact description of how pore pressure affects elastic distortion by Walsh (1965) and Mavko & Nur (1978).

Parameter n^* was obtained as an effective pressure parameter to describe by how much elastic wave velocities are reduced by increasing pore pressure. Values of n^* are frequently used in the estimation of in-situ formation pore fluid pressures, with varying degrees of reliability (Bahmaei & Hosseini, 2020; Bowers, 2002; Haris et al., 2017; Strout & Tjelta 2005). In specimen YB03P, $n^* = 0.8$, independent of effective pressure over a range of 150 MPa (Fig. 6.2). The elastic stiffness is the parameter that dominates P-wave velocity. The reduction of the effective pressure therefore reduces the rock stiffness and displaces the velocity/pressure curve downwards. The value of n^* is also expected to vary with wave frequency, decreasing as frequency increases from seismic to ultrasonic frequencies (Mavko and Vanorio, 2010).

One of the initial premises of this study was that there might be identifiable interrelationships between the effective stress parameters for permeability and acoustic wave velocity. It has not been possible to demonstrate any such relationships. The way that pore pressure affects overall rock stiffness, leading to reduction in acoustic wave velocity, irrespective of its influence on the shape and size of pores is not the same as its effect on permeability, where the shape and size of the pore spaces change in response to the externally applied pressure and also in response to the influence of pore pressure on the geometry of the interior of pores.

In the case of permeability, the distortion of pore shapes depresses the permeability/effective pressure curve increasingly as effective pressure is increased, whilst also influencing the effective stress state on the rock and displacing the permeability curve to the right as pore pressure is increased.

Measurements to test the sensitivity of permeability to Terzaghi effect was carried on sample YB 03 at a constant pore pressure of 10 MPa. The relationship between the permeability and effective pressure was defined, it was fitted to an exponential law from Eq. 5.3, and the fit is shown in Fig. 7.3.

$$k = k_0 \exp(\gamma P_{eff}) \qquad Eqn. 7.2$$

k_0 - Permeability at zero effective pressure

γ – is a pressure sensitivity coefficient

P_{eff} –effective pressure

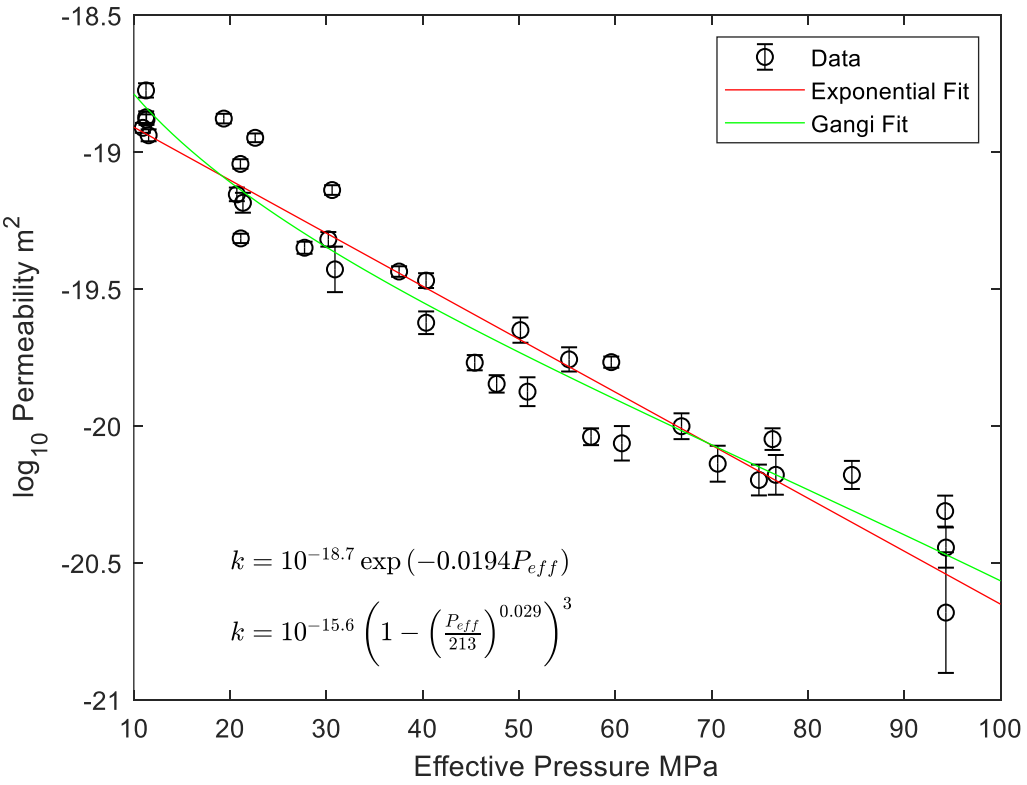

Figure 7.3 Permeability plotted as a function of effective pressure at a constant pore pressure of 10 MPa fitted to an exponential law and the Gangi model (power law) fit.

The sample YB 03 showed moderate sensitivity which gives a value γ = -0.0194. The permeability and effective pressure relationship can also be described empirically using a power- law as thus:

$$k = k_0 = \left(1 - \frac{p_{eff}}{f}\right)^n \qquad Eqn.7.3$$

which has the merit of capturing the upward concavity in the data. It has been suggested that the exponential law is mostly applicable to experimental data while the power-law is most suitable in geological flow models (Bustin et al., 2008; Cui et al., 2009), although this depends on the pressure range over which the data extend and the magnitude of the pressure sensitivity for a particular rock type. Gangi (1978) introduced some empirical equations based on measured reservoir rock properties. Both the exponential law and power law provide transformation equations from exponential fit parameters to parameters for the Gangi models.

7.3 Influence of Porosity on Permeability

In chapter 5, Fig. 5.2, it was established that within the constraints of the present experimental study, no systematic effect of porosity on permeability could be detected. Whilst permeability is relatively difficult to measure, porosity is relatively easy. Therefore, there has long been a desire to establish reliable theoretical interrelationships between these quantities. The most commonly used semi-empirical relationship of this type is the Kozeny-Carman relationship (Carman, 1937), which in its simplest form is.

$$k = \frac{\emptyset^3}{(1-\emptyset)^2 S^2} \qquad Eqn.7.4$$

where *S* is the specific surface area of the granular material (Xu & Wu, 2008).

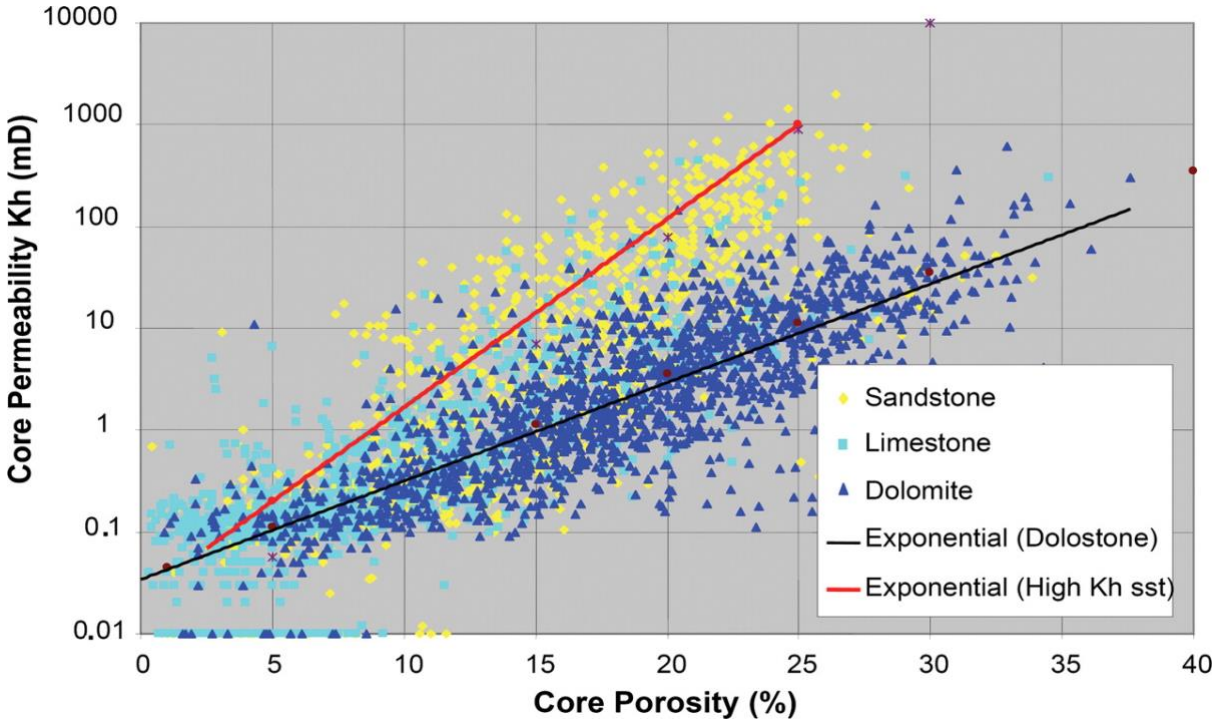

Figure 7.4 log permeability versus porosity organized by lithofacies from a mixed clay-bearing carbonate-siliciclastic reservoir in Offshore Congo (Wonham et al., 2010). Observed variability in the samples of Haynesville shales reported here would fit into one of the squares on this figure, therefore it is not surprising that no trend is evident (in Fig. 5.2)

There are many variants on this equation, including the further simplified form.

$$k = C\emptyset^3 d^2 \qquad Eqn. 7.5$$

in which d is grain size and C is an empirical constant on the order of 1/500.

There have been many studies seeking such relationships in the context of specific formations (e.g., Wang et al., 2019; Ojo et al., 2018). Fig.7.3 shows measured porosity/permeability relationships from a mixed clay-bearing carbonate-siliciclastic reservoir, with the data organized by lithofacies (Wonham et al., 2010). These results are typical of such studies. The porosity/permeability range is large enough to show the trends, but also there are sufficient data to demonstrate typical variabilities and uncertainties.

7.4 Influence of fluid replacement on acoustic wave velocity

The re-use of depleted liquid reservoirs for the storage of gases typically involves replacing water in, for example, a porous sandstone reservoir by the gas to be stored and tracking the replacement through time by acoustic velocity monitoring. Replacing a relatively stiff liquid in pore space by a much more compressible gas reduces the overall stiffness of the rock and hence its P-wave velocity, without much effect on the S-wave velocity. In the case of porous sands, it is usually straightforward to compare

experimentally the velocity of elastic waves with the pores flooded by gas and then filled by water. It is also of interest to know what the effect of such replacement in shale would be.

In the course of this study it was attempted, after all the experiments on YB03P flooded with argon gas, to replace the gas by water through vacuum saturation, and then to measure the velocity behaviour (Chapter 5, section 5.7). However, it was found that the degree of water saturation achieved, even after weeks of post-evacuation soaking, was only about 10% of the initial pore space. Further, instead of the velocity increasing in response to wetting, it decreased, although successive pressure cycles resulted in in progressive increase in the general level of velocity. The decrease in stiffness implied by lower velocities after wetting was attributed to opening of microcracks and pores in response to wetting and water adsorption onto clay mineral surfaces. These observations underline the difficulties of working with wet shale.

There is, however, a well-established body of theory to describe the consequences of pore fluid replacement (Gassman effect), that has been verified mainly through experiments on sandstone (Mavko et al., 2008). Although no experimental verification has been obtained for shale, we can calculate the expected effect of water saturation on shale, making the assumption that the measured K_{dry} will lead to the same value of K_{dry} if the measurements had been made using strain gauges on the outer surface of the specimen.

(Han & Batzle, 2004) provide a critical assessment of the effect of fluid replacement in terms of its effect on velocity.

$$\rho_2 {V_{p2}}^2 = \rho_1 V_{p1} + G(\Phi)\left(K_{f2} - K_{f1}\right) \qquad Eqn. 7.6$$

The product of density with velocity squared is called the compressional modulus. The above equation is equivalent to stating that the saturated bulk modulus equals the dry bulk modulus plus an increment ΔK_{dry}. This approach allows the *P*-velocity effect to be computed without knowing the shear modulus. V_{p1} and V_{p2} are for dry and fluid-saturated rock, ρ_1 and ρ_2 are the corresponding densities, K_{f1} and K_{f2} are corresponding bulk moduli for the pore fluids (fluid $f1$ is unpressurized gas hence K_{f1} is taken to be zero). For water K_f = 2.12 GPa, not significantly affected by pressure above about 10 MPa.

$G(\Phi)$ is the *gain function* of the dry rock frame, given by:

$$G(\Phi) = \frac{[1 - K_n(\Phi)]^2}{\Phi} \qquad Eqn. 7.7$$

in which $K_n = \frac{K_{dry}}{K_0} n$ and is a function of porosity through its dependence on effective pressure. Here, we can try the value of K_{dry} obtained from pore volumometry, and to assume it would be the same as obtained from direct measurement of K_{dry} using strain gauges mounted on the outside surface of the specimen. The only unknown is then V_{p2}, for the water saturated rock. This trend of $K_{dry} = f(P_{eff})$ produces unstable behaviour (non-monotonic), and supports the doubts expressed earlier regarding the significance of K_{dry} obtained from pore volumometry for this rock type. However, Han and Batzle (2004) explore the consequences of making end-member assumptions regarding K_{dry}, according to whether the rock is assumed to be a Voigt or Reuss material. For the Voigt bound (high value of K_{dry}) they show that $K_{dry} = K_0(1 - \phi)$ and that $\Delta K_{dry} = \phi K_f$, hence the simplified gain = ϕ. This gives the minimum stiffening effect due to the liquid saturation. For the Reuss bound they obtain $\Delta K_{dry} \frac{K_0}{\left(1-\phi+\left(\frac{\phi K_0}{K_f}\right)\right)}$, which leads to the maximum stiffening effect and hence greatest velocity increase.

Fig. 7.5 shows fig. 6.7 modified to show additionally the calculated V_p curve for water-saturated Haynesville shale, assuming an averaging of the Voigt and Reuss end members.

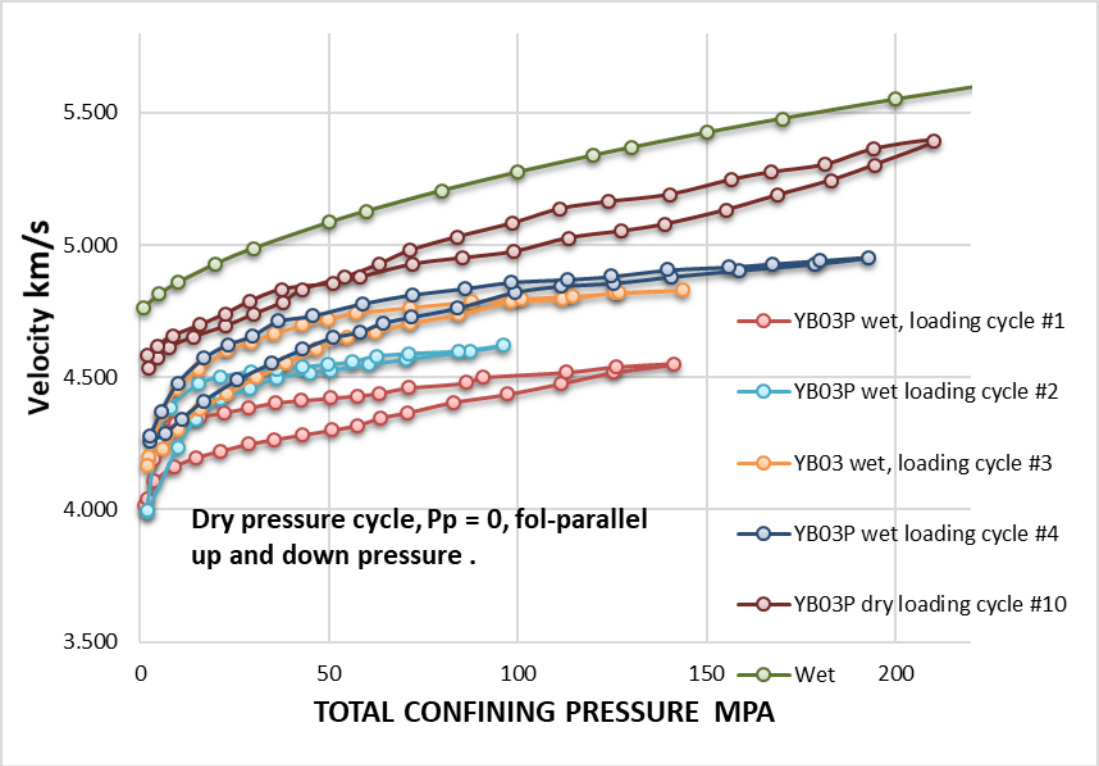

Figure 7.5 Re-presentation of the experimental data shown previously in Fig. 6.7, relating P-wave velocities to confining pressure. The up-down pressure cycling of the dry rock is shown for reference (red points), together with the succession of up-down pressure cycles after attempted saturation with water under vacuum. Successive pressure cycles cause the curves to be progressively displaced to higher velocities. However, all these data still lie below the curves for the dry rock. Additionally, a calculated curve is shown (labelled wet), assuming Voigt-Reuss averaging, to illustrate the faster velocities expected when the rock is fully saturated. Calculated velocities are increased by ca 250 m/s.

The observed behaviour seems to imply that fluid within the pores initially could not escape as a result of pore pressure generated by elastic compaction of the pore/crack space. As we have seen with the effective pressure effect data described above, generation of pore pressure should decrease V_p. Yet we see an increase in velocity with time as the excess P_p is dissipated. Thus, it is inferred that these effects are due to the progressive and cumulative expulsion of pore water from the sample, progressively reducing the capacity for generation of pore pressure with each increase and decrease cycle of confining pressure. This implication of these results is that it is near-impossible to carry out experiments on a tight rock such as shale involving liquid pore pressure in a reasonable period of time.

Experiments on porous, monomineralic sandstones typically display this faster behaviour and accord well with theory based on the Gassman effect. Shales such as this one, with their more complex pore structures and polymineralic compositions, are

expected to require K_{dry} data obtained by direct, external measurement, rather than being calculated indirectly from pore volumometry.

In the field, when the rock is equilibrated with the local pore fluid regime, it would be expected that shales, like sandstones will show higher velocities when saturated with water but, unlike permeable sandstones, may not respond pervasively to the effects of gas injection, owing to the difficulty of displacing existing pore liquids throughout the matrix.

7.5 Incorporating pressure sensitivity into reservoir modelling.

As a shale gas reservoir becomes progressively depleted, the pore pressure falls and the drive to the array of hydraulic fractures and thus to the production well decreases. The assessment of the economic potential of a well depends on establishing the shape of the production drawdown curve and extrapolating it to long periods of time. The economics of shale gas wells is commonly considered on a 20-year timeframe or longer. Fig. 7.6 shows normalized production curves for many wells from the Barnett play. The shape of the curves is typical of many other plays also.

These curves are usually described empirically, by fitting a curve of hyperbolic form or a modified exponential function, and then extrapolating to longer times. Given its importance, a great deal has been written on this topic, e.g. Guao et al. (2017). It has also been noted that as wells become old, the production tends to level off at a low level instead of continuing to decay following the same form as earlier in the history.

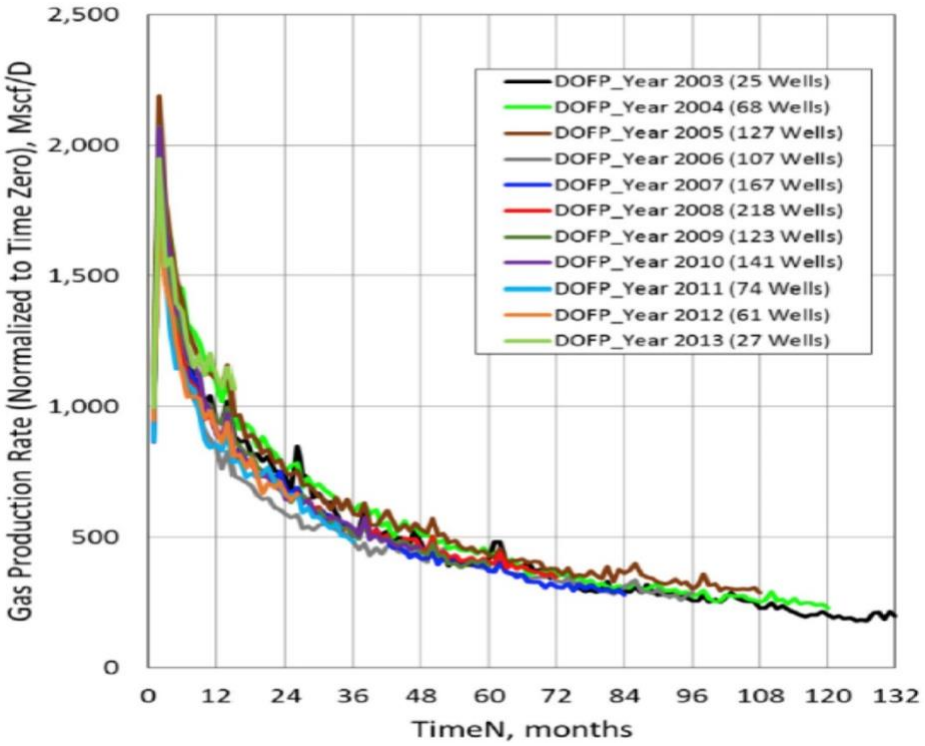

Figure 7.6 Barnett shale average daily gas production rate per well in MSCF/day against time, showing the similarity of the curves (From Kenomore et al. 2018, citing Baihly et al. 2015) MSCF = million standard cubic feet; one standard cubic foot of gas is defined at as 20^{o}C and atmospheric pressure.

Although such curve fitting is not based on physics of flow, at least qualitatively the reasons for the flattening of the decay curve are known (e.g. Wang, 2017):

(a) Most of the pressure decay is from the depletion of free gas in the pore space, but some gas is densely adsorbed onto the surfaces of the organic particles and clay mineral grains. As gas pressure falls below the Langmuir pressure, this adsorbed gas is progressively released, extending the life of the well.

(b) As has been demonstrated in chapter 5.3, slip flow, or Knudsen flow effectively increases the permeability at pore pressures smaller than about 4 MPa (40 atmospheres), increasing the low-pressure production rate.

(c) An additional factor, not previously known about, has emerged from this research. It will be recalled (Chapter 5.5) that (i) only a very small fraction of the total porosity takes part on the flow of gas *through* the specimen, and that (ii) the apparent porosity sampled by the flow is greater for flow across the layering than along it. Bearing in mind that hydraulic fractures are made across the layering, in the expectation that drainage will be more effective along the layering than across it, much of the initially rapid production may arise from only a small proportion of the total porosity, and with the passage of time the

less well-connected blind pores will contribute ever greater fractions to the production, extending it over longer periods of time. Thus, flow *through* (gas in = gas out) a shale is not quite the same thing as drainage of stored gas. This contribution requires further evaluation from experimental and theoretical standpoints.

It is disappointing that the industry has been reluctant to incorporate physical principles into modelling the yield from gas reservoirs, and this is exacerbated by its tendency to characterise permeability as a single number property of a shale, supposedly independent of the pressure state upon it.

The Gas Research Institute gives its name to a method (GRI method), widely used by rock characterization companies, that measures permeability of a sample from the uptake of gas at low pressure into crushed samples of shale (Luffel et al., 1993; Peng & Loucks, 2016). This gives no information on pressure sensitivity; thus, it is assumed that effective pressure has no influence. Given the points made above, that permeability is in fact very sensitive to effective pressure, the information obtained from GRI tests is clearly without significance for reservoir characterisation.

However, a number of authors have drawn attention over many years to the significance of permeability sensitivity to effective pressure in the context of reservoir behaviour, (Rutter et al., 2013; Franquet et al., 2004; Kikani & Pedrosa, 1991; Kwon et al., 2001; and Mckernan et al., 2017) amongst others. It has been common practice to describe the behaviour using a power law or an exponential law of the type

$$k = ko \exp -\gamma(P_C - nP_P) \qquad Eqn. 6.8$$

as was employed here in Chapter 5. The description is purely empirical and is valid only within the limits of the experimental data upon which it is based. It is not based on a physical model, but the important thing is that it adequately describes behaviour for the purpose of reservoir modelling.

Previous work in this laboratory (Rutter et al., 2013; Mckernan et al., 2017) has applied the Lee and Wattenbarger (1996) gas reservoir simulator Gassim6 code (chapter 4, paragraph 4.14) to modelling the behaviour of Whitby shale, and it is extended here to compare with Haynesville shale. The main difference between these two shales in the magnitude of their pressure sensitivity (for the flow of free gas). Whereas Whitby shale exhibits permeability changing by 0.75 orders of magnitude

over the range of typical reservoir effective pressures, Haynesville shale shows a variation of two orders of magnitude.

As the gas pore pressure decreases with production, the pressure drive decreases so that gas flow decreases, even when the permeability is constant. But the rise of effective pressure also reduces the permeability itself, and hence further reduces the production rate. The graphed models (figs. 7.7 through 7.10) show the contrasting behaviour of these two shales. Note, industry field units (psi pressure, distances in feet) are used because these are the units used in modelling. Formation-parallel flow to a single production hydrofracture is modelled, draining into a horizontal borehole (Fig. 7.7). The zone of reduction of permeability propagates away from the hydrofracture into the formation, more rapidly in the case of the Haynesville shale (fig 6.7). The zone of permeability reduction acts like a barrier to gas flow. Note that these models do not incorporate the effect of evolution of adsorbed gas, nor the onset of slip flow at low gas pressures, nor any contribution of slow drainage from less-accessible pore spaces (characterised by a lower permeability) but are potentially significant in the long term. Further, dry gas production is assumed, with no partial saturation of the pore space by formation water.

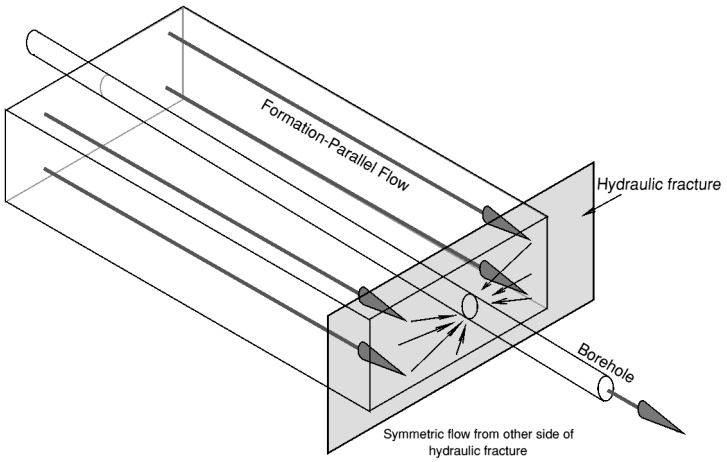

Figure 7.7 Schematic illustration of formation-parallel flow of gas through the rock matrix to a single hydraulic fracture (grey-shaded) draining into a horizontal production borehole. A similar flow is assumed to occur from the other side of the hydraulic fracture. This is the modelled configuration.

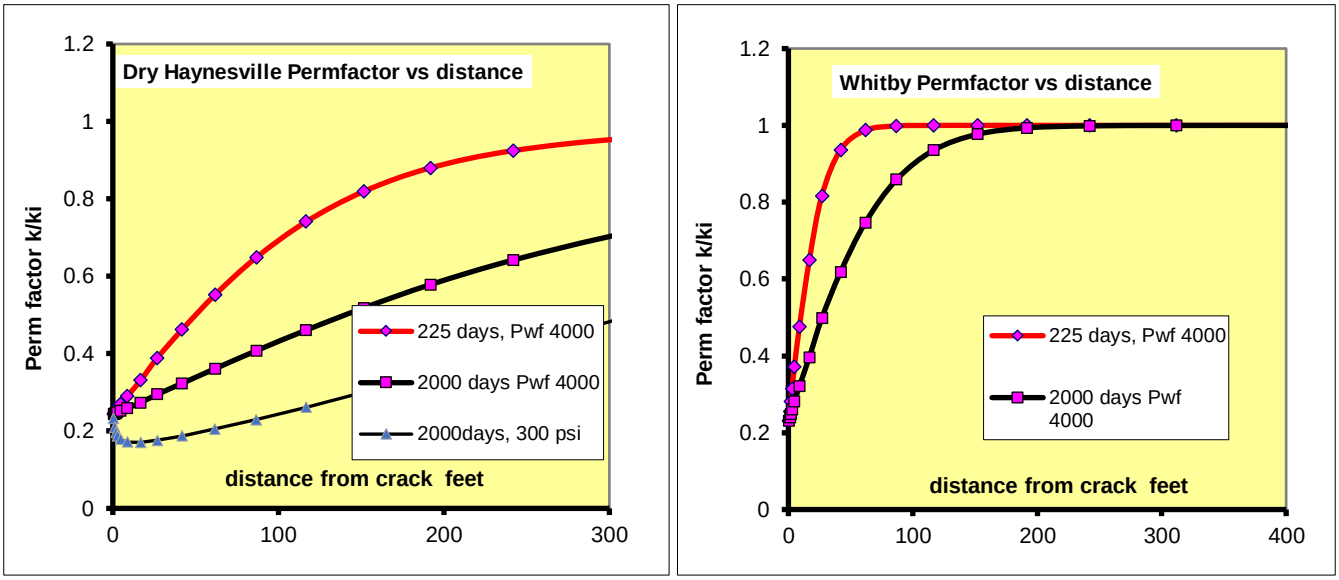

Figure 7.8 Plots of Permeability Factor for Haynesville (left) and Whitby (right) shales versus distance from the hydraulic fracture that drains the gas. Permfactor is the ratio of permeability at distance x divided by initial permeability (or permeability at infinite distance). Permeability decreases near the hydrofracture because gas pressure drawdown increases the effective pressure closer to the fracture. Pwf is downhole gas pressure (psi).

.

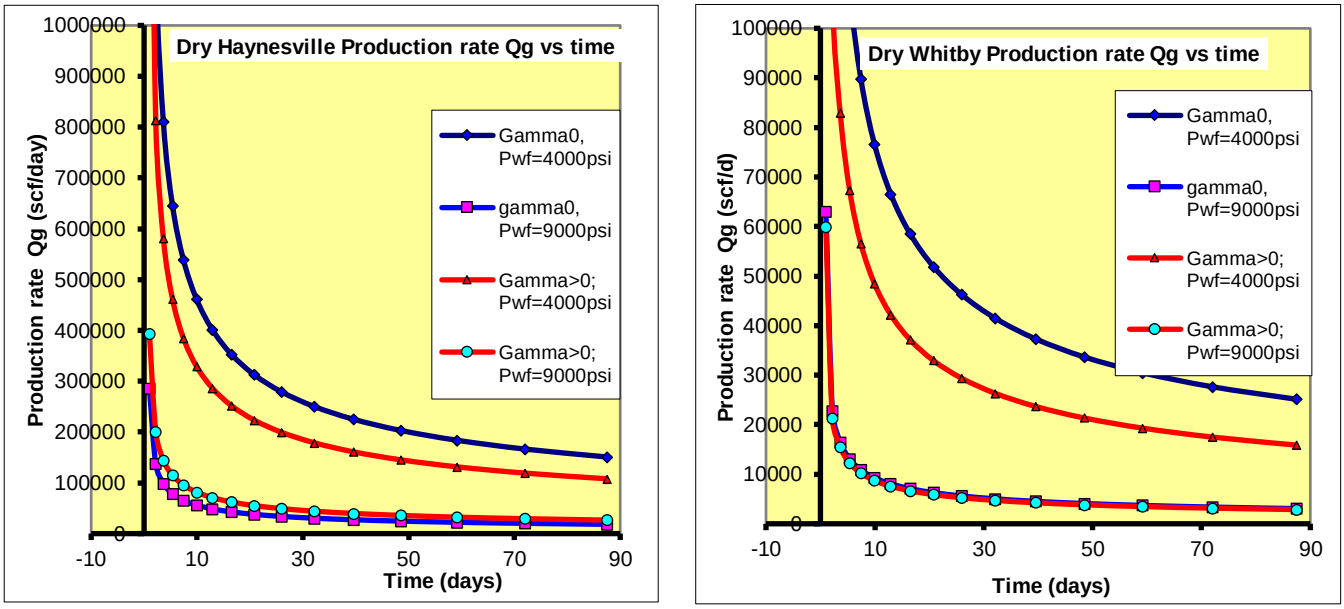

Figure 7.9 Comparative production rates between Haynesville (left) shale and Whitby (right) shale, quantity of gas (scf/day) versus time (days) calculated using Gassim6 (Compare Fig. 6.6) for the first 90 days for a single hydraulic fracture (normally there are 20 or 30 per well). Pwf is the downhole pressure in psi. Gamma is the effective pressure coefficient. When gamma = 0 (blue curves) there is no effective pressure effect on permeability assumed, i.e., permeability is constant. When gamma > 0 the increasing effective pressure drives down the permeability, further reducing production rate (red curves), by about 35% in the case of Whitby shale, and by a smaller amount in the case of Haynesville shale.

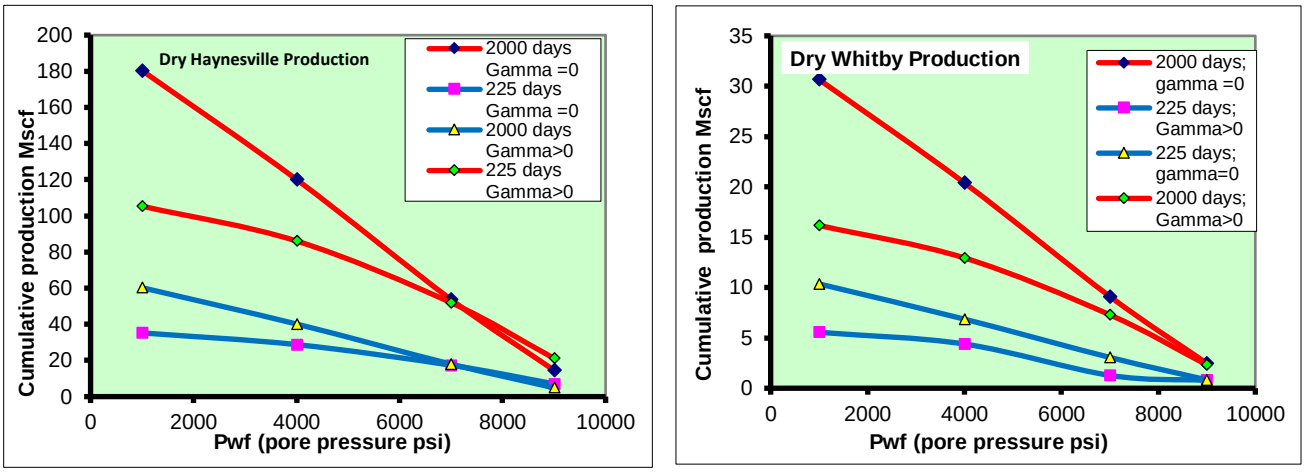

Figure 7.10 Cumulative productions (millions of standard cubic feet) via a single hydraulic fracture calculated using Gassim6 for Haynesville and Whitby shales after 225 days and after 2000 days, each for the case of no permeability sensitivity to effective pressure (Gamma = 0) and with laboratory measured effective pressure sensitivity (Gamma > 0), and each as a function of downhole pressure (Pwf) held constant. The lower the downhole pressure, the greater the pressure gradient driving the gas flow, so the greater the production. The actual downhole pressure would be decided by engineering considerations. In both cases the inclusion of pressure sensitivity to the permeability has a very large effect on the cumulative production, reducing it by around 60%.

The graphics in Figs. 7.8, 7.9 and 7.10 illustrate the dramatic effect of ignoring the effect of pressure sensitivity of permeability if one attempts to estimate the economics of production prior to well development. The propagation of a zone of reduced permeability into the formation acts like a barrier to gas flow (Fig. 7.8), leading to a more rapid decline in production rate with time (Fig. 7.9) and, most importantly, to a substantial reduction in the cumulative gas production (Fig. 7.10). A further source of advance unpredictability is how many of the hydrofrac stages made will be productive. It would be hard to predict this, and against this uncertainty it might be argued that more precise modelling of reservoir behaviour might be of secondary significance.

It is to be expected that shales will often form the cap rock for the storage of gases (CO_2, compressed air, hydrogen, and other waste materials for the 'green' energy revolution). Unlike exploitation of shale gas, which through increase in effective pressure with production tends to reduce production, injection of pressurised gas into an underlying reservoir formation will involve some permeation of gas into the cap formation, increasing its permeability. To ensure minimising of leakage and avoidance of fracturing the seal it will be important to understand well the petrophysical properties of the cap rock. In this thesis only the influence of effective

pressure on the permeability of dry rock only has been explored, but in future the role of partial saturation with water and capillary pressures will have to be taken into account, coupled with a good understanding of the stratigraphy and mineralogy of the cap rock formation(s).

Chapter 8 – Summary and Conclusions

8.1 Summary of the study

With reference to the Jurassic Haynesville shale, an important shale gas play in the southern USA, this study has sought to realise the following aims

- Quantify the relationship between effective stress and permeability in Haynesville Shale over the full range of reservoir total pressure and pore fluid pressure conditions.
- Measure acoustic velocity over the same range of pressure conditions, to characterise the pressure dependence of velocity and how it compares with the influence of pressure on permeability.
- Attempt to identify the influence of mineralogical and microstructural factors controlling permeability.

These aims have been realized to varying degrees. In some respects, the aims were over-ambitious, as far as the range of samples earmarked for study is concerned, and the Covid 19 pandemic adversely influenced the completion of the final stages of the study, data analysis and writing.

A suite of 8 dried samples was prepared from slabbed core from a single well provided by BG International (now Shell) for high pressure testing to measure permeability to argon gas, acoustic wave velocities and pore compressibility by pore volumometry. These included two carbonate-rich intervals and 6 carbonate-poor intervals. In all samples the ratio of phyllosilicates to framework silicate grains was approximately constant. Thin sections were examined optically and some by scanning electron microscopy, and from the microstructures it was pre-supposed that carbonate-rich samples would be of lower permeability and permeability anisotropy. It was aimed to test this inference.

The mineralogy of all samples was determined by quantitative x-ray diffraction and porosity was determined by helium pycnometry combined with gravimetry. These data were used to infer the grain aggregate elastic properties by Voigt-Reuss-Hill (V-R-H) averaging of mineral proportions and V-R-H elastic properties of individual minerals. Total Organic Carbon content of all samples was also measured,.

It proved impossible in the time frame available to test all samples (in two orientations) in equal ways, hence the coverage of the 8 samples has been uneven.

This is reflected in the results overall. Additionally, it was not possible to obtain equally good quality core samples for testing from all the selected 8 intervals chosen from the supplied slabbed cores.Two different items of high-pressure testing equipment were used for the permeability tests, the *CoreTest* rig operating at total pressures up to 60 MPa and the *BigRig* operating to total pressures in excess of 100 MPa. A separate machine *Green Rig* was used for acoustic velocity measurements up to 210 MPa total confining pressure, and for pore volumometry measurements. Permeabilities were measured using three methods, the steady-state flow method, the pulse transient method but mainly the oscillating pore pressure method. The permeabilities of all samples were strongly sensitive to effective pressure, with permeability decreasing rapidly at low pressures and less rapidly at higher pressures, as the effective pressure constricted the conductive pore channels. The influence of pore pressure on the permeability was also measured, and the effective pressure law was found to apply with a pore pressure coefficient close to unity.

8.2 summary of Main Findings

(a) Microstructural observations made optically cannot be correlated to differences in permeability in the Haynesville shale.

(b) The measured samples could not provide a clear answer to the question of the extent to which bulk mineralogy plays a defining role in defining the permeability of Haynesville shale,. Only one carbonate-rich sample was measured, but this was done much more extensively than for other samples. Under comparable conditions, the carbonate-rich sample was less permeable that the more siliceous ones.

(c) Permeabilities were measured over repeated effective pressure cycles, and a detailed characterisation of the permeability characteristics of sample YB03 in particular was obtained. In the first cycle the permeability was higher than in the subsequent ones, which were reproducible and non-linear elastic. The initial pressure cycle is inferred to have repaired much of the damage sustained by cores during recovery from the borehole followed by drilling and cutting.

(d) For the extensively studied carbonate-rich sample YB03, it was shown that only a small fraction of the total porosity was involved in flow through the specimen parallel to the layering and only a slightly larger fraction across the layering. This led to a descriptive model for the pore structure in terms of thin (nanometric), crack like pores lying close to the layering and through which most conduction occurred, and a population of larger, more equant, less-well connected pores that accounted for most of the gas storage capacity.

(e) Most acoustic wave velocities were measured on the same carbonate-rich sample (YB03) as used for permeability measurements, and in parallel pore compressibility was measured by means of pore volumometry.

(f) Sample YB03 was found to follow the effective stress law for velocities with a pore pressure coefficient of close to 0.8. Pore volumometry yielded a measure of bulk rock compressibility that was very sensitive to effective pressure, and this was inferred to account for the observed high-pressure sensitivity of permeability.

(g) It was concluded that the differences in behaviour of the rock in terms of pore pressure influences on the permeability and acoustic wave velocities meant that it was not possible directly to infer information about permeability from acoustic wave velocity measurements.

(h) The implications of the results obtained were explored from the point of view of the behaviour of shales under reservoir conditions. From reservoir modelling using *Gassim6* it was inferred that ignoring the marked sensitivity of permeability to effective pressure would lead to serious overestimation of the rate of yield and cumulative yield of a shale gas reservoir.

(i) Whilst the hydrocarbon industry routinely does not attempt to predict in advance the expected behaviour of a shale gas reservoir based on relevant laboratory testing, this approach would be ill-advised in the context of using shale cap rocks to existing depleted conventional reservoirs that might be used in future to store pressurised gases such as compressed air, carbon dioxide and hydrogen, because pressurising the pores of shales is likely to increase permeability and hence the possibility of leakage or even seal failure. Careful management of the pressure regime will be required.

8.3 Future Work

1. Laboratory permeability measurements may be complemented by multi scale imaging of the experimental samples using multiple techniques, such as Transmission electron microscopy (TEM), FIB (SEM), X-ray radiography in 2D and 3D, or X-ray computed tomography. These techniques can be used for correlative imaging workflow and quantification, whilst bearing in mind that these are complicated and time-consuming techniques to employ. Combining laboratory petrophysical studies with complementary detailed high-resolution imaging, even for one rock type, is clearly a team endeavour and cannot be carried out by a single researcher.

   The laboratory measurement of acoustic wave velocities as a function of confining pressure and pore pressure is an important aim, because it can aid the interpretation of in-situ seismic tomography to infer variations of pore pressure, for example. There is a need to investigate frequency dispersion effects on seismic velocities, so that results from laboratory ultrasonic measurements can be applied to low seismic frequencies. However, such investigations are challenging for shales, owing to the difficulties posed by low permeabilities and a slow pore pressure response to elastic volume strains following confining pressure changes. When the influence of a high viscosity fluid such as water is considered, the technical difficulties become well-nigh impossible, and a polar fluid like water also provokes microstructurally damaging interactions as a result of fluid absorption. It remains unclear how these issues can be successfully overcome using time-of-flight velocity measurement techniques.

2. The variability of mineralogy and microstructures of shales is reflected in corresponding variability of petrophysical characteristics, and this is demonstrated in our recently published comparative study of two very different shales (carbonate-rich Haynesville shale YB03, a phyllosilicate-rich, carbonate-free Bowland shale, and a tight gas sandstone (Rutter, Mecklenburgh, & Bashir 2022). Given the present and future economic importance of shales, further comparative studies are required, extending over a wider range of rock types than it has been possible to consider here, and probably requiring a team-based approach.

References

Al-Hussainy, R., Ramey, H.J., Crawford, P.B. 1966. The flow of real gases through porous media. Journal of Petroleum Technology, 237, 624-636

Anez, L., Calas-Etienne, S., Primera, J., & Woignier, T. (2014). Gas and liquid permeability in nano composites gels: Comparison of Knudsen and Klinkenberg correction factors. Microporous and Mesoporous Materials, 200, 79–85. https://doi.org/10.1016/j.micromeso.2014.07.049

Aplin, A. C., Fleet, A. J., and Macquaker, J. H. (1999). Muds and mudstones: physical and fluid-flow properties. Geological Society, London, Special Publications, 158(1): 1–8.

Bahmaei, Z., & Hosseini, E. (2020). Pore pressure prediction using seismic velocity modeling: case study, Sefid-Zakhor gas field in Southern Iran. Journal of Petroleum Exploration and Production Technology. https://doi.org/10.1007/s13202-019-00818-y. 1051–1062

Baihly, J.D., et al., 2015. Shale gas production decline trend Comparison over time and basins revisited. In: Unconventional Resources Technology Conference. https://doi.org/10.15530/URTEC-2015-2172464.

Bernabé, Y., Mok, U., & Evans, B. (2006). A note on the oscillating flow method for measuring rock permeability. International Journal of Rock Mechanics and Mining Sciences, 43(2), 311–316. https://doi.org/10.1016/j.ijrmms.2005.04.013

Biot, M. A. (1962). Mechanics of Deformation and Acoustic Propagation in Porous Media. Journal of Applied Physics, 33(4), 1482–1498.

Biot, M., & Willis, D. (1957). The elastic coefficients of the theory of consolidation," Journal of Applied Mechanics, Vol. 24, pp. 594-601.

Birch, F. (1960). The velocity of compressional waves in rocks to 10 kilobars, part 1. Elastic Properties and Equations of State, 65, 91–116. https://doi.org/10.1029/sp026p0091

Birch, F. (1961). The velocity of compressional waves in rocks to 10 kilobars, part 2. Elastic Properties and Equations of State, 66(7), 91–116. https://doi.org/10.1029/sp026p0091

Bjorlykke, K. (1999). Principal aspects of compaction and fluid flow in mudstones. Geological Society, London, Special Publications, 158(1), 73–78. https://doi.org/10.1144/GSL.SP.1999.158.01.06

Boggs, S. (2009). Petrology of Sedimentary Rocks. Cambridge University Press, Cambridge UK. https://doi.org/10.1017/CBO9780511626487

Bohacs, K. M., Macquaker, J. O. E. H. S., Schieber, J., & Demko, T. M. (2015). Capturing key attributes of fine-grained sedimentary rocks in outcrops, cores, and thin sections: nomenclature and description guidelines. Journal of Sedimentary Research. 230–246. http://dx.doi.org/10.2110/jsr.2015.11

Bowers, G. L. (2002). Detecting high overpressure. Leading Edge (Tulsa, OK). https://doi.org/10.1190/1.1452608

Brace, W. F., Walsh, J. B., & Frangos, W. T. (1968). Permeability of granite under high pressure. Journal of Geophysical Research, 73(6), 2225–2236. https://doi.org/10.1029/JB073i006p02225

Bush, D., & Jenkins, R. (1970). Proper hydration of clays for rock property determinations. Journal of Petroleum Technology, 22(7). https://doi.org/10.2118/2589-PA

Bust, V. K., Majid, A. A., Oletu, J. U., & Worthington, P. F. (2013). The petrophysics of shale gas reservoirs: Technical challenges and pragmatic solutions. Petroleum Geoscience, 19(2), 91–103. https://doi.org/10.1144/petgeo2012-031

Bustin, R. M., Bustin, A. M. M., Cui, A., Ross, D., & Pathi, V. M. (2008). Impact of Shale Properties on Pore Structure and Storage Characteristics. SPE Shale Gas Production Conference. https://doi.org/10.2118/119892-MS

Carman P.C, 1937. Fluid flow through granular beds. Institution of Chemical Engineers, London, 15: 150-166. https://doi.org/10.1016/S0263-8762(97)80003-2

Christensen, N. I. (1984). Pore pressure and oceanic crustal seismic structure. Geophysical Journal of the Royal Astronomical Society. https://doi.org/10.1111/j.1365-246X.1984.tb02232.x

Cui, X., Bustin, A. M. M., & Bustin, R. M. (2009). Measurements of gas permeability and diffusivity of tight reservoir rocks: different approaches and their applications. Geofluids, 9(3), 208–223. https://doi.org/10.1111/j.1468-8123.2009.00244.x

David, C., Wassermann, J., Amann, F., Klaver, J., Davy, C., Sarout, J., Esteban, L., Rutter, E. H., Hu, Q., Louis, L., Delage, P., Lockner, D. A., Selvadurai, A. P. S., Vanorio, T., Hildenbrand, A. A.,

Meredith, P. G., Browning, J., Mitchell, T. M., Madonna, C., … Clark, A. (2018). KG2B, a collaborative benchmarking exercise for estimating the permeability of the Grimsel granodiorite-Part 2: Modelling, microstructures and complementary data. Geophysical Journal International. https://doi.org/10.1093/GJI/GGY305

David, E. C., and Zimmerman, R. W., 2012, Pore structure model for elastic wave velocities in fluid-saturated sandstones: Journal of Geophysical Research: Solid Earth, v. 117, no. B7, p. B07210.

Day-Stirrat, R. J., Schleicher, A. M., Schneider, J., Flemings, P. B., Germaine, J. T., & van der Pluijm, B. A. (2011). Preferred orientation of phyllosilicates: Effects of composition and stress on resedimented mudstone microfabrics. Journal of Structural Geology, 33(9), 1347–1358. https://doi.org/10.1016/j.jsg.2011.06.007

Dandekar. (2013). Petroleum Reservoir Rock and Fluid Properties. Florida: Chapman and hall/CRC. https://doi.org/10.1192/bjp.112.483.211-a

Dicker, A. I., & Smits, R. M. (1988). A Practical Approach for Determining Permeability From Laboratory Pressure-Pulse Decay Measurements. International Meeting on Petroleum Engineering. https://doi.org/10.2118/17578-MS

Doebelin, N., & Kleeberg, R. (2015). Profex: A graphical user interface for the Rietveld refinement program BGMN. Journal of Applied Crystallography. https://doi.org/10.1107/S1600576715014685

Dowey, P. J., & Taylor, K. G. (2019). Diagenetic mineral development within the Upper Jurassic Haynesville-Bossier Shale, USA. Sedimentology. https://doi.org/10.1111/sed.12624

Eberhart-Phillips, D., Han, D. H., & Zoback, M. D. (1989). Empirical relationships among seismic velocity, effective pressure, porosity, and clay content in sandstone. Geophysics. https://doi.org/10.1190/1.1442580

Faulkner, D. R., & Rutter, E. H. (2010). Comparisons of water and argon permeability in natural clay-bearing fault gouge under high pressure at 20°C. Journal of Geophysical Research: Solid Earth, 105(B7), 16415–16426. https://doi.org/10.1029/2000jb900134

Fischer, G. J. (1992). Chapter 8 The Determination of Permeability and Storage Capacity: Pore Pressure Oscillation Method. International Geophysics, 51(C), 187–211. https://doi.org/10.1016/S0074-6142(08)62823-5

Franquet, M., Ibrahim, M., Wattenbarger, R. A., & Maggard, J. B. (2004). Effect of pressure-dependent permeability in tight gas reservoirs, transient radial flow. Canadian International Petroleum Conference 2004, CIPC 2004. https://doi.org/10.2118/2004-089

Geertsma, J. (1957). A remark on the analogy between thermoelasticity and the elasticity of saturated porous media. Journal of the Mechanics and Physics of Solids. https://doi.org/10.1016/0022-5096(57)90042-X

Gipson, J. (1965). Application of the Electron microscope to the study of particle orientation and fissility in shale. Sedimentary Research, 408-414.

Ghanizadeh, A., Gasparik, M., Amann-Hildenbrand, A., Gensterblum, Y., & Krooss, B. M. (2014). Experimental study of fluid transport processes in the matrix system of the European organic-rich shales: I. Scandinavian Alum Shale. Marine and Petroleum Geology, 51, 79–99. https://doi.org/10.1016/j.marpetgeo.2013.10.013

Gosman, A., & Sedlaček, J. (1969). Radiochemical study of selfdiffusion and isotope exchange in aqueos solutions part i. selfdiffusion of t1(i) and tl(iii) ions in a perchloric acid medium. Radiochimica Acta. https://doi.org/10.1524/ract.1969.11.2.112

Gosman, A.L., R.D. McCarty, and J.G. Hust (1969), Thermodynamic properties of argon from the triple point to 300 K at pressures to 1000 atmospheres. National Standard Reference Data Series, National Bureau of Standards, 27, US Department of Commerce, Washington, DC.

Guo, K., Zhang, B., Wachtmeister, H., Aleklettb,K. Höök, M. 2017. Characteristic Production Decline Patterns for Shale Gas Wells in Barnett International Journal Sustainable Future for Human Security J-Sustain Vol. 5, No. 1 P. 12-21.

Hammes, U. (2009). Sequence stratigraphy and core facies of the Haynesville Mudstone, East Texas. Gulf Coast Association of Geological societies, V. 59, p. 321–324.

Hammes, U., & Gale, J. (2013). Introduction. Memoir 105: Geology of the Haynesville Gas Shale in East Texas and West Louisiana, 11–14. https://doi.org/10.1306/13441841M1053596

Hammes, U., Hamlin, H. S., & Ewing, T. E. (2011). Geologic analysis of the upper jurassic Haynesville shale in east Texas and west Louisiana. AAPG Bulletin, 95(10), 1643–1666. https://doi.org/10.1306/02141110128

Han, D. H., Nur, A., & Morgan, D. (1986). Effects of porosity and clay content on wave velocities in sandstones. Geophysics. https://doi.org/10.1190/1.1442062

Han, De Hua, & Batzle, M. L. (2004). Gassmann's equation and fluid-saturation effects on seismic velocities. Geophysics. https://doi.org/10.1190/1.1707059

Haris, A., Parlindungan, E., & Riyanto, A. (2017). Pore pressure prediction in laminated shaly sand reservoir: A case study of Bintuni Basin. AIP Conference Proceedings. https://doi.org/10.1063/1.4991265

Healy, D., Erik Timms, N., & Alan Pearce, M. (2020). The variation and visualisation of elastic anisotropy in rock-forming minerals. Solid Earth. https://doi.org/10.5194/se-11-259-2020

Heller, R., Vermylen, J., & Zoback, M. (2014). Experimental investigation of matrix permeability of gas shales. AAPG Bulletin. https://doi.org/10.1306/09231313023

Jaeger, J., Cook, N. G., & Zimmerman, R. (2007). Fundamentals of Rock Mechanics, 4th Edition. In Journal of Chemical Information and Modelling. https://doi.org/10.1017/CBO9781107415324.004

Kenomore, M. Hassan, M. Malakooti, R, Dhakal, H. Shah, A (2018) Shale gas production decline trend over time in the Barnett Shale. Journal of Petroleum Science and Engineering 165 (2018) 691–71)

Jones, L. E. A., & Wang, H. F. (1981). Ultrasonic velocities in Cretaceous shales from the Williston basin. Geophysics, 46(3), 288–297. https://doi.org/10.1190/1.1441199

Kikani, J., & Pedrosa, O. A. (1991). Perturbation analysis of stress-sensitive reservoirs. SPE Formation Evaluation. https://doi.org/10.2118/20053-pa

Kranz, R. L., Saltzman, J. S., & Blacic, J. D. (1990). Hydraulic diffusivity measurements on laboratory rock samples using an oscillating pore pressure method. International Journal of Rock Mechanics and Mining Sciences And, 27(5), 345–352. https://doi.org/10.1016/0148-9062(90)92709-N

Kundt, A. and Warburg, E., 1875, Poggendorfs, Annu. Rev. Plant Physiol. Plant Mol. Biol., 155, pp. 337-525

Kwon, O., Kronenberg, A. K., Gangi, A. F., & Johnson, B. (2001). Permeability of Wilcox shale and its effective pressure law. Journal of Geophysical Research: Solid Earth. https://doi.org/10.1029/2001jb000273

Lafargue, E., Marquis, F., & Pillot, D. (1998). Rock-Eval 6 Applications in Hydrocarbon Exploration, Production, and Soil Contamination Studies. Revue de l'Institut Français Du Pétrole, 53(4), 421–437. https://doi.org/10.2516/ogst:1998036

Lazar, R., Bohacs, K. M., Macquaker, J., & Demko, T. (2012). Mudstone Primer: Society for sedimentary Geology. SEPM Volume12 https://doi.org/10.2110/sepmcsp.12.

Lazar, O. R., Bohacs, K. M., Macquaker, J. H., Schieber, J., and Demko, T. M. (2015). Capturing key attributes of fine-grained sedimentary rocks in outcrops, cores, and thin sections: nomenclature and description guidelines. Journal of Sedimentary Research, 85(3):230–246

Lee, J., Wattenbarger, R. A., 1996. Gas reservoir engineering. Society of Petroleum Engineers Textbook Series v. 5, Richardson, Texas, 34p 9p

Luffel, D. L., & Guidry, F. K. (1992). New Core Analysis Methods for Measuring Reservoir Rock Properties of Devonian Shale. Journal of Petroleum Technology, 44(11), 1184–1190. https://doi.org/10.2118/20571-PA

Luffel, D. L., Hopkins, C. W., & Schettler, P. D. (1993). Matrix permeability measurement of gas productive shales. Proceedings - SPE Annual Technical Conference and Exhibition. https://doi.org/10.2118/26633-ms

Ma L, Patrick J. Dowey , Ernest Rutter , Kevin G. Taylor , Peter D. Lee. (2019). A novel upscaling procedure for characterising heterogeneous shale porosity from nanometer-to millimetre-scale in 3D. https://doi.org/10.1016/j.energy.2019.06.011

Ma, L. 2016. Multi-scale 3D imaging of the microstructure in organic-rich shales. PhD thesis, University of Manchester,Manchester, UK.

Ma, L., Taylor, K.G., Lee, P.D., Dobson, K.J., Dowey, P.J. & Courtois, L. 2016. Novel 3D centimetre-to nano-scale quantification of an organic-rich mudstone: the Carboniferous Bowland Shale, Northern England Marine and Petroleum Geology, 72, 193–205, https://doi.org/10.1016/j.marpetgeo.2016.02.008

Ma, L., Slater, T., Dowey, P. J., Yue, S., Rutter, E. H., Taylor, K. G., & Lee, P. D. (2018). Hierarchical integration of porosity in shales. Scientific Reports. https://doi.org/10.1038/s41598-018-30153-x

Ma, Y., Zhong, N., Li, D., Pan, Z., Cheng, L. & Liu, K.2015. Organic matter/clay mineral intergranular pores in the Lower Cambrian Lujiaping Shale in the northeastern part of the upper Yangtze area, China: a possible microscopic mechanismfor gas preservation. International Journal of Coal Geology, 137, 38–54, https://doi.org/10.1016/j.coal.2014.11.001

MacQuaker, J. H. S., & Gawthorpe, R. L. (1993). Mudstone lithofacies in the Kimmeridge Clay Formation, Wessex Basin, southern England; implications for the origin and controls of the

distribution of mudstones. Journal of Sedimentary Research, 63(6), 1129–1143. https://doi.org/10.1306/D4267CC1-2B26-11D7-8648000102C1865D

Mavko, G., & Vanorio, T. (2010). The influence of pore fluids and frequency on apparent effective stress behavior of seismic velocities. Geophysics. https://doi.org/10.1190/1.3277251

Mavko, G., Mukerji, T., and Dvorkin, J., 2009, The rock physics handbook: tools for seismic analysis of porous media, Cambridge, Cambridge University Press. Cambridge, UK. (Vol. 112, Issue 483). https://doi.org/10.1192/bjp.112.483.211-a

MATLAB (2013). version 8.10.0 (R2013a). The MathWorks Inc., Natick, Massachusetts.

Mckernan, R. E., Rutter, E. H., Mecklenburgh, J., & Taylor, K. G. (2014). SPE 14UNCV-167762-MS Influence of Effective Pressure on Mudstone Matrix Permeability: Implications for Shale Gas Production. SPE/EAGE European Unconventional Conference and Exhibition Held Vienna, 13. https://doi.org/10.2118/167762-MS

Mckernan, R., Mecklenburgh, J., Rutter, E., & Taylor, K. (2017). Microstructural controls on the pressure-dependent permeability of Whitby mudstone. Geological Society Special Publication, 454(1). https://doi.org/10.1144/SP454.15

Nur, A., & Byerlee, J. D. (1971). An exact effective stress law for elastic deformation of rock with fluids. Journal of Geophysical Research. https://doi.org/10.1029/jb076i026p06414

Ojo, S.A., Olatinsu, O.B., Ozebo, V.C., 2018. Rock type based poroperm and continuous permeability predictions in a tight gas formation. Ife Journal of Science vol. 20, no. 1 (2018). https://dx.doi.org/10.4314/ijs.v20i1.2

Peng, S., & Loucks, B. (2016). Permeability measurements in mudrocks using gas-expansion methods on plug and crushed-rock samples. Marine and Petroleum Geology. https://doi.org/10.1016/j.marpetgeo.2016.02.025

Philipp, T., Laurich, B., Desbois, G., Littke, R., Urai, J. L., Geology, S., Group, M. R., Resources, M., & Division, S. P. (2017). The effect of microstructural heterogeneity on pore size distribution and permeability in Opalinus Clay (Mont Terri, Switzerland): insights from an integrated study of laboratory fluid flow and pore morphology from BIB-SEM images. Geomechanical and Petrophysical Properties of Mudrocks, Special Publications 454, 85–106.

Potter, P. E., Maynard, J. B., & Depetris, P. J. (2005). Mud and mudstones: Introduction and overview. In Mud and Mudstones: Introduction and Overview. https://doi.org/10.1007/b138571

Reading, H.G. (2001) Clastic Facies Models: A Personal Perspective. Bulletin of the Geologic Society of Denmark, 48, 101-125.

Rutter E, Mecklenburgh J, Bashir y (2022) Matrix gas flow through "impermeable" rocks – shales and tight sandstone YSolid Earth 13(3) 725-743

Rutter E. H. and Mecklenburgh J.: Hydraulic conductivity of bedding-parallel cracks in shale as a function of shear and normal stress, in: Geomechanical and petrophysical proper- ties of mudrocks, edited by: Rutter, E., Mecklenburgh, J., and Taylor, K., Geological Society of London Special Publica- tion, Vol. 454, London, UK, Geological Society of London, https://doi.org/10.1144/SP454.9, 2017.

Rutter, E. H, R. McKernan, J. Mecklenburgh, S. E. May. (2013) Permeability of Stress-sensitive Formations: its Importance for Shale Gas Reservoir Simulation and Evaluation. Petro Industry News Aug/Sept:44-45, September, 44–45.

Rutter, E. H., Mckernan, R. E., Mecklenburgh, J., and May, S. E. (2013b) EIA. (2011). Haynesville-Bossier Shale Play, Texas-Louisiana Salt Basin. 2011. http://www.eia.gov/pub/oil_gas/natural_gas/analysis_publications/maps/maps.htm

Rutter, E. H., and Mecklenburgh, J., 2018, Influence of Normal and Shear Stress on the Hydraulic Transmissivity of Thin Cracks in a Tight Quartz Sandstone, a Granite, and a Shale: Journal of Geophysical Research: Solid Earth, v. 123, no. 2, p. 1262-1285.

Rutter, E. H. and Mecklenburgh, J.: Experimental data on tight rock permeability, NERC EDS National Geoscience Data Cen- tre [data set and code], https://doi.org/10.5285/7dca47c4-1542- 4b14-9505-72666b78938b, 2022.

Rutter, E., Mecklenburgh, J., and Bashir, Y. (2022) Datafile DF1 + Matlab Scripts, Zenodo [data set and code], https://doi.org/10.5281/zenodo.5914205, 2021.

Sayers, C. M. (2013). The effect of anisotropy on the Young's moduli and Poisson's ratios of shales. Geophysical Prospecting. https://doi.org/10.1111/j.1365-2478.2012.01130.x

Seeburger, D. A., & Nur, A. (1984). A pore space model for rock permeability and bulk modulus. Journal of Geophysical Research. https://doi.org/10.1029/JB089iB01p00527

Shi, J. Q., & Durucan, S. (2016). Near-exponential relationship between effective stress and permeability of porous rocks revealed in Gangi's phenomenological models and application to gas shales. International Journal of Coal Geology. https://doi.org/10.1016/j.coal.2015.12.014

Skempton, A. W. (1960). The Pore-Pressure Coefficient in Saturated Soils. Geotechnique. https://doi.org/10.1680/geot.1960.10.4.186

Smith, T. M., Sondergeld, C. H., & Rai, C. S. (2003). Gassmann fluid substitutions: A tutorial. Geophysics. https://doi.org/10.1190/1.1567211

Somvanshi, P. R., & Venkatesh, K. V. (2013). Hill Equation. In Encyclopedia of Systems Biology. https://doi.org/10.1007/978-1-4419-9863-7_946

Sone, H., & Zoback, M. D. (2013). Mechanical properties of shale-gas reservoir rocks — Part 1: Static and dynamic elastic properties and anisotropy. GEOPHYSICS, 78(5), D381–D392. https://doi.org/10.1190/geo2013-0050.1

Spain, D. R., & Anderson, G. a. (2010). Controls on Reservoir Quality and Productivity in the Haynesville Shale, North-western Gulf of Mexico Basin. Gulf Coast Association of Geological Societies Transactions, 60, 657–668.

Sprunt, E. S., & Nur, A. (1980). Another look at pore structure: Cathodoluminescence petrography. Trans SPWLA Annual Logging Symposium 21st. http://www.scopus.com/inward/record.url?eid=2-s2.0-0019286994&partnerID=40&md5=d100ae03ebd01b1fcc2df2a7428536a7

Steiner, S., Ahsan, S. A., Raina, I., Dasgupta, S., & Lis, G. P. (2016). Interpreting Total Organic Carbon TOC in Source Rock Oil Plays. https://doi.org/10.2118/183050-ms 7–10

Stow, D. A. V. (1981). Fine-grained sediments: Terminology. Quarterly Journal of Engineering Geology and Hydrogeology, 14(4), 243-244. https://doi.org/10.1144/GSL.QJEG.1981.014.04.02

Strout, J. M., & Tjelta, T. I. (2005). In situ pore pressures: What is their significance and how can they be reliably measured? Marine and Petroleum Geology. https://doi.org/10.1016/j.marpetgeo.2004.10.024

Suganuma, T. (1985). Measurement of surface topography using SEM with two secondary electron detectors. Journal of Electron Microscopy, Volume 34, P. 328–337, https://doi.org/10.1093/oxfordjournals.jmicro.a050525

Taylor, R. L., Rutter, E. H., Nippress, S. E. J., & Brodie, K. H. (2015). Seismic velocity modelling of the Carboneras Fault Zone, SE Spain. Tectonophysics. https://doi.org/10.1016/j.tecto.2015.01.001

Terzaghi, K. 1923. Theoretical Soil Mechanics. John Wiley, New York.

Todd, T., & Simmons, G. (1972). Effect of pore pressure on the velocity of compressional waves in low-porosity rocks. Journal of Geophysical Research. https://doi.org/10.1029/jb077i020p03731

Varfolomeev, I. (2016). Integrated study of thin sections: Optical Petrography and Electron Microscope. SPE, 1-7. Paper presented at the SPE Russian Petroleum Technology Conference and Exhibition, Moscow, Russia, https://doi.org/10.2118/182071-MS

Walsh, J. B. (1965). The effect of cracks on the compressibility of rock. Journal of Geophysical Research, 70(2), 381–389. https://doi.org/10.1029/jz070i002p00381

Wang, F P, & Reed, R. M. (2009). Pore Networks and Fluid Flow in Gas Shales. SPE Annual, SPE 124253, 8. https://doi.org/10.2118/124253-MS

Wang, Fred P., Hammes, U., & Li, Q. (2013). Overview of the Haynesville Shale Properties and Production. Memoir 105: Geology of the Haynesville Gas Shale in East Texas and West Louisiana, 155–177. https://doi.org/10.1306/13441848M1053527

Wang, H. 2017. What Factors Control Shale Gas Production and Production Decline Trend in Fractured Systems: A Comprehensive Analysis and Investigation. SPE Journal, Vol 22(02): 562-581. http://dx.doi.org/10.2118/179967-PA

Wonham, J. P, M. Cyrot, T. Nguyen, J. Louhouamou & O. Ruau.2010. Integrated approach to geomodelling and dynamic simulation in a complex mixed siliciclastic–carbonate reservoir, N'Kossa field, Offshore Congo Jolley, S. J., Fisher, Q. J., Ainsworth, R. B., Vrolijk, P. J. & Delisle, S. (eds) Reservoir Compartmentalization. Geological Society, London, Special Publications, 347, 133–163.

Wyllie, M. R. J., Gregory, A. R., & Gardner, L. W. (1956). Elastic Wave Velocities in Heterogeneous and Porous Media. Geophysics, 21(1), 41–70. https://doi.org/10.1190/1.1438217

Zoback, M. D., & Byerlee, J. D. (1975). The effect of cyclic differential stress on dilatancy in westerly granite under uniaxial and triaxial conditions. Journal of Geophysical Research, 80(11), 1526–1530. https://doi.org/10.1029/jb080i011p01526

Zolotukhin, J. & Rune. U. (1997). Fundamentals of Petroleum Reservoir Engineering. Norwegian Academic Press, Gubkin Russian State University of Oil and Gas (Moscow, Russia) p. 31-79